IMPROVING THE PERFORMANCE OF NATURAL RUBBER USING GRAPHENE AND ITS DERIVATIVES

A Thesis submitted by

Dongning HE, M Eng

For the award of

Doctor of Philosophy

2018

Abstract

In this research project, modified graphene was employed as filler to enhance the electrical conductivity and to reinforce mechanical properties of natural rubber (NR). The defect sites in the graphene sheets were investigated for further modification. The latex mixing and mechanical mixing methods to load functional graphene sheets into the NR matrix, improved the mechanical and electrical properties of the composite material. Graphene was prepared by a chemical oxidation-reduction approach to fill the NR matrix. The oxidation approaches were employed in progress, which will induce various defects in the final product. It is known that these defects decrease the properties of the graphene and graphene/natural rubber composites, which are prepared by traditional method as well. However, these defects could cause improvements in performance of the graphene composites with re-designed methods, the main focus of this thesis.

Before loading into NR matrix, the defect information of graphene oxide (GO) prepared using Hummers method was examined through positron testing, which is known to be highly effective in the study of the defects in graphite and its derivatives. The different types of defects were detectable, which revealed that the vacancy clusters and vacancy-oxygen group complexes were present on the GO sheets. No large open-volume hole was detected in GO.

The reduction of GO by potassium carbonate (K_2CO_3) as a green noble preparation approach was developed, and the oxygen groups dispersion status in the GO sheet was further investigated. K_2CO_3 was used as a reusable reduction agent to convert GO to reduced graphene oxide (RGO) in two steps, based on the conversion of the different types of oxygen groups detected. Carbon dioxide was the only by-product of this process, which was absorbed by K_2CO_3. In addition, the study further elucidates the structure of GO sheets. The oxygen groups on the GO sheets not only aligned but also randomly dispersed in different areas.

Antistatic NR nanocomposites with partly interconnected graphene architectures offer significant enhancement in various properties. RGO/NR composites were prepared using latex mixing and *in-situ* reduction process. The oxygen groups on the GO played

a key role in attaching GO sheets to the surface of NR particles. Segregated current transfer routes were partly constructed in an NR matrix with an electrical conductivity of 0.1 S/m and reinforcing the tensile strength and elongation-at-break as well.

Silver nanoparticles (AgNPs) were used to decorate GO, which further increased the electrical conductivity of NR nanocomposites. Electrically conductive AgNPs/RGO filled NR with well-organized three-dimensional (3D) microstructures were prepared through electrostatic self-assembly integrated latex mixing. The oxygen groups in GO acted as an anchor for AgNPs growth, resulting in the electrical conductivity of 31000 S/m for the AgNPs/RGO. A honeycomb-like AgNPs/RGO 3D network was constructed in the NR matrix after freeze-drying and hot compression moulding. The AgNPs/RGO/NR nanocomposites show a percolation threshold of 0.63 vol.% and electrical conductivity of 196 S/m at AgNPs/RGO content of 4.03 vol.%.

The oxygen groups can not only be used to improve the electrical conductivity of NR but also used to reinforce mechanical properties. The effect of functionalized GO on the mechanical properties of NR was investigated through two strategies. In the first strategy, one layer of silica particles were attached to the GO surface through hydrogen bonds. The strength were reinforced because of well-dispersed SiO_2/GO in the NR matrix. GO acted as a surfactant dispersed by silica into the NR matrix to reinforce the mechanical properties using latex mixing. Oxygen groups on the graphene sheets banded with silica to achieve the target.

In the second strategy, the strength reinforcement of NR nanocomposites was achieved by construction of an interpenetrating network between the NR molecules and porous graphene. In this project, porous graphene loaded NR nanocomposites were prepared through an ultrasonically assisted latex mixing and *in-situ* reduction process. The oxygen groups showed chemo-selectivity etched by potassium permanganate ($KMnO_4$), forming pores possessing suitable dimensions in graphene sheets. Porous graphene/NR nanocomposites show strong interactions between the NR molecules and porous graphene than RGO/NR, which contributed to an increase in tensile strength compared to the RGO/NR nanocomposites. Furthermore, the scorch time compared to RGO/NR was decreased, and density of cross-linking was increased, which demonstrate the pores on the graphene sheets formed a mass transfer route, indicating an interpenetrating network was constructed.

Thesis certification

This Thesis is entirely the work of **Dongning He** except where otherwise acknowledged. The work is original and has not previously been submitted for any other award, except where acknowledged.

Principal Supervisor: Hao Wang

Associate Supervisor: Venkata Chevali

Associate Supervisor: Zheng Peng

Student and supervisors signatures of endorsement are held at the University.

Acknowledgements

I want to thank all the people who have assisted me throughout this research. In particular, I would like to acknowledgment my supervisors, Prof Hao Wang, Prof Zheng Peng, and Dr Venkata S. Chevali. This is an amazing supervisory team with a strong academic background in materials science, natural rubber composites, project management, and engineering experiences. Prof Hao Wang and Prof Zheng Peng gave many assistances in the experimental environments and discussions on the project. The discussions with them were always helpful. Dr Wei Gong helped me on analysis positron tests. Prof Bin Tang, and Dr Jinlong Tao helped me on the synthesis of silver nanoparticles and analysis the tests results. Mr. Joey Wang help me on proofreading this thesis. All of their understanding, advice, encouragement, and assistance were valuable resource leading to the success of this thesis.

The scholarship support of International Postgraduate Research Scholarship (IPRS) that is given by Australia government and University of Southern Queensland is acknowledged. The project support of Fundamental Scientific Research Funds for Chinese Academy of Tropical Agricultural Sciences (Project no. 1630062013011) is acknowledged.

I would take this opportunity to thank my family, who provided me with the help and encouragement on the way of pursuing this degree.

Publications

1. Gong, W, **He, D**, Tao, J, Zhao, P, Kong, L, Luo, Y, Peng, Z & Wang, H 2015, 'Formation of defects in the graphite oxidization process: a positron study', Rsc Advances, vol. 5, no. 108, pp. 88908-14.
2. Luo, Y, Qian, J, **He, D (corresponding author)**, Tao, J, Zhao, P, Gong, W, Zhang, Z, Peng, Z, Chen, X & Wang, H 2016, 'Preparation of natural rubber/silica nanocomposites using one-and two-dimensional dispersants by latex blending process', Polymer Composites, doi: 10.1002/pc.24081.
3. Zhang, Z, Li, L, **He, D**, Ma, X, Yan, C & Wang, H 2016, 'Novel self-supporting zeolitic block with tunable porosity and crystallinity for water treatment', Materials Letters, vol. 178, pp. 151-4.

Table of Contents

List of Figures

Chapter 1

Chapter 2

Chapter 3

Chapter 4

Chapter 5

Chapter 6

Chapter 7

List of Tables

Chapter 3

Chapter 4

Chapter 5

Chapter 6

List of Abbreviations

0D	Zero dimension
1D	One dimension
2D	Two dimensions
2D-DBAR	Two-detector coincidence Doppler broadening of annihilation radiation
3D	Three dimensions
ACD	Analogue-to-digital converter
AFM	Atom force microscopy
AgNPs	Silver nanoparticles
AgNPs/RGO	Silver nanoparticles decorated reduced graphene oxide
BET	Brunauer-Emmett-Teller (technique of characterizing solids)
CF DISC	Constant fraction differential discriminators
C=C/C-C	Non-oxygenated ring carbon
C-O-C	Epoxy
C-OH	Hydroxyl
DCFC	Direct carbon fuel cell
DMA	Dynamic mechanical analysis
DRC	Dry rubber content
DSC	Differential scanning calorimetry
fcc	Face centred cubic
FTIR	Fourier transform infrared spectroscopy
FWHM	Full width at half maximum
GO	Graphene oxide
GPC	Gel-permeation chromatography
HS-SPME-GC-MS	Headspace solid-phase microextraction-gas chromatography mass spectroscopy
ICP-MS	Inductively coupled plasma mass spectrometry
M_{100}	100% modulus
M_{200}	200% modulus
M_{300}	300% modulus
M_{500}	500% modulus

MD	Molecular dynamics
NG	Nitric acid treated graphite
NMR	Nuclear magnetic resonance
NR	Natural rubber
NSG	Mixed acid (98% sulfuric acid and 65% nitric acid with a ratio of 3 : 1 in volume) treated graphite
O=C-OH	Carboxyl
OG	Pure original graphite
P_0	Wallace rapid plasticity
PALS	Positron annihilation lifetime spectroscopy
PDDA	Poly(diallyl dimethyl ammonium chloride)
PG	Porous graphene
phr	Parts to a hundred parts of rubber
PMT	Photomultiplier tubes
PRI	plasticity retention index
Ps	Positronium
PSS	Poly(sodium p-styrene sulfonate)
RGO	Reduced graphene oxide
RI	Refractive index
SAED	Selected area electron diffraction
SC	Fast scintillators
SEM	Scanning electron microscope
SERS	Surface Enhanced Raman Spectrum
TAC	Time-to-amplitude converter
TEM	Transmission electron microscopy
TGA	Thermogravimetric analysis
THF	Tetrahydrofuran
XLD	Crosslink density
XPS	X-ray photoelectron spectra
XRD	X-ray diffraction
ZDC	Zinc diethyl dithio carbamate
$\pi \rightarrow \pi^*$	Shake-up line of aromatic compounds

Chapter 1: Introduction

Natural rubber (NR) has been widely used in industry, and daily life since mixing and vulcanisation processes were developed in the 19th century. However, the conventional NR products cannot meet the ever-increasing demand for applications (Thomas & Stephen 2010). Therefore, the research on innovative multi-functional NR-based composites is very important. Since 2011, the first paper published in graphene/NR composites field, the using graphene filled NR composites to achieve high performance including reinforcing mechanical and increasing electrical conductivity became a hot topic (Wang et al. 2017) because the inherent properties of fillers to impart functions to the host polymer. Monolayer defect-free graphene sheets have a theoretical breaking strength of 42 N/m, Young's modulus of 1.0 TPa, and fracture strength of 130 GPa (Rao et al. 2009). The electrical conductivity of graphene at room temperature is 1000000 S/m, which is higher than all other reported materials (Bolotin et al. 2008). Therefore, graphene is chosen as a filler to enhance the electrical conductivity and reinforce mechanical of NR composites.

However, the performance of graphene is strongly dependent on its structural integrity, which is controlled by the manufacturing process (Banhart et al. 2011). Currently, graphene used in the NR nanocomposites is prepared by an oxidation-reduction method. This method oxidized graphite to graphite oxide first, then graphite oxide was exfoliated by ultrasonic irradiation to achieve graphene oxide (GO), and then GO reduced by chemicals to reduced graphene oxide (RGO). The structure of GO is filled with defects, which have not fully understood. These defects cannot be fully removed during the reduction procedure, which not only decreases the physical properties of graphene but also disturbs the interaction between the graphene sheets and NR matrix. The defects weakened the improving properties of NR nanocomposites including electrical conductivity and stretchability (Yang et al. 2017). Furthermore, the dispersion and exfoliation problem of graphene in the cross-linked NR matrix need be investigated. However, almost no research involved the utility of defects on the graphene sheets to solve such problem. In this study, the utility of the defect on the graphene sheets for increasing electrical conductivity and reinforcing mechanical properties will be forced.

The defect characterisation of GO prepared by Hummers method is studied first. Then, remove some of the defects to obtain RGO, based on reusable and eco-friendly chemical were investigated. Based on developing intelligent, the GO used as filler attached to the surface of NR particles through hydrogen bonds those are attributed to the oxygen groups in the GO sheets. Then the *in-situ* reductions occurred after vitamin C added to prepare RGO/NR composites latex with a dark colour. The partly segregated RGO network was constructed in NR matrix through latex mixing integrating into situ reduction approach. In this research, vitamin C used as reduction instead of hydrogen hydrate to become eco-friendly. The RGO/NR nanocomposites showed conductivity of 0.1 S/m. Furthermove, oxygen groups acted as an anchor for silver nanoparticles (AgNPs) decorated RGO sheets to improve the conductivity of graphene up to 31000 S/m. The AgNPs/RGO used as filler through ultrasonically-assisted latex mixing to prepare AgNPs/RGO/NR nanocomposites with three-dimensional AgNPs/RGO honeycomb-like architecture in the NR matrix. The conductivity of AgNPs/RGO/NR is up to 196 S/m with 4.03 vol. % AgNPs/RGO loaded. The structure and mechanism of electrical conductive were investigated.

To reinforce the mechanical properties of NR nanocomposites, the oxygen groups and pores with tuneable size was the focus. The oxygen groups in the GO sheets was employed leading GO as a surfactant. GO assistance silica particles dispersed into NR matrix through latex mixing. The structure and property of the obtained NR nanocomposites were examined. The porous graphene with tuneable porous was realized using $KMnO_4$. The porous graphene/NR was prepared through ultrasonically assisted latex mixing and *in-situ* reduction process. Porous graphene-filled NR showed strength reinforcement. The structure and the interaction between the filler and NR were investigated.

In Chapter 2, the literature review discusses the issues of improving the NR product properties, based on NR structure and graphene. The spherical morphology of NR particles in the NR latex provides opportunities to prepare segregated graphene networks in the NR matrix. The NR particles acting as templates with negative charges assemble with the modified graphene carrying positive charges through electrostatic interaction force. However, the graphene used in composites usually has defects because of the preparation method. The types of defects, the influence of defects on graphene's properties, and methods of regulating graphene defects are summarised.

The recent research findings on graphene/NR nanocomposites are also reviewed in this chapter, including highlighting NR and graphene structures, graphene/NR nanocomposite preparation and control of properties.

In Chapter 3, the structure of the thesis is explained. The properties of raw materials including NR and graphite are given. Especially, details of the physical properties of NR used as a host polymer are measured. All the materials and chemicals employed in this investigation are outlined. The preparation method of graphene reduction, modification, and graphene/NR nanocomposite preparation are described in details.

Chapter 4 investigates on graphene oxide structure with defects by using the positron annihilation lifetime spectroscopy (PALS) and X-ray diffraction (XRD) studies. Followed by, the green reduction method of GO with a reusable reductant was developed. Based on the analysis of the positron results, it was found that different types of defects, including the vacancy cluster and vacancy-oxygen complexes can be detected for integral graphite oxide and exfoliated graphene oxide. The mechanism of the novel GO-reduction route is proposed. The reduction process GO by K_2CO_3 involves two steps. Firstly, carbonyl groups on the GO sheets are converted to CO_2, and the rings of epoxy groups are opened by the reductant at 50 ^oC. Secondly, the hydroxyl and epoxide groups, which oxidize to carbonyl groups, finally converted to CO_2 at 90 ^oC to finish the reduction procedure.

In Chapter 5, the electrical conductivity of graphene/NR is enhanced in two ways, based on Chapter 4 shows that oxygen groups detected on the GO sheets. One method is with the use of the oxygen groups on the graphene sheets that can suspend GO sheets into an NR latex, attaching to the NR particles surface by hydrogen bond. The mixture of GO and NR latex have a one-pot reaction to prepare antistatic NR composites with vitamin C. Another method is employing AgNPs to cover the defects on the RGO sheets to increase the electrical conductivity of RGO. The electrically conductive NR nanocomposites with low percolation threshold were prepared using AgNPs/RGO as filler, and electrostatic self-assembly, latex mixing, and freeze-drying. The electrical conductivity of NR nanocomposites is 196 S/m with AgNPs/RGO content of 4.03 vol. % of, and the percolation threshold is 0.63 vol. %.

In Chapter 6, the mechanical reinforcement of NR nanocomposites is investigated using two methods based on the defects that depict in Chapter 4. One is to use oxygen

groups on the GO sheet inducing GO to act as a surfactant, assembling silica particles on its surface to prevent the re-aggregation of the GO and silica. Moreover, hybrid filler was reconstructed into NR matrix for mechanical reinforcement. The other is to employ the porous defect on the graphene sheet for construction of an interpenetrating network of porous graphene and NR molecule. The 2 phr porous graphene loaded NR nanocomposites performs strength reinforced on M100, M200, M500 with 81.4%, 400.0%, and 212.9% higher than neat NR, respectively. 2Mp-RGO/NR is 67.1%, 217.1%, and 87.8% higher than the RGO/NR specimen with the similar loading. The hypothesis of the construction of an interpenetrating network between the porous graphene and NR molecules are confirmed using different characterizations.

Chapter 7 concludes the research undertaken in this thesis. Some problematic issues are noted in the graphene/NR compounds preparation. Detailed suggestions are proposed for graphene/NR development in the future.

The flowchart in **Figure 1-1** shows an overall schematic of the investigation.

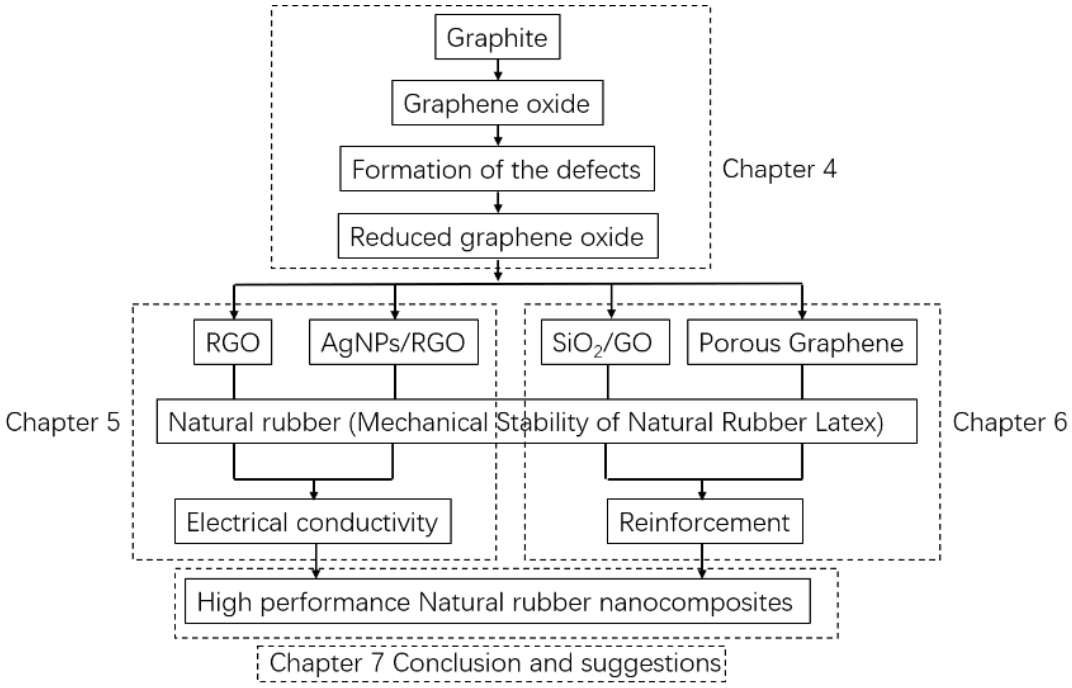

Figure 1 - 1 *Research organization of this thesis.*

Chapter 2: Literature review

The background knowledge of graphene/NR nanocomposites is summarised in this chapter as four parts.

a. The structure of NR and NR latex;

b. NR nanocomposites preparation methods;

c. The graphene preparation and the formation, properties, modification of the non-perfect graphene, the influence of defect and its regulation;

d. Graphene/NR nanocomposites preparation methods and properties.

2.1 Natural rubber

Figure 2 - 1 *An hevea tree under cultivation.*

Natural rubber is widely used in daily life. Some advantages of NR are summarized as follows:

(1) NR is extracted from a tropical plant in which the cis-1, 4-polyisoprene molecule is bio-synthesized (Mark et al. 2013).

(2) The bio-synthesized, cis-1, 4-polyisoprene is only composed of hydrogen and carbon atoms. All other biopolymers contain other covalently bonded elements such as oxygen, nitrogen, sulphur, in addition to hydrogen and carbon.

(3) NR is obtained almost entirely from *Hevea brasiliensis* (Van & Poirier 2007). At present, 99% of natural rubber is obtained from Hevea trees in Asia. **Figure 2-1** shows an Hevea tree under cultivation. The latex is used in an original form or coagulated with sequence processes to obtain NR gum.

(4) Chemical synthesis of natural rubber is not yet successful (Chen et al. 2015).

(5) NR is renewable as it is an agricultural product (Kargarzadeh et al. 2015).

(6) NR is scientifically special because of its elasticity and stain-induced crystallization properties. From a thermodynamics viewpoint, its entropy changes resemble that of an ideal gas. The elastic energy generation is different than metallic, inorganic, or organic solid materials (Candau et al. 2015).

(7) NR has become an essential material used in plane and truck tires and gloves (Ramarad et al. 2015).

NR collected from trees as biomass, and renewable material cannot be replaced by any of the reported statistic materials based on its even and stabilized properties. These advantages of NR come from its unique structure. There are about 15-40% of NR in the NR latex, namely serum of the Hevea trees. NR presents as sphere covered by partly lipids and proteins all suspended in serum (Ho & Khew 1999) as shown in **Figure 2-2**. The diameter of NR particles is approximately 0.1-3 μm (Thomas & Stephen 2010). Moreover, there are also approximately 5% non-rubber components in the serum including neutral lipids, glycolipids and phospholipids, proteins, carbohydrates, ash, and others.

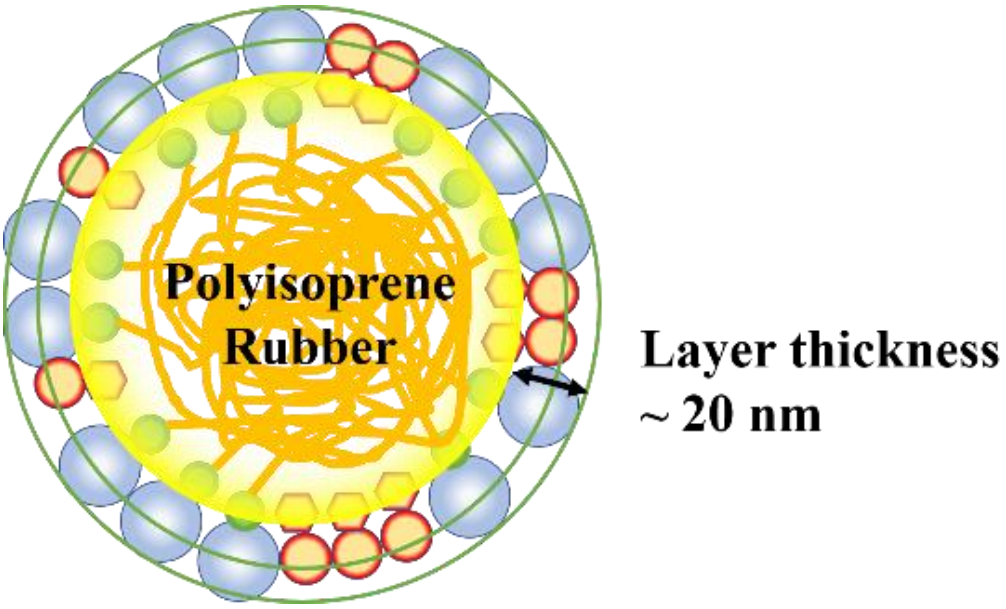

Figure 2 - 2 *The model of the NR latex particle surrounded by a non-rubber layer.*

The nano-matrix of non-rubber components were developed as Kawahara reported (Kawahara et al. 2011; Kosugi et al. 2012). These nano-matrices are inherently formed when the NR latex directly cast film. The NR particles, with an average diameter of 0.5 µm are celled and dispersed in these non-rubber matrices. These non-rubber components significantly influenced stress at break, viscoelastic properties, and storage modulus. The 3D image of the nano-matrix structure was reported by Fukuhara, based on the NR was fabricated to the graft-copolymer of de-proteinized NR with employing focused ion beam and transmission electron micro-tomography (Fukuhara et al. 2015). The nano-matrix structure as shown in **Figure 2-3**. These nano-matrix structures will be employed as a template to fabricated segregated graphene or its derivative networks in the NR matrix. Based on the percolation threshold theory the segregated additives networks given lower percolation threshold compared to the homo-dispersed.

It is well known that high ammonia concentrated latex has a negative charge. The test result is given as shown in **Figure 2-4**, and the Zeta potential is -70 mV. The negative charge comes from the basic hydrolysis of the non-rubber components on the surface of NR particles (Thomas & Stephen 2010). Based on the electrostatic self-assembly principle, the modified graphene will attach to the surface of the NR particles to avoid of graphitization because of the modified graphene presenting positive charge (Li et

al. 2017). The hydrogen bond interaction between the modified graphene (like graphene oxide) and NR particles could avoid graphitization as well (Li et al. 2013).

However, these nano-matrices also have a disadvantage to the NR system, as Tan reported (Tan 2006). Mechanical reinforcement formula cannot achieve the mechanical reinforcement required, because of the absence of intensive treatment during latex mixing. Moreover, the non-rubber components on the surface of NR particles prevent the interaction between the additives and the NR macromolecule. Traditionally, to reinforce NR through latex mixing, the resin, and lignin are always used under suitable conditions (Keilen & Pollak 1947; Weeraratne et al. 1972). Otherwise, mechanical treatment is employed after drying the NR compounds using masterbatch (Zhan et al. 2011; Yan et al. 2014; Aguilar-Bolados et al. 2017).

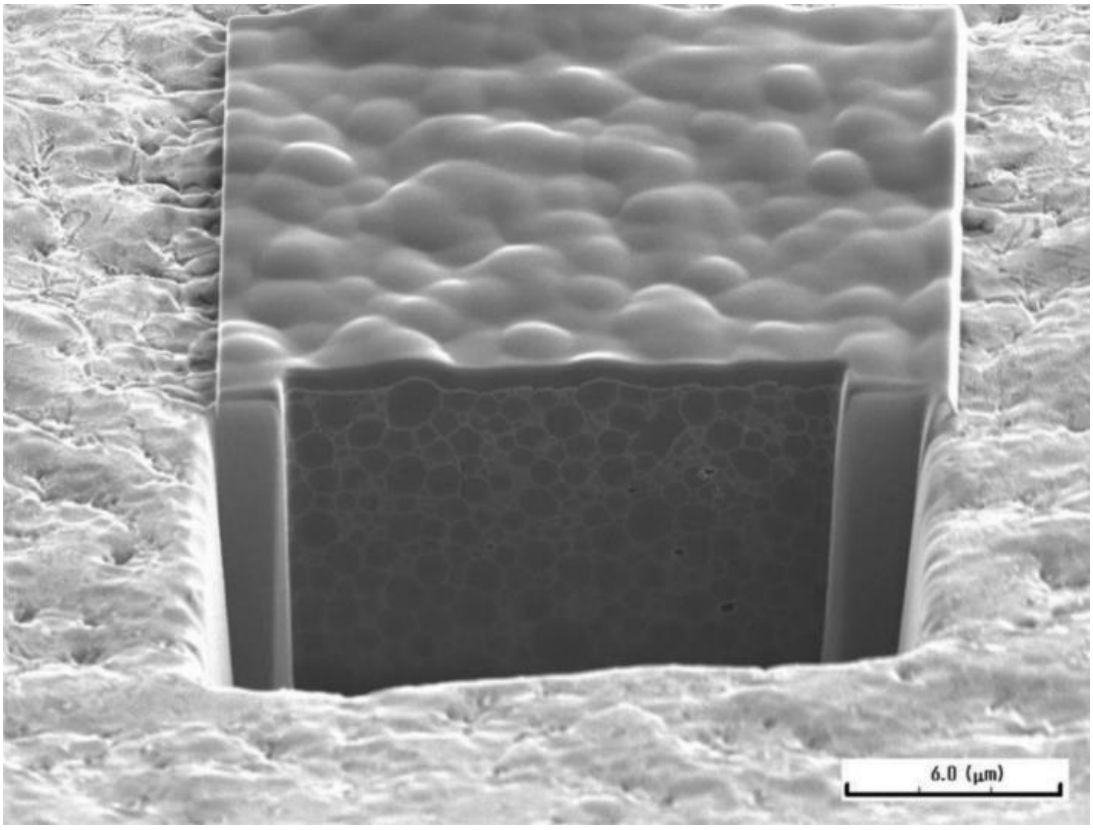

Figure 2 - 3 *The SEM image of graft-copolymer of deproteinized NR were taken after etching its surface (Fukuhara et al. 2015).*

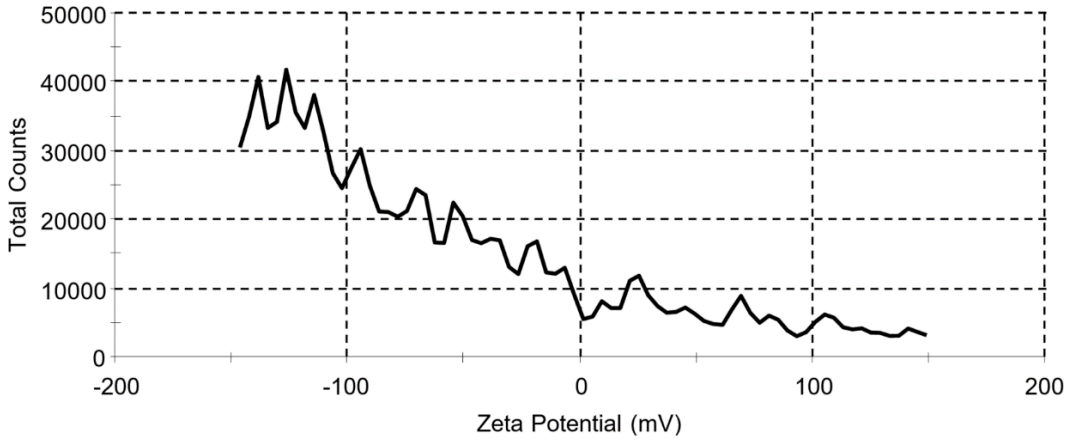

Figure 2 - 4 *The Zeta potential distribution of high ammonia concentration latex.*

It is well known that the mechanical mixing procedures can decrease the molecular weight of the NR by strong shear, and extrusion (Leblanc 2002). The structure of NR particles can be broken in the procedure (Paul & Robeson 2008). The drying process of the NR gum fabrication can also destroy it. The main part of NR, polyisoprene, can interact with additives to achieve the functionalization (Leblanc 2002). In the last decade, the relationship between properties characteristic of NR and its macromolecular structure investigation has become a hot spot (Kohjiya & Ikeda 2014). Based on the recent investigation by SEC, FTIR, NMR, and dilute solution viscosity, the chemical structure of the NR molecule is almost clear (Tarachiwin et al. 2005; Marckmann & Verron 2006; Wu et al. 2017). The NR molecule is a branched macromolecule with the bimodal of molecular weight distribution. Moreover, the molecular weight distribution can be influenced when the conditions change, including tree species, growing environment, and rubber tapping conditions. Therefore, the study on the NR micro-structure is ongoing. Until now, achieving a consensus on NR molecular structure which can be divided into four parts. They are initiating terminal (ω-terminal) with an unidentified structure, and phosphate terminal (α-terminal). The α-terminal form branch points by micelle, ionic bond, or hydrogen bond formation linked to both terminal groups (Gent & Cho 1999; Wu et al. 2017). After that two trans-isoprene, and 1000-3000 cis-isoprene persent as main body (Tanaka & Tarachiwin 2009).

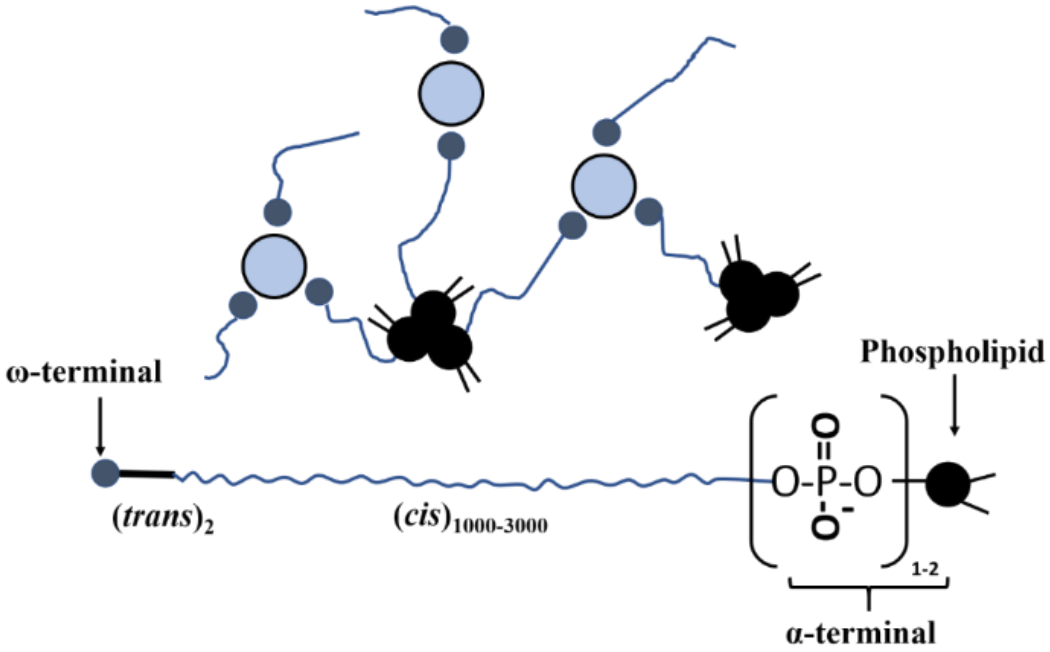

Figure 2 - 5 *The diagram of NR molecule structure. (Adapted from (Tangpakdee & Tanaka 1997))*

2.2 NR nanocomposites

NR has been widely used since typical manufacturing sequence development, including compounding, forming, and vulcanization process. The disadvantages of neat NR, such as large free volume, low crystallization, and low tensile strength cannot meet requirements for many applications (Thomas & Stephen 2010). Recently, all NR products need to be reinforced. Conventional inorganic fillers mainly include carbon black (CB) (Garishin et al. 2017), silica (Sengloyluan et al. 2017), clay (Siririttikrai et al. 2017), shell powder (Zhou et al. 2018), and fiber (Sanhawong et al. 2017).

2.2.1 Compounding

Compounding additives into NR matrix to prepare NR nanocomposites is achieved through the mixing process, *in-situ* polymerization, and sol-gel approaches.

2.2.1.1 Mixing process

The mixing process can be divided into mechanical mixing, solution mixing, and latex mixing. Mixing is widely used to fabricate inorganic nano-particles into NR matrix in the industrial fields.

The mechanical mixing employs open two-roll mixer or internal mixer, which is energy extension, particulate contamination, and even hazardous to worker health.

Solution mixing dissolves the NR gum into a suitable organic solution first, then adding nano-filler with stirring or ultrasonic irradiation procedures to gain uniform filler dispersion. Latex mixing puts fillers into NR latex directly with stirring and ultrasonic irradiation procedures. The disadvantages of latex mixing are that the filler cannot be homogeneously dispersed leading to a failure to reinforce the NR. Because latex particles cannot be filled with the fillers inside (Jeon et al. 2003; Potts et al. 2012).

Mechanical mixing uses high shear force to uniformly disperse fillers into the NR matrix. In mechanical mixing, the fillers contact with the polyisoprene directly, to obtain a glassy layer on the fillers, which can ultimately increase tensile properties. Because the fillers disperse uniformly in the NR matrix, the electronic transfer route is difficult to construct compared to latex mixing (Potts et al. 2012). The final product also has a high electrical percolation threshold value. The latex mixing approach fabricates graphene/NR nanocomposites, which easily establishes segregated graphene networks exhibiting higher electrical conductivity with lower percolation threshold than a uniformly dispersed sample (Yaragalla et al. 2013).

2.2.1.2 In-situ polymerization

In-situ polymerization can be categorized as *in-situ* dispersion polymerization and *in-situ* formation polymerization. These methods are widely used for silica NR nanocomposite fabrication (Yanhua 2012). The *in-situ* polymerization obtains the different chemical structure of the filler. The *in-situ* polymerization improves mechanical properties, abrasion resistance, compression fatigue properties, rebound performance, and aging resistance, over the mechanical mixing process. Because the interaction between additive and NR, the dispersion, the static and dynamic properties are all improved (Nie et al. 2010).

The *in-situ* polymerization method has several advantages. First, the reaction conditions are usually moderate. Therefore, the microstructure of the matrix is not broken. Second, the dispersion of the filler is much more homogeneous than the latex mixing and mechanical mixing methods. However, the disadvantages of solvent contamination, reaction time, and the quality control of the product in the unclear NR latex system are all very difficult to handle.

2.2.1.3 Sol-gel method

The sol-gel process is an efficient method to prepare organic/inorganic compounds, which can effectively control the *in-situ* growth particle size and particle distribution into the matrix to obtain a homogeneous dispersion. The interfacial bonding between particles and base materials can be designed (Yuan & Mark 1999). The method is based on an inorganic salt or metal alkoxide as a reaction precursor, through hydrolysis and condensation reaction gelatinization. Finally, using the corresponding post-processing *in-situ* synthesis particles in the NR matrix (Xianjian et al. 2000). Mechanical properties of the sol-gel method samples are significantly better than the mixing processes sample, especially tensile strength (Tanahashi et al. 1998).

2.2.2 Forming

The NR composites can be plastic and ready for manufacturing into a desired shape for vulcanization after mixing process. A compression mould is widely used after mechanical and solution mixing. The NR composites are moulded under suitable pressure in a heated mold with temperature from 120 ^{o}C to 165 ^{o}C (Kohjiya & Ikeda 2014).

2.2.3 Vulcanizing

Historically, vulcanization was defined as the process of heating NR, sulfur, and white lead. Recently, the cross-linking process of rubber, the final process in the manufacturing sequence is called vulcanization. After curing under certain conditions including temperature, pressure, and time, the NR composites take up a shape in a mold. The vulcanization process involves chemical reactions occurring in the NR matrix to construct cross-linking. There are a variety of vulcanization approaches, including, sulfur vulcanization, peroxide cross-linking, sulfur-free and peroxide-free cross-linking and radiation-induced cross-linking. In this research, the sulfur vulcanizing process was applied at 150 ^{o}C.

2.2.4 Nano-fillers in NR nanocomposites

NR nanocomposites show better compatibility, machinability, and mechanical properties than the neat NR, because of small-size effect, quantum effect, electron-tunneling effect, and unsaturated bond effect of nano-additives (Sabu & Ranimol 2010). There is three main factors about nano-additives influence the reinforcement of NR nanocomposites: (1) Size, (2) Surface structure, and (3) Surface activity. The

particle size dictates the level of reinforcement. Smaller particles have the stronger quantum effect, inducing a stronger interaction between the additives and NR, improving mechanical reinforcement. In the NR system, particles with a size smaller than 10 μm will show mechanical reinforcement, and performance increases with decreasing dimension (Thomas & Stephen 2010).

Additives of NR nanocomposites have been widely studied including clay (Luo & Daniel 2003), silica (Joseph et al. 2004; Xu et al. 2017), carbon nanotubes (George et al. 2017), and graphene (Potts et al. 2012; Dong et al. 2017). The exfoliated additives includes clay filled into NR, which exhibit better mechanical properties than the aggregated additives. The mechanical reinforcement of clay/NR composites depends on the concentration of clay, the degree of clay layer separation, and clay networks in the composites (Luo & Daniel 2003).

Intercalated nanocomposites are defined as the contents of host polymers inserted in between exfoliated clay layers (Ruiz‐Hitzky 1993; Sinha Ray & Okamoto 2003). In nanocomposites with an exfoliated filler, clay layers 1 nm thick are exfoliated and dispersed in a continuous NR matrix (Sinha Ray & Okamoto 2003), with distances between clay layers relying on the volume concentration of clay layers. However, the major challenge in intercalated nanocomposite area is to obtain a fully exfoliated additive structure.

Graphene possesses high Young's modulus, ultrahigh mechanical strength, large specific surface area, structural flexibility, excellent electrical and thermal conductivity and single optical transmittance of approximately 97%, which is better than all other reported materials (Zhu et al. 2010; Rychagov et al. 2017). Employing graphene as an additive in the rubber matrix has many advantages:

1. The mechanical properties of graphene/NR can be better than the traditional NR composites because of Young's modulus of 1.0 TPa with a flexible structure.

2. The nanocomposites have high thermal and electrical conductivity because the relative properties of graphene are much higher than other filler.

3. Gas barrier properties of graphene/NR nanocomposites can be better than clay/NR nanocomposites because of structural advantage and large specific surface area.

4. Large specific surface area of graphene also good for increasing the interaction between the additives and NR molecule, and strain-induced crystallization.

5. The graphene/NR nanocomposites may have fire retardant properties because of a gas barrier and thermal conductivity.

6. The graphene or GO can be multifunctional for different applications, based on they have different types of oxygen groups which could be functionalized easily by chemical modification.

Therefore, graphene as a novel additive has provided potential properties observed in graphene/NR nanocomposites materials. Consequently, graphene/NR nanocomposites can be widely used in high barrier conductive seals, tires, shock absorbers, and electromagnetic shielding seals (Yang et al. 2017). Graphene or its derivatives will expand the role of NR and their nanocomposites to the new application field.

2.3 Graphene and defects of graphene

The name "graphene" was formally accepted by IUPAC in 1997 to replace the term "graphitic layers". Graphene is one of the diverse morphologies of carbon allotrope as shown in **Figure 2-6**. Graphene is made of pure carbon with a two-dimensional crystalline material with honeycomb lattice structure, even at one atom thickness as about 0.34 nm with a carbon-carbon bond length of 0.142 nm. The carbon atom in the graphene sheets present as sp^2 hybridized. It acts as the fundamental material of C60, carbon nanotube, and graphite. In 2004-2005, the research of graphene intensified with many key publications (Berger et al. 2004; Novoselov et al. 2004; Novoselov et al. 2005; Novoselov et al. 2005; Zhang et al. 2005). Graphene has extraordinary physical properties including high mechanical stiffness (Lee et al. 2008), electrical conductivity (Novoselov, et al. 2005; Stankovich et al. 2006; Castro et al. 2009), thermal conductivity (Balandin et al. 2008), and impervious properties (Bunch et al. 2008).

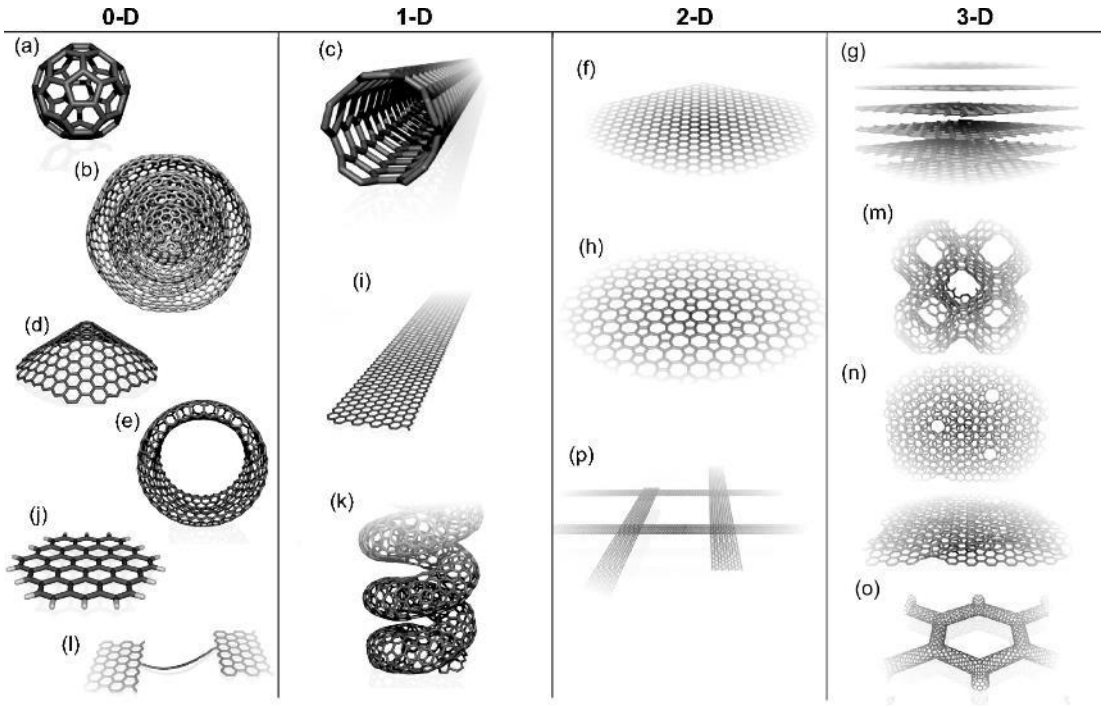

Figure 2 - 6 *The molecular models of different types of sp^2-like hybridized carbon nanostructures exhibiting different dimensionalities, 0D, 1D, 2D and 3D (Terrones et al. 2010).*

2.3.1 Mechanical and electrical conductivity of graphene

Graphene possesses unique mechanical properties and electrical conductivity based on its structural integrity.

2.3.1.1 Mechanical properties

Atomic force microscopy (AFM) was employed to test Young's modulus of few-layer graphene with force-displacement and force-volume measurements (Zhu et al. 2010). The inherent strength and elastic properties of freestanding monolayer graphene were also tested by AFM because of the nanoindentation as shown in **Figure 2-7**. Lee reported that the monolayer defect-free graphene sheet has a breaking strength of 42 N/m, Young's modulus of 1.0 TPa, and fracture strength of 130 GPa, theoretically (Rao et al. 2009).

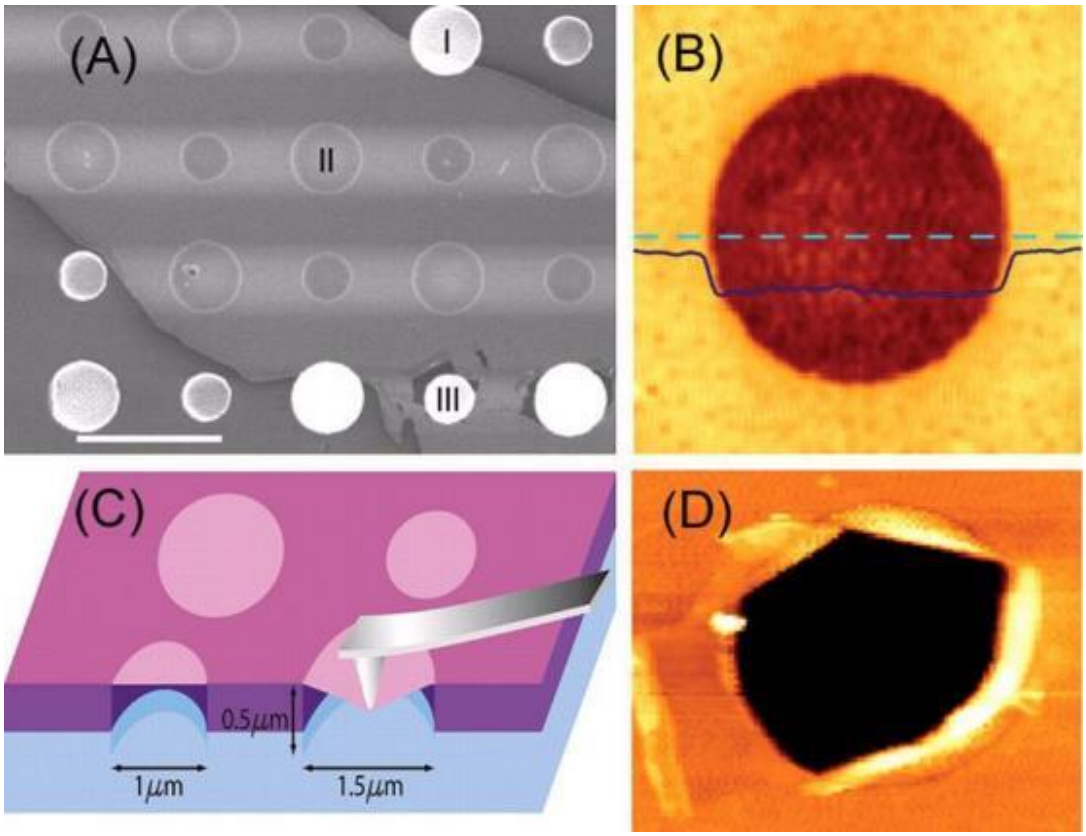

Figure 2 - 7 *Images of suspended graphene membrane (Lee et al. 2008).*

2.3.1.2 Electrical conductivity

Theoretically, defect-free graphene constitutes of sp^2 hybridized carbon atoms, and each carbon atom gives an electron from p orbital to obtain delocalized π bonds. The properties of π electron endow graphene with high electrical conductivity. These charge carriers behave as the Dirac fermions or massless relativistic particles. It has been proved that graphene is a zero-gap 2D semimetal. Furthermore, graphene has a small overlap between conductance bands and valence. Moreover, there is a little scattering of its charge carriers' movement under the ambient condition. Bolotin reported the electron mobility of monolayer graphene could achieve 200,000 $cm^2V^{-1}s^{-1}$ which are approximately 140-fold of silica. The electrical conductivity of graphene at room temperature is 1,000,000 S/m, which is the highest known electrical conductivity material (Bolotin et al. 2008).

2.3.2 Graphene preparation methods

Graphene was successfully prepared by micromechanical cleavage of graphite, firstly. Recently, there are dozens of methods to obtain graphene. The two preparation

methods of graphene can be summarized as a bottom-up approach and a top-down approach.

2.3.2.1 The Bottom-up approach

This approach involves the conversion of carbonous, or other carbon allotropes to graphene under certain conditions including chemical vapor deposition (CVD) (Reina et al. 2009; Senyildiz et al. 2017), epitaxial growth (Li et al. 2009; Subramanian et al. 2017), chemical synthesis (Yang et al. 2008), arc discharge (Fan et al. 2010), carbon nanotube conversion (Hirsch 2009) and self-assembly of surfactants (Zhang et al. 2009). Although this approach can fabricate graphene with less extrinsic defects than most of the top-down approach, the bottom-up approach is only suitable for bench scale preparation with high cost based on technical limitations until now. In addition, the graphene prepared by the bottom-up approach present chemical inertness, and with non-polar physical properties. These properties resulted in graphene having broad application in the electronic, energy field. However, in the nanocomposites field which not only need dozens of tonnes of additives in the manufacturing process, but also the additives can be functionalised easily to match the apply for a different application.

2.3.2.2 The top-down approach

The top-down approach prepared graphene by exfoliating graphite or graphite derivatives on a large scale. The method can donate some heteroatoms and topological defects. These defects increase the chemical reactivity, and diverse structures, which give graphene millions of potential applications. The graphene prepared by top-down approach exhibits unlimited possibility in the graphene filled nanocomposites field, including presenting high performance containing reinforcement and electrical conductivity (Khalid et al. 2017), after employing the different fabrication strategies and modifications (Yang et al. 2017).

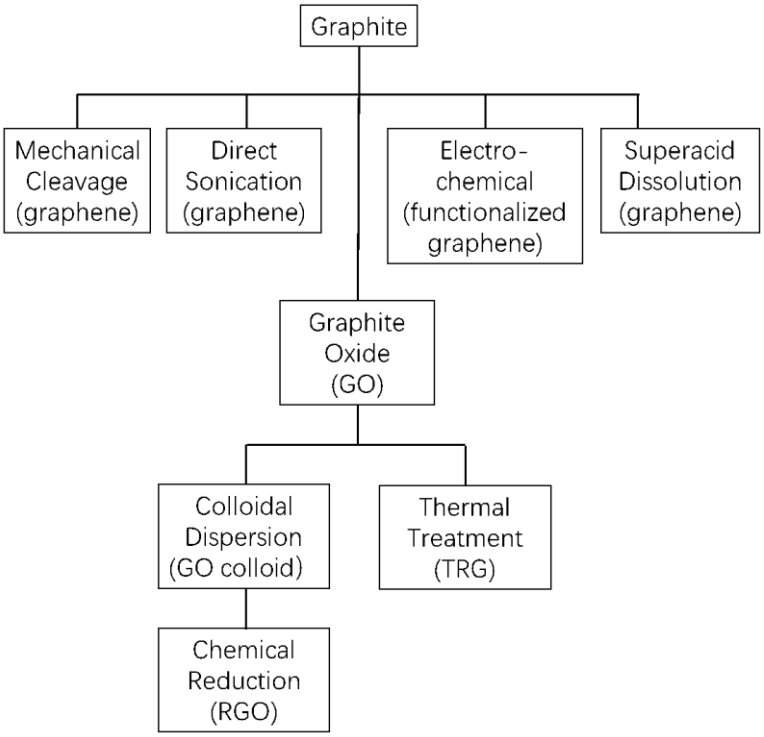

Figure 2 - 8 *The top-down methods for production of graphene.*

RGO that prepared by top-down approach has been known as an attractive and promising filler for polymer nanocomposites. The investigation of the precise structure of GO is still relatively unknown. The most well-known hypothesis of GO structure is built by Lerf and Klinowski as shown in **Figure 2-9**They have published several papers on the hydration behaviour and structure of GO by using NMR, and XRD to characterize GO (He et al. 1998; Lerf et al. 1998).

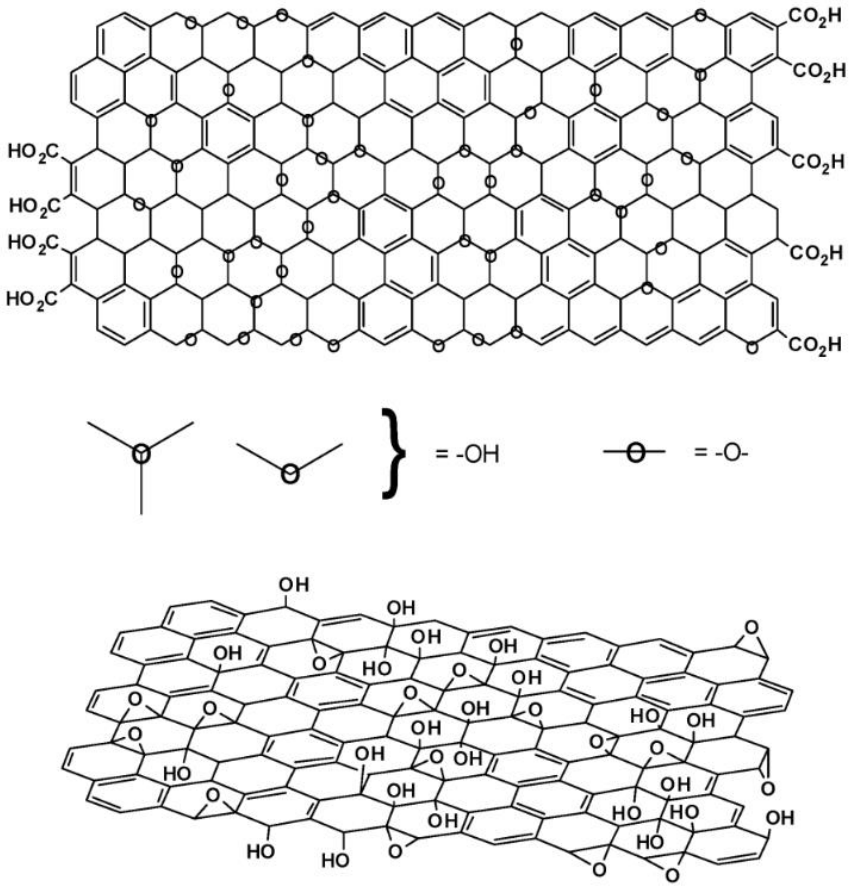

Figure 2 - 9 *Variations of the structure of GO (Dreyer et al. 2010).*

The oxidation-reduction method is one of the most widely used top-down approaches in the polymer nanocomposites field. The oxidation-reduction method has several procedures. It would employ graphite as raw material, and then add a strong acid and oxidant to obtain graphite oxide. Graphite is exhaustively oxidized employing the methods developed by Brodie (Brodie 1860), Staudenmaier (Staudenmaier 1898), or Hummers (Hummers & Offeman 1958). Strong acids and oxidants are applied to produce graphite oxide because the epoxide groups, hydroxyl, and carboxyl are decorated on the graphene sheets. Taking Hummers method, for example, sulfuric acid and potassium permanganate are mixed as a combination. Although potassium permanganate is used as the oxidant, commonly, the active chemical is diamanganese heptoxide. It is obtained as shown in **scheme 2-1**. The colour of dimanganese heptoxide is a dark red oil that could be easily seen during the preparation procedure, adding potassium permanganate into graphite and sulfuric acid mixture. Diamanganse heptoxide is synthesised under the reaction of $KMnO_4$ with H_2SO_4 (Koch 1982). The

bimetallic heptoxide has a much higher reactivity than the monometallic tetraoxide counterpart.

$$KMnO_4 + 3H_2SO_4 \rightarrow K^+ + MnO_3^- + H_3O^- + 3HSO_4^- \quad (2\text{-}1)$$

$$MnO_3^- + MnO_4^- \rightarrow Mn_2O_7 \quad (2\text{-}2)$$

Scheme 2 - 1 *Formation of dimanganese heptoxide (Mn_2O_7) from KMnO4 in the presence of sulfuric acid.*

The exfoliated graphite oxide, namely GO, is achieved by the help of ultrasonic irradiation. After specimens were purified by filtration, centrifugation, and, dialysis, the GO can be reduced by dozens of reductants to obtain RGO as shown in **Figure 2-10**. The conventional chemical reductants for converting GO to reduced GO include hydrazine hydrate (Stankovich et al. 2007), H_2 (Li et al. 2008), hydroquinone (Wang et al. 2008), $NaBH_4$ (Muszynski et al. 2008), Na/CH_3OH (Mohanty et al. 2010), propylene carbonate (Zhu et al. 2010), vitamin C (Fernández-Merino et al. 2010), aluminium powder (Fan et al. 2010), and molten halide salts (Abdelkader et al. 2014) which are either hazardous, unrecyclable or high cost. Therefore, it is essential to develop a green chemical reduction processes for graphene preparation. Recently, benzylamine (Liu et al. 2011b), poly(diallyldimethylammonium chloride) (Zhang et al. 2011), tea polyphenols (Wang et al. 2011), and others are employed as eco-friendly chemicals to synthesize of graphene.

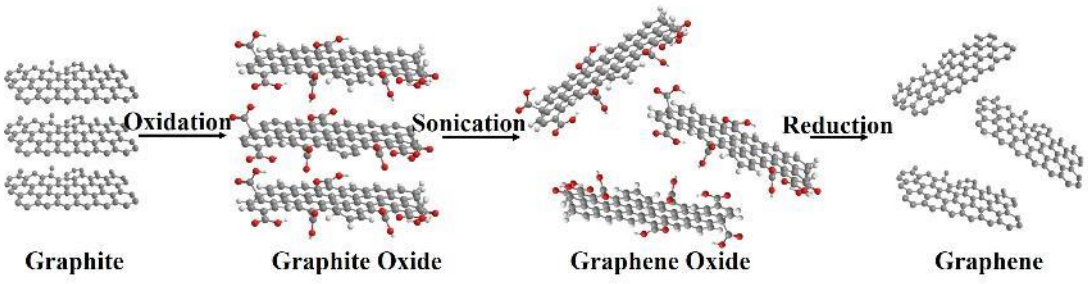

Figure 2 - 10 *The chemical oxidation-reduction route to reduced graphene oxide.*

Reduced graphene oxide with fewer defects will present higher chemical stability and lower interaction with solvents. The Van der Waals' forces between the RGO sheets are also very strong. Therefore, RGO can easily become aggregated and graphitize.

There are two strategies focused on to obtain single sheets of RGO. One is to use small removable molecules during the reduction process including hydrazine hydrate with ammonia (Stankovich et al. 2007), and tea polyphenols (Wang et al. 2011) as a reductant. Another method is to employ different processing methods such as latex mixing. The polymer particles act as a template, which prevents the graphitization process (Zhan et al. 2012; Luo et al. 2014; Suriani et al. 2017; Sarkawi et al. 2017).

2.3.3 The defect of graphene

Graphene does not exist in nature and is prepared using various methods all of which will cause different defects (Banhart et al. 2011). As shown in **Figure 2-11,** based on AFM testing, Lui reported that graphene that is made through mechanical exfoliation was not ultra-flat with an extended honeycomb network (Lui et al. 2009). Because of these defects, the physical and chemical properties of the graphene are much lower than the theoretical level, and TEM (Girit et al. 2009), AFM (Lui et al. 2009), STM (Ugeda et al. 2010) are used at atomic resolution level. The defects of graphene can be divided into two sections. One is an intrinsic defect that is formed by non-sp2 hybridized carbon, because of the decreasing number of carbon atoms or the increasing number of the carbon atoms (Ugeda et al. 2010). Therefore, non-hexatomic rings, or vacancies with points and linear shape could be detected. Another type is an extrinsic defect that is formed by non-carbon atom bonding on the graphene sheets (Nemec et al. 2006). Since different kinds of atoms have unique properties, the charge distribution of the graphene sheets will be disturbed, and the physicochemical properties changed (Banhart et al. 2011).

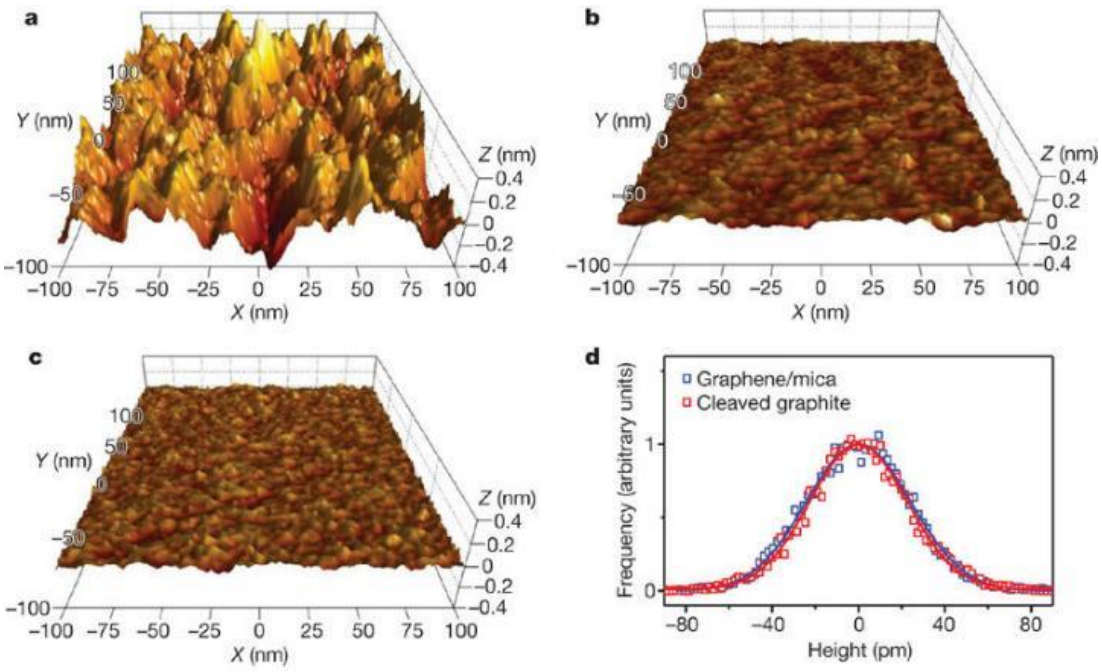

Figure 2 - 11 *Three-dimensional representations of the AFM topographic data for graphene on SiO_2 (Lui et al. 2009).*

2.3.3.1 Intrinsic defect

The intrinsic defect can be divided into four types: (1) point defect, (2) reconstructed vacancy defect, (3) linear defect, and (4) interstitial atoms defect.

Point defect is formed by the reconstruction of the graphene lattice by obtaining non-hexagonal rings. The point defect formed by electron beam bombardment or high-temperature rapid cooling procedure (Ma et al. 2009) as shown in **Figure 2-12**. One example is the Stone-Wales defect, which does not involve any added or remove carbon atoms (Stone & Wales 1986). Graphene sheets with point defect retain the same number of carbon atoms and have no dangling bonds. This defect has high formation energy at about 5 eV. 1000 ^{o}C or higher temperature is needed, to indicate a negligible equilibrium concentration.

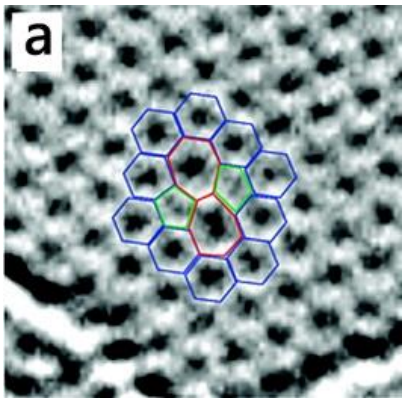

Figure 2 - 12 *The TEM image of Stone-Wales defect in graphene (Banhart et al. 2011).*

Reconstructed vacancy defect is formed by removing one or more carbon atoms from the lattice including single vacancy and multiple vacancies, as shown in **Figure 2-13**. Single vacancy in graphene lattice could be experimentally presented by STM (Ugeda et al. 2010), and TEM (Meyer et al. 2008). The single vacancy undergoes Jahn-Teller distortion leading the formed dangling bonds toward the missing atom. Based on the geometrical reasoning, a dangling bond always remains, leading to the formation of different-membered rings. Multiple vacancies can be created either by removing several neighbouring carbon atoms from graphene lattices or by coalescence nearby single vacancies. After atom disappearance of, the graphene lattice and the lattices structures changed will give a serial alter to decrease the energy of the whole sheet (Banhart et al. 2011). Moreover, the physiochemical properties will change as well.

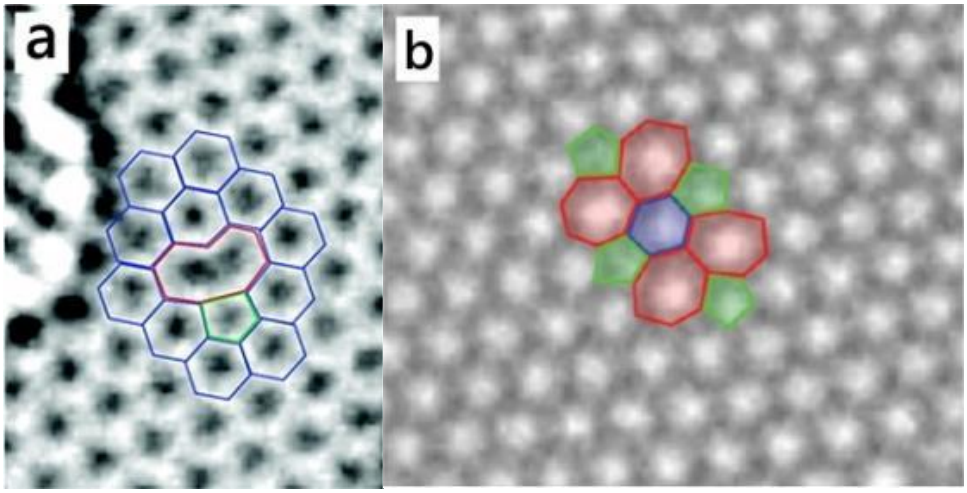

Figure 2 - 13 *The TEM image of reconstructed vacancy defect on graphene sheet (Banhart et al. 2011).*

The linear defect is formed by CVD procedure, because of the coalescence graphene growing on different domains as shown in **Figure 2-14**. This kind of defect is depicted as a linear structure (Coraux et al. 2008), which is particularly important occurring on the grain bounding in graphene lattice. It is well known that the physiochemistry properties of polycrystalline materials are normally controlled by the size of the grains and the atomic structure of its boundaries. Since the adsorption energy is low, it is possible that graphene with different orientations relative to the metal surface. These different domains of graphene coalescence lead to the formation of a linear defect, consisting of octagons and pentagons. Especially, the grain boundaries control the electronic transport in graphene lattices (Yazyev & Louie 2010).

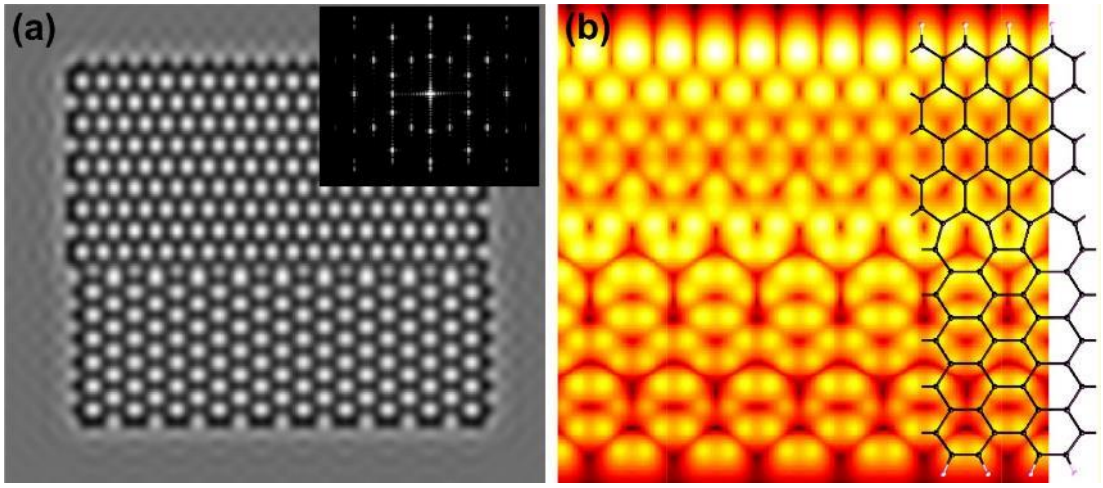

Figure 2 - 14 *The simulated high-resolution electron microscopy image and STM image of linear defect of graphene (Terrones et al. 2010).*

Interstitial atoms, as they show in 3D crystals, do not exist in graphene. In the reconstructed vacancy, the defect is formed by lost carbon atoms. These atoms may not separate from the graphene plane. Sometimes these carbon atoms become delocalized atoms, shifting on the graphene plane to construct new bonds. When they come to a vacancy defect, the defect may be repaired. However, when interstitial atoms come to a defect-free area, a new defect will appear which will turn the original plane structure into a spatial structure, as shown in **Figure 2-15**. Recently, these defects cannot be investigated by micro-technique directly. Based on research on the mechanism of activated carbon preparation, carbon and oxygen atoms can shift on the carbon plane surface (Marsh & Rodríguez-Reinoso 2006). Therefore, interstitial atoms

defect can exist. In this field, there are some theoretical investigations which revealed the electrical conductivity is disturbed because the defect will change the hybridized structure from sp^2 to sp^3 (Lusk et al. 2010).

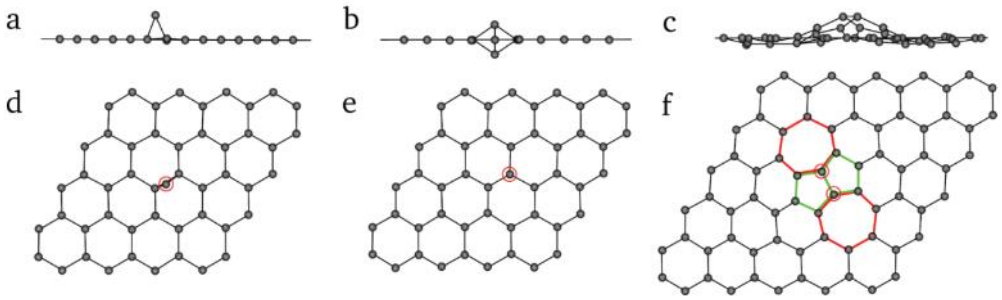

Figure 2 - 15 *The carbon adatoms defects in graphene: (a-c) space structures (d-f) positions of carbon adatoms (Terrones et al. 2010).*

2.3.3.2 Extrinsic defect

The extrinsic defect can be divided into (a) introduced impurities defects, and (b) substitutional impurity defects.

Introduced impurity defects are formed by CVD or strong oxidizing conditions. Metal ions and oxygen groups can be introduced into the graphene sheets considering the metal or oxidant employed. The introduced parts bond with the carbon atoms to form defects by chemical bonds or Van der Waals' force. It is reported the metal ion formed introduced impurity defects could shift on the graphene plane, which has been revealed by experimental investigation directly (Cretu et al. 2010).

Compared to the metal ion, impurities formed by oxidant affect the physio-chemical properties even stronger. The atoms introduced by the oxidant include oxygen, hydroxyl, carboxyl, and other oxygen groups. These groups are introduced into the graphene plane because of the procedure of oxidation-reduction technology. Take Hummers method for example H_2SO_4 (100 g) is added to a flask immersed under an ice-bath. The flask contained natural graphite powder (4 g) and $NaNO_3$ (2 g). After 30 min, $KMnO_4$ (18 g) is added gradually. The reaction mixture is stirred for 10 h at 30 ^oC. As the reaction progressed, the suspension became paste-like and brownish (Hummers & Offeman 1958). The graphite changed into graphite oxide after ultrasonic irrigation to obtain GO, the XPS image of the specimens as shown in **Figure 2-16**.

There is a large number of oxygen groups on the graphene sheets. Even after the reduction procedure as shown in **Figure 2-16 (b)** there are still some oxygen groups left on the graphene plane. After introducing oxygen groups on the graphene sheets, removing them completely is impractical no matter through chemical reduction or thermal reduction method. Employing Raman for the further investigation, the results show the intensity ratio between the disorder induced D band (I_D 1345 cm^{-1}) and the G band (I_G 1585 cm^{-1}) do not change or even rise (Yang et al. 2009; Sheng et al. 2011; Cheng et al. 2012). After reduction process, the relative amount of the defect on graphene sheets do not change or even increase. This effect is because the pores remain on the graphene plane after removal of the oxygen groups (Cheng et al. 2012).

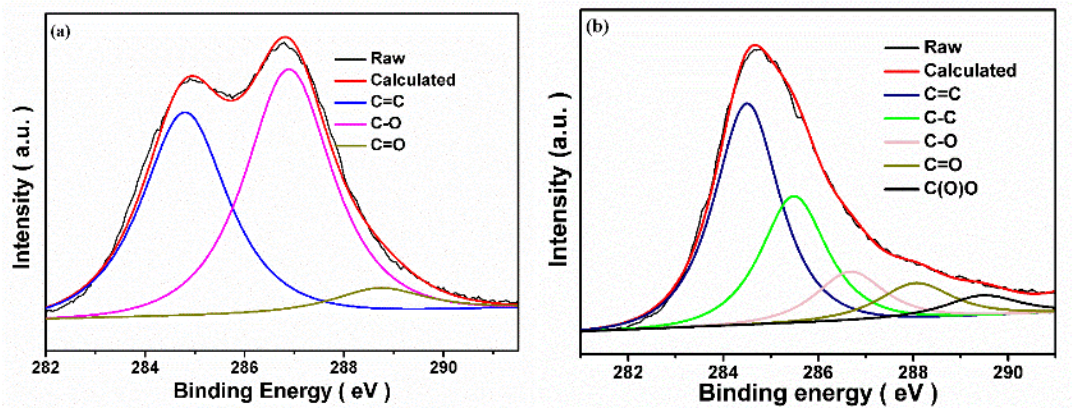

Figure 2 - 16 *The XPS of GO, and RGO. (a) XPS of carbon in GO and (b) XPS of carbon in RGO as obtained from my experiments.*

Substitutional impurities defect non-carbon atoms could be incorporated into graphene lattices with an impure atom replacing one or two carbon atoms, such as boron or nitrogen. Acting as the natural dopants in carbon materials, they could form three chemical bonds with roughly the same atomic radius. Transition metal impurity defects have also appeared as defects on the graphene sheets (Nemec et al. 2006). Substitutional impure defects receive particular attention since they not only shift the position of Fermi level but also alter the electronic structure of graphene (Boukhvalov & Katsnelson 2008; Ci et al. 2010). Boron or nitrogen can be artificially introduced into graphene plane, to functionalize the graphene by increasing catalytic activity (Qu et al. 2010) or the electrical conductivity (Wu et al. 2011).

2.3.3.3 The formation of graphene defects

Based on the recent investigation, graphene defects can be obtained by three methods: beam irradiation, chemical treatment, and lattice growth.

Beam irradiation introduces defects into the graphene plane by using electron-beam irradiation with a suitable amount of energy. The carbon atom is then removed from the graphene plane or shifted. These dislocated atoms serve as introducing atoms potentially repairing or forming defects as discussed. Based on this mechanism, graphene oxide reduction has been studied (Zhu et al. 2010). Because of the experimental investigation, not only electron-beam but also ion-beam (Krasheninnikov & Banhart 2007; Krasheninnikov & Nordlund 2010), and γ-beam (Zhang et al. 2012) with suitable energy all can change the structure of graphene. Lucchese reported low energy (90 eV) Ar^+ ion irradiate the graphene sheet to receive disorder (Lucchese et al. 2010). Raman spectra showed that at the determined intensity ratio I_D/I_G on the Ar^+ ion, the relative intensity of the D band would increase with rising Ar^+ ion concentration (10^{11}-10^{14} Ar^+/cm^2) as shown in **Figure 2-17**. The defect of graphene was increased by Ar^+ ion irradiation.

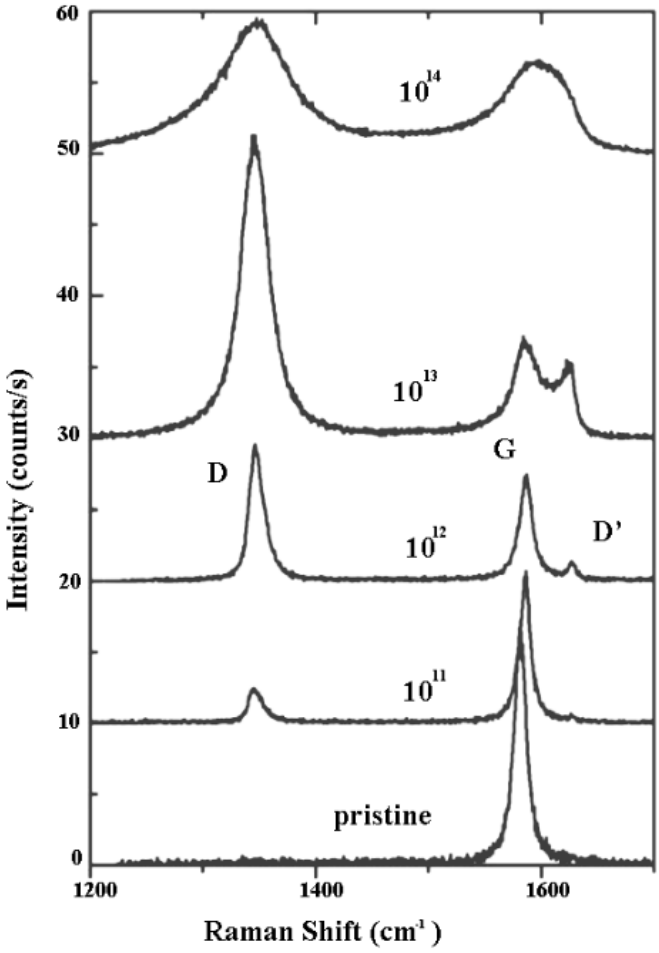

Figure 2 - 17 *The Raman spectra of graphene with different concentrations of Ar^+ ion irradiation treatment (Lucchese et al. 2010).*

Chemical treatment induced graphene defects occurred during the preparation process, which can be used to modified graphene as well. The foreign atoms introduced into graphene lattices with the chemical agents include oxygen, nitrogen, and boron (Wang et al. 2012; Bo et al. 2013). Chemical treatment induced graphene defects are sometimes because of the limitations of graphene preparation, such as the chemical reduction procedure, and others methods to induce foreign atoms for unique properties (Wang et al. 2012).

The graphene sheets grown in large-scale by one nucleus cannot be obtained normally, but the multi-nuclei growth method for preparing large-scale graphene sheets will induce defects (Zandiatashbar et al. 2014). Take CVD for example. When the different graphene sheets coalescence together, a linear defect is achieved (Terrones et al. 2010).

The point defect can be overcome by high temperature through relaxation toward thermal equilibrium (Terrones et al. 2010).

2.3.4 The influence of defects on graphene properties

The prepared graphene sheets are normally more or less defective (Banhart et al. 2011). The properties of defective graphene are very different from the defect-free sample because its theoretical properties being governed by its structural integrity (Rutter et al. 2007). Therefore, the influence of defects on properties of graphene needs to be investigated.

2.3.4.1 Chemical properties

Recently, the investigation of defective graphene is mainly focused on graphene with extrinsic defects because intrinsic defective graphene has similar chemical inertness as defect-free graphene. Graphene doped with nitrogen or boron atoms can increase the chemical activity, which is useful in the electrochemical (Bo et al. 2013), and Li-ion battery fields. Modified graphene often can be used in the photocatalytic field, after doped with boron atoms to increase light absorption.

2.3.4.2 Electrical properties.

The electrical properties of graphene are strongly affected by defects. Theoretically, defects changing lattice structure of graphene induced modification of the Dirac equation for electrons in graphene. This situation can change the electronic structure of graphene. Recently scholars reported, GO is an insulating material with a block resistivity of approximately 10^{12} Ω or higher (Becerril et al. 2008; Zhao et al. 2010). However, Zhiping reported that if the oxygen groups, such as C-O-C, are located in a suitable area the conductive properties of GO could be as high as metal (Zhiping & Kun 2010). Until now, the influence of defects in graphene sheets on its electronic properties still lacks experimental investigations to support and compare with a large number of theoretical simulation results. However, all defects cause scattering of change of electron trajectories and electron waves (Cortijo & Vozmediano 2007; Rutter et al. 2007). Consequently, preparing intrinsic defect-free graphene can improve the electronic properties of the graphene products.

2.3.4.3 Mechanical properties

Defect-free graphene has unique mechanical properties (Rao et al. 2009). It is stronger than most known engineering materials. Based on the limitations of the experimental

methods, investigations into the influence of defects on mechanical properties stay at a theoretical level. Theoretically, the tensile strength and Young's modulus will be decreased because of point defects, especially vacancies. Nevertheless, the reconstruction of the delocalized carbon atom not only cause defects but also can heal some vacancy defects to minimize the negative effect (Banhart et al. 2011).

Hao reported on the influence of point defects and single vacancy defects on the mechanical properties of graphene by simulation (Hao et al. 2011). As the concentration of the two defects increased, Young's modulus decreased. The concentration of single vacancy defects and the percent change of Young's modulus are linear dependence, but the concentration of point defect appeared to follow a non-linear dependence. Zandiatashbar reported on the sp^3-type and vacancy defects influence on mechanical properties. The elastic modulus of defective graphene is maintained even at high concentrations of sp^3-type defect (Zandiatashbar et al. 2014). The results show that the breaking strength of sp^3-type defective graphene is slightly reduced (about 14%) compared to a pristine sample. However, vacancy filled graphene shows a significant drop in its mechanical properties.

The mechanical properties of defective graphene with introduced impurity defects was also investigated. The Young's modulus of the defective graphene is 42.4% smaller than its pristine counterpart, while the tensile strength is almost unchanged in the C-O-C defect regime. The C-O-C is a foldable structure that causes Young's modulus to be reduced. The influence of epoxidation groups on the mechanical properties depends on the symmetry and concentration of oxidation (Zhiping & Kun 2010). In summary, of the intrinsic defects, vacancies particularly strongly affect tensile strength, while introduced impurity defects cause modulus changes to graphene sheets.

2.3.5 Methods for controlling graphene defects

The defects of graphene are closely related to its properties. Graphene is required to regulate its defects to use graphene under certain conditions. The method of regulating defective graphene can be divided into two parts: (1) healing defect for defect-free graphene sheets, and (2) increasing the defect for certain properties.

2.3.5.1 Graphene with less defect

There are two ways to achieve the healing defects. First, choose a suitable preparation method. The bottom-up approach prepared graphene has less defect than top-down

approach (Zhu et al. 2010). The bottom-up approach prepares graphene from carbon atoms or other small molecular feedstock to grow a graphene lattice. Although the intrinsic defects almost cannot be overcome when the graphene is grown on a large scale, under certain situations the graphene sheets can grow as almost perfect graphene lattices (Niu et al. 2017). At the same time, top-down prepared graphene has numerous extrinsic defects, which are difficult to heal (Stankovich et al. 2007). Take oxidation-reduction technology. Therefore, the reduction procedure is used to heal defects as always. On the other hand, to remove oxygen groups as clean as possible, thermal (Choi et al. 2017), chemical reductant (Stankovich et al. 2007), electrochemical (Rychagov et al. 2017), and even microwave reduction (Ates et al. 2017) methods are employed. In the chemical reductant method, hydrazine was employed to remove the oxygen groups, healing some of the defective graphene structure. Since the hydrazine can form aminoaziridine moiety, diimide, under the certain thermal condition can be eliminated to gain double bonds (Stankovich et al. 2007), as shown in **Scheme 2-2**. Although some chemicals can heal the graphene structure theoretically, carbon atoms removed by oxidation and reduction procedures, forming intrinsic defects are non-repairable. As Raman spectra shown, the intensity ratio between the disorder induced D band (I_D 1345 cm^{-1}) and the G band (I_G 1585 cm^{-1}) do not change or even are discernibly increased.

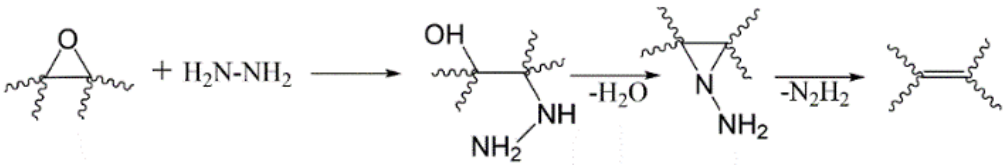

Figure 2 - 18 *A proposed reaction pathway for epoxide reduction with hydrazine.*

Using bottom-up approach to repair the defective graphene shows feasibility (Dai et al. 2011; Cheng et al. 2012). Meng reported a methane plasma repairs defects in graphene oxide. The parts of intrinsic defects on graphene sheets can be repaired. The I_D/I_G is decreased, as shown in **Figure 2-19** (Cheng et al. 2012). Because of the complicated process, this repair route is not suitable for preparing defect-free graphene on a large scale.

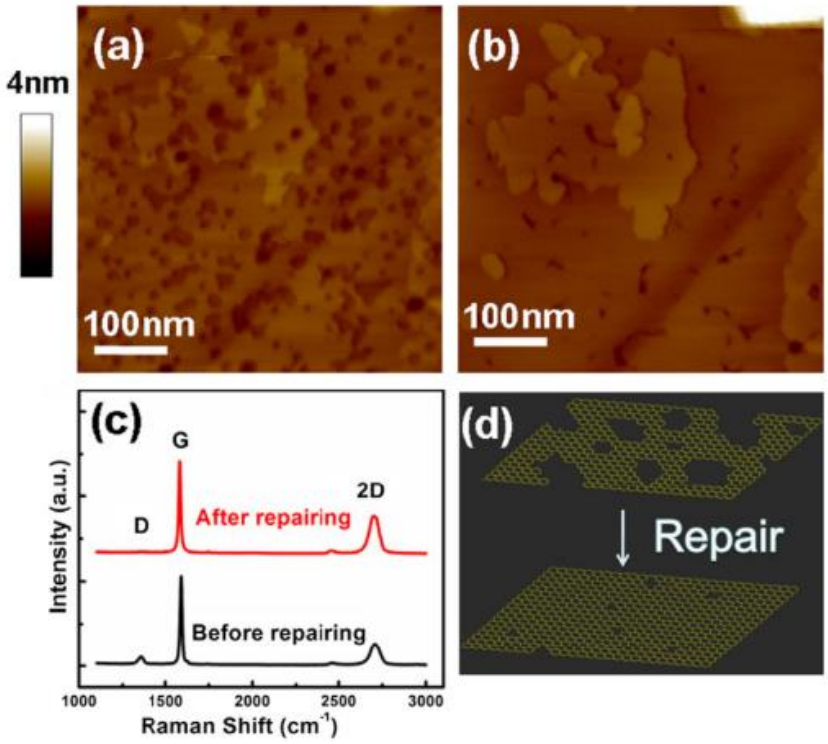

Figure 2 - 19 *Defect repair on graphene surface (Cheng et al. 2012).*

2.3.5.2 Modifying defects

The intrinsic and extrinsic defects on graphene all can be prepared in the laboratory (Banhart et al. 2011; Taluja et al. 2016; Hu et al. 2017). Extrinsic defects are much easier to fabricate than intrinsic ones. This is because extrinsic defects can be prepared based on GO, which has a higher chemical activity than graphene. The chemical agent can react with GO easily. Also, GO is a kind of extrinsic defect filled graphene (Dreyer et al. 2010). The elements can be doped into the graphene plane using a bottom-up approach. Eduard reported boron atom doped graphene nanoribbons using a chemical substitution (Carbonell-Sanromà et al. 2017). Giang reported sulfur-doped graphene prepared using substitutional doping (Nguyen et al. 2016).

The preparation of the intrinsic defect filled graphene has also been investigated. Max reported that a He-ion beam etching of the graphene sheet could be used to obtain intrinsic defects (Lemme et al. 2009). Nima reported the fabrication of downscaled graphene by He-ion beam milling, which good prospect in the construction of graphene nano-devices (Kalhor et al. 2014). Except for doped foreign elements, remove carbon atoms from the graphene plane to fabricate porous graphene as nano

filter membrane for a different aqueous solution (Kim et al. 2016), gas sorption (Han et al. 2017), and ionic transfer and energy storage (Zhu et al. 2017) are all been focused.

2.3.6 Porous graphene

Recently, substantial effort has been focused on the preparation of porous graphene (PG) based on the top-down approach, which possesses the advantages of both graphene and controlled pore structures. PG has great potential applications (Aghigh et al. 2015; Huang et al. 2015) in the energy and filtration fields. PG shows more stability than graphene obtained through the top-down approach and the tunable pore structure on the graphene plane can be designed as mass transfer route, which could be suitable for nanocomposites in the future.

2.3.6.1 Template method to fabricate porous graphene

Polymethyl methacrylate was employed as a hard template to obtain a three-dimensional bubble graphene film, with controllable and uniform porous and tailorable microstructures (Chen et al. 2012). The metal was also employed as a template, which demonstrated a great benefit to the large-scale application (Wang et al. 2013). The pores sizes were uniform and controlled by choosing different sizes of the template.

2.3.6.2 Chemical activation method to fabricate porous graphene

The chemical activation method is a simple way to fabricate PG with microspores, but it is difficult to obtain uniform pores. KOH is widely used as the pore-forming agent in activated carbon fabrication. Nowadays, KOH is employed to obtain PG (Marsh et al. 1984; Lozano-Castelló et al. 2002; Zhu et al. 2011). KOH activation method has also expanded to include different carbon sources including mixing thermal polymerization of phenolic resin or another precursor (Zhang et al. 2013). HNO_3 reacted with coordinated unsaturated carbon atoms at the defect, and the edge sites of GO sheets, leading to partial detachment to obtain dangling bonds or removal of serials of carbon atoms from the GO sheet gaining PG (Wang et al. 2009; Zhao et al. 2011; Wang et al. 2013). However, the adjustment of the pore sizes was difficult. PG fabricated by HNO_3, with many oxygen groups on the graphene sheets, reduced the compatibility between the non-polar polymers to obtain PG, metal (Lin et al. 2013; Kumar et al. 2015), metallic oxide (Fan et al. 2012), and nonmetallic oxide (Yi et al. 2013) catalysts were all developed. Because some of the noble metal salt interacting with the surface of GO, modified GO was reduced to gain PG (Tang et al. 2010). This

method fabricates PG with high efficiency, and could be produced on a large scale. Recently, researchers found other efficient ways to create pores on the graphene sheets. A gallium ion gun was used (O'Hern et al. 2014). A wet-spinning assembly can also be employed to "open pores" (Kou et al. 2015). With increased research, various methods have been developed.

2.4 Graphene/NR nanocomposites

Based on the physical properties of NR, inorganic additives are always employed for mechanical reinforcement. Graphene is a novel material with a unique 2D structure, excellent thermal and electrical conductivity, and exceptional physical properties. Therefore, graphene as an additive in the NR industrial holds promises for practical applications.

2.4.1 Preparation of graphene/NR nanocomposites

Recently, graphene used in the NR nanocomposites is prepared by chemical reduced GO, because it has low cost and large-scale production potential. Graphene doped into NR matrices can improve the mechanical properties, and electrical conductivity (Wang et al. 2017). Nevertheless, the properties of the NR nanocomposites improvements were strongly dependent upon the nanocomposite morphology and processing history. The preparation of graphene/NR nanocomposites was achieved through mixing processes, which can be divided into mechanical mixing, solution mixing, and latex mixing.

2.4.1.1 Mechanical mixing

For mechanical mixing, NR composites, or even neat NR, the NR gum, and other additives including vulcanization agents, softeners, pigments, fillers, and multi-functional additives have to be mixed. The main challenge in preparation is the viscosity of the NR matrix and the interaction between the additive and the NR molecule. The mixing procedure can be realized through mechanical mixing, solution mixing, and latex mixing. The mechanical mixing method employs two kinds of basic machines directly mixing all the additives with either NR gum or the masterbatch. One is the two-roll mill in which all materials penetrate through the space between two metal rollers, which are mounted on the machine with a tuneable space between two rollers. Another one is the internal mixer in which materials are blended between the internal rollers and the inside of the casing. The advantages of mechanical mixing are

that it is solvent free, is a simple technical process, and is low cost. The disadvantage is loss of energy, and difficulty of obtaining samples with uniform dispersion.

The mechanical mixing used in graphene/NR nanocomposites was first investigation approach reported by Zhan (Zhan et al. 2011). This is the first paper published in the graphene/NR area, which uses latex mixing to obtain graphene/NR masterbatch first and then use mechanical mixing to finish the final process for the target of reinforcement. Although mechanical mixing was not employed individually, it showed the potential of dispersing graphene sheets into an NR matrix uniformly. Mechanical mixing has always been the first choice. Recently, mechanical mixing is often combined with latex mixing in graphene/NR composites. The graphitization tendency of the graphene during the mixing procedure is not easy to be overcome by mechanical mixing individually as Zhan (Zhan et al. 2011; Zhan et al. 2012; Li et al. 2013; Yan et al. 2013; Scherillo et al. 2014; Yan et al. 2014; Wang et al. 2017) and Potts Jeffrey R (Potts et al. 2012) reported. Although the thermal and electrical conductivity of graphene/NR nanocomposites can increase with graphene content within a certain concentration range, the percolation threshold is much larger than the latex mixing approach (Potts et al. 2012; Luo et al. 2014; Lee et al. 2017; Li et al. 2017).

2.4.1.2 Solution mixing

For the solution mixing approach, NR needs to be dissolved in suitable solvent initially. The solvent used is always same examples include coal oil, butylene oxide, and cyclohexane. Considering the small amount of soft gel appearing in the NR gum, several percents of ethyl alcohol can be added. Moreover, the 'neat NR' solution still needs to be filtered before being used as a hard gel, and dust is formed. The additives also have some special properties that are the additives can be wetting the solution. The advantages of this method are that the additives can disperse into the NR matrix uniformly. The disadvantage is it always employs an organic solvent, which can cause pollution.

Solution mixing was employed into graphene/NR nanocomposites fabrication just after the latex mixing and mechanical mixing by Ozbas (Ozbas et al. 2012) which focused on mechanical reinforcement and the phenomenon revealed by investigated the strain induced crystallization of graphene/NR nanocomposites fabricated by solution mixing. NR is normally dissolved in a non-polar organic solution, but

graphene suspension stability shows better performance under strong-polar organic solutions (Hernandez et al. 2008).

2.4.1.3 Latex mixing

The investigation in latex mixing in the NR system has a shorter history than mechanical and solution mixing because the latex mixing cannot be as easily reinforced as mechanical mixing and cannot achieve of uniform dispersion additives in an NR matrix as solution mixing because of the NR particles the non-rubber components covering the polyisoprene. However, the advantages of latex mixing include energy efficiency and eco-friendliness without an organic solution or dust pollution; furthermore, latex is collected from trees and is used directly. Therefore, in this study latex mixing will be employed to use NR particles as template constructed segregate graphene network and prevent the graphitization of the reduction process of the GO as shown in **Figure 2-20**.

The first published paper in graphene/NR nanocomposites was based on is latex mixing combined with mechanical mixing. The latex mixing obtains a web-like morphology consisting of graphene sheet networks among NR particles. It was reported that this graphene network was beneficial for electrical and thermal conductivity properties with greatly increased stiffness, but the elongation to break and other mechanical properties become detrimental because latex mixing being unable to mechanically reinforce easily (Tan 2006; Potts et al. 2012b; Li et al. 2017). Therefore, latex mixing of nanocomposites followed by mechanical mixing of the masterbatch processing approach that can be used to achieve the mechanical reinforcement. There are two key steps in the latex mixing. One is the latex mixing need sonication assistant to disperse of the GO in the NR latex, and *in-situ* reduction of the GO to RGO.

Ultrasonication assisted dispersion is good for uniformly dispersing GO sheets unevenly disperse into the NR latex to reach the surface of NR particles with a single layer. Another core step is to transform the polar GO to non-polar RGO that will increase the compatibility with the non-polar NR molecule to obtain mechanical reinforcement. Recently, the latex mixing is employed because of improved thermal conductivity, electrical conductivity, and gas barrier properties of the product.

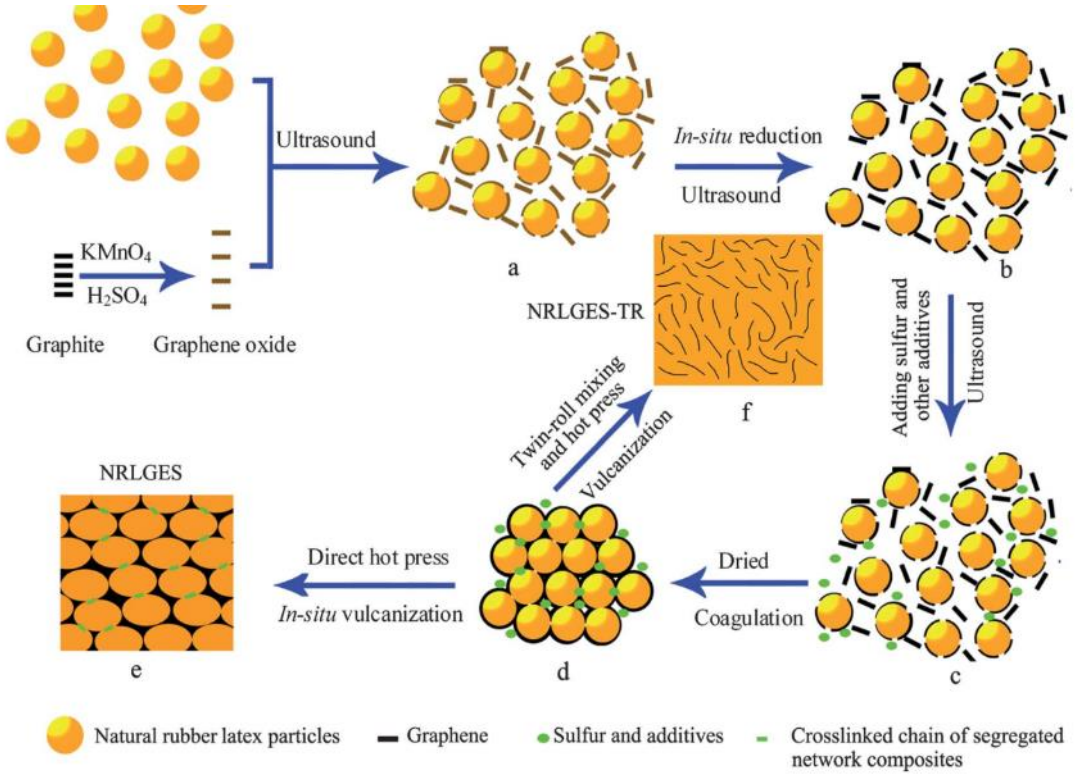

Figure 2 - 20 *The preparation of graphene/rubber composites with a conductive segregated network of graphene by self-assembly in latex and static hot press (Zhan et al. 2012).*

2.4.2 Performance of graphene/NR nanocomposites

Graphene is an ideal nano-filler in the nanocomposites area. Today, mechanical mixing, liquid mixing, and latex mixing are all studied (Zhan et al. 2011; Potts et al. 2012; Zhan et al. 2012).

2.4.2.1 Mechanical properties

An ultrasonically assisted latex mixing combined with the mechanical mixing process prepared graphene/NR nanocomposites. The mechanical properties were dramatically increased, even the addition of less than 2% which was reported by Zhan (Zhan et al. 2011). The results showed that latex mixing combined with the mechanical mixing process produces much better dispersion and mechanical performance than the mechanical mixing only specimen. With an increasing quantity of graphene, the maximum torque, elastic modulus, cross-linking density, and thermal conductivity properties were all increased. The surfactant decorated graphene was also investigated (Aguilar-Bolados et al. 2015), increasing the interaction between graphene and NR particle surface by electrostatic self-assembly, inducing a significant increase of the mechanical strength of NR nanocomposites (Dong et al. 2017; Lee et al. 2017; Zhang

et al. 2017). As the recent investigation has revealed, graphene presents more efficiency in improving mechanical reinforcement of NR nanocomposites compared to other carbonous nanofillers. Firstly, graphene has an initial structure of as 2D nano-plates, possessing a theoretical special surface area that is 2630 m^2/g. Furthermore, Gao reported that a polymer glassy layer exists near the nano-plate surface for attractive interfacial interaction (Gao et al. 2014). Therefore, graphene can perform higher adhesion and absorption compared to CB and CNTs.

As Lee reported that, the monolayer defect-free graphene sheets have a breaking strength of 42 N/m, Young's modulus of 1.0 TPa, and fracture strength of 130 GPa in theory (Rao et al. 2009). This is higher than almost all the reported additives used in NR nanocomposites. It is reported the mechanism of mechanical reinforcement of graphene, GO, and CNT in NR matrix using experimental synchrotron WAXD, and theoretical entanglement bound rubber tube (EBT) model (Li et al. 2013; Fu et al. 2015), revealing that strain-induced crystallization plays a key role in NR mechanical reinforcement. Furthermore, it was found that graphene produces a faster strain induced crystallization rate, and higher crystallinity than GO, and CNTs. Finally yet importantly, Wu, and Yan reported separately that graphene could participate in the vulcanization process of NR nanocomposites (Wu et al. 2013; Yan et al. 2014). Graphene can act as a vulcanization accelerator and increase the cross-linking density of the NR matrix for mechanical reinforcement. Although graphene is reported to be a flexible material, it still performs decreasing the elongation to break and hardness of

2.4.2.2 Electrical conductivity

NR as a stretchable material, possess excellent biocompatibility, which acts as the potential material for the flexible electronic devices of the next generation (Sekitani et al. 2008). The conductivity of NR nanocomposites depends on the additives content with a power law relationship as shown in Equation 1-1 (Edelstein et al. 1987). Two traditional approaches are used for increasing the electrical conductivity of graphene/NR. One is building a segregated graphene three-dimensional web-like network (Zhan et al. 2012; Korattanawittaya & Sirivat 2014; Li et al. 2017; Yu et al. 2017). Another is using modified graphene, include highly reduced, and chemically modified. Zhan prepared Graphene/NR nanocomposites using this latex mixing procedure with *in-situ* reduction (Zhan et al. 2012). Graphene/NR nanocomposites had a conductive segregated network exhibiting electrical conductivity, water vapor

permeability, and mechanical properties. Rouff et al. compared the nanocomposites performances between the latex mixing and mechanical combined (Potts et al. 2012a). The latex mixing treated sample showed a much higher electrical conductivity and lower electrical conductivity percolation threshold than the mechanical mixing sample.

$$\sigma = \sigma_0(\varphi - \varphi_c)^s \ (\varphi > \varphi_c) \qquad (2-3)$$

where σ is the conductivity of NR nanocomposites, φ is the volume fraction of additives, φ_c is percolation threshold, and σ_0 is a constant, determined from the conductivity of additives. Exponent s is the correlation between φ and φ_c.

Recently, most graphene/NR nanocomposites are prepared by mechanical mixing and latex mixing. Mechanical mixing shows better mechanical properties than the latex mixing. Because mechanical mixing is having a uniform dispersion of graphene in the NR matrix and obtain the glassy layer on graphene sheets (Gao et al. 2014), which is an insulator, resulting in the reduction of the electrical conductivity properties of nanocomposites. The latex mixing product shows better electrical conductivity than the mechanical mixing product, but the tensile strength and tear strength are lower than the mechanical mixing sample (Li et al. 2017; Mondal et al. 2017; Suriani et al. 2017; Zhan et al. 2017), because the segregation of the graphene and smaller amount of glassy layer is achieved than mechanical mixing. The amount of glassy layer is smaller than mechanical mixing because of the non-rubber materials covering the surface of the NR particles, the surfactants (Luo et al. 2014; Suriani et al. 2017) or small molecule (Suriani et al. 2016; Zhang et al. 2018) those using for enhance the interface interaction, and the dispersion of graphene. However, dispersants cause the graphene web-like network to become 3D structure with a low percolation threshold to approximately 0.2 vol. % (Dong et al. 2016).

2.4.2.3 Other properties

As NR has a variety of applications, gas barrier properties, thermal properties, wear resistance, and rolling resistance are all been studied. Graphene sheets need dispersion unevenly to obtain extremely high standards regarding gas barrier properties, and gases diffusion in the NR matrix be reduced by graphene with large lateral dimension, which

also leads to the increase of the tortuous pathway for gases. Thermal stability of NR nanocomposites is a crucial parameter. There are three reactions that occur under the thermal oxygen aging process, i.e., (1) pendant oxidation and scission, (2) main chain scission, and (3) formation of new cross-linking.

The effect of modified graphene prepared graphene/NR nanocomposites performed increasing thermal stability was reported by Zhang (Zhang et al. 2018), and modified graphene not only synergistic antioxidant, and a barrier to the oxygen dispersion. Recently, it was also found the mechanism of graphene sheet improve the thermal stability for two main reasons. First, the 2D structure of graphene leads to the host polymer adhesive on its surface to reduce the movability of polymer. Second, graphene can quench the free radicals. As Qiu reported multilayer, GO presents the better effect of quenching free radicals than graphene (Qiu et al. 2014). Liu also reported similar phenomenon in graphene/NR system (Liu 2016).

2.5 Literature review summary

As a whole, the application of NR materials encompasses more than half of the rubber industry and all aspects of daily life. Modifying the mechanical properties and electrical conductivity of NR materials paves the way for the next generation of rubber products, including tires, electromagnetic interference shielding, and sensors, all made possible by the unique properties of graphene. Because structure determines the properties of materials, the structure of NR was reviewed on a microstructural. Furthermore, approaches to the preparation of NR nanocomposites are studied and summarised. In the polymer nanocomposites field, the inherent properties of nano-additives to impart novel function after the host polymer has been chosen. Using graphene as an additive can make these potentials applicable to the real world, but only based on the unique properties of theoretically defect-free graphene. In this section, the preparation and performance of graphene/NR are reviewed. The graphene used in the NR nanocomposites field, however, is prepared by the oxidation-reduction method, with a variety of defects due to cost and efficiency maximisation. The defects on this graphene reduce the effectiveness of graphene/NR nanocomposites due to its properties being much weaker than defect-free examples. Hence, the types, formation and effects of these defects, and methods for regulating them are reviewed in this Chapter.

2.5.1 Research gaps

Based on the literature reveal section, there are several research gaps should be noticed:

a. The structure of GO especially made by specific parameters still requires investigation (Dreyer et al. 2010). The GO is a very useful intermediate product in the reduced graphene oxide preparation. However, the structure of the GO is changeable using different experimental parameters. Moreover, the regulation of the structure of GO still requires investigation. Moreover, the reductant is the hazardous, unrecyclable or high cost, nowadays (Zhu et al. 2010).

b. Recently, the complex graphene/NR prepared process including latex mixing and freeze-drying lead to high energy consumption and time loss (Luo et al. 2014). A simplified processing method is warranted.

c. Graphene with defects reduces the electrical conductivity of graphene (Banhart et al. 2011). The preparation of a high electrical conductivity graphene filler for the electrical conductivity NR composites is very important.

d. Polar filler and nonpolar NR molecular present poor compatibility (Wang et al. 2017). The numbers of fillers cannot disperse into the NR matrix evenly, including silica.

e. The structure of graphene could block the interaction between the different NR particles reducing the crosslink density of NR molecules (Yang et al. 2016; Wang et al. 2017). The crosslink density of NR composites decreased will influence the mechanical properties. Increase the crosslink density in the graphene/NR composites need further investigation.

2.5.2 Current work adaptation

To overcome the challenge, modified defect-filled graphene focuses on using the pores and oxygen groups on the graphene sheets beneficially. Investigations include repairing pores, using pores as mass transfer tunnels and using the oxygen groups on the graphene sheets to load graphene in the NR matrix. The target of this thesis is to realize from a practical perspective the mechanical reinforcement and enhancement of electrical conductivity of graphene/NR nanocomposites.

a. Characterise the defects on the graphene sheets prepared in this study, and regulate defects. Positrons study was employed in this study to characterise the defects. Positron measurements were found to be very effective in the investigation of defects in graphite and its derivatives. Positrons are mainly annihilated in vacancy-like defects on the particle surface and in large open-volume holes associated with the interface of graphite and graphite oxide (Gong et al. 2015). Furthermore, a green reusable reductant was developed based on regulating defects to achieve reduced graphene oxide, eco-friendly.

b. Enhance the electrical conductivity of NR composites. The one-pot reaction strategy was employed to simplify the manufactory of the graphene/NR nanocomposites. The graphene evenly dispersed in the NR latex, based on the oxygen groups. This graphene can bond with NR particles by hydrogen bonds, and the oxygen groups on the graphene sheets can be reduced by reductant in the NR latex, directly.

c. The inherent properties of fillers to impart functions to the host polymer. Therefore, the high electrical conductivity graphene filler was investigated for high electrical conductivity. The silver with high electrical conductivity was employed to decorate the graphene sheet. The technology aimed to regulate the defects set resulting in the electrical conductivity of the graphene increased.

d. Reinforce the mechanical properties of graphene/NR nanocomposites. The defects including oxygen groups and pores was used to achieve the target. The oxygen groups of graphene induce defect filled graphene acting as a surfactant. These defects filled graphene is dispersed with silica particles into the NR matrix by latex mixing to create mechanical reinforcement. Graphene with oxygen groups solves the problem of the polar filler and the nonpolar NR molecular present poor compatibility.

e. Pores defect on the graphene was also investigated for the mechanical reinforcement of NR nanocomposites. The construction of an interpenetrating network between the NR and porous graphene was studied.

Chapter 3: Research plan and methodology

3.1 Introduction

From the literature review in Chapter 2, it is apparent that the inherent property of additives imparting novel functions to the host polymer was broadly explored in the polymer nanocomposites field. Graphene was employed as an additive to enhance the performance of NR nanocomposites, including mechanical strength and electrical conductivity, as graphene possesses better physical properties than other reported NR additives. However, graphene has defects that form during the manufacturing processes, which reduce the properties of the graphene, even converting a conductive material to an insulating one. Furthermore, defective graphene presents weaker interfacial interactions with the host polymer than defect-free variants. Therefore, graphene with purposeful, designed defects to achieve high-performance graphene/NR nanocomposites is the focus of this thesis.

This Chapter describes the research plan and methodology of this thesis. In the following sections and chapters, the term RGO is used to describe graphene prepared by the chemical oxidation-reduction approach. DGO is used in Chapter 4 to highlight the deoxygenated mechanism of GO reduction. “Laboratory conditions” refer to a temperature of 23 ^{o}C - 25 ^{o}C, a humidity of 50% RH - 70% RH and under normal atmospheric pressure without special instructions.

3.2 Research workflow

In this investigation, there are several current challenges need to answer in the graphene/NR nanocomposites field. The aims of this project include:

(1) The structure of GO bears a potential to form defects in the RGO, and achieve RGO using a green and reusable route.

(2) Investigation of NR nanocomposites with high electrical conductivity and low electrical conductivity percolation threshold.

(3) Investigation of the interfacial interaction between porous graphene and NR molecules to achieve mechanical reinforcement.

This thesis will provide a better understanding of how the GO structure, modifies the defect-filled graphene, and will investigate the interfacial interaction between the porous graphene and NR, which can fill the research gap between the additives and NR.

The following sections present the materials and methods used in this investigation.

3.3 Materials

3.3.1 Natural rubber

NR is employed as the host polymer in this investigation. NR as raw materials has two kinds of status, (1) concentrated NR latex and (2) NR gum. In this research, concentrated NR latex is used. As the physical properties of concentrated NR latex can be quite different from one batch to another, the physical properties of concentrated NR latex will be determined before experimentation. In this thesis, each section used concentrated NR latex made from the same raw materials, which was collected from different rubber trees of the Hevea brasiliensis (RRIM 600 clone) in a local experimental farm was supplied by Guang ken Rubber Group Co., Guang Dong province. The NR latex was stabilized in ammonium hydroxide (0.6 vol.%). The dry rubber content (DRC) of the latex was approximately 61.4 wt.%. The detail of the concentrated NR latex is given as shown in **Table 3-1**.

Table 3 - 1 *The properties of concentrated NR latex*

	Unit	NR latex used in section 5.2	NR latex used in section 5.3	NR latex used in section 6.2	NR latex used in section 6.3	Testing method
Total solids content	%(m/m)	61.70	61.40	61.50	61.40	ISO 124
Dry rubber content	%(m/m)	60.50	60.00	61.00	60.00	ISO 126
Non-rubber content*	%(m/m)	1.20	1.20	1.80	1.40	
Alkalinity	%(m/m)	0.60	0.60	0.60	0.60	ISO 125
Mechanical stabilization	(s)	854.00	912.00	786.00	900.00	ISO 35
Coagulum content	%(m/m)	0.02	0.01	0.03	0.01	ISO 706
Copper content	(mg/kg)	4.00	2.00	2.00	4.00	ISO 8053
Manganese content	(mg/kg)	2.00	3.00	3.00	3.00	ISO 7780
Sludge content	%(m/m)	0.05	0.02	0.04	0.03	ISO 2005
Volatile fatty acid number		0.03	0.02	0.08	0.02	ISO 506
KOH number		0.60	0.50	0.50	0.60	ISO 127

* The difference between total solids content and dry rubber content.

The NR gum was fabricated from NR latex and was tested for the ash content, the volatile matter, the ash content, the nitrogen content, the Wallace rapid plasticity (P_0), and plasticity retention index (PRI). The detail is given as shown in **Table 3-2**.

Table 3 - 2 *The NR properties of ash content, the volatile matter, the ash content, the nitrogen content, P_0, and PRI*

	NR gum used in section 5.2	NR gum used in section 5.3	NR gum used in section 6.2	NR gum used in section 6.3	Testing method
Ash content	0.40%	0.20%	0.40%	0.40%	ISO 247
Volatile matter	0.60%	0.50%	0.80%	0.80%	ISO 248
Dirt content	0.01%	0.01%	0.01%	0.01%	ISO 249
Nitrogen content	0.34%	0.40%	0.36%	0.49%	ISO 19051
P_0	46	42	35	44	ISO 2007
PRI	71	82	86	85	ISO 2930

The zeta potential of NR latex is -70.0 mV. The average particle size D_{50} is 0.595 µm in diameter with two peaks in distribution. The first peak is approximately 0.138 µm, and the second peak is approximately 0.724 µm as shown in **Figure 3-1**. The NR particles were also tested using TEM, it is apparent that they are approximately round particles. As shown in **Figure 3-2**, the NR particles can act as a template with a negative charge using the electrostatic self-assembly approach, which is broadly used for rubber nanocomposites preparation achieved by the polar additives distribution, segregated network formation, and interfacial interaction adjustment. Therefore, in this study, latex mixing is employed. The NR molecule weight distribution plots are given.

As shown in **Figure 3-3,** M_n is 260386; M_w is 1270780, and M_z is 2656666. The large molecular weight (approximately a million) and broad distribution provide NR with excellent processability properties and elasticity.

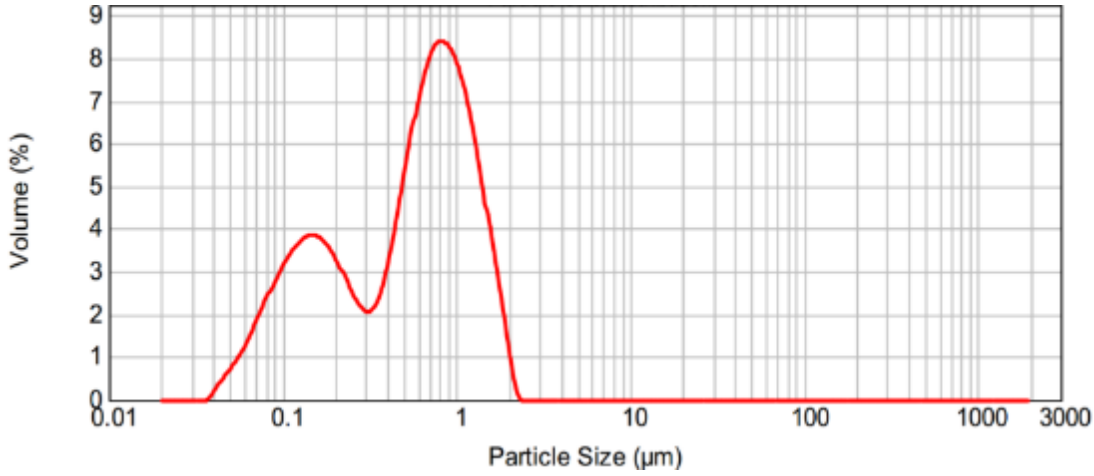

Figure 3 - 1 *The particle size distribution of NR latex.*

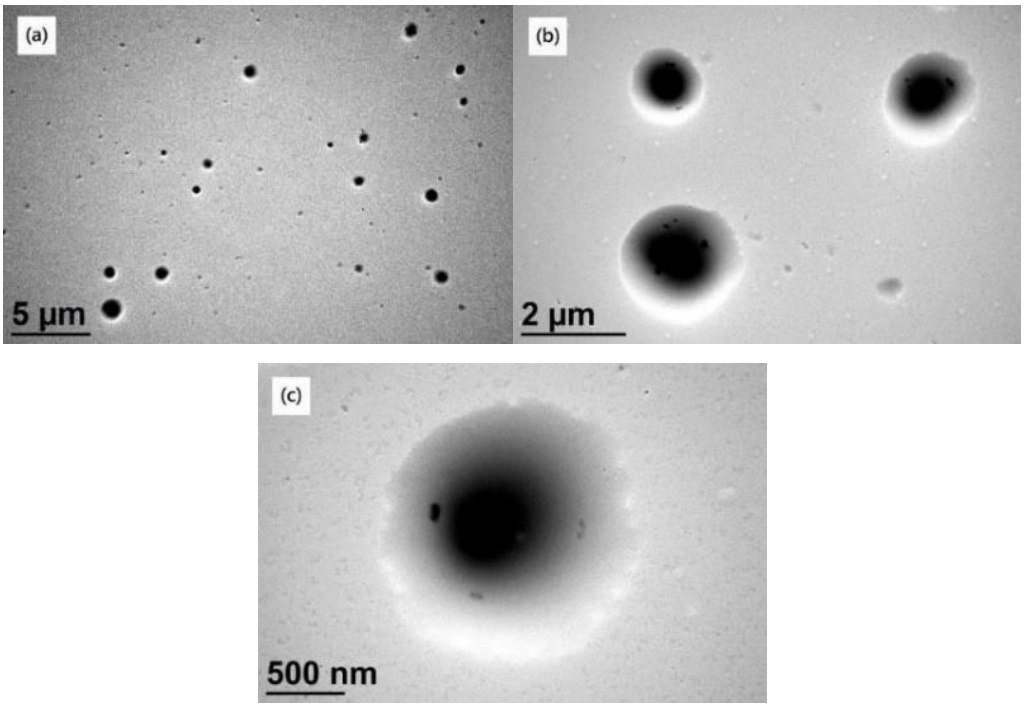

Figure 3 - 2 *The TEM image of the NR latex particles with around in shape and dimensions under 3 µm.*

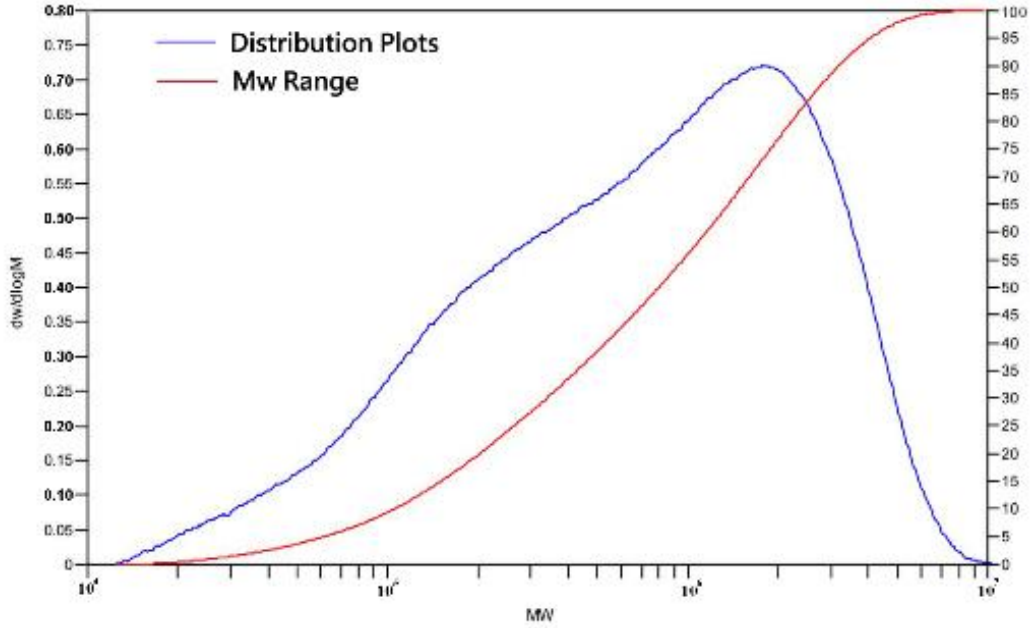

Figure 3 - 3 *The molecular weight distribution plots and Mw range of NR used in this investigation.*

3.3.2 Graphite

Graphite is a key raw material used in this research to prepare graphene and associated derivative materials. The graphite was purchased from Sinopharm Chemical Reagent Co., Ltd. (Shanghai, PR China), as natural graphite powder (density ρ= 2.26 g/cm^3, CP). The SEM image of graphite is given as shown in **Figure 3-4**. The graphite particles exhibit a layered irregular shape.

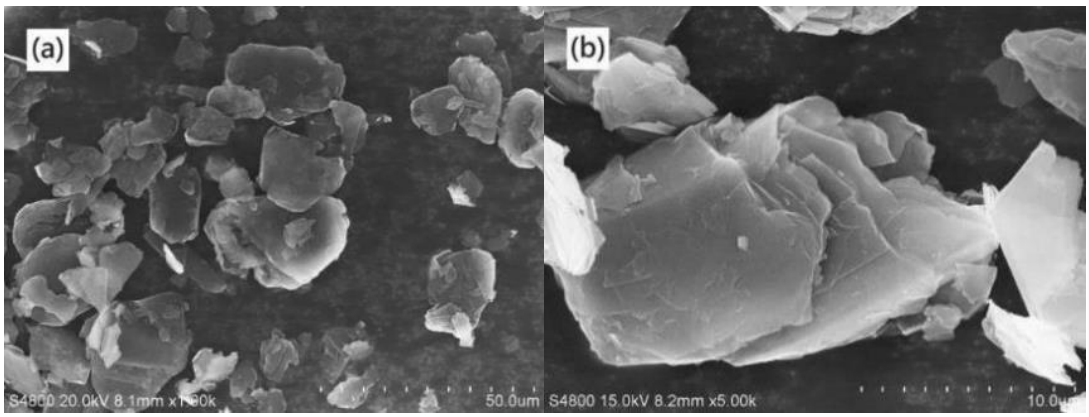

Figure 3 - 4 *The SEM image of graphite with a layered structure.*

3.3.3 Vulcanization of graphene/NR nanocomposites

The curing agents for vulcanization were all chemically pure grade supplied by Guangdong DUBA Materials Sci-Tech. Co., Ltd. (Guangzhou, PR China), was used without further purification. The experimental formulas are given in **Table 3-3**, **3-4**.

Table 3 - 3 *The experimental formula of curing agents in section 5.2 and 6.2*

Compound	Content (phr[a])
Sulphur	1.00
ZDC[b]	1.00
Zinc oxide	0.50
Casein	0.05
NF[c]	0.10
Ammonia	0.50

[a]Parts per hundred parts of rubber, [b] Zinc diethyl dithiocarbamate, [c] Disodium methylenebisnaphthalenesulphonate.

Table 3 - 4 *The experimental formula of curing agents in section 5.3 and 6.3*

Compound	Content (phr)
Sulphur	1.80
Zinc oxide	5.00
Stearic acid	3.00
NS[a]	0.70
MB[b]	2.00
Triton-100[e]	3.00
Casein	0.43

[a]2-Mercaptobenzothiazole, [b]2-Mercaptobenzimidazole, [c]t-Octylphenoxypolyethoxyethanol.

3.3.4 Other chemicals and materials

Water

In this investigation, two kinds of water were used. The first is deionized water, which was used for all aqueous solutions prepared in this thesis produced by an ultrapure water manufacturer (ABW-2001-V, Chongqing Ailepu, China). The second one is

pure water, which used in experiments in Chapter 5, and 6. The pure water was purchased from Hangzhou Wahaha Group Co., Ltd.

Sodium nitrate

Analytical grade sodium nitrate was supplied by Guanghua Sci-Tech. Co., Ltd. (Guangzhou, PR China), was dissolved in concentrated sulfuric acid (98 wt.%) as a pre-oxidation agent at 0 ^{o}C.

Sulfuric acid

Concentrated sulfuric acid (98 wt.%) supplied by Guanghua Sci-Tech. Co., Ltd. (Guangzhou, PR China) dissolved sodium nitrate and potassium permanganate to oxidized graphite.

Potassium permanganate

Analytical grade potassium permanganate was supplied by Guanghua Sci-Tech. Co., Ltd. (Guangzhou, PR China) and was reacted with concentrated sulfuric acid (98%) to form manganese heptoxide. The manganese heptoxide oxidized graphite to graphite oxide.

Hydrogen peroxide

Hydrogen peroxide (30 wt.%) was supplied by Guanghua Sci-Tech. Co., Ltd. (Guangzhou, PR China) for reaction with by-products from the potassium permanganate reaction with graphite under acidic conditions to create two valent manganese ions dissolving into the water, leading to the manganese being easily removed from the water.

Nitric acid

Nitric acid (65 wt.%) was supplied by Tianjin Institute of Chemical Agents and was used for mixing with concentrated sulfuric acid to obtain mixed acid to oxidized graphite.

Potassium carbonate

Analytical grade potassium carbonate was supplied by Tianjin Institute of Chemical Agents and was used to prepare RGO as a reusable reductant.

Silver nitrate

Analytical grade silver nitrate was supplied by Tianjin Institute of Chemical Agents and was used to prepare silver nanoparticles.

Sodium hydroxide

Analytical grade sodium hydroxide was supplied by Tianjin Institute of Chemical Agents dissolved in pure water to prepare NaOH solution for preparing AgNPs as a reductant.

Ascorbic acid

Analytical grade ascorbic acid was supplied by Tianjin Institute of Chemical Agents, and dissolved into pure water to reductant GO to RGO.

Poly(diallyldimethylammonium chloride)

Poly(diallyldimethylammonium chloride) (20 wt.%) was supplied by Sigma-Aldrich (Sigma-Aldrich, Louis, MO). PDDA aqueous solution was used to modify the surface charge properties of the additive to apparent positive charge. Because NR particles have negative charges, the modified additives can attach to the surface of NR particles by electrostatic force.

Hydrazine hydrate

Hydrazine hydrate (50 wt.%) was supplied by Guanghua Sci-Tech. Co., Ltd. (Guangzhou, PR China). Hydrazine hydrate acted as a reductant in the GO or porous GO reduction reaction.

PSS

PSS (M_w 200,000) was supplied by Sinopharm Chemical Reagent Co., Ltd, which is an anionic surfactant. PSS was employed to modify the surface charge of materials for the stable suspension.

Silica

Fumed silica was supplied by Sigma Co. (New York City, New York, America) with a particle size of 0.007 μm. Silica was attached to the oxygen groups of GO sheets to increase the interfacial interaction between NR and the additives.

3.4 Procedures

3.4.1 Characterization of raw materials

3.4.1.1 NR particle size distribution

The particle size distribution of NR particles was determined by a Malvern Mastersizer 2000 laser particles sizer, with size range resolution of 0.02 µm to 2000 µm. The accuracy of the equipment is ±1% at D_{50}. NR particles in the latex within a range of approximately 0.02 µm to 5 µm are suitable for testing using this equipment. During measurement, water was used as a dispersant with a Refractive index (RI) of 1.33. Triplicate measurements were taken for each sample, and the data were calculated by the instrument software.

3.4.1.2 Determination of molecular weight

The molecular weight analysis of NR was determined according to the method of Tangpakdee (Tangpakdee & Tanaka 1997) with some modifications, using GPC PL220 with parallax detector (Agilent Technologies, US). After NR latex was dried, NR was dissolved into tetrahydrofuran (THF) with a concentration of 0.1 mg/mL stirred with a vortex mixer for 48 h in the absence of light. Then, the solution was penetrated through a 0.45 µm membrane filter. The column temperature was 50 °C, with a flow rate of 1 mL/min. The data was collected from the response of an on-line detector.

3.4.1.3 TEM-SEAD analysis

The shape and the size of NR particles were determined using TEM (JEOL JEM 1400, 1010 JEOL Ltd. Japan). The NR latex was diluted as 0.1 mL added into 50 mL pure water with 30 min ultrasonic dispersion. Then, the 7 µL of diluted NR latex was dropped onto carbon-coated copper TEM grids, and dried under room temperature. The samples tested in Chapters 4, 5, and 6 all employed similar dropwise addition of sample treatment. JEOL HR-TEM was operated at an accelerating voltage of 200 keV, to obtain the crystal structure of AgNPs and the SAED pattern. For NR nanocomposites, a section of the sample was cut by EM-UC6+FC6 cryo-ultramicrotome (Leica Microsystems, Wetzlar, Germany) with a diamond knife. The knife temperature was -95 ^{o}C, and the chamber temperature was kept at -120 ^{o}C. The section thickness was approximately 70 nm, which was collected on copper grids for observation. The particles size was analysed using Image-J. TEM was employed to

characterise the particles size distribution in nano-particles research, therefore, in Chapter 5, TEM was employed as effective research approach to determine the nano-particles size and distribution.

3.4.1.4 SEM-EDS analysis

The morphology was carried out using SEM (Hitachi High-Technologies, S4800, Japan). The aqueous sample was dropwise onto a polished silicon wafer or aluminum foil. Bulk samples or powdered samples were pasted on the carbon-based conductive adhesive. The sample was coated with a platinum-palladium layer under magnetron sputtering with about 2-5 nm thickness, only when the size of observed objects larger than 100 nm, using Ion Sputter E-100 coating system (Hitachi High-Technologies, Tokyo, Japan). The EDS analysis sample normally exists without coated electrical conductivity layers (EDAX (Octane Super), AMETEK Co., Ltd, US).

3.4.1.5 Zeta potential

Zeta potential measurements were performed using a Zetasizer Nano-ZS (Malvern, UK) with irradiation from a 632.8 nm He-Ne laser. The testing sample was diluted and filled into a capillary cell and a mixed mode method was employed. The Zeta potential was determined from the measurement of electrophoretic mobility, μ through the Smoluchowski Equation (3-1):

$$\mu = \frac{\zeta \epsilon_m V}{4\pi\eta D} \tag{3-1}$$

In Eqn 3-1, ϵ_m is the dielectric constant of the medium, V is the voltage, η is the viscosity, and D is the electrode separation. The Smoluchowski equation is suitable as it is rigorously valid for spherical particles only, and the NR particles are spherical particles according to the TEM images as shown in **Figure 3-2**.

3.4.2 GO and graphene preparation

3.4.2.1 GO preparation and structure characterization

GO was prepared using a Hummers method. First, a flask containing natural graphite powder (4 g) and $NaNO_3$ (2 g) were mixed using a glass rod. Precooled H_2SO_4 (100 g, cooling under 0 ^oC condition) was added to a flask immersed in an ice-water bath. 30 min after that, $KMnO_4$ (18 g) was added gradually for 30 min. The reaction system was heated to 30 ^oC and stirred for 10 h at 30 ^oC. As the reaction progressed, the suspension became paste-like and brownish. The reaction was stopped by adding pure

water into the reaction system under vigorous mechanical stirring. After cooling the mixture to room temperature, H_2O_2 was added into the mixture to convert the high valence manganese to soluble Mn^{2+} under acidic conditions. The precipitate was purified by centrifugation with deionized water until the pH value reached approximately 7. Purified graphite oxide was dispersed into purified water with the aid of ultrasonic irradiation (200 W, 40 kHz, 10 min) to obtain GO. The GO used for RGO investigation was washed with HCl (5 wt.%) to exchange the H_2SO_4 in the system. Finally, the suspension was freeze-dried.

3.4.2.2 Graphite oxide preparation via acid route

Two graphite powders were prepared: nitric acid treated graphite (NG), and mixed acid (98% sulfuric acid and 65% nitric acid with a ratio of 3:1 in volume) treated graphite (NSG).

500 mg of pure original graphite (OG) was directly dispersed into 300 mL of 65% nitric acid (mixed acid) in a round-bottom flask at 98 ^oC in a nitrogen-filled dry box while stirred for 4 h. The resulting stable suspension was filtered through an ultrafiltration membrane with an average hole size of 0.22 μm and washed with deionized water several times until the pH value reached 7. The residue was collected and dried in a vacuum freeze drier.

3.4.2.3 Green graphene oxide reduction

Freeze-dried suspension (1 mg/mL) was obtained by dispersing purified GO in purified water and irradiating with ultrasonic irradiation (200 W, 40 kHz, 10 min). 75 ml of brown GO suspension and 75 mL of 4M K_2CO_3 solution were added to a flask with water bath with mild sonication (9 W, 50 kHz). After heating at 90 ^oC for 2 h, the mixture was cooled down to room temperature. The obtained solid was purified using purified water 15 times, which was followed by centrifugation and freeze-drying. DGO could be prepared by simply heating GO suspension with carbonate at a temperature of 90 ^oC. Typically, 50 mL of GO suspension and 50 mL of 4M K_2CO_3 solution were added to a flask and then placed in an ultrasonic (9 W, 50 kHz) bath basin. The temperature was accurately controlled to ensure a precise reaction temperature and homogeneous dispersion of the suspension. The color of the suspension changed from brown to dark brown, and finally to black during deoxygenation as shown in **Figure 3-5**.

Figure 3 - 5 *The color change of exfoliated GO suspension in a different procedure. (A) is GO; (B) is GO heated at 90 °C for 2 h; (C) is GO mixed with the K_2CO_3 solution and heated at 90 °C for 2 h.*

3.4.2.4 Characterization of modified graphene materials

Atomic force microscopy

Atomic force microscopy (AFM) was employed to appear the morphology of DGO surface. AFM characterization of DGO was performed with a SPI4000 probe station (SIINT Instruments Co., Japan) and XE-100 (Park System Co., South Korea) operated in normal tapping mode. The DGO was dispersed into pure water under a dilute solution. Then using a transfer liquid gun, the solution was deposited on mica, drying under room condition for AFM test.

Raman spectroscopy

Raman was employed to characterize the structure of the graphene-based materials. The intensity ratio between the disorder induced D band (I_D 1345 cm^{-1}) and the G band (I_G 1585 cm^{-1}) (I_D/I_G) shown the disorder of the structure. The Raman spectroscopy was performed on a JY-T64000 Raman spectrometer (Horiba, Japan) with an excitation wavelength of 785 nm, and an integration time of 10 s.

Fourier transform infrared spectroscopy

The changes of the oxygen-containing groups on GO sheets were measured with Fourier transform infrared spectroscopy (FTIR) with a wave scan range of 4000-400 cm^{-1} (PE, USA). The dried samples powder was treated using conventional KBr disc method. Approximately 1 mg of the tested sample was ground together with 200 mg IR grade KBr for 15 min in an agate mortar, followed by drying at 105 °C for 12 h in

an infrared oven. Pellets were pressed, and testing was performed at a resolution of 1 cm^{-1} with 192 scans referenced against a blank KBr pellet.

X-ray diffraction

The crystal structures of graphene-based materials were characterized by X-ray diffraction (XRD) which was performed on a Bruker D8 ADVANCE (Bruker AXS, Karlsruhe, Germany) with Cu K_α radiation (λ=1.54 Å). The characteristic of the corresponding layer distances d_{002}, and main peak (002) positions were calculated by the Bragg Equation (3-2). The mean dimensions (L_c and L_a) of graphene sheets was calculated from the width of individual peaks by the Debye-Scherrer Equation (3-3):

$$d = \frac{\lambda}{2 \sin \theta} \tag{3-2}$$

$$L_{hkl} = \frac{K\lambda}{\beta \cos \theta} \tag{3-3}$$

Where L_c and L_a are the average sizes of the ordered crystalline structures; K is a shape factor, with a value close to unity, and here K=0.89; λ is the X-ray wavelength, and λ=0.154 nm, β is FWHM. Θ is the Bragg angle. These values were calculated using XRD pattern analysis software, with instrumental broadening taken into consideration.

Thermogravimetric analysis-Differential scanning calorimetry

The thermal stability of graphene and GO was tested with a Thermogravimetric analysis (TGA), and Differential scanning calorimetry (DSC) using the NETZSCH STA 449 thermoanalyzer (NETZSCH, Germany) under pure nitrogen or air flow with a heating rate of 2 $^oC\ min^{-1}$ with sample weight approximately 5-10 mg at once.

X-ray photoelectron spectra

X-ray photoelectron spectra (XPS) of graphene derivatives were recorded on a Kratos Axis Ultra-DLD system (Shimadzu, Japan) with Al Kα, 1486.6 eV, and 200 W. XPS was used in this investigation was to describe the electronic state of the carbon, oxygen that exists within graphene relative materials. The changes of oxygen groups in the GO sheets can be presented clearly.

Headspace solid-phase microextraction-gas chromatography-mass spectroscopy

Headspace solid-phase microextraction-gas chromatography-mass spectroscopy (HS-SPME-GC-MS) was employed to monitor and analyze the materials that run out from

the reaction system to reveal the mechanism of GO reduction process. The samples were tested by GCMS-5050A (SHIMADZU, Japan).

Nuclear magnetic resonance

The structures of the GO and DGO were also characterized by ^{13}C-NMR using Bruker-500 (Bruker AXS, Karlsruhe, Germany). Comparing the GO reduction sample in each reaction state revealed the mechanism of the GO reduction process.

Positron annihilation lifetime spectroscopy

Positron annihilation lifetime spectroscopy (PALS) of the samples was tested by homemade equipment in Wuhan University, China. A 30 Ci ^{22}Na positron source that sealed between Kapton foils was employed for PALS and two-detector coincidence Doppler broadening of annihilation radiation (2D-DBAR). The source correction component was 355 ps with an intensity of approximately 17%. Two equal samples handle the source in the middle. PALS measurements were measured by a fast-fast coincidence system, which has a time resolution of ~270 ps (FWHM). γ-Rays with energies of 1.27 MeV that emitted from γ-decay of the ^{22}Na source and 0.511 MeV that emitted from positron annihilation in samples were monitored with detectors as the start and stop impulse signals, respectively. Collecting each spectrum with a million counts to detect the annihilation of the positron with core electrons. Doppler experiment with a two-detector coincidence system was employed. To measure the S parameter, W parameter, and the longitudinal component PALS the detector installed with the two high pure Ge detectors that have an energy resolution of 1.05 keV at 511 keV was used as shown in **Figure 3-6**.

The collected data was calculated by the program (PATFIT) after the background and source correction subtracted. The PALS were resolved into suitable components by the same fit parameters. A variance of fit was less than 1.20. Nevertheless, it is impossible to directly distinguish all the states from the resolved components of PALS, because each state may contribute a certain fraction. In this investigation, PALS resolved into 2 to 3 components according to the electron and momentum density distribution in defective graphene study.

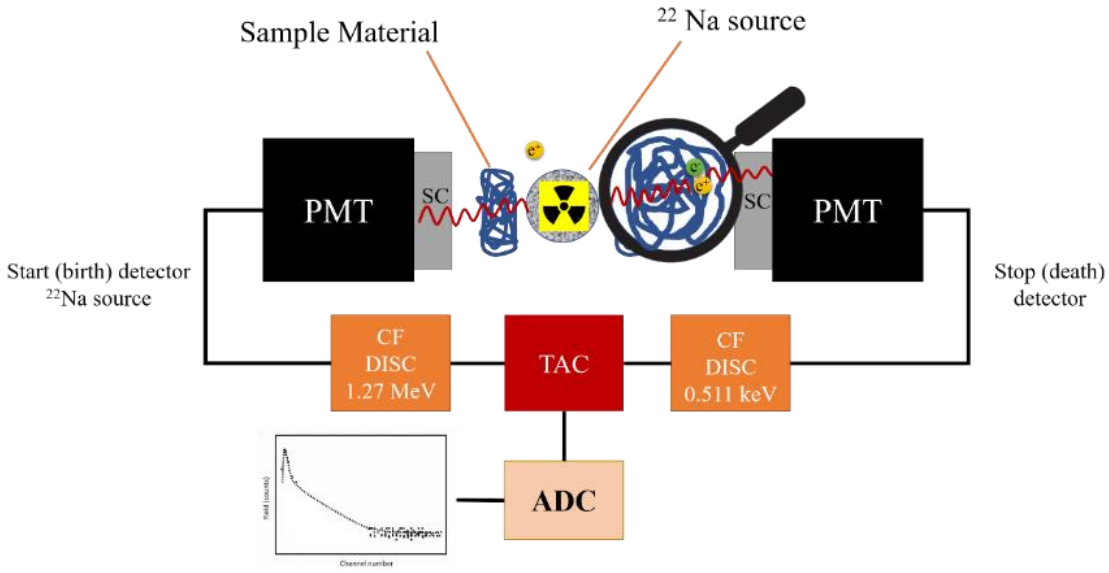

Figure 3 - 6 *Schematic of the PALS spectrometer and sub-nanosecond timing electronics, including fast scintillators (SC), photomultiplier tubes (PMT), constant fraction differential discriminators (CF DISC), time-to-amplitude converter (TAC), and an analogue-to-digital converter (ACD). The resulting PALS spectrum is a histogram of the number of annihilation events with a particular lifetime.*

3.4.3 Investigation of electrical conductive of NR nanocomposites

In Chapter 4, NR was modified by RGO and AgNPs/RGO as additives to prepare electrical conductivity NR nanocomposites.

3.4.3.1 Preparation of RGO/NR nanocomposites

GO was prepared from graphite powder using Hummers method. GO was purified with deionized water by a high-speed refrigerated centrifuge, then dried by vacuum freezing. The antistatic NR was fabricated by mixing NR latex, GO, vitamin c (Vc) and vulcanization agents using a multi-step process, as shown in **Figure 3-7**. The process is as follows:

(1) The NR latex was diluted to 40 wt.% with deionized water.

(2) 1 % stabilizer alcohol ethoxylate was added to the NR latex, and the pH value was adjusted to 10 by $NH_3 \cdot H_2O$ because it is reported that the Vc reduction can be more efficient in a mildly alkaline condition, the colour of the NR latex is white.

(3) GO powder was dispersed to the NR latex under stirring and ultrasonic conditions at room temperature for 2 h to achieve a homogeneous brown suspension.

(4) Vc was added to the mixture, and kept at 90 °C for 2 h, under mechanical stirring. The colour of the composite latex changed from brown to black, obtaining RGO/NR nanocomposites latex.

(5) Vulcanization agents (listed in **Table 3-3**) were added to the mixture and cured at 90 °C for 2 h.

(6) An antistatic film was cast and dried in the open air at room temperature. The total solid content of NR latex in the mixture was kept at 30 wt. %, so that film can be cast easily. After being completely dried, the film was placed in an air blowing oven at 90 °C for 2 h, as shown in **Figure 3-7**.

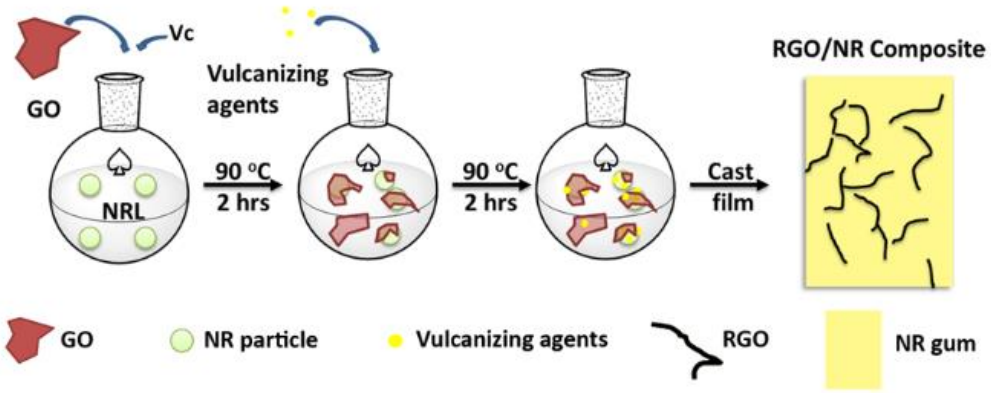

Figure 3 - 7 The schematic shows the preparation of antistatic RGO/NR nanocomposites.

3.4.3.2 Preparation of silver nanoparticles modified RGO

GO was prepared according to a Hummers method. Based on the review in Chapter 2, the electrical conductivity of RGO will decrease because of the defects on the graphene sheets. These defects, including oxygen groups and vacancies, affect the sp^2 hybridized carbon structure of graphene. Based on the research in Chapter 4 the vacancy is surrounded by oxygen groups. These oxygen groups like hydroxyl groups could act as an anchor for AgNPs growth (Liu et al. 2011). Li reported that the open edge and defect sites of graphene sheets favour banding with Ag atoms (Li et al. 2011). Therefore, if the AgNPs grow to suitable size, they can cover the defects on the graphene sheets to increase the electrical conductivity of RGO.

AgNPs/RGO was prepared using silver nanoparticles *in-situ* synthesis on the GO surface with NaOH as reductant, and finally, Vc removes the extra oxygen groups. NaOH was chosen as the main reductant because the NR latex is under base condition

by ammonia. Briefly, 150 mL of 0.05 wt. % GO dispersion was placed in a conical flask followed by the addition of 17 mL of 0.1 M $AgNO_3$ aqueous solution under vigorous mechanical stirring to produce a quasi-homogeneous dispersion. After heating the mixture to 90 ^oC, 3 mL of 8 M NaOH aqueous solution was added. Finally, the solution was refluxed at 90 ^oC in a water bath for 30 min under magnetic stirring to produce a homogeneous suspension.

To obtain the fine decorated AgNPs/RGO different conditions were investigated including varying $AgNO_3$ and NaOH content, reaction temperature, and reaction time. The experiment design of this section did not compare the purely modified with AgNPs decorated NR as blank test. Because graphene is acted as the main filler, and silver nanoparticles (AgNPs) is employed to modify graphene sheets for higher performance. Therefore, the purely RGO modified natural rubber (NR) was compared in this thesis only. Moreover, the AgNPs synthesis on the GO sheets is different from purely synthesised AgNPs particles, which have a different mechanism of synthesis and surface structures. Therefore, the purely AgNPs is no comparability in the thesis reaction system even as a blank test.

Although N doping graphene (NG) can increase the conductivity of the graphene also, the experimental cost performance of the NG is much lower than AgNPs/RGO. N doping graphene (NG) could prepare in two ways: direct synthesis and post synthesis treatment. The direct synthesis method includes CVD approach, segregation growth approach, solvothermal approach, and arc-discharge approach (Wang et al. 2012). They all difficult to synthesis large scale of NG. The NG prepared in these approaches are much expensive and not suitable for NR composites preparation. The post synthesis includes thermal treatment, plasma treatment, and hydrazine hydrate treatment (Wang et al. 2012). The thermal, and plasma treatments need special facilities and take a much longer time to prepare the NG than AgNPs/RGO. Therefore, NG prepared in these methods are more expensive than AgNPs/RGO prepared in this thesis. The electrical conductivity of NG prepared by hydrazine hydrate treatment is only 400 S/m, which is much lower than AgNPs/RGO (31000 S/m). I compare this when I experimented. Although the NG prepared by hydrazine hydrate treatment is cheaper than AgNPs/RGO, the lower electrical conductivity of NG than AgNPs/RGO induced the NG eliminated.

NaOH addition

In Chapter 5, A1, A2, A3, N1, N3, and N4 were added with NaOH by transfer liquid gun with a suitable volume of 8 M NaOH to the reaction system directly as shown in **Table 3-5** and **3-6**. In this section, L1 was added with 3 mL of 8 M NaOH diluted with 27 mL of pure water. This done to prevent the NaOH from being unevenly dispersed.

$AgNO_3$ content

In Chapter 5 the influence of the different $AgNO_3$ content on the AgNPs/RGO synthesis was investigated. The experimental formula is given in **Table 3-5**.

Table 3 - 5 *The experimental formula of AgNPs decorated RGO under different silver nitrate content*

	$AgNO_3$ (mL)	Synthesis temperature (°C)	Synthesis time (min)	NaOH content (mL)	GO content (mg)
AgNPs/RGO (A1)	4	90	30	3	75
AgNPs/RGO (A2)	17	90	30	3	75
AgNPs/RGO (A3)	21	90	30	3	75

NaOH content

In Chapter 5, the influence of the different NaOH content on the AgNPs/RGO synthesis was investigated. The experimental formula is given in **Table 3-6**.

Table 3 - 6 *The experimental formula of AgNPs decorated RGO under different NaOH content*

	$AgNO_3$ (mL)	Synthesis temperature (°C)	Synthesis time (min)	NaOH content (mL)	GO content (mg)
AgNPs/RGO (N1)	17	90	30	1	75
AgNPs/RGO (A2)	17	90	30	3	75
AgNPs/RGO (N3)	17	90	30	5	75
AgNPs/RGO (N4)	17	90	30	22	75

Vc addition

To increase the electrical conductivity of AgNPs/RGO, Vc was employed in the reaction system. After NaOH was added and reaction occurred for 30 min at 90 ^{o}C, the Vc solution was added in suspension. The Vc solution was prepared using 0.2 g Vc dissolved in 20 mL of pure water. The Vc reacted at 90 ^{o}C for 15 min as shown in **Table 3-7**.

Table 3 - 7 *The experimental formula of AgNPs decorated RGO with Vc*

	$AgNO_3$(0.1 M) (mL)	Vc (g)	NaOH (mL)	GO (mg)
AgNPs/RGO (L1)	17	0	3	75
AgNPs/RGO (V1)	17	0.2	0	75
AgNPs/RGO (V2)	17	0.2	3	75

3.4.3.3 Preparation of AgNPs/RGO/NR nanocomposites via electrostatic self-assembly with latex compounding

AgNPs/RGO/NR nanocomposites with 3D AgNPs/RGO networks were prepared by electrostatic self-assembly in an NR latex. The AgNPs/RGO aqueous solution was obtained by diluting the appropriate amounts of AgNPs/RGO suspension with a VC500 Ultrasonic Cell Disrupter (Sonics, USA). The NR latex appears to have a negative charge, as investigated in Chapter 3, and if the AgNPs/RGO possesses positive charges, they can interact by electrostatic self-assembly. However, the synthesized AgNPs/GO appears to have negative charges. Therefore, PDDA was used to change the surface charge of AgNPs/RGO from negative to positive charge. 20 wt. % of PDDA was diluted into 2 wt.% by pure water and then dropped to the AgNPs/RGO suspension under mechanical stir and ultrasonication. The AgNPs/RGO water system went through flocculation and quickly dissolved, and then the extra PDDA was removed until the zeta potential of the supernatant is approximately zero.

Then, the diluted modified NR latex (10 wt.%) and conventionally vulcanized aqueous suspension (as listed in **Table 3-4**) were successively mixed with the AgNPs/RGO suspension under mechanical stirring at 1000 rpm for 2 h. AgNPs/RGO/NR nanocomposites were collected by filtration and frozen drying. Finally, the resulting

composites were compress molded into 100 × 100 × 0.5 mm sheets at 150 ºC for 12 min and quenched by ice water.

3.4.3.4 NR nanocomposites electrical conductive characterization

XLD testing

The crosslink density was tested by NMR, which is an important parameter of interfacial behaviour, which reveals the status of NR molecule in the nanocomposites. Bloembergen, Purcell, and Pound reported the relationship between molecular reorientation and relaxation time in 1948 for the first time, which is known as the BPP theory. XLD-15 NMR crosslink density analyzer (IIC Dr. Kuhn Innovative Imaging Co. KG, German) tested XLD. The equipment is designed based on BPP theory. Molecular motions happen across a broad range of frequencies because of a consequence of network inhomogeneities in polymer networks. The molecular fragments could vibrate with different frequencies. These frequencies correspond to molecular fragments shapes, sizes, dangling free chain-ends, and the overall molecular weight distribution. Therefore, an approach to the analysis of NMR relaxation decay could be an approximation by exponential strategy. A better approach is to assume a distribution of molecular correlation times, as in the Kohlrausch-William-Watt correlation Equation 3-4:

$$\emptyset(t) = e^{-(\frac{t}{\tau_c})^{\alpha}} \tag{3-4}$$

Where $\Phi(t)$ is a relaxation function, and t is time. τ_c represents an "average" relaxation time, and α *as* a measure of the distribution of relaxation times.

The corresponding exponential correlation function needs to be replaced by a "stretched exponential function":

$$M(t) = A_0 + A_1 e^{-\left(\frac{t}{T_{21}}\right)^{\alpha_1}} + A_2 e^{-\left(\frac{t}{T_{22}}\right)^{\alpha_2}} \tag{3-5}$$

Where A_0 is a constant. A_1 is the observed signal contributed by the crosslinked polymer concerning the total amount of polymer. A_2 is the signal contributed by mobile free dangling chain-ends. The stretching parameters α_1 and α_2 are employed to describe the molecular motion within the corresponding molecular environments, which are characterized by the T_{21} and T_{22}. The software in the equipment calculates the final data.

The samples were cut into a cylindrical shape with 2 mm diameter and 8-10 mm long and put into standard glass tube supplied by equipment.

Volume resistance

Volume resistance (Rv) characterization of samples with two silver pastes coated profiles were performed with ZC-68 (Rv > 10^7 Ω) and RTS-5 four-probe conductivity test meter (Rv < 10^7 Ω) (4 probes Tech. Co. China). The conductivity (σ), was calculated according to the Equation (3-6):

$$\sigma = \frac{l}{w \cdot t \cdot R_v} \tag{3-6}$$

where w is the width of the samples, l is the length of the samples, and t is the thickness of the sample.

Tensile testing

The tensile test was measured to examine the mechanical reinforcement performance of NR nanocomposites, according to ISO 37. Tensile test measurements were tested on a U-CAN Automated Materials Testing System (U-can, Taiwan, China) at room temperature. The crosshead running speed was 500 mm/min. The sample cuts into C-type dumbbell samples according to ASTM D 412.

Dynamic mechanical analysis

Dynamic mechanical analysis (DMA) test is measurement on rectangular specimens (20 × 4 × 0.5 mm) in tensile mode at a frequency of 5 Hz using a DMA242C Dynamic Mechanical Analyzer (Netzsch, Germany) from -120 ^{o}C to 100 ^{o}C at 5 ^{o}C/min heating rate.

Inductively coupled plasma mass spectrometry

Inductively coupled plasma mass spectrometry (ICP-MS) (Agilent Technologies, US) was employed to determine the content of the remaining silver nitrate by ICP-MS7500, to calculate the yield of AgNPs in this synthesis. The remaining silver nitrate was separated from the AgNPs/RGO through centrifugation (18000 rpm for 30 min) and obtained in the supernatant. The yield was calculated according to the following Equation as Tao reported (Tao et al. 2015):

$$\text{Yield} = \frac{M - M_1}{M} \quad (3\text{-}7)$$

Where *M* is the total content of silver nitrate before synthesis. *M1* is the remaining content of silver nitrate after synthesis.

3.4.4 Investigation of graphene reinforcement NR

Electrostatic self-assembly and chemical bonds are frequently used to increase the interfacial interaction (Li et al. 2017; Wang et al. 2017; Yu et al. 2017). However, these methods face the issue of adding surfactants or chemically modified graphene and NR molecules. The surfactant will reduce the mechanical properties, the chemical modification will change the physical properties of graphene, NR, including reducing the electrical conductivity of graphene and reducing the elasticity of NR. In this study, silica was employed to cover the oxygen groups on graphene sheets as a hybridisation filler. Moreover, PG was used as an additive with similar mechanical properties as graphene but would increase the interfacial interaction by allowing NR molecules to penetrate through pores on the PG sheets, forming physical crosslinks.

The distribution property of the filler was tested by SEM, TEM, and DMA. The crosslink bonds were analyzed by FTIR, and NMR. The interfacial behavior was studied using NMR to investigate the mobility of polymer chain segments in mixtures of rubber and PG. The other interfacial behaviors were analysed using DSC investigating segmental dynamics and glass transition in a series of NR matrix filled with PG, and a gradual change of relaxation times near the surface of the nanoparticles.

3.4.4.1 Preparation of silica/graphene filled NR nanocomposites

Silica, as a well-known reinforcement filler, was used to cover the oxygen groups on the GO sheets through hydrogen bonding as SEM images shown in **Figure 3-8.** Silica/GO acted as a new 2D nano-additive, which prevents the aggression of silica particles. GO decorated by silica not only covers the oxygen groups (defects) on graphene sheets, but also as a 2D dispersant to silica dispersion into the NR matrix. PSS could act as a 1D dispersant, similar to reported research (Peng et al. 2007). NR, silica/NR nanocomposites, and silica/PSS/NR nanocomposites were compared in this section.

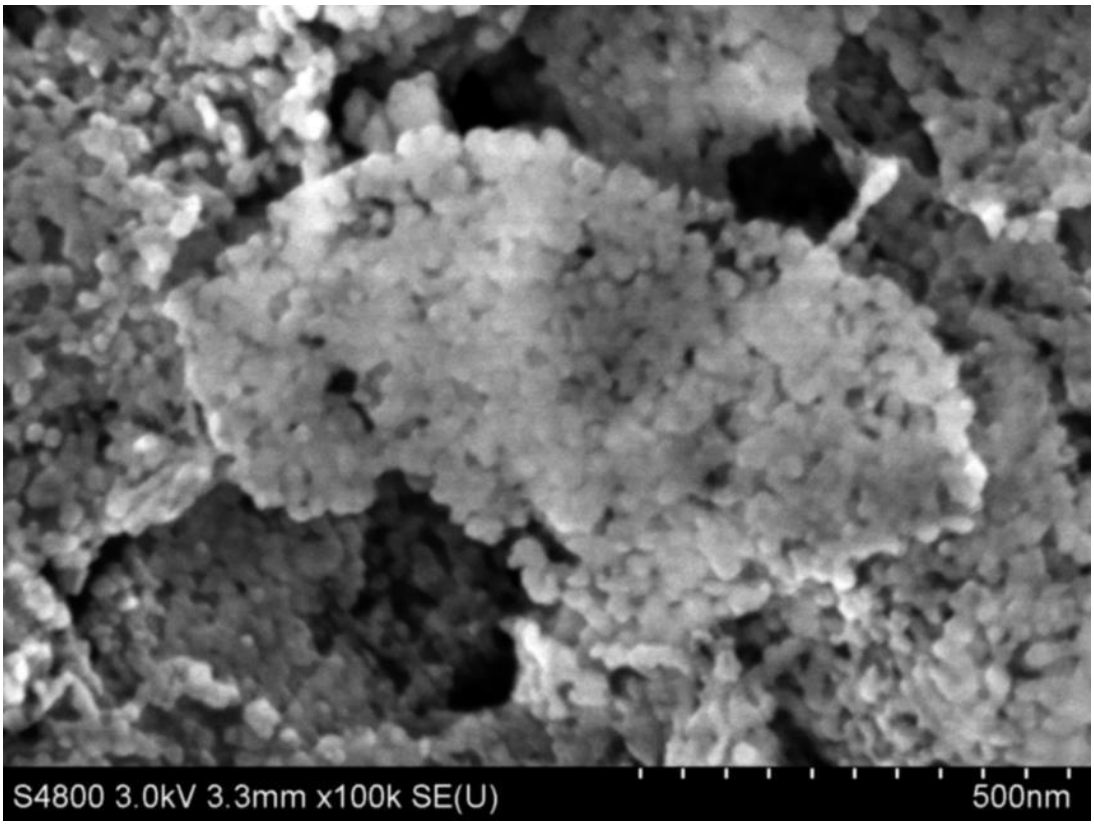

Figure 3 - 8 *The SEM image of silica attached to GO sheets forming a layer of silica on the GO sheets.*

3.4.4.1.1 Preparation of Silica Suspension

The silica suspension was prepared as follows:

(1) The dispersant, GO or PSS, was added to a beaker that contained H_2O (200 mL).

(2) SiO_2 was added and dispersed into pure water using ultrasonic irradiation (50 W) at room condition for 30 min.

(3) GO, or PSS solution prepared in step (1) was added to silica suspension prepared in step (2).

The ratio of silica to dispersant was 100:1 by weight. The control sample was prepared under the same conditions, only without any other dispersant.

3.4.4.1.2 Preparation of NR nanocomposites

Each specimen was prepared with NR latex (60 g) and an appropriate amount of NH_3. The latex was filtered with 100-mesh stainless-steel gauze to remove the gel. The silica suspension was slowly added to the NR latex drop by drop. The composite latex was stirred with a magnetic stirrer for 30 min, and then left for 1 h without stirring. The

latex was spread on a flat glass plate, and the sample was dried in a backlit, ventilated area. In these systems, the NR: SiO_2 weight ratio was maintained at 20:1. NR/GO, and NR/PSS were used as a control group for XLD measurements and mechanical tests. The SiO_2/PSS/NR and SiO_2/GO/NR specimens consisted of 100 g of NR and 0.05 g of GO or PSS dispersant. A schematic diagram of the SiO_2/PSS/NR and SiO_2/GO/NR preparation procedures are shown in **Figure 3-9**.

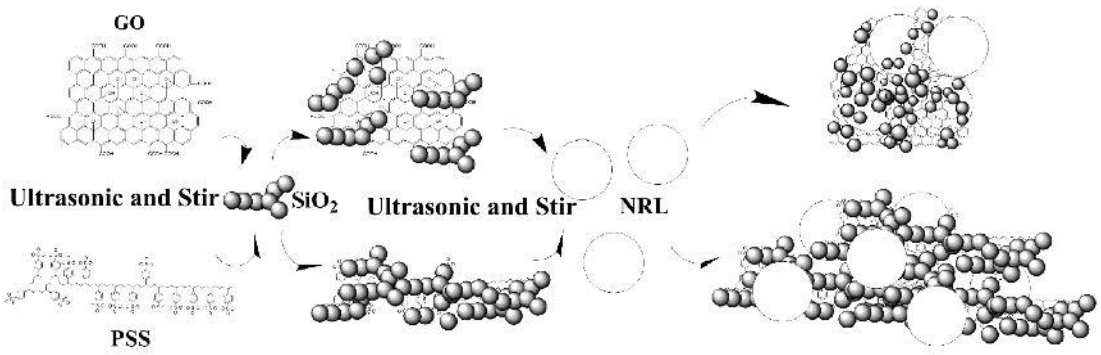

Figure 3 - 9 *The schematic diagram of the preparation of the SiO_2/PSS/NR and SiO_2/GO/NR.*

3.4.4.2 Preparation of porous graphene filled NR nanocomposites

Porous graphene will be employed as filler to achieve mechanical reinforcement of NR because the porous structures on the graphene sheets can increase the crosslink density of the NR molecules.

3.4.4.2.1 Preparation of porous graphene

Graphite was used as a raw material by employing Hummers method to prepare graphene oxide. The porous graphene was fabricated by microwave corrosion and hydrazine hydrate reduction based on GO (Fan et al. 2012). The GO powder was dissolved into pure water with a concentration of 0.5 mg/mL. Then, then dissolving $KMnO_4$ into the suspension for 10 mg/mL, the system vigorously stirred for 30 min. The suspension was heated in a microwave oven under an output power of 700 W, 500 W, and 300 W, respectively. The product was purified by adding dilute HCl 5 wt.%, and H_2O_2 30 wt.% to reduce manganese ion to the divalent manganese that could dissolve into water and remove by centrifugal cleaning and filtering, which leaves porous graphene. Finally, the porous GO was freeze-dried. The porous GO was dissolved in pure water with a concentration of 0.5 mg/mL, and then reduced by

hydrazine hydrate at 100 ^{o}C for 4 h and was finally purified by deionized water and was freeze-dried.

3.4.4.2.2 Preparation of porous graphene/natural rubber nanocomposites

The porous graphene/NR sample was prepared by the latex mixing process. Briefly, A certain amount of porous GO powder was added into the NR latex under vigorous mechanical stirring for 1 h followed by 30 min ultrasonic irradiation to obtain porous GO/NR latex. A certain amount of hydrazine hydrate was dropped into the porous GO/NR latex during mechanical stirring. After 2 h ultrasonic irradiation, the porous GO/NR latex was co-coagulated with alcohol. The masterbatch was mixed with vulcanization agents at 55 ^{o}C through a two-roll miller. The solid was cut and washed until pH neutral with deionized water. After that the composites were vacuum dried in an oven at 55 ^{o}C for 30 h to obtain the well-dispersed PG/NR nanocomposite, they were vulcanized under compression moulding into 100 × 100 × 0.5 mm sheets at 150 ^{o}C for certain minutes which tested by pressure rheometer under 150 ^{o}C. Different contents of PG used for loading into the NR matrix were 0.5 phr PG filled NR nanocomposite (0.5Mp-RGO/NR), 1 phr PG filled NR nanocomposite (1Mp-RGO/NR), and 2 phr PG filled NR nanocomposite (2Mp-RGO/NR). Samples with constant RGO loading was used as control groups i.e. 0.5RGO/NR, 1RGO/NR, and 2RGO/NR.

To identify the impact of the hot press procedure to the formation of an interpenetrating network of PG and NR molecule, the experiment given below was performed.

(1) NR gum, sulphur, and Zinc diethyldithiocarbamate (ZDC) were separately dissolved in toluene. The PG and RGO were dispersed into toluene under ultrasonic irradiation.

(2) NR was mixed, with 2 phr of sulphur, 1 phr ZDC, 1 phr of PG marked as 1Mp-RGO/NR-T. Another sample of NR was mixed with 2 phr of sulphur, 1 phr ZDC, 1 phr of RGO marked as 1RGO/NR-T. The mixture was stirred in a fume hood for 2 days under 600 rpm with the temperature at 20 ^{o}C. After stirring for 2 days, toluene was removed by evaporation in a large open beaker under airflow with a temperature of 20 ^{o}C. The dried mixture was collected, and hot pressed under 150 ^{o}C with 10 min for curing.

The characterization of PG/NR nanocomposites was performed using the testing equipment and processes discussed before. The mechanical reinforcement will be focused in Chapter 6. The morphology of the PG was tested by TEM and BET (NOVA 4000e, Quantachrome, US). The SEM, TEM, XLD, and DMA were employed to reveal the additive dispersion and the interfacial interaction between the PG and NR molecule.

3.4.4.2.3 Morphology analysis

To observe the morphology, the NR nanocomposites were cut into small pieces, and then the fracture surface was obtained after the brittle failure of bulk samples in liquid nitrogen. The cross-sections of samples were examined using SEM without gold spraying to observe the original surface with low voltage and small working distance. The TEM sample was prepared as a thin section with a thickness of approximately 70 nm, through cryo-ultramicrotome as detailed in 3.4.1.3.

3.4.4.2.4 Molecular dynamics simulation

Molecular dynamics (MD) simulation are realized by the DISCOVER code in the Materials Studio 2017. The purpose of this simulation is to monitor the formation of an interpenetrating network by the α-terminal of NR molecules penetrating through the pore in a porous graphene sheet. The interaction of the α-terminals of NR molecules and porous graphene are described by COMPASS, which is a force field parameterized based on the condensed-phase optimized molecular potential. The NHL method was used to govern the compound system at a temperature of 423 K. The Ewald method was applied for the calculation of electrostatic interactions.

The atomic structure of the porous graphene is obtained by removing carbon atoms from defect-free graphene, forming a pore with a diameter of 2 nm, and 5 nm as shown in **Figure 3-10 (a)**, **(b)**. The oxygen groups of graphene with the pore of 5 nm as shown in **Figure 3-10 (c)**. The graphene sheet is made up of sp^2 hybridized carbon atoms. The α-terminal of NR molecule is approximated as a phospholipid added with two isoprene monomers to facilitate the experiment as shown in **Figure 3-10 (d)**.

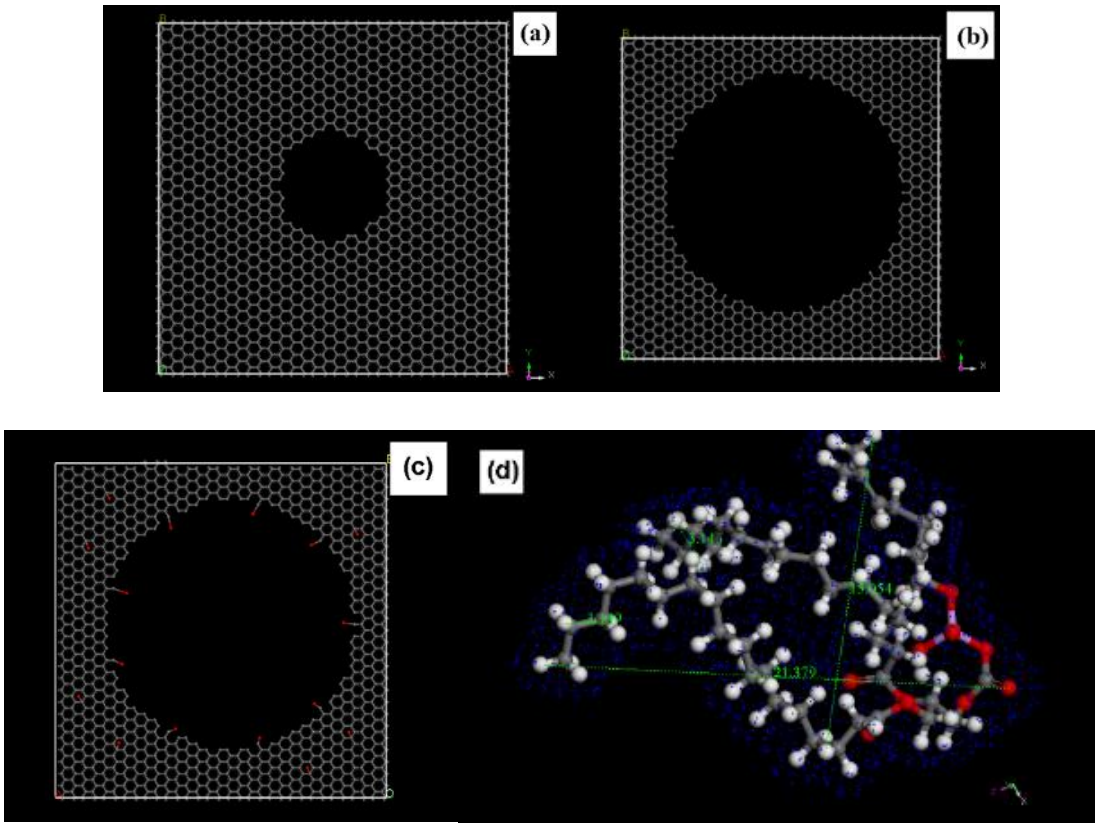

Figure 3 - 10 *The composites structure model of porous graphene and α-terminal of NR molecule. (a) graphene sheet with the pore of 2 nm, (b) graphene sheet with the pore of 5 nm, (c) oxygen groups of graphene with the pore of 5 nm, and (d) α-terminal of NR molecule.*

Based on the Takaba method, (Takaba et al. 1996) the model is constructed by Amorphous Cell with dimensions of 68.17Å × 68.88 Å × 80.00 Å. Periodic boundary conditions were used in all three dimensions. The porous graphene sheet is located in the middle of the box, and the α-terminal of NR molecules and the vacuum phase are placed on both sides of a respectively. The density of α-terminal of NR molecule is defined as 0.2 g/cm^3 at the initial step as shown in **Figure 3-11**. The dynamics calculation is achieved by Forcite Plus modules, where the model is put into an NVT ensemble. The time step is 1.0 fs, and total simulation time is 1000 ps, and the data is collected every 5 ps.

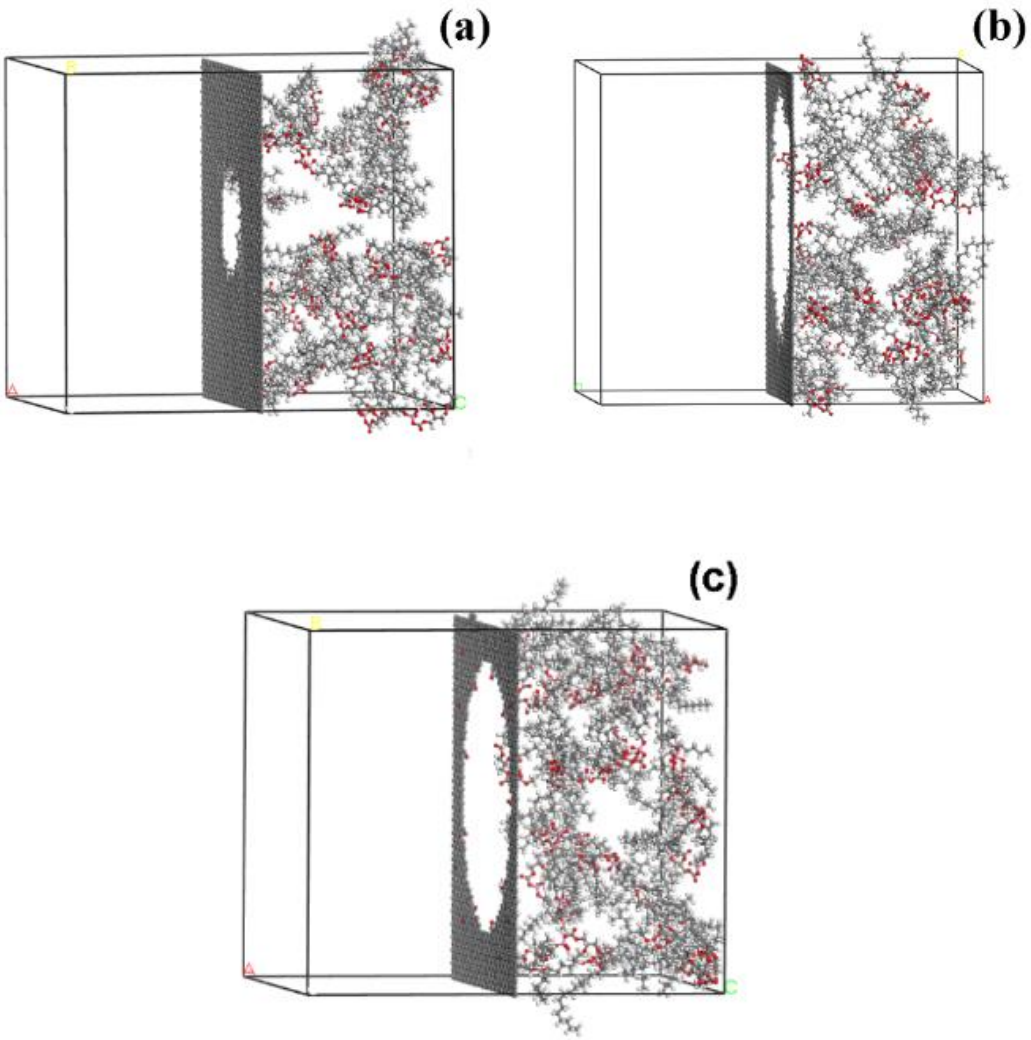

Figure 3 - 11 *A complex structural model for the formation of α-terminal of NR molecules and porous graphene. A complex structural model for the formation of α-terminal of NR molecules and graphene with the pore of 2 nm (a), graphene with the pore of 5 nm (b), and oxygen groups modified graphene with the pore of 5 nm (c).*

3.5 Concluding remarks

This chapter gives details of the materials, and testing approaches employed in this investigation. Subsequent chapters will reference materials and approaches when appropriate.

Chapter 4: The structure of graphene oxide and mechanism of a green graphene oxide reduction with reusable potassium carbonate

4.1 Introduction

This chapter investigates the defect on graphene sheets tested using the PALS, and a novel GO-reduction approach is developed by employing potassium carbonate as a green reductant. The mechanism of the GO reduction was revealed using experimental analysis.

Graphene, 2D carbon sheets constructed from sp^2-hybridized carbon with unique physicochemical properties, is prepared by micromechanical cleavage from graphite. Recently, there are several methods of obtaining graphene. The preparation methods of graphene can be summarized as a bottom-up approach or top-down approach (Rutter et al. 2007) which are reviewed in Chapter 2. The only graphene prepared using the chemical oxidation-reduction approach can be used as an additive in composite materials. In this study, GO was prepared using the modified Hummers method to prepare intercalation oxidation of graphite (Dreyer et al. 2010). The GO sheets were exfoliated with the help of ultrasonication, (Stankovich et al. 2007). The defects that were introduced into graphene could directly affect the physicochemical properties of the product as discussed in Chapter 2. Defect characterization is therefore essential for GO preparation. The defects on graphene were studied by different measurements, including XRD, XPS, and PALS.

Based on the defect information of GO, a novel and efficient method to deoxidize exfoliated GO using potassium carbonate was developed and analyzed, which is an eco-friendlier option compared with other conventional methods. The resulting deoxygenation process is simple, green, and can be easily scaled up. In addition, the deoxygenation agent is recyclable and the only by-product of the process is carbon dioxide.

4.2 Investigation of formation of defects in the graphite oxidization process

In this investigation, GO acted as a type of defect filled graphene with oxygen groups and other types of defects. The PALS and 2D-DBAR techniques were employed on graphite oxide and GO, to reveal the structure of the defects. A control group has been designed by graphite, graphite oxide to investigate the variation of the structure before and after the exfoliation of graphene sheets. The four specimens used in this research are OG, NG, NSG, and GO, which prepared using different oxidation method as shown in Chapter 3. Hummers method provided a higher degree of oxidation than mixed acid-treatment, which itself had a higher degree of oxidation than nitric acid-treatment.

4.2.1 Investigation of the morphology of graphite oxidization

The morphology of OG and its derivatives was clearly shown by SEM images as shown in **Figure 4-1**. Compared to graphite, the sizes of the samples of GO were smaller. The higher the degree of oxidation, the smaller the size of the sample was. As shown in **Figure 4-1 (a)**, the average size of OG was approximately 40 μm (the vendor labeled the average size as 45 μm). However, the distribution of the particles sizes appears to have a range of less than 1 μm to larger than 50 μm. After graphite was oxidized using nitric acid-treatment, and mixed acid treatment, the particle size of NG and NSG shrunk to 5~10 μm with a very small number of particles larger than 20 μm. It is also observed that the graphite treated by the Hummers method, which underwent the highest degree of oxidation, had the smallest average particle size, at approximately 2 μm. The main difference between nitric acid-treated graphite and mixed acid-treated graphite lies in the distribution of particle size, rather than the size range. The distribution of NSG particles size is more uniform than the NG. However, the SEM images could not elucidate whether the layered structural integrity was disordered. Regardless, the stronger the oxidising agent applied, the smaller was the size of the produced particles.

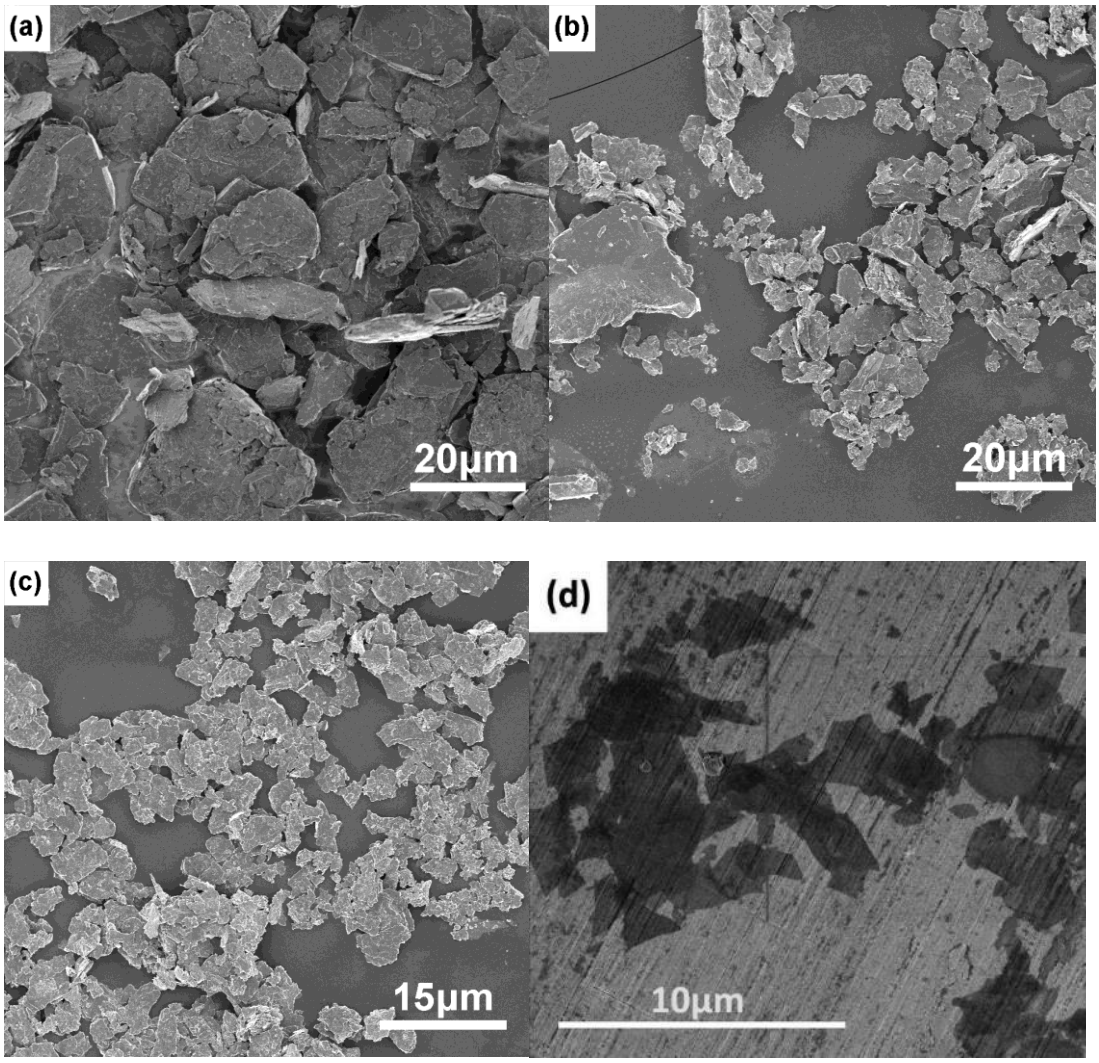

Figure 4 - 1 *The SEM images of graphite and its derivatives (a) OG; (b) NG; (c) NSG; and (d) GO samples.*

4.2.2 Investigation of the structure of graphite and its derivatives

The structure of four specimens is investigated by XRD as shown in **Figure 4-2**. The main peak (002) position data was calculated by the instrument's software, as listed in **Table 4-1**. It can be seen that OG, NG, and NSG exhibit a similar characteristic peak which lies at approximately $2\theta = 26.5^{o}$. Namely, the significant changes observed on the layer structure of OG after nitric acid-treatment, and mixed acid-treatment. However, the XRD pattern of GO, showed a wide peak at approximately $2\theta = 11.07^{o}$, which corresponded to the comparatively regular layered structure of GO (Chen et al. 2008). The layer distance and mean dimensions of the graphene sheet were calculated as described in Chapter 3. The layer distance between neighboring GO sheet was

approximately 0.798 nm, which was larger than OG by approximately 0.335 nm, because of the oxygen groups in between.

The intensity of diffraction peaks of specimens decreased with an increased degree of oxidation. Meanwhile, *Lc* was reduced from 37.9 nm to 5.51 nm, and *La* dropped from 37.9 to 0 nm, respectively. This reduction occurred because the higher degree of oxidation led to higher damage to OG structure resulting smaller product particles (Dreyer et al. 2010), which consistent with SEM results as shown in **Figure 4-1**. Furthermore, another piece of evidence that basic oxidative treatments are given from the peak position listed in **Table 4-1**. The main peak position of NG shift to lower 2θ approximately 0.07^{o} compared with OG. Moreover, the main peak position of NG shifts to the left side by approximately 0.11^{o} compared to NG. Meanwhile, GO exhibited the largest shift up to $2\theta = 11.07^{o}$, which indicates that GO underwent the highest degree of oxidation among the four specimens. The Hummers method treated specimen appears that the structural integrity of the graphitic network was affected by the distance between the neighboring graphene sheets. This was observed to expand to 0.798 nm from the original 0.335 nm of OG, while the structural integrity of the nitric acid and mixed acid treated samples were deemed to be intact.

Table 4 - 1 *XRD peak and corresponding parameters of specimens*

Samples	Peak(º)	Distance(Å)	Lc(nm)	La(nm)
OG	26.56	3.35	37.9	35.4
NG	26.49	3.36	32.7	20.4
NSG	26.38	3.38	10.1	11.8
GO	11.07	7.98	5.5	0

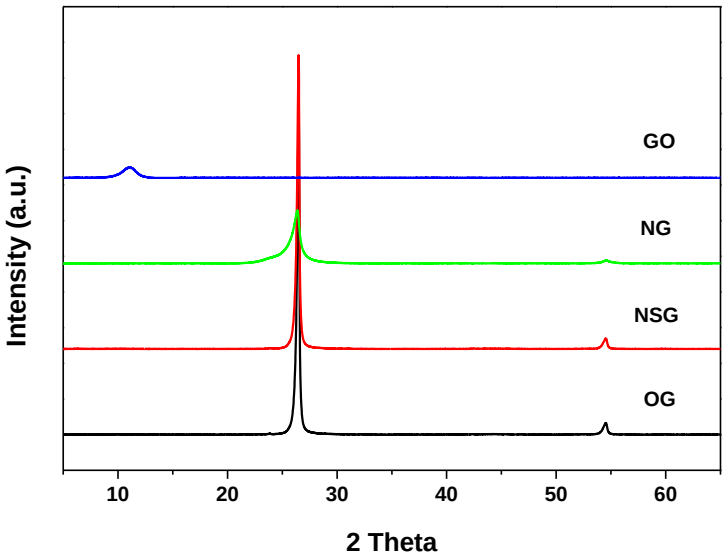

Figure 4 - 2 *The XRD patterns of OG, NG, NSG, and GO samples.*

The XPS spectra of NG, NSG, and GO are investigated to detect the chemical structure changes of the oxidation products as shown in **Figure 4-3**. Each XPS spectrum is fitted with five Gaussian peaks corresponding to carbon atoms presented in different chemical environments. The lists of different functional groups are given in **Table 4-2**. The $\pi \rightarrow \pi^*$ of NSG, as characteristic of aromatic systems, showed an obvious decrease compared with the one in NG. Based on the calculation of the integrated areas of the C1s peaks of XPS spectrum, the content of the $\pi \rightarrow \pi^*$/C-C decreased from 5.6% to 1.3%, and even disappeared in the GO specimens. Such a decrease can be attributed to the increasing decomposition of the graphite structure due to the increasing degree of OG oxidation. Between the NG and NSG specimens, the amount of the C-O-C defect was much higher in NSG than NG, and the amount of C-OH defect showed the opposite trend. More specifically, nitric acid-treatment favored the formation of C-OH rather than C-O-C, and mixed acid-treatment showed the contrary. The GO specimen had the highest oxidation degree, with C:O = 1.99. The chemical formula could be written as C_2O. The structural integrity of graphitic network was altered which is consistent with XRD and SEM test results.

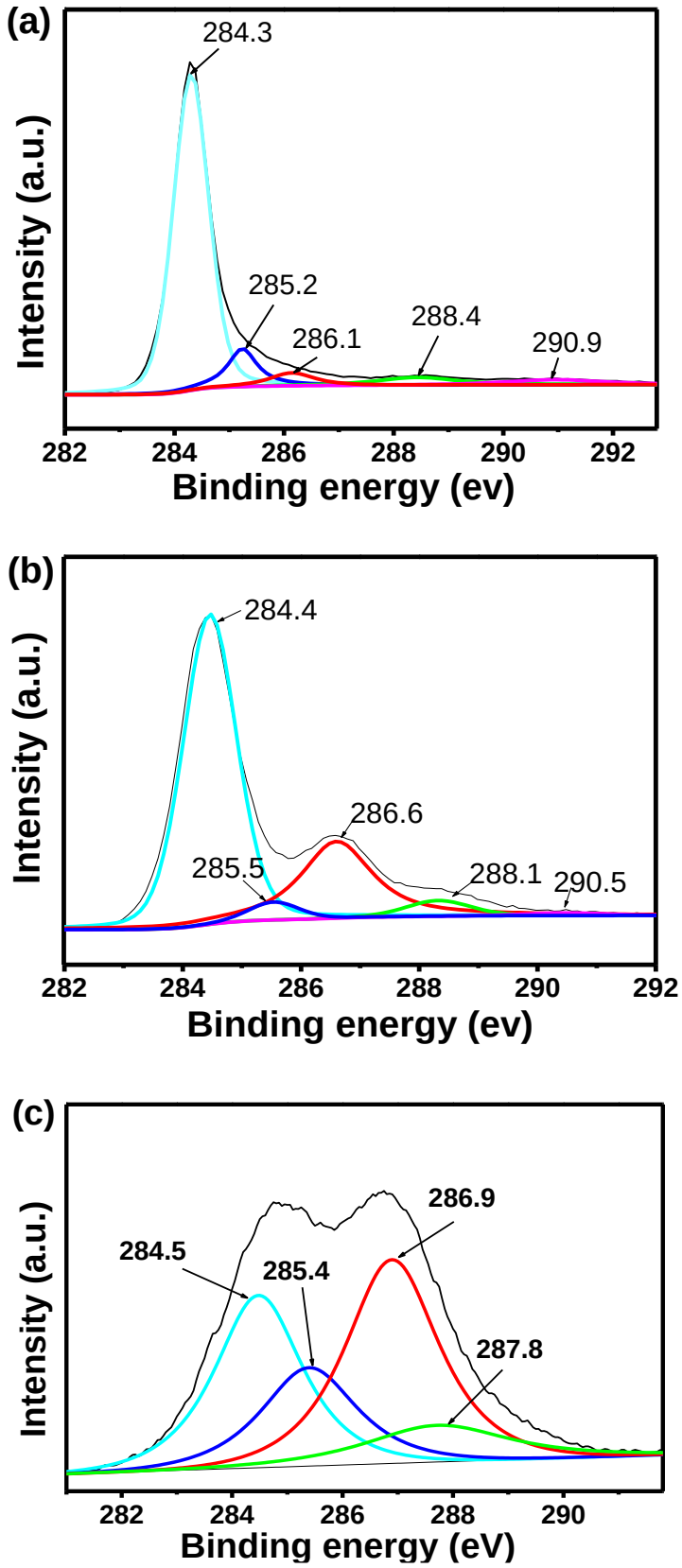

Figure 4 - 3 *The C1s core-level spectra of graphite oxidations a) NG, b) NSG, and c) GO samples.*

Table 4 - 2 *The different functional groups on the NG, NSG, and GO*

	C=C/C-C	C-OH	C-O-C	O=C-OH	$\pi \rightarrow \pi^*$
NG	284.3 (eV)	285.2 (eV)	286.1 (eV)	288.4 (eV)	290.9 (eV)
NSG	284.4 (eV)	285.5 (eV)	286.6 (eV)	288.3 (eV)	290.4 (eV)
GO	284.5 (eV)	285.4 (eV)	286.9 (eV)	287.8 (eV)	-

4.2.3 The positron study of graphite and derivatives

As described in Chapter 3, the PALS is resolved into three components. They are τ_1, τ_2, and τ_3 for describing the lifetime; I_1, I_2, and I_3 for the intensity, which is summarized in **Table 4-3**. Each component is attributed to the positron annihilation in a particular state.

The τ_1 value, as the short time component, is mainly based on the positron annihilation in bulk graphite as Wang reported (Wang & Jean 1988). The τ_1 value of OG and NG are similar. A minor increase was noted for the NSG and GO specimens. The phenomenon can be attributed to the slight expansion of NSG and GO lattice structure as seen in XRD patterns. The I_1 valve decreased with the increasing oxidization intensity because the I_1 valve is attributed to diminished graphite particle size with I_1 valve decreased the graphite particles size decreases as well. This result is consistent with the SEM and XRD measurements.

The τ_2 value could be attributed to the vacancy-like defects on the surface of the graphene structure as Wang reported (Wang & Jean 1988). The τ_2 value of GO observes slightly larger than other three specimens, which indicated that the defect size had increased and the graphite lattice had expanded. The I_2 value increases with the increasing oxidization intensity, which could be attributed to swift growth of vacancy-like defects on the graphite outer surface. I_2:I_1 of the four specimens were gradually enhanced with the increasing oxidization intensity indicating an increased the number of defects on the specimens.

It is well known that there exists a relationship between the *ortho*-positronium lifetime that is present in the third composite in the PALS resolution, and free volume size (Sharma 1988), the void diameters of the specimens are larger than 5 Å. It could be seen easily that the particles sizes of OG, NG, and NSG are much greater than the C-C distance (0.335 nm) along the c-axis between two graphene planes. Therefore, τ_3 and

I_3 could be attributed to the average size of particles, and the number of interfacial voids for specimens, respectively. In the GO specimen, the distance between the graphene sheets was enlarged to 0.798 nm as XRD shows, which was a greater than that of the detected void (Diameter=2R=0.61 nm), the possibility of *ortho*- positronium trapping at this place was increased because of a large number of oxygen groups between the layers. The τ_3 value of the OG, NG, and NSG decreased from 3.07 ns to 1.97 ns, indicating that the interfacial void size was decreased with the rising oxidizing intensity. Combining with the SEM, and XRD measurements, the inherent interfacial void on the OG specimen acted as the beginning of the diminishing of the graphite particles. The OG particles (average size 40 μm) decreased to NG and NSG with only 5-10 μm. Comparing the NSG and GO specimen, the particles changed from 5 μm to 2 μm. However, the oxygen groups on the graphene sheets were much greater in number than NSG as shown by XPS. Therefore, the τ_3 value of GO is larger than that of NSG.

2D-DBAR was recorded by a high-purity Ge detector. The broadening is described by the conventional low momentum parameter (S) and the high momentum parameter (W as Didosyan reported (Didosyan et al. 2004). The S parameters and W parameters correspond to the momentum distribution of valence, and core electrons, respectively. Therefore, the chemical environment of annihilation position could affect the S parameters and W parameters. The gradual reduction of the S parameter and the increase of the W parameter are just responses to the oxidation of graphite (Jean et al. 1984; Lee et al. 1987). Additionally, positron annihilation with the electrons of the oxygen atom will cause parameter S to be lower than that of pure vacancies in OG as shown in **Table 4-3**.

To further ascertain that the τ_3 corresponds to the positrons annihilation in between the neighbouring graphene sheets, the 2D-DBAR spectra of the NG, NSG, and GO samples were collected, as shown in **Figure 4-4**. It is difficult to directly tell the differences between one and another because of the change of the 2D-DBAR spectra based on the positrons annihilation with core electrons being small. However, to enhance the differences among spectra, ratio curves are commonly constructed. In this investigation, NSG was used as a reference, which was used to divide the spectra of NG and GO. In the high momentum part, a clear difference in the 2D-DBAR ratio curves could be seen, which indicated different electron environments of the NG and

the GO specimens. The possibility of positron annihilation in the NG specimen in the low-momentum part is greater than that of the OG for *ortho*- positronium. This reveals different vacancy-like defects present in unexfoliated NG and exfoliated GO (Chen et al. 2002). The vacancy-oxygen complexes in-between the graphene sheets, and a vacancy cluster at the interface were present because of a large number of oxygen groups in the GO specimen. Thus, the τ_3 value has mainly corresponded to *ortho*-positronium annihilation in the interfacial void. Additionally, the τ_3 value of the GO specimen occurred firstly from the annihilation of the *ortho*-positronium in-between the graphene layers for the largely expanded graphene layers, and large numbers of oxygen-groups in-between the neighbouring graphene sheets.

Table 4 - 3 *Positron lifetimes, intensities and other parameters measured in the present work*

Sample	τ_1 (ns)	I_1 (%)	τ_2 (ns)	I_2 (%)	τ_3 (ns)
OG	0.172±0.006	30.17±3.08	0.363±0.05	69.56±3.0	3.07±0.21
NG	0.177±0.006	27.87±1.86	0.363±0.03	71.80±1.8	2.28±1.64
NSG	0.198±0.009	27.67±1.74	0.366±0.04	72.06±1.3	1.97±0.20
GO	0.197±0.009	21.39±2.12	0.388±0.03	78.44±2.1	2.19±0.30
I_3 (%)	R (nm)	I_2/I_1	T_{12}(ns)	S	W
0.27±0.02	0.3681	2.30	0.289	0.5033	0.0102
0.33±0.03	0.3099	2.57	0.310	0.4888	0.0125
0.27±0.04	0.2823	2.60	0.319	0.4739	0.0162
0.17±0.03	0.3023	3.68	0.347	0.4719	0.0167

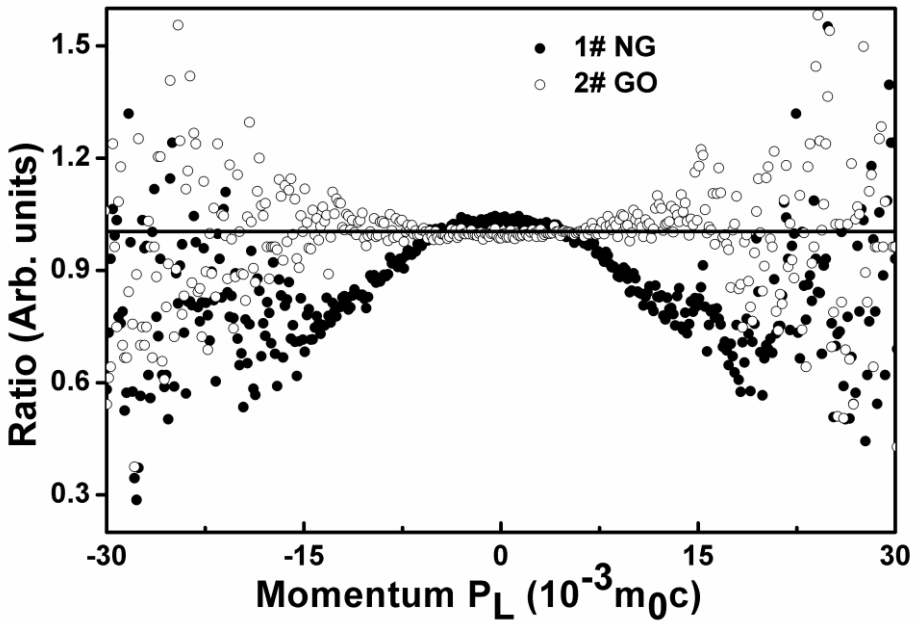

Figure 4 - 4 *The 2D-DBAR ratio curves of NG, and GO divided by NSG.*

4.3 Mechanism of a green GO reduction with reusable potassium carbonate

Graphene prepared by the oxidation-reduction approach is a promising method, particularly for preparing graphene for composite materials. The GO sheets possess hydroxyl, carboxyl, and epoxide groups, which have to be deoxidized when converting GO to graphene. The chemical reductants include hydrazine hydrate (Stankovich et al. 2007), H_2 (Li et al. 2008), hydroquinone (Wang et al. 2008), $NaBH_4$ (Muszynski et al. 2008), Na/CH_3OH (Mohanty et al. 2010), propylene carbonate (Zhu et al. 2010), Vc (Fernández-Merino et al. 2010), aluminium powder (Fan et al. 2010), and molten halide salts (Abdelkader et al. 2014) which are either hazardous, unrecyclable or high in cost. Therefore, it is essential to develop a green chemical reduction processes for graphene preparation. Recently, benzylamine (Liu et al. 2011), poly(diallyldimethylammonium chloride) (Zhang et al. 2011), and tea polyphenols (Wang et al. 2011) were employed as eco-friendly chemicals for sthe ynthesis of graphene. However, none of these can be reused. In this research, K_2CO_3 as a green, eco-friendly, and reusable GO reductant will be investigated. The K_2CO_3 reduced GO under mild reaction condition, which was given detail in Chapter 3.

4.3.1 GO reduction with reusable potassium carbonate

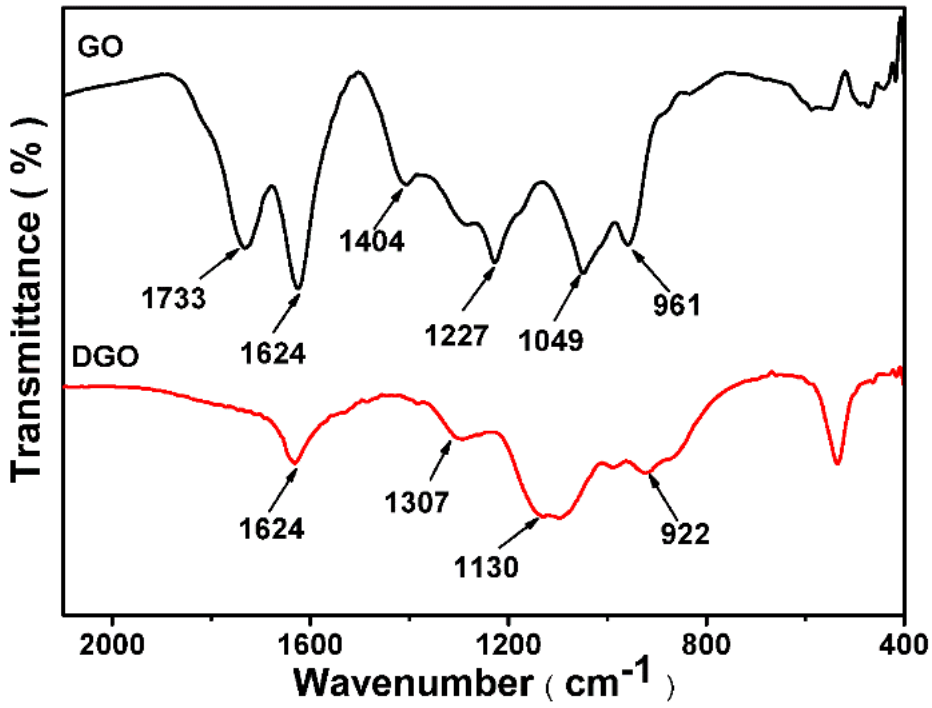

Figure 4 - 5 *The FTIR spectra of graphene oxide, and deoxygenated graphene oxide.*

The FTIR spectrum of GO is shown in **Figure 4-5**. It can be seen that a large number of epoxides, carboxyl, and hydroxyl groups are shown by the characteristic peaks. There are the peroxide or epoxy groups bands at 957 cm^{-1}, stretching vibration of C-O (alkoxy) groups bands at 1049 cm^{-1}, stretching vibration of C-O (epoxy) groups bands at 1227 cm^{-1}, deformation of the O-H groups bands at 1404 cm^{-1}, and stretching vibration of C=O groups bands at 1733 cm^{-1}, respectively. After GO reduction by K_2CO_3, the intensities of the oxygen groups decrease significantly. Meanwhile the peak bands at 1624 cm^{-1} increase, which corresponds to non-oxidized graphitic remains and domains.

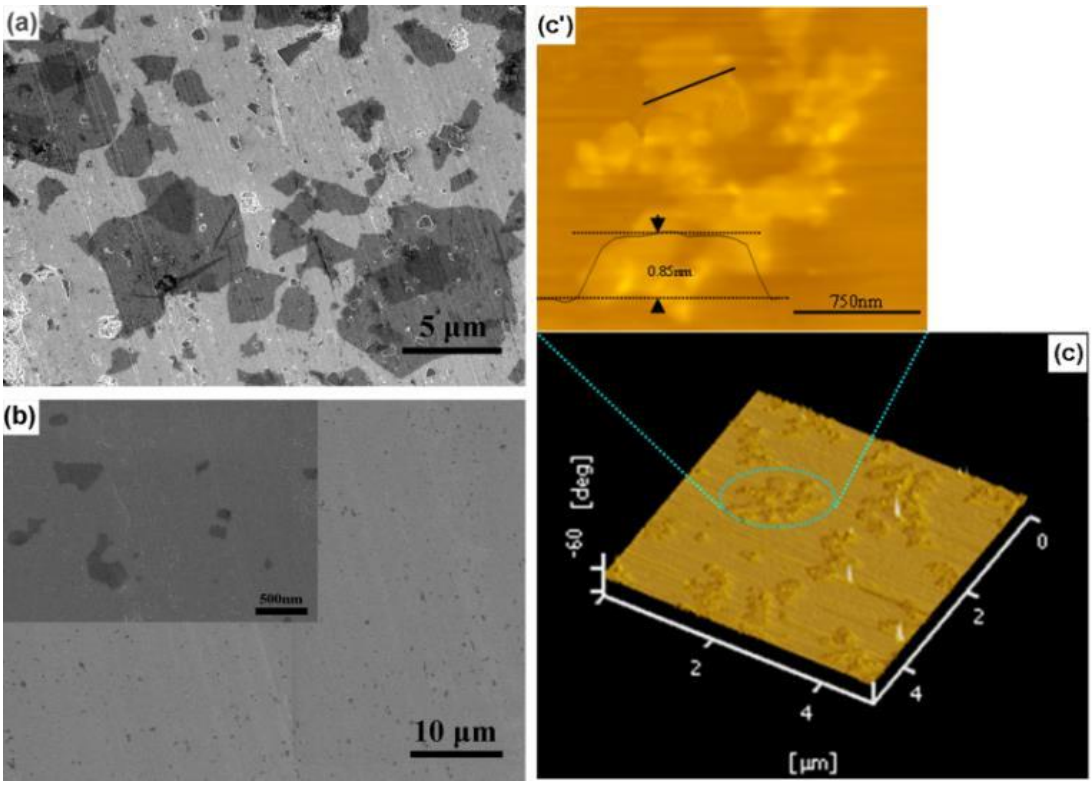

Figure 4 - 6 *The SEM images of (a) graphene oxide, and (b) deoxygenated graphene oxide sheets. AFM images of DGO sheets: (c) 3D representation of 5 µm × 5 µm AFM scan showing the morphology of the graphene sheets, and (c') AFM topography image showing sheets of DGO sheets.*

As shown in **Figure 4-6 (a)** the GO sheets had a size of approximately 1 to 5 µm. However, the DGO sheets are only approximately 100-200 nm as shown in **Figure 4-6 (b)**. Although a suspension of DGO water drying on mica appears to display a tendency to self-aggregate, the AFM tests demonstrate that DGO sheets present similar dimensions to the SEM image as shown in **Figure 4-6 (c)**. The thickness of DGO is approximately 0.85 nm as shown in **Figure 4-6 (c')**. The thickness indicates that the DGO sheets have a thickness of approximately two graphene layers because a single layer of graphene is 0.335 nm (Janowska et al. 2012). The characteristic structure of graphene is confirmed by the XPS spectra as well, where an increase in the content of sp^2 carbon is presented with a significantly decrease content of C-O groups. Moreover, the content of C(O)O and C=O groups showed a slight increase, as shown in **Figure 4-7**. The XRD and TGA test results also confirm the formation of graphene as shown in **Figure 4-8**, **9**.

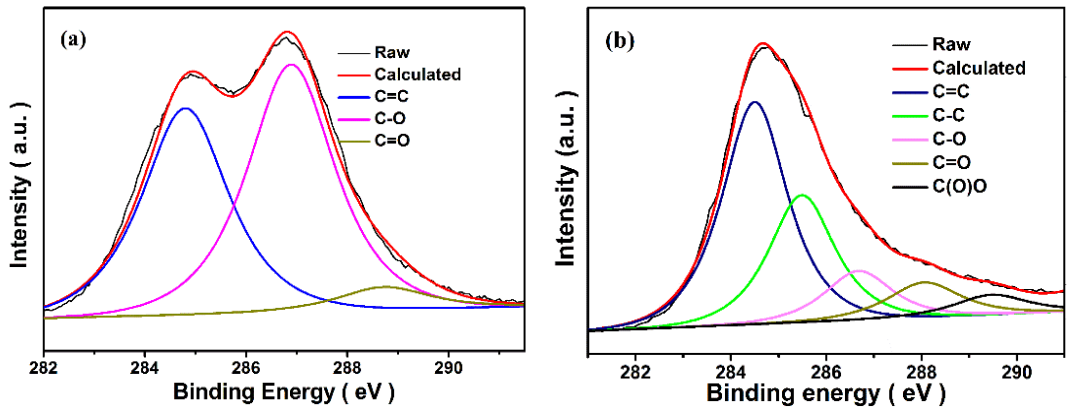

Figure 4 - 7 *The XPS spectra of GO and DGO. (a) C1s core-level spectra of GO, and (b) C1s core-level spectra of DGO.*

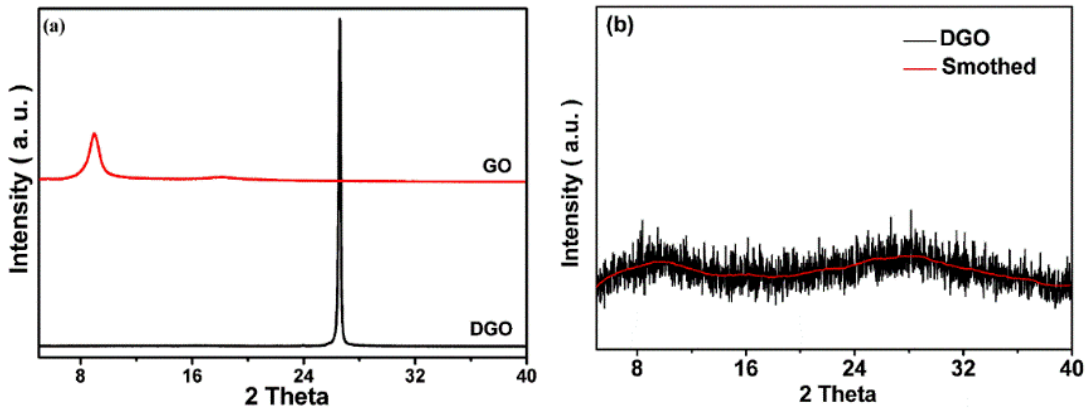

Figure 4 - 8 *The XRD patterns of graphite, GO (a), and DGO (b).*

As shown in **Figure 4-8**, the XRD patterns observe a dominant peak at 2θ=26.61º from graphite powder, corresponding to an interlayer distance of 0.33 nm, while the peak of GO is located at 8.96º, which corresponds to a distance of 0.99 nm. XRD patterns of DGO show two weak peaks at approximately 9.64º and 27.26º, corresponding to an interlayer spacing of approximately 0.92 nm and 0.33 nm, respectively, indicating that DGO mainly contains graphene.

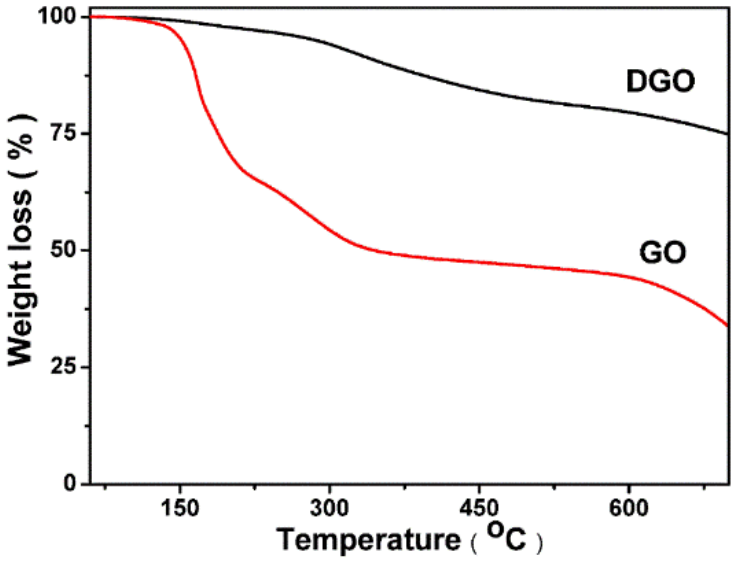

Figure 4 - 9 The TGA curves of the GO, and DGO.

As shown in **Figure 4-9**, the different weight loss presents in the TGA curve of GO may come from the different oxygen groups breakdown from the GO sheets, as described in the proposed reduction mechanism. After the deoxygenated procedure, the TGA curve of DGO became much flatter compared to that of GO. 66.58 % weight loss at 700 ^{o}C is observed for the GO specimen, while only 25.21 % is present for the DGO specimen, which indicates that most of the oxygen groups have been removed from the GO sheets to form graphene.

Oxygen groups on the graphene sheets are highly reactive even at mild conditions (Dreyer et al. 2010). The ionic oxygen (all types of ionic oxygen in this system; O_x^{x-}) reacts with the oxygen groups (CO_x) on the GO sheets first, which does not destroy the C=C framework when the reaction occurs under low temperature. The diagrammatic sketch of GO being converted to DGO is depicted in **Figure 4-10**. First, ionic oxygen attacks the oxygen groups (epoxide groups, carboxyl, and hydroxyl) as shown in **Figure 4-10 (a)**. Second, these groups are removed from the graphene plane as CO_2 (shown in **Figure 4-10 (b)**). Finally, a graphene sheet is formed with defects including pores as shown in **Figure 4-10 (c)**.

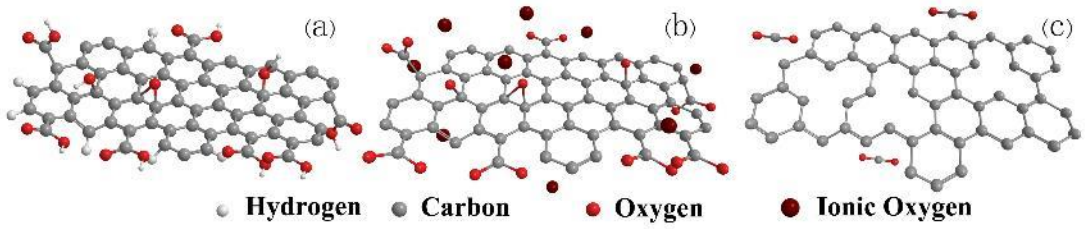

Figure 4 - 10 *The reaction procedure of GO deoxygenation by potassium carbonate: a) the structure of GO; b) ionic oxygen attacks the oxygen functional groups on GO; and c) graphene is formed with defects.*

4.3.2 Investigation of mechanism of reduction

To better comprehend the procedure of the DGO preparation process, it is important to identify the source of the O_x^{x-} which can involve oxygen dissolving in water, oxygen molecules attached to the sheets of GO through the π-π conjugate bonds, and by reactions between hydroxyl ions and carbonate ions. In controlled experiments as shown in **Figure 4-11**, there is lack of O_x^{x-} from oxygen dissolving in water or absorption on the GO. O_x^{x-} is only formed by the reaction between the O_2 and OH^- when K_2CO_3 is added in the reaction as shown in Equations 4-1 to 4-3 (Zecevic et al. 2004). The reaction of K_2CO_3 under this anaerobic situation is illustrated in Equation 4-4 (Zecevic et al. 2004).

$$O_2 + 4OH^- \rightarrow 2O_2^{2-} + 2H_2O \quad (4\text{-}1)$$

$$3O_2 + 4OH^- \rightarrow 4O_2^- + 2H_2O \quad (4\text{-}2)$$

$$6OH^- \rightarrow 3O^{2-} + 3H_2O \quad (4\text{-}3)$$

$$CO_3^{2-} \leftrightarrow CO_2 + O^{2-} \quad (4\text{-}4)$$

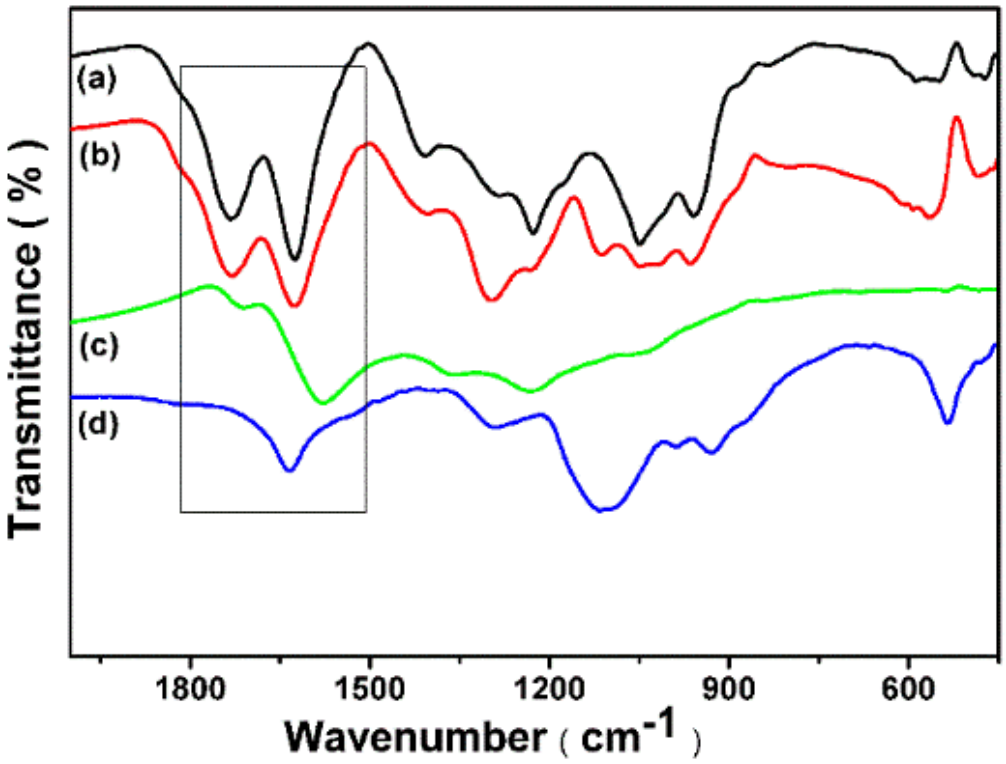

Figure 4 - 11 The FTIR spectra of samples from different controlling experiments (a) heating the GO suspension in air condition, (b) heating the GO suspension in nitrogen condition, (c) heating the GO suspension mixed with the K_2CO_3 solution in nitrogen condition, and (d) heating the GO suspension mixed with the K_2CO_3 solution in air condition.

To further reveal the sources of ionic oxygen the controlled experiments were designed. FTIR spectra of GO treated under different conditions is shown in **Figure 4-11**. It was found that GO suspensions of (a), and (b) remain coloured dark brown, indicating there is no ionic oxygen to launch the deoxygenation of GO when K_2CO_3 is not introduced into the system. This was demonstrated by the FTIR spectra, which appeared to have the same spectra as GO. The color of the GO suspensions of (c), and (d) changed to black, and the FTIR patterns showed that (d) was completely deoxygenated while (c) had remaining carbonyl groups, suggesting that when K_2CO_3 is introduced, the ionic oxygen can be generated with ionization and electrochemical reactions as shown in Equation 4-4.

The DSC temperature scanning model demonstrates that the O_x^{x-} reaction with GO is a two-step reduction because there are two peaks located at 50 °C and 90 °C, respectively in **Figure 4-12 (a)**. The FTIR measured the specimens collected at 50 °C, as the first deoxygenation step, and demonstrated that the carbonyl groups disappeared

whereas the hydroxyl groups appeared as shown in **Figure 4-12 (b)**, indicating the first step is the elimination of the carbonyl group and opening of the epoxide groups. This is detailed in Equation 4-5. Comparing to **Figure 4-12 (b)**, **(c)**, it is obvious that the epoxy/ether groups on the 1227 cm^{-1} were converted to 1115 cm^{-1} under a base condition of 50 ^{o}C. This change indicated that the epoxy/ether groups were converted to hydroxyl groups at 50 ^{o}C. As shown in **Figure 4-12 (c)**, the peaks of the hydroxyl and epoxide groups decrease, as expected. However, the carbonyl group presents at the second deoxygenation step occurred at 90 °C. This phenomenon explains that the epoxide and hydroxyl groups were converted into carbonyl group before they were converted into CO_2 shown in Equations 4-6 and 4-7, which is similar to the mechanism of the DCFC system proposed by Vicente (Gómez-Serrano et al. 1994). The corrosion inducing the carbonaceous materials in the DCFC system is completely converted to CO_2 (Li et al. 2009; Cao et al. 2010; Li et al. 2010). The reaction products of GO deoxygenation were conjugated carbon and CO_2.

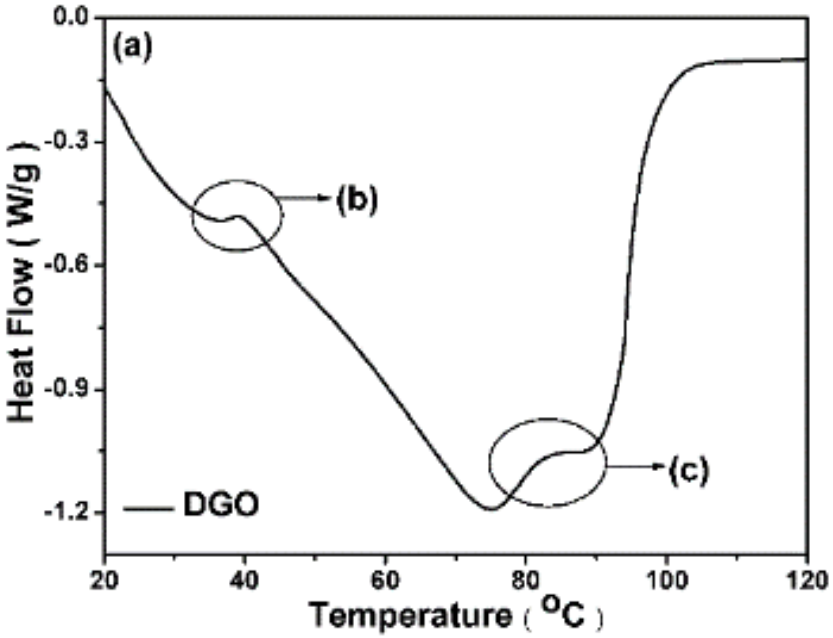

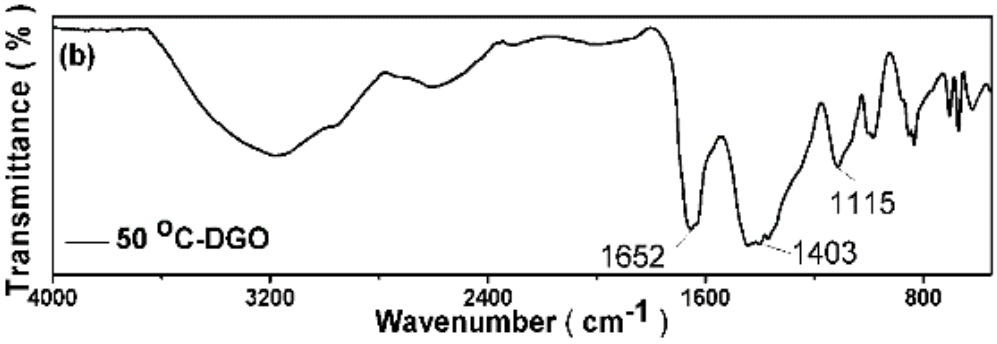

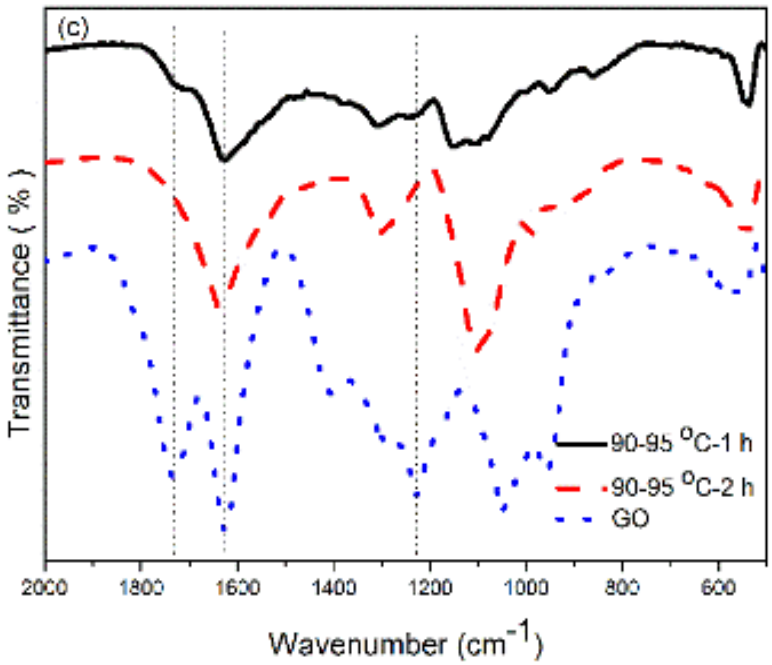

Figure 4 - 12 *The two-step deoxygenation of GO: (a) DSC curve of GO-K_2CO_3 suspension heated with a rate of 2 °C /min from 20-120 °C; (b) FTIR spectrum of the suspension heated at 50 °C for 2 h; and (c) FTIR spectra of pure GO (green), and the suspension heated at approximately 90 °C for 1 h (black) and 2 h (red).*

Two-Step deoxygenation can be described by the following equations:

Deoxygenation at 50 °C: $G - C = O + O_x^{x-} \xrightarrow{K_2CO_3\ 50\,℃} G + CO_2$ (4-5)

Deoxygenation at 90 °C: $G - C - O + O_x^{x-} \xrightarrow{K_2CO_3\ 90\,℃} G - C = O$ (4-6)

Deoxygenation at 90 °C: $G - C = O + O_x^{x-} \xrightarrow{K_2CO_3\ 90\,℃} G + CO_2$ (4-7)

Equations 4-6 and 4-7 can be combined and expressed as:

$$G - CO_x + O_x^{x-} \xrightarrow{K_2CO_3\ 90\ ℃} G + CO_2 \quad (4\text{-}8)$$

After CO_2 is released, a defect appears on the graphene sheet because some carbon atoms have been removed. The D mode in the Raman spectrum increases because DGO has in-plane carbon atom removed. The ratio between the D mode and the G mode (I_D/I_G) that can describe the number of defects on graphene (Nguyen et al. 2014). For DGO, I_D/I_G is greater than one, as shown in **Figure 4-13 (a)**, which indicates that DGO has many defects. The reduction process with CO_2 as a by-product leaves a defect on the DGO sheet.

The ultimate products of deoxygenation of GO are CO_2 and graphene sheets. The K_2CO_3 is converted to $KHCO_3$ by absorbed CO_2 as shown in **Figure 4-14**. The HS-SPME-GC-MS results confirm the formation of CO_2 and other by-products as shown in **Figure 4-16**. N-dodecanal presents when deoxygenation of GO is processed, indicating that the oxygen functional groups are aligned near the edge sites of GO sheets (**Figure 4-16 (c)**) (Fujii & Enoki 2010). However, the 4-ethylbenzoic acid cyclopentyl ester also appears as shown in **Figure 4-16 (b)**, which suggest that oxygen groups on GO sheets have not only aligned but have also been randomly dispersed in some areas of the GO sheets.

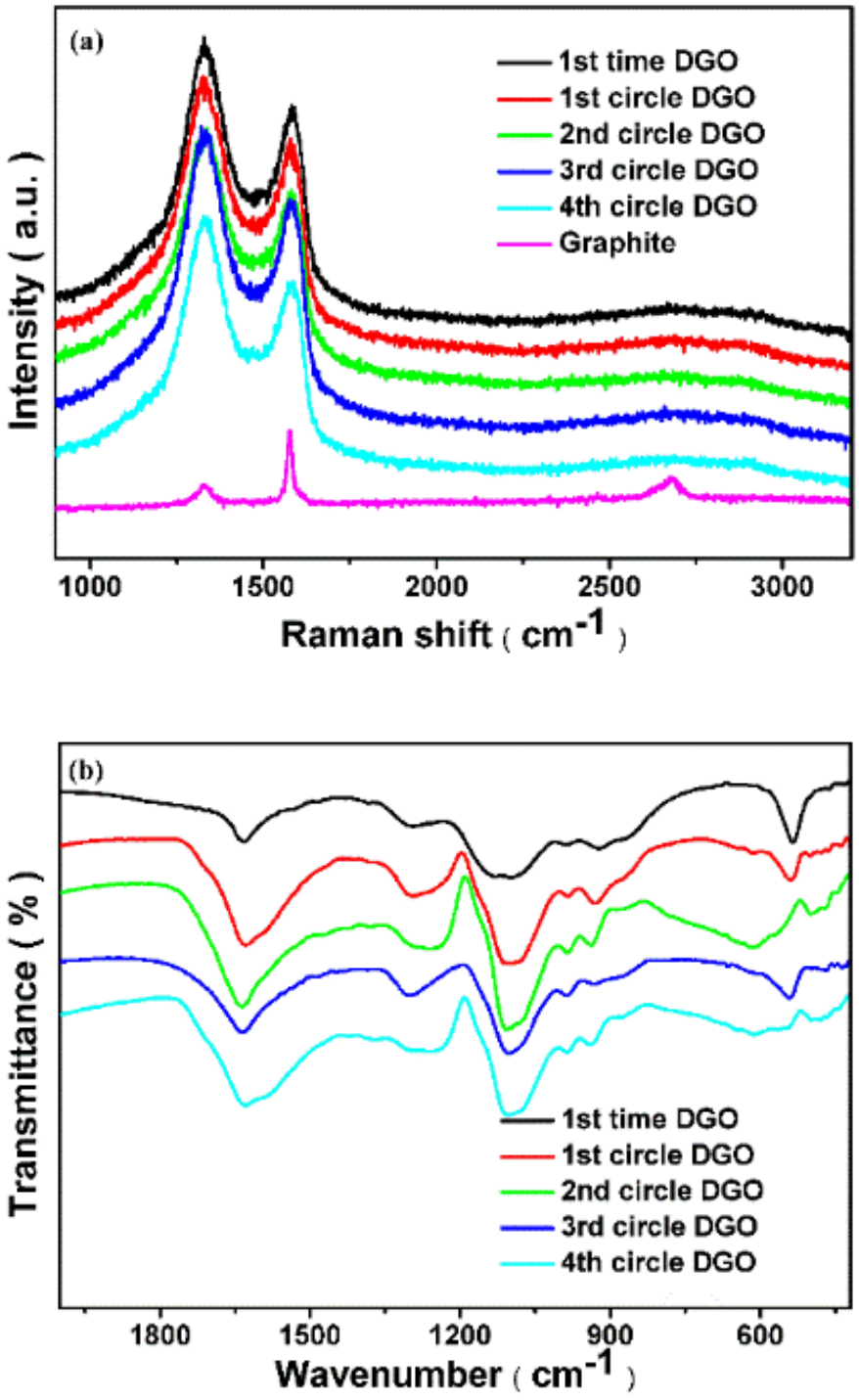

Figure 4 - 13 *The Raman and FTIR spectra of DGO that deoxygenated with recycling K_2CO_3.*

As shown in **Figure 4-13**, the Raman spectroscopy and the FTIR show the cycle time of K_2CO_3 has no impact on the structure of DGO, indicating that K_2CO_3 as the deoxygenation agent can be reused, and the process is eco-friendly compared to other reduction processes where strong acidic or alkaline agents are usually employed.

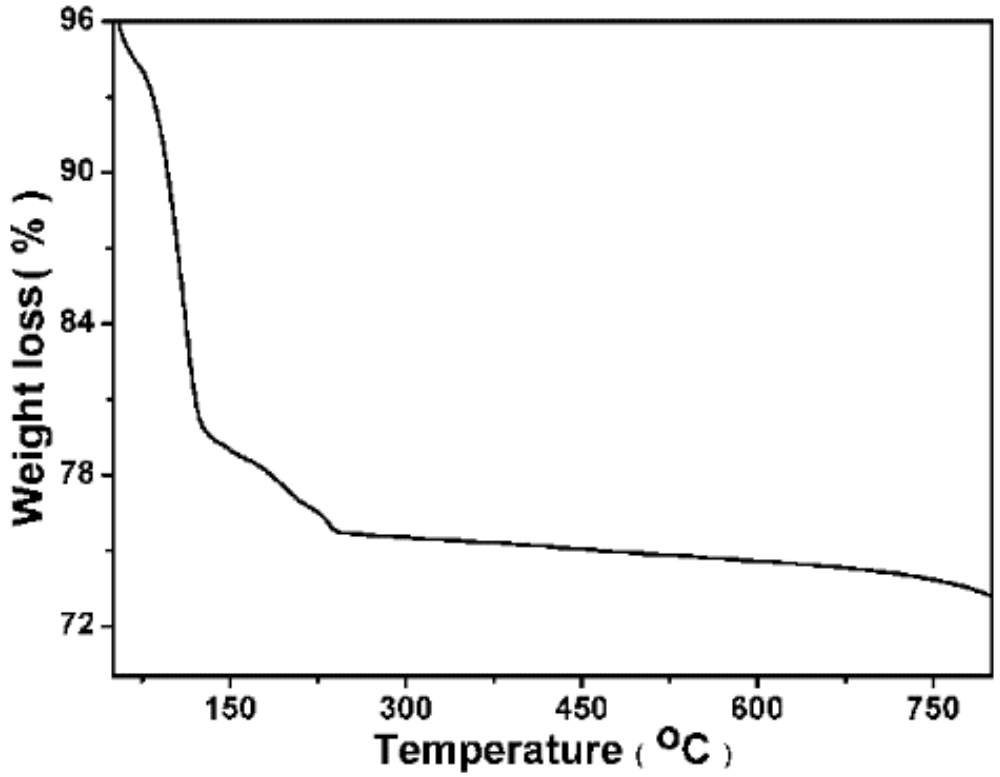

Figure 4 - 14 the TGA curves of K_2CO_3 after being reused for 4 rounds under oxygen.

As shown in **Figure 4-14**, after being reused 4 times, the solution is collected and dried in a freeze drier and is ready for the TGA test. The weight loss before 120 °C corresponds to the water inside of the sample, while that between 120-230 °C corresponds to the typical weight loss of $KHCO_3$. The deoxygenation of GO can generate carbon dioxide, which is absorbed by K_2CO_3 and produces $KHCO_3$, and the $KHCO_3$ can reverse to K_2CO_3 when it is heated.

As shown in **Figure 4-16** the ^{13}C NMR spectra were collected before and after the deoxygenation of GO by K_2CO_3. The ^{13}C NMR spectra of GO indicates the existence of abundant hydroxyl groups and epoxide groups (Li et al. 2008), with carboxyl groups located at the edges of GO sheets. The peak located at 130 ppm belongs to the sp^2 carbon. Subsequently, after the system reacts at 90 °C for 1 h, the number of carboxyl groups increases whereas the amount of hydroxyl and epoxide groups decline. Finally, only a small number of the carboxyl groups are left after deoxygenation at 90 °C for 2 h. The NMR results show a significant decline in the number of hydroxyl groups and epoxide groups, which demonstrated those groups, are converted into a carboxyl group

and then reduced. The increase in the peak located at 90-150 ppm showed that the content of sp^2 carbon increases, indicating the formation of graphene.

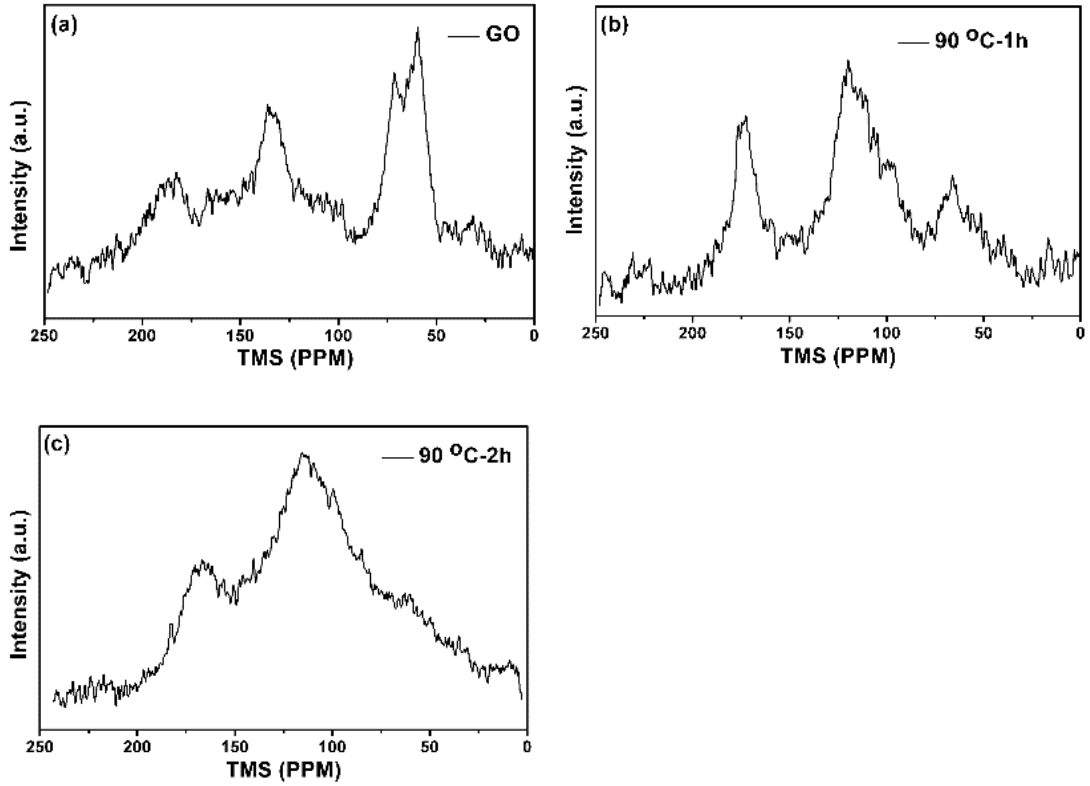

Figure 4 - 15 *The ^{13}C-NMR results: (a) ^{13}C-NMR result of graphene oxide (GO); (b) ^{13}C-NMR of GO sample treated with K_2CO_3 at 90 °C for 1 h; and (c) ^{13}C-NMR of GO sample treated with K_2CO_3 at 90 °C for 2 h.*

Compared to other reductants, K_2CO_3 can be reused easily. Concentrated K_2CO_3 is obtained by centrifugation of the reaction mixture to separate the DGO, followed by vacuum distillation to remove the extra water. To evaluate the catalyzing activity of recycled K_2CO_3, the resulting solution is applied to react with GO again. As shown in **Figure 4-13 (a)** the K_2CO_3 is recycled 4 times, during which the FTIR spectra of the DGO under different recycled K_2CO_3 showed no difference. During the deoxygenation process, the CO_2 is released from GO sheets, with defect remaining on the DGO sheets, as shown in **Figure 4-13 (b)**. All Raman spectra are similar to the I_D/I_G ratio, all being significantly larger than one. Because of the recyclability of the deoxygenation agent, K_2CO_3 makes it possible to produce graphene on a large scale.

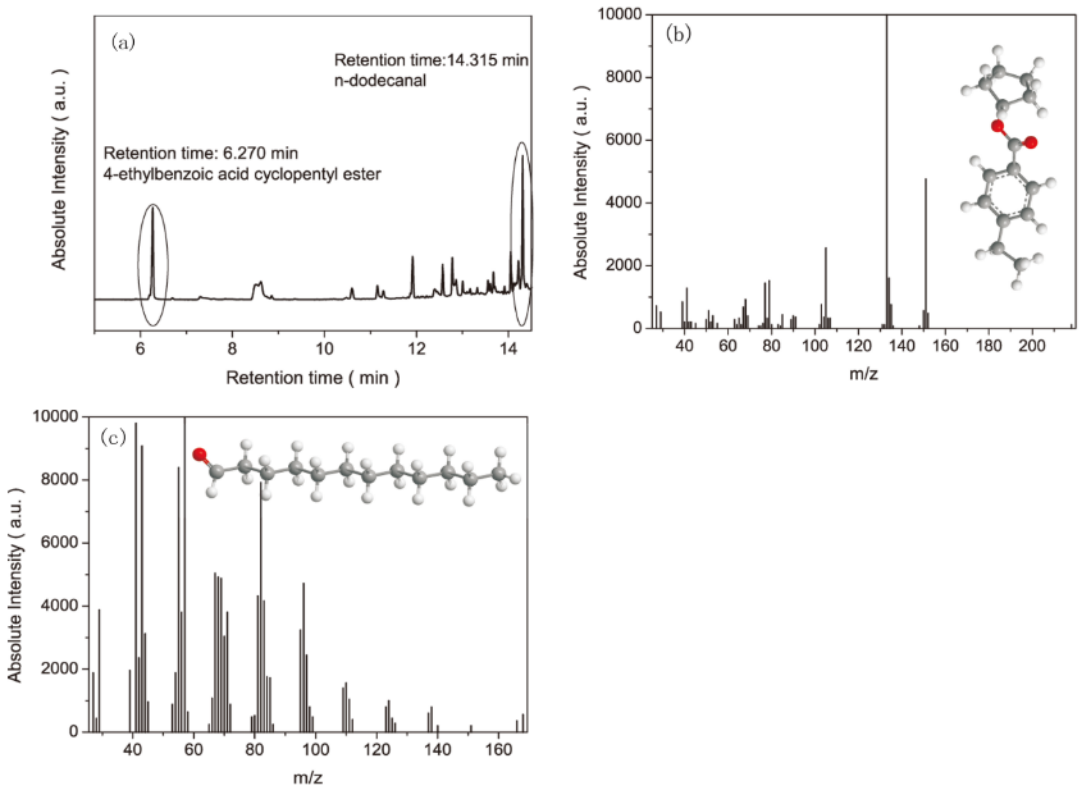

Figure 4 - 16 *The HS-SPME-GC-MS analysis of deoxygenation procedure of GO: (a) HS-SPME-GC-MS spectrum of the deoxygenation process of GO; (b) products at the retention time of 6.270 min; and (c) products at the retention time of 14.315 min.*

The PALS are analysed for discrete components employing the computer programs spectra (Kirkegaard & Eldrup 1974; Provencher 1982; Gregory & Zhu 1990). The spectra of the three specimens are resolved into two well-isolated components, with the error of each component being less than 5% The results are shown in **Table 4-4**. From the short-lived component results, τ_1= 185-266 ps and I_1= 5-30%, meanwhile the τ_2=337-397 ps, and I_2=70-94%. Wang reported that the τ_1 of natural graphite is 180±20 ps (Wang et al. 1988). Therefore, it is confirmed that vacancy-like defects are present on the GO sheets and DGO sheets, with τ_2, show the lifetime of positrons trapped at the defect sites. Because the decomposition of PALS in the GO specimens are always difficult, the average lifetime (τ_m) is calculated using Equation (4-9)

$$\tau_m = I_1 \tau_1 + I_2 \tau_2 \qquad (4\text{-}9)$$

τ_m is a very accurate parameter that a little change in values can reflect the changes in characteristics of defect (Hautojärvi 1994).

Table 4 - 4 *The Positron lifetime spectrometer results of the specimens*

Samples	τ_1(ps)	I_1(%)	τ_2(ps)	I_2(%)	τ_m(ps)	I_2/I_1
Graphite	183.4±5.1	29.84±1.47	375.1±2.5	70.16±1.45	317.7	2.351
GO	265.9±24.3	18.95±1.32	397.9±6.4	81.05±1.41	373.55	4.277
DGO	193.2±7.5	5.22±0.24	337.6±4.4	94.78±5.29	329.8	18.16

As shown in **Table 4-4,** the I_1 of DGO is smaller than that of the GO and the Graphite specimens, which indicate that crystalline grain crash into a smaller one than the other two. In addition, the decrease in the annihilation of positrons in the graphene bulk appeared which can lead to the increasing of defects. The I_2 value of the DGO larger than others, which confirms that the concentration of defects increases. The I_1 and τ_1 values of DGO are smaller than GO which indicates that the oxygen groups are removed from the graphene sheets, and the crystalline grains crash during the DGO deoxygenation process, which is confirmed by the SEM and XRD tests.

Compared to the other two specimens, an obvious increase in the I_2 value of the DGO specimen showed that the deoxygenation process induced a large increase in vacancy-like defects on the surface. Because the average numbers of graphene sheets in the investigated specimen is approximately two layers, as shown by AFM testing, τ_2 and I_2 can be directly correlated with the annihilation of positrons in the defects of the graphene sheets. However, a decrease in τ_2 value appeared which revealed a slight decrease in the size of the defects. This decrease can be attributed to the oxygen groups on the surface of the GO sheets, which will be converted into CO_2 and remove carbon atom from the graphene surface, to generate smaller defects (Banhart et al. 2011). In addition, the intensity ratios of I_2:I_1 of the three specimens gradually increased with increasing defects on each crystalline grain. Such behaviour is most likely because of a decreased size of the graphene sheets and increased number of defects. The peaks in the XRD pattern of DGO decrease with the FWHM increasing significantly, which is equivalent to the crystalline grain becoming smaller than that of GO. As SEM image shows, the size of GO sheets was decreased to a hundred nanometres when GO is deoxygenated to DGO. τ_m of GO is 373.55 ps, which is larger than that of DGO. Providing strong evidence of the existence of larger vacancy-type defects in the GO specimen than that of DGO specimen. The high-resolution AFM in **Figure 4-17** shows that the RGO is full of pores.

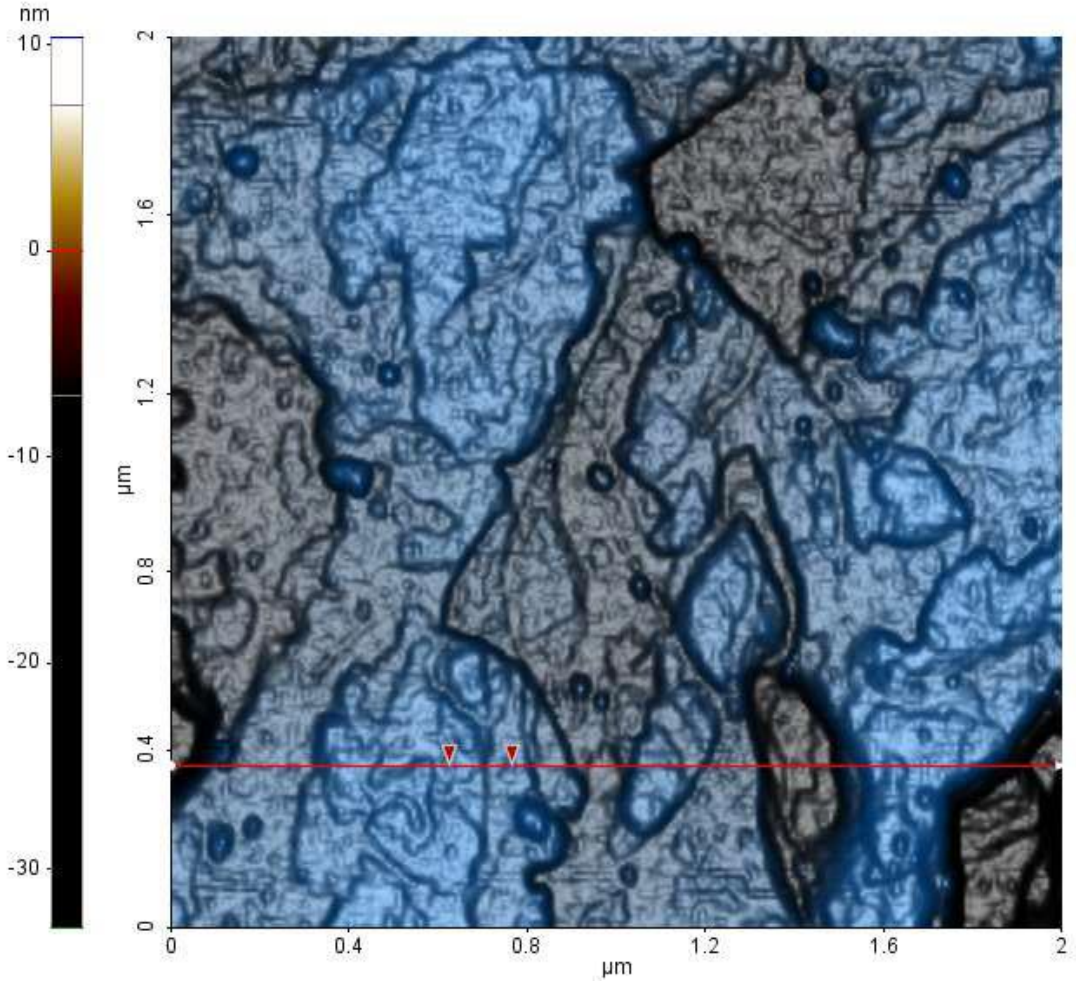

Figure 4 - 17 *The AFM of DGO prepared in the lab, and the DGO sheets were full of cracks.*

DGO has small sheet size based on a crashed crystalline grain with a large number of defects in the graphene sheets. Firstly, the deoxygenation, which happened, occurs from the edge of the defects, and then the larger defects destroyed which the graphene sheets crash into a small one. The deoxygenation process decreases the concentration of oxygen groups. However, removing oxygen groups from GO sheets will generate new vacancies or pore defects by removing carbon atoms, which correspond to the proposed mechanism.

4.4 Concluding remarks

The PALS and 2D-DBAR were employed to detect information about the defects of graphite and its oxide derivatives including the nitric acid treated specimen, mixed acid treated specimen, and the Hummers method treated specimen. The different types

of defects were revealed. For unexfoliated graphite oxide (NG, and NSG) they are vacancy cluster defects, and exfoliated graphite oxide (GO) they are vacancy-oxygen complexes defects based on 2D-DBAR measurements. It was also observed that the calculated diameter of large open-volume defects of GO was similar to the distance between the layers, based on the XRD investigation, which indicates that the positron annihilation of the third component might occur in the area between the neighbouring graphene sheets; no large open-volume has been detected in GO specimen.

In this research, DGO was prepared using K_2CO_3 as a deoxygenation agent. Moreover, the K_2CO_3 is confirmed to be recyclable by at least 4 times. The characterization of AFM indicated that the DGO product possesses 2 graphene layers in thickness with a hundred nm in width. XRD patterns observe that there is no significant evident graphitization tendency in the DGO specimen. The Raman spectrum and PALS show that defects remained on the DGO because the oxygen groups were removed. The oxygen groups are almost completely reduced by K_2CO_3, and recycled K_2CO_3 as well. The carbon dioxide as a by-product was completely adsorbed by K_2CO_3 in the water solution, avoiding release into the air.

AFM and PALS reveal the deoxygenation process resulted in the GO sheets splitting into smaller pieces, which was also demonstrated by SEM. K_2CO_3 deoxygenation process starts from the edge of the defects sites generated by the oxygen groups in GO sheets.

Chapter 5: Enhancement of electrical conductivity of NR nanocomposites

5.1 Introduction

Conductive materials are widely used in daily life. One example is in automobile parts. The interaction between fillers in the tire, driver clothing, and automotive trim can lead to static electricity accumulation (Matsuda et al. 1995), which could affect the radio signal, attract dust, and even cause safety issues (Dalziel 1972). A static discharge is used to transfer the static electricity charge. Tires are the only part of the car that contacts the road. If the tire can act as a static discharger, it can simplify the car structure. Therefore, antistatic rubber is developed to achieve this goal. According to the ASTM D991, antistatic products are considered to have a resistance of $10^4 \sim 10^8$ Ω, and conductivity of $10^{-7} \sim 10^{-2}$ S/m. However, neat NR is an electrical insulator, and its conductivity is $10^{-12} \sim 10^{-13}$ S/m because NR has a large band gap, and lacks free charge carriers (Warman et al. 2004). Hence, it is necessary to modify and enhance the antistatic performance of NR.

As discussed in the previous chapter, novel fillers have the potential to impact properties of the host polymer. Graphene as an additive in NR composites could be used to enhance electrical conductivity. However, the defects on RGO prepared by the oxidation-reduction method limit its practical application. While the electrical conductivity of defect-free graphene is 1,000,000 S/m, the electrical conductivity of RGO prepared by the oxidation-reduction method can only reach up to approximately 9000 S/m. To further investigate the electrical conductivity of RGO/NR nanocomposites, AgNPs were employed to decorate RGO for the preparation of the electrical conductive NR nanocomposites.

Highly conductive nanocomposites can be fabricated by using a low fraction of graphene when compared to conductive fillers such as conductive carbon black (Zhan et al. 2012). Because of the inherent disadvantages of RGO, including re-aggregation and graphitization, the latex mixing approach has been chosen as the graphene dispersion method. Although conductive NR products based on graphene nanocomposites have been developed through the latex mixing approach (Ozbas, et al.

2012; Potts et al. 2012; Wu et al. 2013), the reductants used are mainly hydrazine, and sodium borohydride, which degrade the NR molecules, and cause a health hazard (Ravindran et al. 1988; Dahlan et al. 2000). Therefore, it is vital to develop an eco-friendly strategy to fabricate antistatic natural rubber based on graphene. In this chapter, a one-pot antistatic NR nanocomposite is developed.

To prepare the high electrical conductivity graphene filler, silver nanoparticles (AgNPs) were used as the surface modifier. Silver nanoparticle decorated reduced graphene oxide (AgNPs/RGO) has a negative charge with higher electrical conductivity than RGO. The surface charge of AgNPs/RGO can be converted from negative to positive. Based on electrostatic self-assembly integrating latex mixing, the positive charge carrier of AgNPs/RGO can attach to the surface of NR particles with the negative charges because of proteins on its surface appearing to have negative charge in alkaline conditions. Meanwhile, honeycomb-like three-dimensional (3D) interconnected additive networks can be constructed in the NR matrix. Because of the well-organized AgNPs/RGO network, NR nanocomposites exhibit an electrical conductivity of 196 S/m with 4.03 vol.% AgNPs/RGO loaded, with a low percolation threshold of 0.63 vol.%.

5.2 Antistatic NR nanocomposites prepared by green one-pot reaction

5.2.1 Morphology analysis of the antistatic NR nanocomposites

A one-pot strategy was used to construct the current transfer route and reduce GO into RGO in an NR latex matrix. Vitamin C (Vc) was employed as the reductant, and the reduction reaction was conducted at 90 °C. The fabrication approach with a moderate reducer avoided both the use of toxic reductants and the decomposition of NR during the reduction process. The TEM image of the NR latex particles with RGO sheets is shown in **Figure 5-1 (a)**. It can be seen that the NR latex particles were encapsulated by the RGO, indicating that the NR latex particles could act as blockers and prevent graphitization from occurring during the GO reduction procedure. The SEM cross-sectional images of the samples are shown in **Figure 5-1 (b)** to **(d)**. The control of neat NR without GO is shown in **Figure 5-1 (b)**, in which is a smooth surface of an NR specimen. However, RGO is homogeneously dispersed in the NR matrix after reduction, as can be seen from **Figure 5-1(c)**, **(d)**. **Figure 5-1 (c)** shows the

morphology of doping NR latex with 1.5 phr GO. RGO sheets are well dispersed, and they are not connected to each other. As the content of GO was increased to 2 phr as shown in **Figure 5-1 (d)**, a partly segregated RGO network was observed in the NR matrix, forming an electronic transfer path, and this structure can explain the antistatic property of RGO/NR nanocomposites.

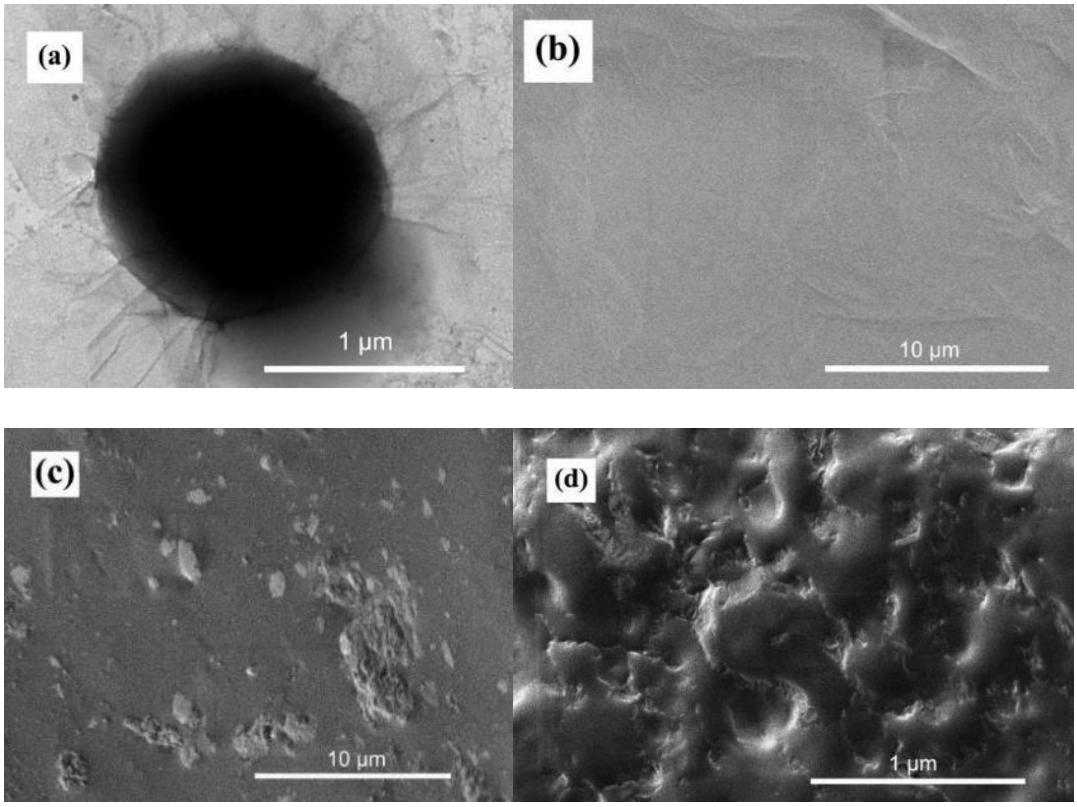

Figure 5 - 1 *The images of the morphology of NR nanocomposites. (a) TEM image of the RGO covered NR latex particles; (b) SEM image of the neat NR; (c) SEM image of the cross-section of anti-static NR nanocomposites with 1.5 phr of GO; and (d) SEM image of the cross-section of antistatic NR nanocomposites with 2 phr of GO.*

5.2.2 XRD and NMR analysis of the antistatic NR nanocomposites

The XRD patterns of the neat NR and RGO/NR nanocomposites are shown in **Figure 5-2**. There are no differences between these two specimens in peak shape and position. No crystalline phase of graphene was visible, which confirmed that graphitization did not occur during the reduction of GO and the curing of NR. The NR particles prevented the graphitization of the GO sheets during the reduction process because the RGO sheets were attached to the surface of the NR particles, as shown in **Figure 5-1 (a)**.

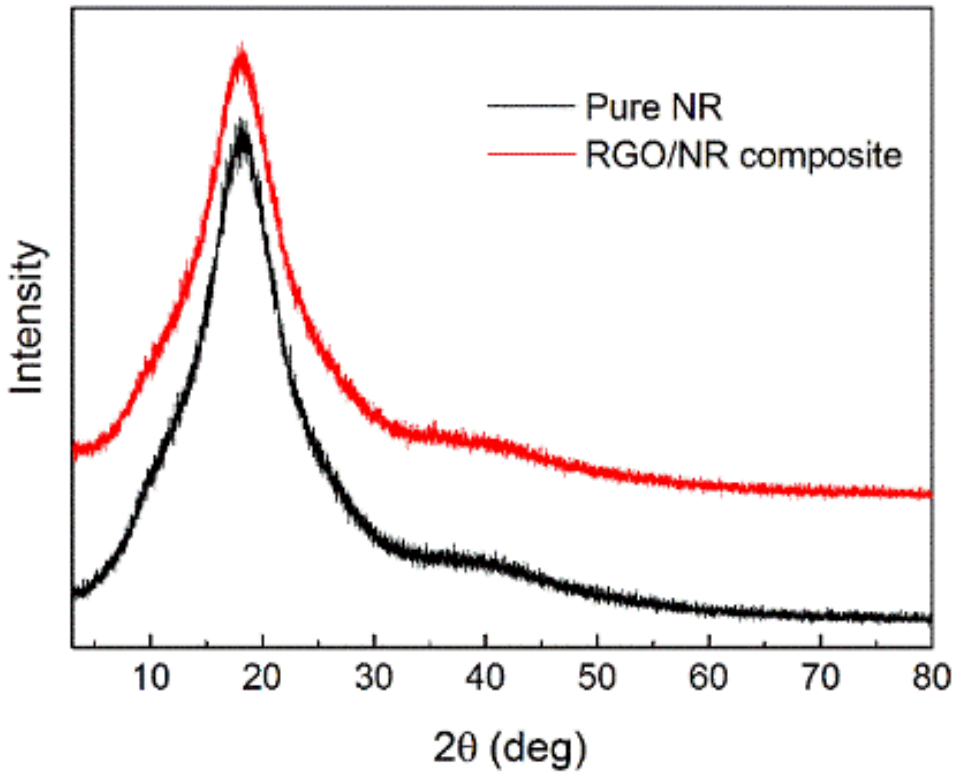

Figure 5 - 2 *XRD patterns of neat NR, and NR/ RGO nanocomposites.*

NMR was used to measure the cross-linking density (XLD) of the samples. The sample was cut into a rod (3 mm in diameter, and 10 mm in length), and loaded into a sample chamber covered by electromagnet coils. The samples were preheated at 60 °C for 5 min to accelerate the molecular movement to allow the hydrogen signal to become strong enough to be measured. The physical and chemical XLD of the specimen are shown in **Table 5-1**. These results indicate that the NR molecules could attach to the surface of the 2D filler. The physical XLD decreases because the twisting of the NR molecules was prevented by RGO. However, the chemical XLD of the sample was increased after curing. Considering the physical and the chemical XLD, the overall XLD exhibited an increase after RGO curing. This increase is caused by the reaction between RGO and vulcanisation agents (sulphur as an active agent), which could lead to bonding between RGO and sulphur molecules, hence improving the stabilisation of the electronic transfer for the antistatic performance. Sichuan University gave a serials studies on the vulcanization process after doping graphene, which reveals that the sulphur reacts with graphene sheets. The final product of this reaction is S-C species

that are connecting the rubber matrix with graphene sheets (Wu et al. 2013; Kaciulis et al. 2015).

Table 5 - 1 *The cross-linking density values of neat NR, and RGO/NR nanocomposites*

	Physical XLD (mol/cm^3)	Chemical XLD (mol/cm^3)	Total XLD (mol/cm^3)
NR	5.91×10^{-5}	12.61×10^{-5}	13.93×10^{-5}
RGO/NR	5.73×10^{-5}	13.81×10^{-5}	14.95×10^{-5}

5.2.3 Conductivity of the antistatic NR nanocomposites

The conductivity of the neat NR was 3.79×10^{-12} S/m. However, the conductivity of RGO/NR nanocomposites was significantly improved with the increased content of GO as shown in **Figure 5-3**. The conductivity of the RGO/NR nanocomposites went up to 1.00×10^{-1} S/m after the GO was reduced into RGO in NR matrix, which is nine orders of magnitude higher than that of NR/GO nanocomposites. The experiment shows that when the content of GO was higher than 2.0 phr, demulsification occurred in the mixture solution, resulting in the termination of the reaction. In addition, **Figure 5-3** also shows the effect of curing on the bulk conductivity for the RGO/NR nanocomposite. The result shows that the vulcanization agents can further enhance conductivity. It was also reported in the literature review that the vulcanization agent could increase the conductivity of NR by one or two orders of magnitudes when an inorganic salt was added into the system (Tan 2006). As a result, the cured nanocomposites present better antistatic properties compared to the uncured sample.

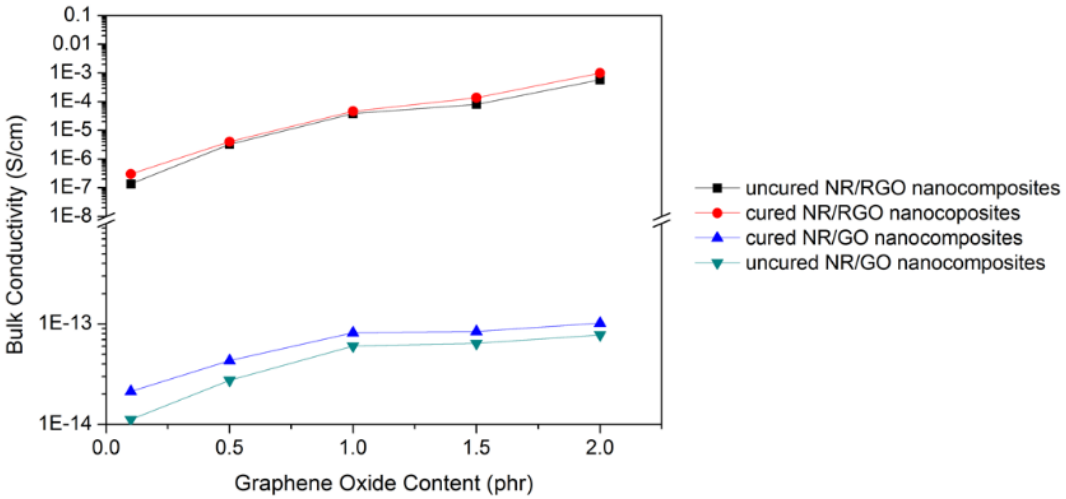

Figure 5 - 3 *Electrical conductivity of NR with unreduced GO, and RGO as a function of GO addition.*

5.2.4 Mechanical properties of the antistatic NR nanocomposites

The data on the mechanical properties of RGO/NR nanocomposites with different loading contents of RGO are shown in **Table 5-2**. It is evident that incorporation of RGO improves the tensile strength and elongation at break of NR. In detail, the modulus at 100% elongation at break, 300% elongation at break of RGO/NR with RGO loading content above 0.1 phr consistently increases when compared to that of the neat NR. With the increase of loading of RGO, the tensile strength, and the elongation at break are both decreased, because the RGO sheets cover the NR particles and as a result, prevent the interaction between the NR molecules.

Table 5 - 2 *Mechanical properties of neat NR, and RGO/NR nanocomposites*

Sample (phr)	Tensile strength (MPa)	Modulus (MPa)		Elongation at break %
		100%	300%	
0	11.37	1.22	2.18	675
0.1	13.42	1.83	5.59	632
0.5	13.11	2.26	5.83	607
1.0	10.73	2.68	4.73	517
1.5	9.13	3.79	6.22	463
2.0	6.75	4.11	6.34	407

5.3 AgNPs decorated RGO filled NR for electrical conductivity

The electrical conductivity of the RGO prepared by $N_2H_4 \cdot H_2O$ is only approximately 200 S/m. If the electrical conductivity of the additives increases, the NR nanocomposites could present higher electrical conductivity than RGO/NR nanocomposites. In this research, the RGO is decorated by AgNPs to increase the electrical conductivity properties of RGO. AgNPs/RGO acts as a new additive for fabricated NR nanocomposites through latex mixing.

5.3.1 Characterization of AgNPs/RGO

The electrical conductivity of RGO was improved using AgNPs declared on its surface. The oxygen groups of GO served as an anchor site for AgNPs synthesis which causes oxygen groups to interact with AgNPs (Liu et al. 2011). This interaction may be through charge-transfer interaction to improve the electrical conductivity as proven using Raman and UV-vis (Han et al. 2013; Wu et al. 2013). Based on the discussion in Chapter 4, the oxygen groups could be present surrounding vacancies. Moreover, when the AgNPs grew large enough, they could cover the vacancy clusters nearby. Li reported that the open edges and the defect sites favour binding with silver atoms (Li et al. 2011). As discussed in Chapter 4, the size of a defect on the GO sheets can be up to approximately 1 nm diameter, which can be covered by the AgNPs when the diameter of AgNPs is approximately 2 nm. In this research, several impact factors on AgNPs synthesis and the electrical conductivity will be discussed.

5.3.1.1 Silver nitrate content

It is reported that the silver nitrate content increase is inducing the dimension of AgNPs increase (Yuan et al. 2012). Therefore, the impacts of silver nitrate content on the AgNPs synthesis are discussed in this section with three levels of silver nitrate content at 4 mL, 17 mL, and 21 mL labeled as A1, A2, and A3, respectively.

The AgNPs decorated on the RGO sheets is shown in **Figures 5-4**, **5-5**, and **5-6**. A1 shows the lowest fraction of coverage among the three samples because it contains the lowest amount of silver nitrate (Yuan et al. 2012). There are some AgNPs smaller than the 0.6 nm as shown in **Figure 5-4** in the red circle, which had not be found in the A2, and A3 specimens. The small particles exist because the content of the silver nitrate was too low to grow from nuclei to AgNPs (Liu et al. 2016; Wiley et al. 2007). There

is no dissociation of AgNPs present after centrifugal cleaning and ultrasonic dispersion, which indicates the AgNPs and RGO have strong bonding.

The electrical conductivity of A1 is the lowest in these three samples as shown in **Table 5-3**, which also supports this hypothesis. In the TEM image of A1 and A2, the AgNPs/RGO sheets are almost mono-layer dispersion on the copper grids. The AgNPs decorated on the RGO sheets is much more unique with a diameter of approximately 2.44 nm, and no dissociation of AgNPs present as well. However, when the silver nitrate content was increased to 21 mL the AgNPs/RGO present serious aggregation that difficult to disperse even under ultrasonic irradiation, and a large amount of dissociated AgNPs appeared in the image as shown in **Figure 5-6**. The distribution of particle size in A3 was very broad from 2 nm to 20 nm, with average 7.25 nm. Although A3 showed the highest electrical conductivity out of the three specimens, the aggregation performance resulted in its inability to disperse even in water. In addition, the size of the A3 present in the TEM image is much smaller than the A2, and A1 specimens. Because the 3D structure of the A3 specimen could not disperse in the water, the preparation of TEM test of A3 specimen was ultrasonically irradiated for is 3 times longer than A1, and A2, which broke the A3 into smaller pieces than A1, and A2 as shown in **Figure 5-6**. In addition, the A3 specimen presented the lowest yield of three specimens, which indicated the high content of silver nitrate could not convert all the Ag^{+} to AgNPs under the same amount of NaOH. Therefore, the 17 mL of silver nitrate added into the synthesis system is employed for the further investigation.

Table 5 - 3 *The electrical conductivity and size information of A1, A2, and A3*

Specimens	Electrical conductivity （S/m）	Yield %	Mean size (nm)	Standard deviation
A1	6369	98.7	12.11	4.28
A2	10870	98.3	3.85	3.49
A3	12660	95.1	7.53	6.69

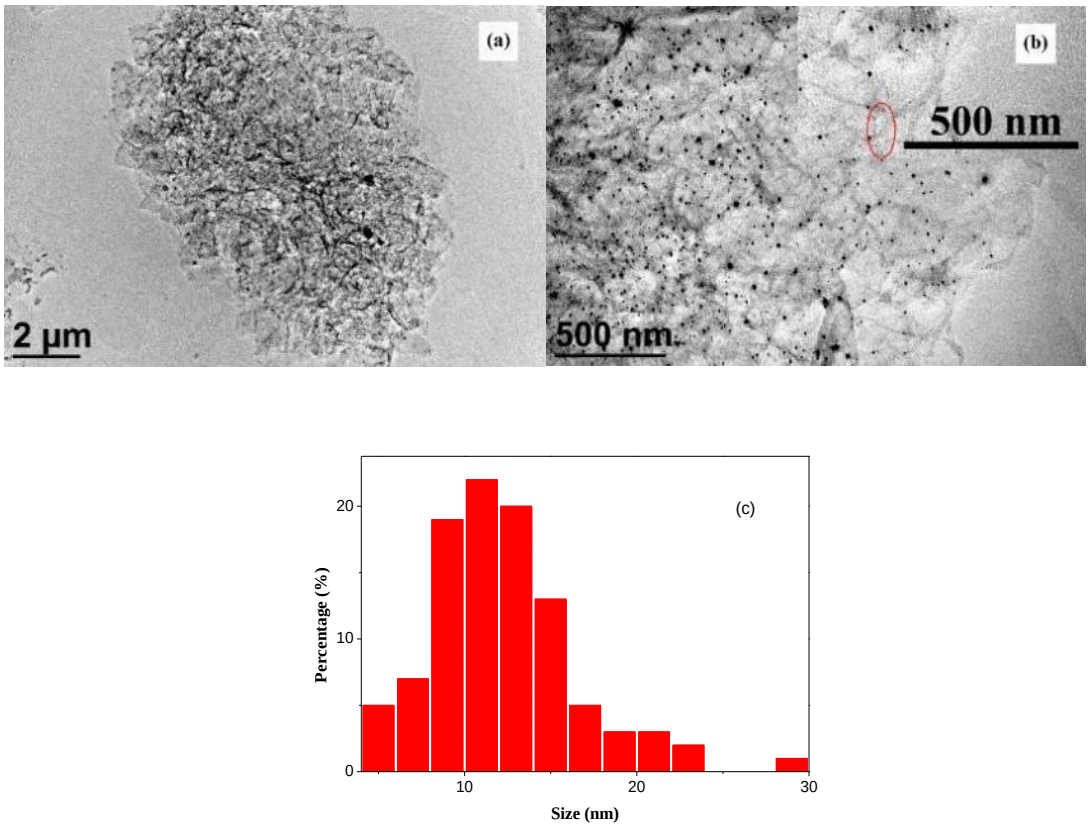

Figure 5 - 4 *The TEM image of A1 sample presenting the dimension and distribution of AgNPs. (a) and (b) The AgNPs decorated GO with different magnification. (c) The size distribution of AgNPs.*

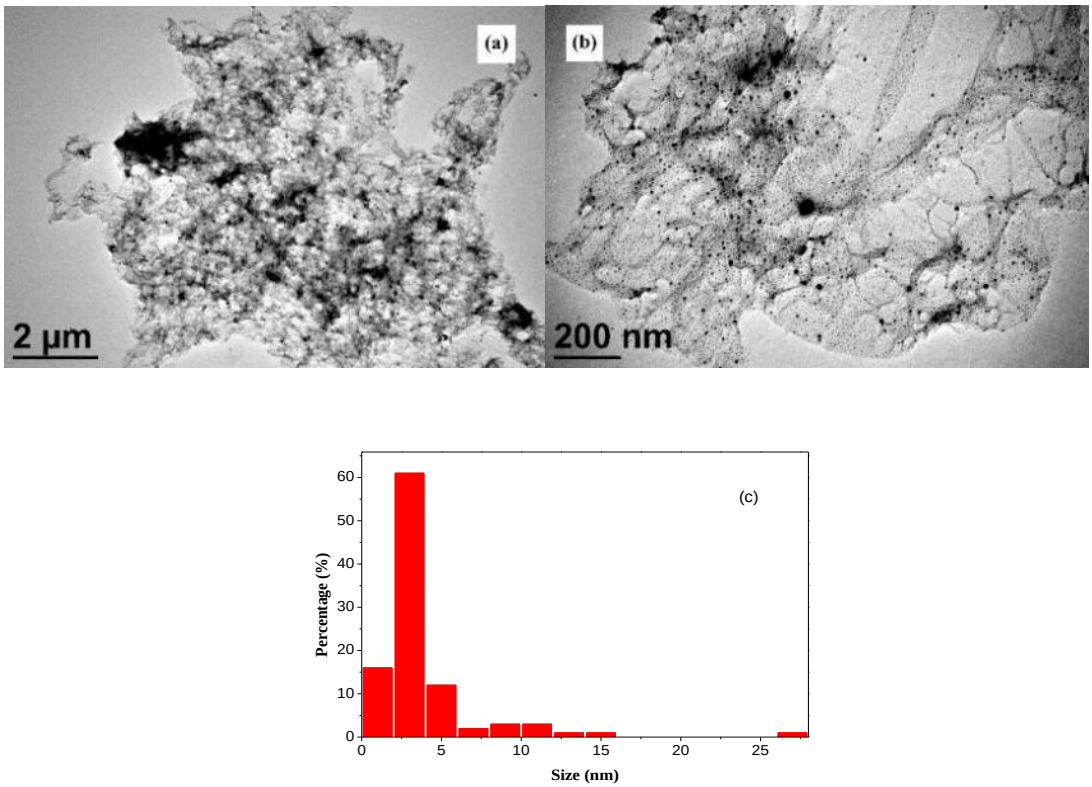

Figure 5 - 5 *The TEM image of A2 sample presenting the dimension and distribution of AgNPs. (a) and (b) The AgNPs decorated GO with different magnification. (c) The size distribution of AgNPs.*

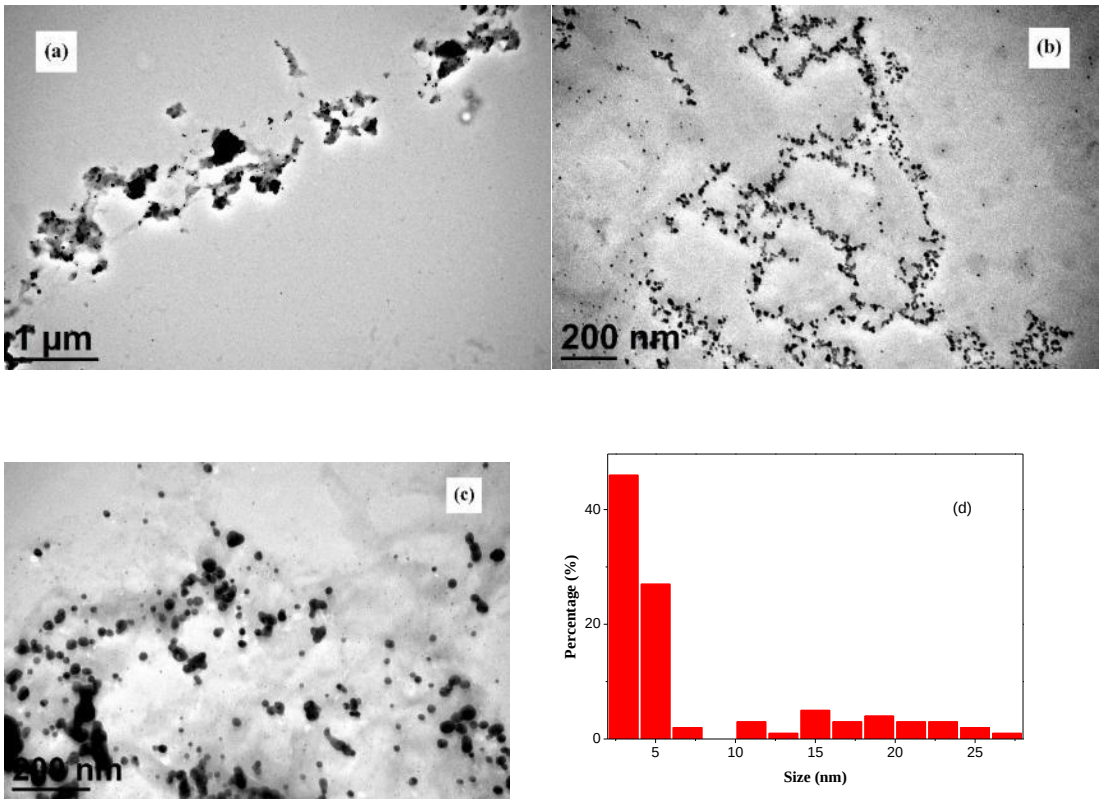

Figure 5 - 6 *The TEM image of A3 presenting the dimension and distribution of AgNPs. (a), (b), and (c) The AgNPs decorated GO with different magnification. (d) The size distribution of AgNPs.*

5.3.1.2 NaOH content

It is reported that the different content of reductant can result in the AgNPs with different dimensions and fractional conversion of Ag^{+} ions (Kausar et al. 2018). Therefore, the NaOH with different usage was employed at 1 mL, 3 mL, 5 mL, and 22 mL labeled as N1, A2, N3, and N4.

Table 5 - 4 *The electrical conductivity and size information of N1, A2, N3, and N4*

Specimens	Electrical conductivity (S/m)	Yield %	Mean size (nm)	Standard deviation
N1	8333	96.2	2.34	2.18
A2	10870	98.3	3.85	3.49
N3	9346	98.6	4.46	3.78
N4	9009	98.5	12.95	6.20

The AgNPs decorated RGO with different NaOH content was investigated in this section. The electrical conductivity of the AgNPs/RGO is shown in **Table 5-4**. The N1 specimen showed the lowest electrical conductivity in these specimens, which also has the smallest average particle size of 2.34 nm, and the lowest yield in this sample was because of the low NaOH content. As shown in **Figure 5-7**, more than 90% of particles had a size smaller than 2 nm, and there was no dissociation of AgNPs. The electrical conductivity of specimens from A2 to N3 as shown in **Table 5-4** have decreased tendency with NaOH content increase. A higher content of NaOH solution is favorable for the formation of AgNPs with large size and wide particle size distribution. The standard deviation value increased with NaOH content increase supporting this idea. Although the degree of GO reduction can increase with NaOH content increase (Fan et al. 2008), the electrical conductivity decrease indicated that more defects appeared on the graphene sheets as discussed in Chapter 2. The average size of the AgNPs is an increase from 2.34 nm to 12.95 nm, and the minimum size of AgNPs all have a similar trend, with size increasing with NaOH content increase. However, the maximum size of the specimens was disorderly due to the NaOH being unevenly distributed is uncontrollable in this experiment. This will be discussed. Further. The yield of specimens has no significant change from A1 to N4, which revealed that most of the silver nitrate was reduced and transformed into AgNPs when the content of NaOH was 3 mL. Comparing **Figures 5-7 (a)**, **5-8 (a)**, and **5-9 (a)**, it can be observed that the AgNPs/RGO size decreases with increase NaOH content under the same treatment (Fan et al. 2008). The electrical conductivity of AgNPs/RGO increased first from 1 mL NaOH to 3 mL because of silver nitrate conversion and then decreased with increased content of NaOH due to the heterogeneous AgNPs size caused by NaOH being unevenly distributed.

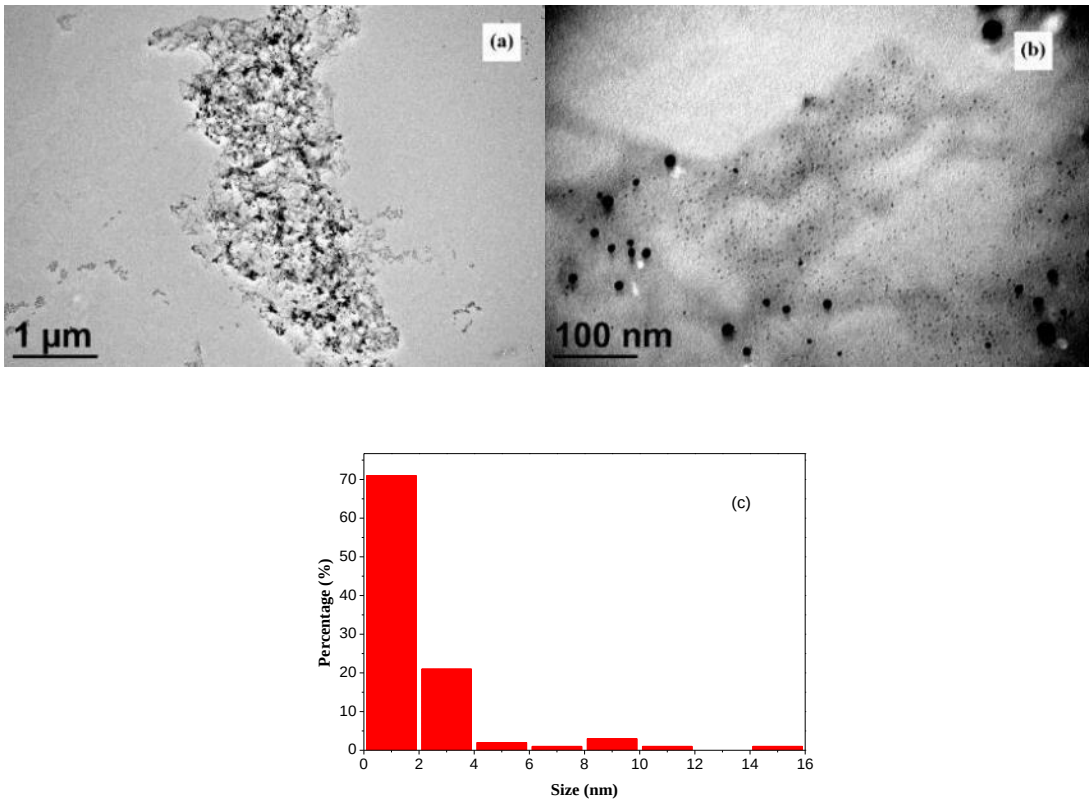

Figure 5 - 7 *The TEM image of N1 presenting the dimension and distribution of AgNPs. (a) and (b) The AgNPs decorated GO with different magnification. (c) The size distribution of AgNPs.*

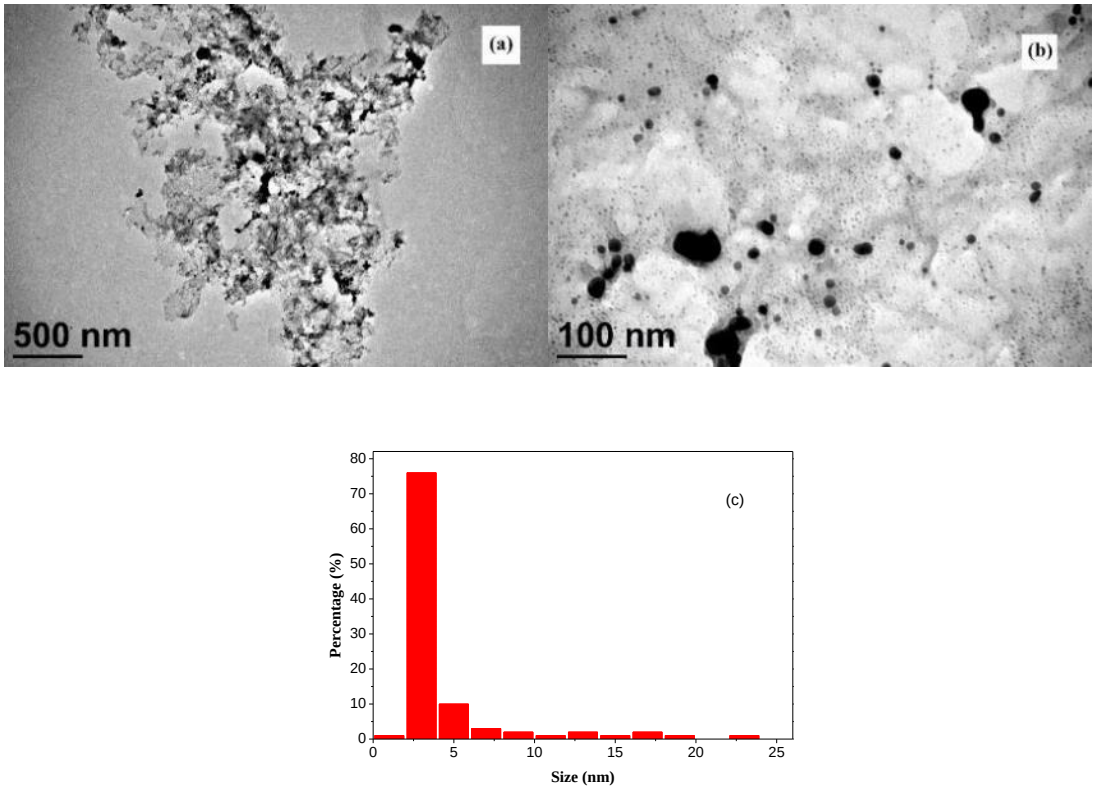

Figure 5 - 8 *The TEM image of N3 presenting the dimension and distribution of AgNPs. (a) and (b) The AgNPs decorated GO with different magnification. (c) The size distribution of AgNPs.*

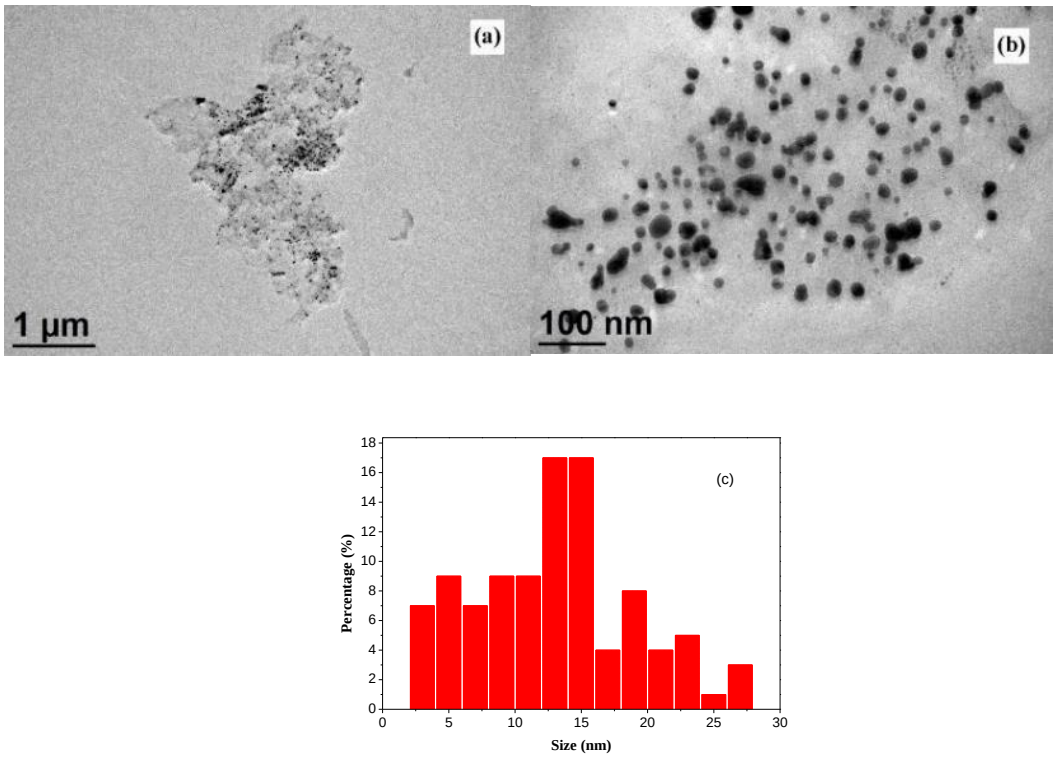

Figure 5 - 9 *The TEM image of N4 presenting the dimension and distribution of AgNPs. (a) and (b) The AgNPs decorated GO with different magnification. (c) The size distribution of AgNPs.*

5.3.1.3 NaOH adding method

The NaOH adding methods of the AgNPs synthesis are discussed in this section. A2 was adding NaOH by transfer liquid gun with the 3 mL of 8 M NaOH to the reaction system directly. L1 was added with 3 mL of 8M NaOH diluted with 27 mL pure water first, and then the diluted NaOH was added to the reaction system.

Table 5 - 5 *The electrical conductivity, and size information of A2, and L1*

Specimens	Electrical conductivity (S/m)	Yield %	Mean size (nm)	Standard deviation
L1	10990	98.3	2.44	0.88
A2	10870	98.3	3.85	3.49

The methods of adding NaOH solution are investigated in this section. It is obvious that L1 display much smaller particle size and narrower size distribution as shown in **Figure 5-10**. However, the yield of AgNPs are similar, and the electrical conductivity showed similar performance after NaOH dilution. The NaOH solution was diluted before addition to the synthesis system, which can reduce the NaOH being unevenly dispersed, resulting in more uniform AgNPs growth and higher conductivity than the undiluted specimen. Therefore, the AgNPs/RGO prepared using diluted NaOH was used for further investigation.

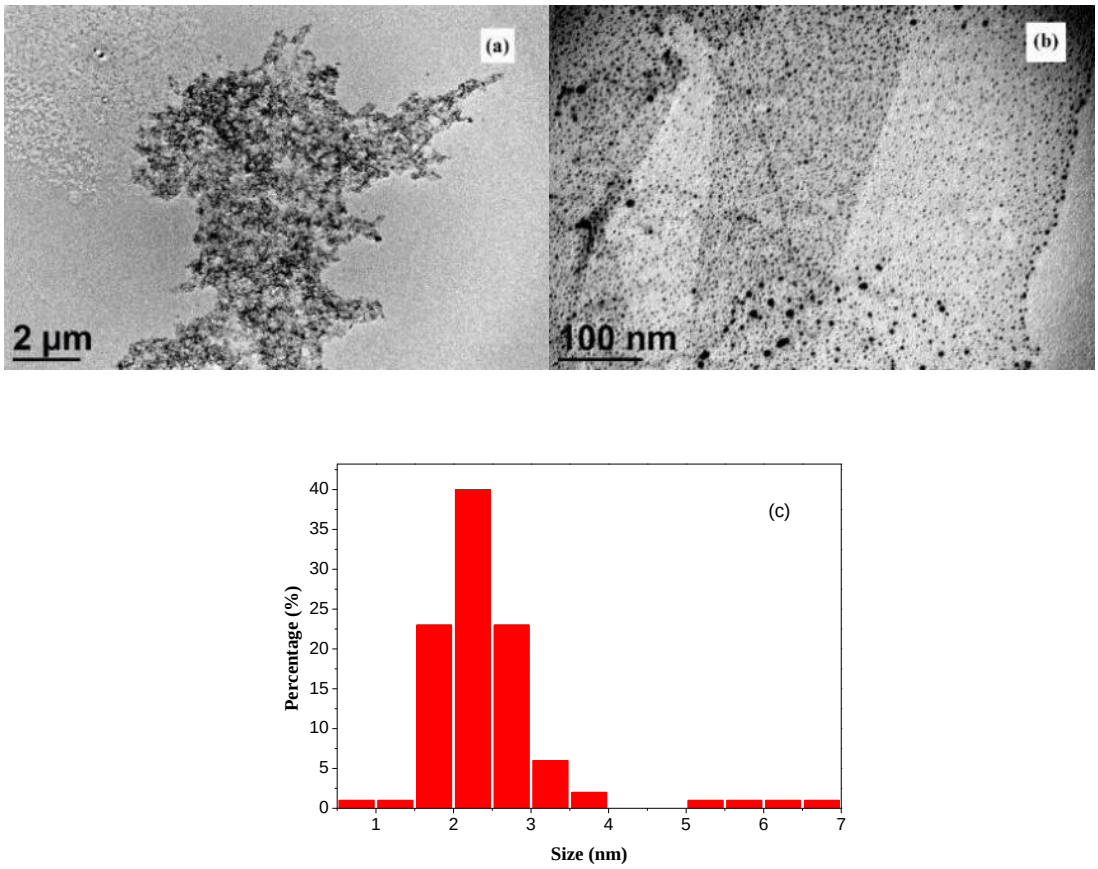

Figure 5 - 10 *The TEM image of L1 sample presenting the dimension and distribution of AgNPs. (a) and (b) The AgNPs decorated GO with different magnification. (c) The size distribution of AgNPs.*

5.3.1.4 Vc added into reaction system

Vc was added to the reaction system because Vc reduced GO showed higher electrical conductivity than NaOH reduced samples (Fernández-Merino et al. 2010). The

reaction where Vc was added after NaOH was labelled as V2. The reaction system with only Vc added was labelled as V1.

Table 5 - 6 *The electrical conductivity, and size information of L1, V1, and V2*

Specimens	Electrical conductivity （S/m）	Yield %	Mean size (nm)	Standard deviation
L1	10870	98.3	2.44	0.88
V1	10000	98.7	47.88	44.82
V2	31000	99.2	3.15	0.97

L1 specimen reduced by Vc for 15 min could obtain the sample properties of V2. The electrical conductivity of the specimen increased to 31000 S/m, and the yield increased from 98.3% to 99.2%. In addition, the mean size, minimum size, and maximum size all increased from 2.44 nm to 3.15 nm, from 0.88 nm to 0.97 nm, and from 6.66 nm to 8.64 nm, respectively. The TEM of the V1 specimen confirms this. In the V1 specimen, AgNPs was prepared by Vc only, Although the yield of AgNPs of V1 is a little bit higher than L1, the heterogeneous particle sizes limited the electrical conductivity. The size of AgNPs grew up to 327.17 nm, mean size was 47.88 nm, and the standard deviation was 44.82 nm.

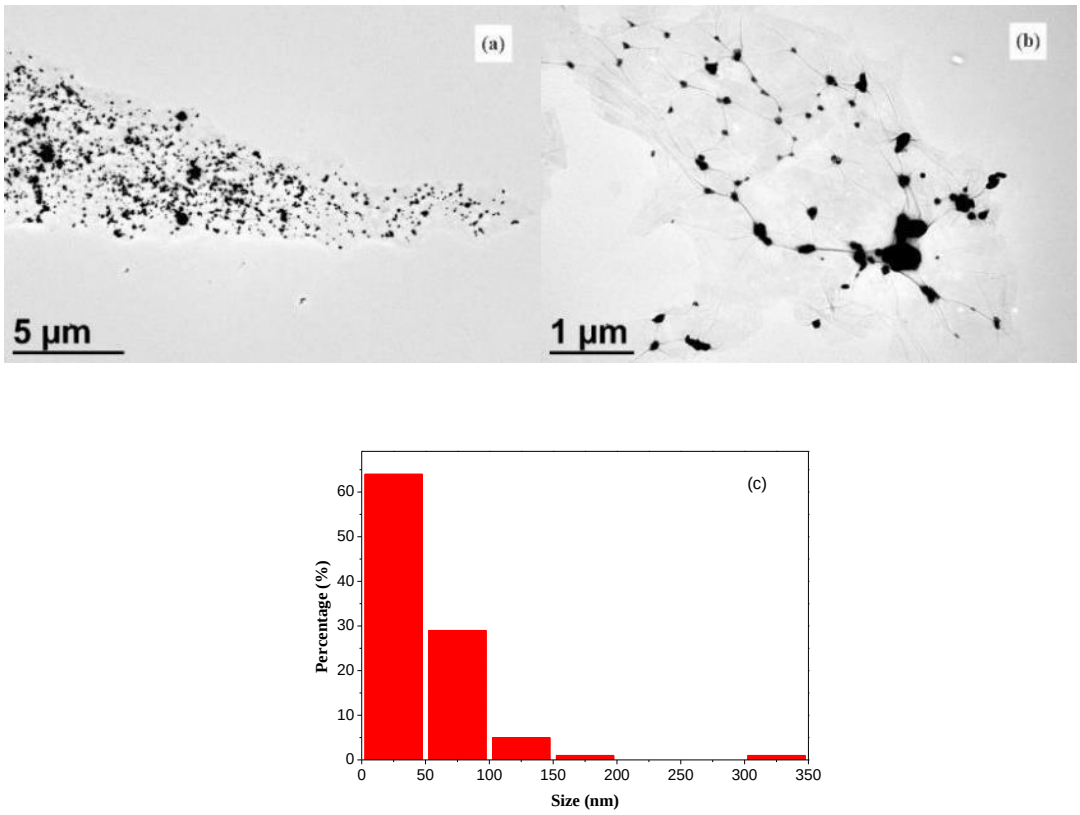

Figure 5 - 11 *The TEM image of V1 sample presenting the dimension and distribution of AgNPs. (a) and (b) The AgNPs decorated GO with different magnification. (c) The size distribution of AgNPs.*

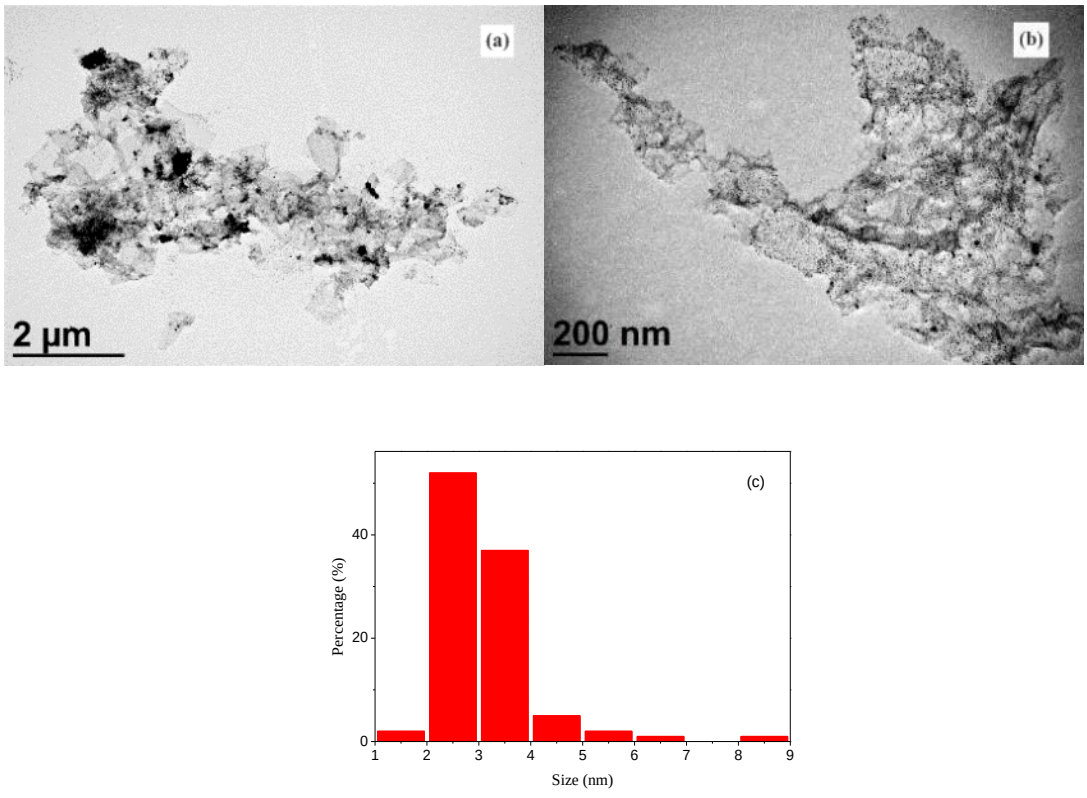

Figure 5 - 12 *The TEM image of V2 sample presenting the dimension and distribution of AgNPs. (a) and (b) The AgNPs decorated GO with different magnification. (c) The size distribution of AgNPs.*

The UV-vis absorption spectra of L1 and V2 was shown in **Figure 5-13**. The absorption peak at approximately 411.6 nm of L1 is AgNPs after Vc treatment observed redshift to the 418.0 nm in the V2 specimen, which agreed with the TEM images appeared the size of the AgNPs increased. The absorption peak between approximately 210.0 nm and 280.0 nm belongs to the conjugated C=C bonds. After GO is reduced, this absorption peak can present redshift (Fu et al. 2010). There are two absorption peaks in the L1 specimen at approximately 217.2 nm, and 251.2 nm, respectively, which all shifted to 252.2 nm after Vc treatment in the V2 specimen, which indicated that the extensive conjugated sp^2 carbon framework is reconstructed. Therefore, Vc not only increases the yield of AgNPs but also reduces the extra oxygen groups from RGO sheets. Therefore, in the following section, V2 was employed as an electrical conductivity additive used for improving the electrical conductivity of NR nanocomposites. It is reported that the plasmon resonance of dissociative AgNPs with an average diameter of approximately 6 nm is near 405 nm (Hebeish et al. 2011). It is known that smaller sized AgNPs could cause blueshift. However, in this investigation, the plasmon resonance of L1 is 411.6 nm. It is indicated that the local surface plasma enhancement presented. It is common in surface enhanced Raman spectrum (SERS) to observe a difference between the maximum of the excitation profile, and the plasmon resonance. The performance of this experiment is similar to that of Haruka, who reported pyridine on Ag films that the peaks of Ag performance redshift (Hebeish et al. 2011). Yuan decorated RGO using AgNPs for antibacterial application. The redshift of GO to RGO is also reported, and the banding between RGO and AgNPs corresponds to the surface plasmon resonance absorption band (Yuan et al. 2012).

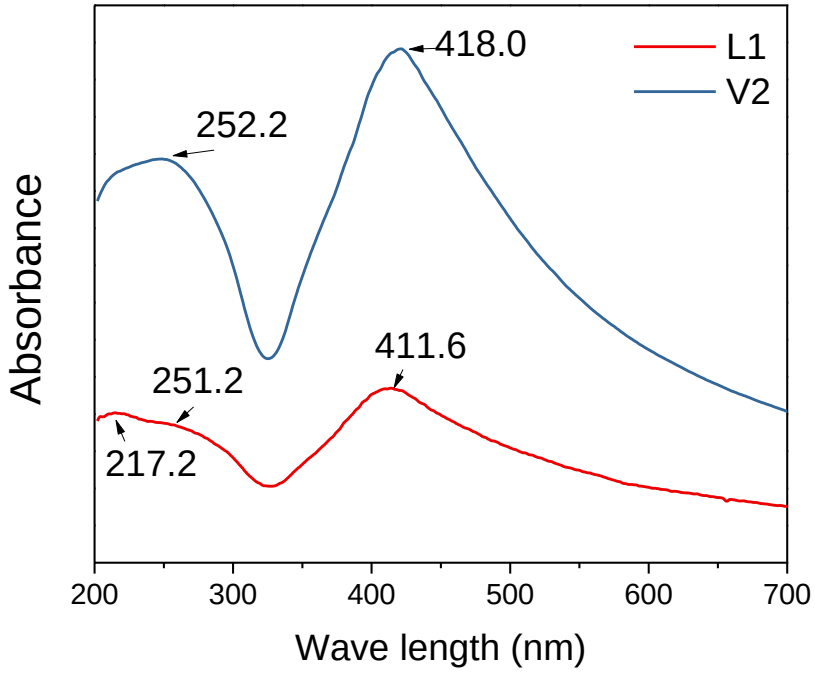

Figure 5 - 13 *The UV-vis spectra of L1, and V2.*

5.3.1.5 Characterization of V2

Because V2 was employed as the additive to increase the electrical conductivity of NR nanocomposites, the systematic characterization of V2 is provided in this section, to reveal the structure of AgNPs/RGO, and how to use them in an NR matrix.

The Raman spectra of the GO, V2, and L1 are shown in **Figure 5-14**, which is effective for observing the disorder of sp^2 carbon material. The typical features for graphene in a Raman spectrum is a D band and a G band. D band is approximately 1351 cm^{-1}, representing the defects or disorder in graphene sheets including vacancies, dangling bonds, and some oxygen groups, and the G band is approximately 1602 cm^{-1} which introduce the E_{2g} phonon of the carbon sp^2 atoms (Lucchese et al. 2010; Zhu et al. 2010). The intensity of D band and G band in L1 increased by 502% and 261% in comparison to the GO specimen, respectively. The intensity of the D band and G band in V2 increased 4090% and 2448% in comparison to the GO specimen, respectively, which indicated SERS activity, which indicated the formation of an interaction between the AgNPs and RGO (Fu et al. 2010; Li et al. 2011).

It is accepted that charge transfer and electromagnetism are two mechanisms of SERS. The electromagnetic enhancement usually can contribute factors of about 10^4-10^6 to the enhancement. Meanwhile, the charge transfer mechanism involves the metal-adsorbate charge transfer and chemisorption interaction, and it usually contributes 10-100 of the order of magnitude enhancement. It is reported that these two mechanisms are intimately linked, but one may dominate under special conditions (Lombardi & Birke 2008). Hui synthesized AgNPs/GO using an *in-situ* ultrasonication approach, which showed AgNPs decorated on the defect site of GO and under the chemical interaction between the AgNPs and GO, with a similar enhancement of 680% (Hui et al. 2014). Zhen synthesized AgNPs decorated GO with enhancement which had a G band higher than D band, which indicated that AgNPs were grown on the defect site of GO, because Raman scattering from defect sites enhanced stronger than sp^2 carbon framework (Li et al. 2011). In this investigation, enhancement of G band was almost 2 times stronger than D band indicating that AgNPs grew on the defect site of RGO. In addition, the G band of the L1 at 1589.4 cm^{-1} and V2 at 1590.5 observed blueshifts compared with that of GO. Das reported that the G peaks sharpen and stiffen for both electron and hole doping, and the blue shift of the G peak was attributed to charge transfer between the RGO and AgNPs (Das et al. 2008). As shown in **Figure 5-14** the SERS enhanced performance, and the NaOH and Vc *in-situ* growth strategies inducing strong bond between the AgNPs and RGO sheets resulted in a lower Shottky barrier. V2 obtained a better interaction of AgNPs with RGO sheets, and more facile equilibration of Fermi level of AgNPs and RGO than L1 (Singha et al. 2014). Although this approach increased the disorder of the system, the charge transfer is facilitated between AgNPs and RGO increasing the electrical conductivity.

In this investigation, the I_D/I_G were calculated to reveal the integrity of RGO in L1 and V2 specimens. The I_D/I_G ratio of GO was 0.825, L1 was 1.59, and value of V2 was 1.38. It is obvious that GO had been reduced after decorated with AgNPs. The sp^2 carbon framework of RGO is further restored after Vc was added as UV-vis tests shown. Raman spectra show I_D/I_G of V2 was smaller than that of L1, which indicated that the by-product of Vc reduction was connected to the AgNPs/RGO (Veliko et al. 2003). Furthermore, the structure of RGO is closer to graphene, leading to the properties of RGO being closer to the theoretical value, which explains why the electrical conductivity of V2 is higher than L1.

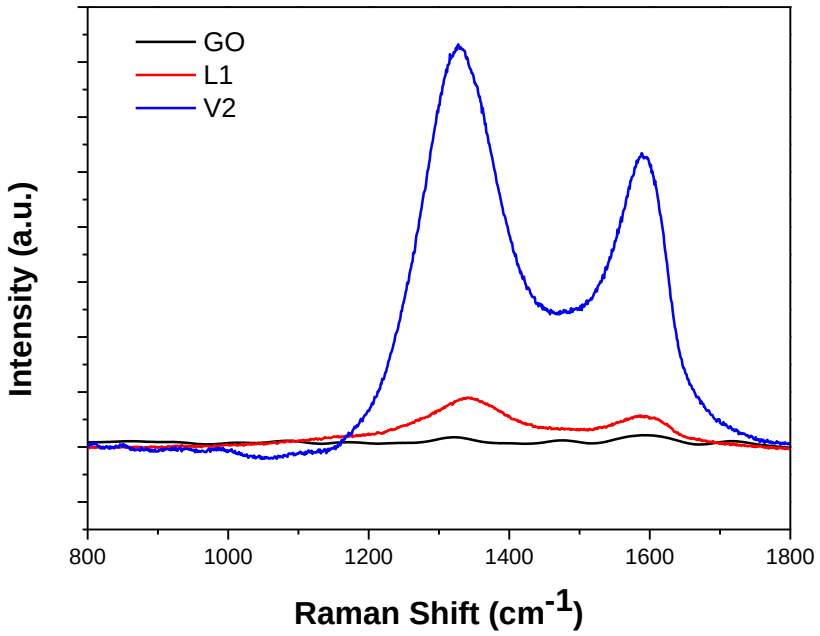

Figure 5 - 14 *The Raman spectra of GO, L1, and V2 specimens.*

The XPS spectra of L1 and A2 are shown in **Figure 5-15**. Each XPS spectrum was fitted with five Gaussian peaks corresponding to carbon atoms presented in different chemical environments. The fitted curves of C1s spectra of GO, L1, and V2 correspond to carbon atoms in different functional groups: C=C/C-C (non-oxygenated ring carbon, 284.5 eV), C-OH (hydroxyl, 285.3 eV), C-O-C (epoxy/ether, 286.7 eV), C=O (carbonyl, 288.0 eV), and CO(O) (carboxyl, 289.1 eV) (Park et al. 2008).

It is obvious that GO is converted to RGO after NaOH and Vc treatment. The epoxy/ether groups in GO were converted to -C-OH groups as shown in **Figure 15-15 (a)**, **(b)**, which occurred because of alkaline conditions discussed in Chapter 4. The large amount of -C-OH groups left on the RGO sheets supported by the Tian reported that -C-OH groups give an anchor for AgNPs growth (Tian et al. 2012). In the L1 specimen, the ratio of C: O increased from 1.99 to 3.27, but in specimen V2, the ratio of C: O is decreased to only 2.53. In addition, the XPS spectra show the content of carbonyl groups in V2 is more than that of the L1 specimen as shown in **Figure 5-15**, of which the content increased from 8.5% to 10.8%. These phenomena indicate that by-products of Vc reduction remained attached to the surface of the AgNPs/RGO. Meanwhile, the electrical conductivity of the V2 becomes approximately 3 times larger

than L1, and the relative amount of silver increases from 10.74% to 16.18% as shown by the XPS measurement. The addition of Vc gives RGO a higher degree of reduction than NaOH as depicted in the XPS spectra, presented as the decreased peak for -C-OH. It is reported that Vc appeared to cause a higher degree of reduction attainable than an alkaline reductant (Fernández-Merino et al. 2010). In addition to this, the content of C=O is increased, which indicated that the by-product of Vc reduction was attached to the AgNPs/RGO (Goia & Matijevic 1999). The higher degree of reduction and higher relative amount of silver made the electrical conductivity of V2 higher than L1. Furthermore, the mechanism of Vc reduced silver nitrate to metallic silver according to the following reaction (Velikov et al. 2003):

$$C_6H_8O_6 + 2Ag^+ \rightarrow 2Ag^0 + C_6H_6O_6 + 2H^+$$

As Velikov reported the by-product of Vc could be adsorbed in the surface of AgNPs by carboxyl groups, and the AgNPs could show the negative charge, which also explains why the ratio of C: O is lower in V2 than L1 (Velikov et al. 2003). The Zeta potential of the V2 was measured to be -46.1 mV. The result is detailed in **Figure 5-16**.

Shown in **Figure 5-15 (d)**, **(e)** is the Ag 3d spectra of L1 and V2, respectively. The Ag 3d peaks of L1 are centered at 368.6 eV, and 374.6 eV and the Ag 3d peaks of V2 are located at 368.3 eV, and 374.3 eV. Pol reported that the metallic Ag 3d peaks are centered at 367.9 eV, and, 373.9 eV respectively (Pol et al. 2002). Cai reported Ag(I) exhibits two 3d peaks at 369.6 eV and 375.8 eV (Cai et al. 1998). It is obvious that composites thus formed exhibit two strong peaks centered at positions between the metallic silver and Ag(I) reported by Tian (Tian et al. 2012). Therefore, the components of AgNPs in this investigation are metallic silver and Ag(I). The Ag(I) is the reaction of the metallic silver and oxygen groups in the reaction solvent to form a silver oxide layer covering the AgNPs (Tian et al. 2012). However, the two Ag 3d peaks of V2 are both closer to that of the metallic Ag than L1, which indicates that AgNPs in V2 content has more metallic silver, which increases the electrical conductivity. However, in the XRD and TEM tests, only the metallic AG was observed, indicating that the Ag(I) is very rare in the AgNPs.

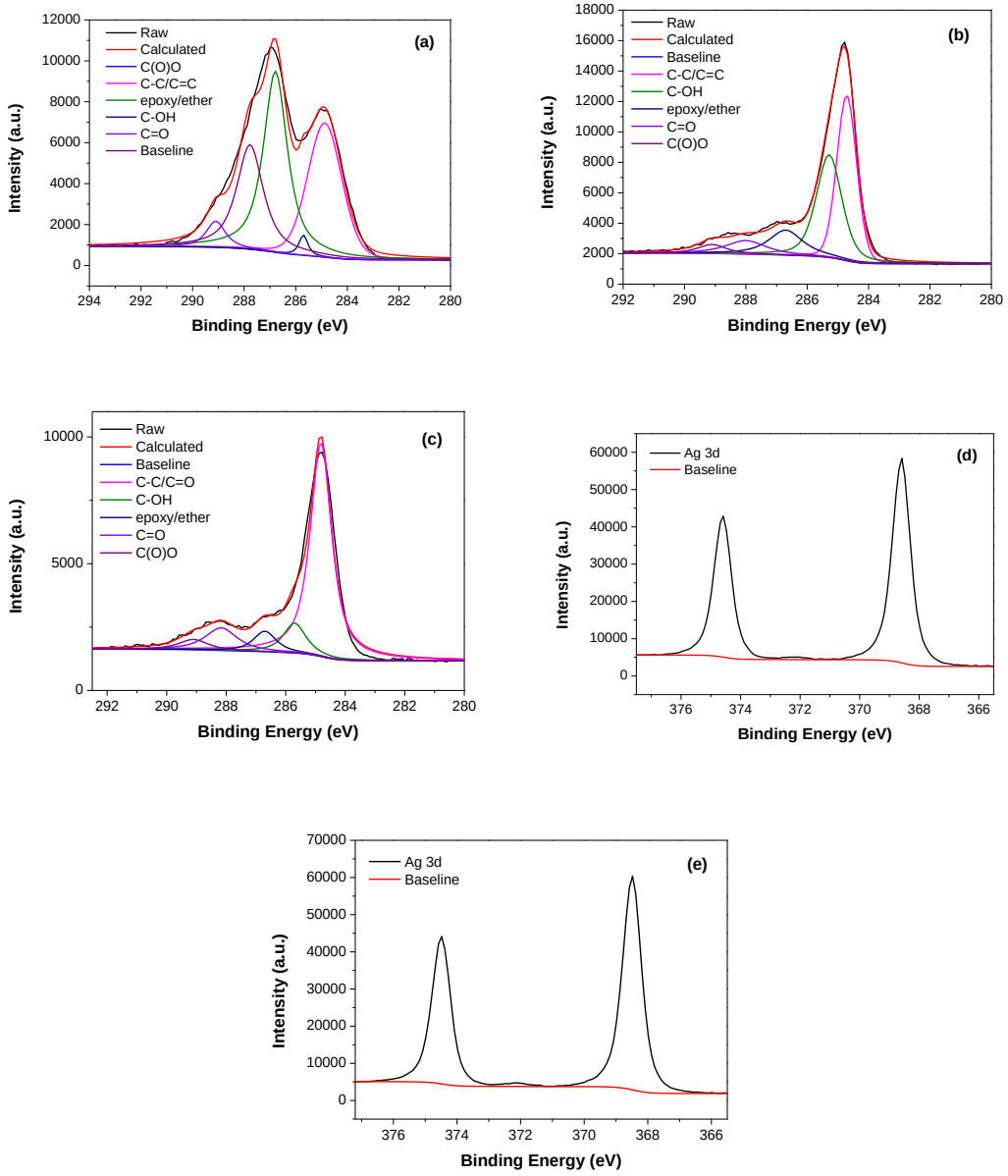

Figure 5 - 15 *The XPS spectra of specimens. (a) C1s core-level spectra of GO, (b) C1s core-level spectra of L1, (c) C1s core-level spectra of V2, (d) Ag 3d spectra of L1, and (e) Ag 3d spectra of V2.*

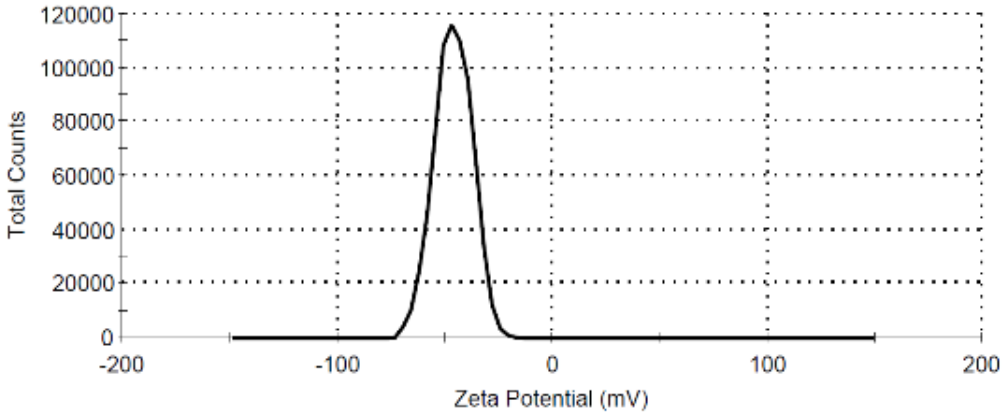

Figure 5 - 16 *The Zeta potential distribution of V2.*

To further elucidate the structure of AgNPs/RGO, XRD, TEM, and SEAD patterns of AgNPs/RGO were analyzed. The indexing process of powder diffraction pattern is performed, and *Miller Indices* of each peak are assigned as shown in **Table 5-7**. There are six strong Bragg reflections of RGO and AgNPs shown, which are (002) of RGO, and (111), (200), (220), (311), and (222) of face-centred cubic silver. There are no spurious diffractions indicating crystallographic impurities to be found (Vineis et al. 2010). The (002) reflection of RGO is 8.38^{o} in L1 and 8.20^{o} in V2, which are both smaller than the GO 11.07^{o} with *d* value is 7.98 Å as it was discussed in Chapter 4. The AgNPs decorated on the surface of the RGO enlarge the distance between the interfacing graphene sheets from 7.98 Å to 10.77 Å because an AgNPs growth on the surface of RGO extended the distances of the neighbouring graphene layers. Five peaks at 2θ values of 38.11^{o}, 44.26^{o}, 64.44^{o}, 77.33^{o}, and 81.52^{o} were found in L1, and 38.12^{o}, 44.25^{o}, 64.44^{o}, 77.35^{o}, and 81.40^{o} were found in V2. These correspond to (111), (200), (220), (311), and (222) planes of silver and were compared to the standard powder diffraction card of Joint Committee on Powder Diffraction Standards, File No. 04-0783. The FWHM of V2 is narrower than L1 as shown in **Table 5-7**, revealing that the V2 sample had higher crystallisation than L1. XRD testing also supported the higher electrical conductivity of V2 over L1. The high-resolution TEM and selected area electron diffraction pattern is shown in **Figure 5-18**, and **Figure 5-19**. High-resolution TEM image of a typical nanoplate shows parallel fringes with a spacing of 2.40 Å corresponding to (111) of the *fcc* silver lattice, and 2.03 Å corresponding to (200) of the *fcc* silver lattice. The SEAD pattern further confirms the *fcc* structure of AgNPs. In the high-resolution TEM image, the (111), (200), (220), (311), and (222) all been defined.

Table 5 - 7 *The Peak index of L1 and V2*

	2θ (°)	d	FWHM	hkl
L1	8.38	10.54	1.20	002
	38.11	2.36	1.12	111
	44.26	2.05	1.24	200
	64.44	1.45	1.24	220
	77.33	1.23	1.32	311
	81.52	1.18	1.20	222
V2	8.20	10.77	0.40	002
	38.12	2.36	1.04	111
	44.25	2.05	1.16	200
	64.44	1.45	1.12	220
	77.35	1.23	1.12	311
	81.40	1.18	1.16	222

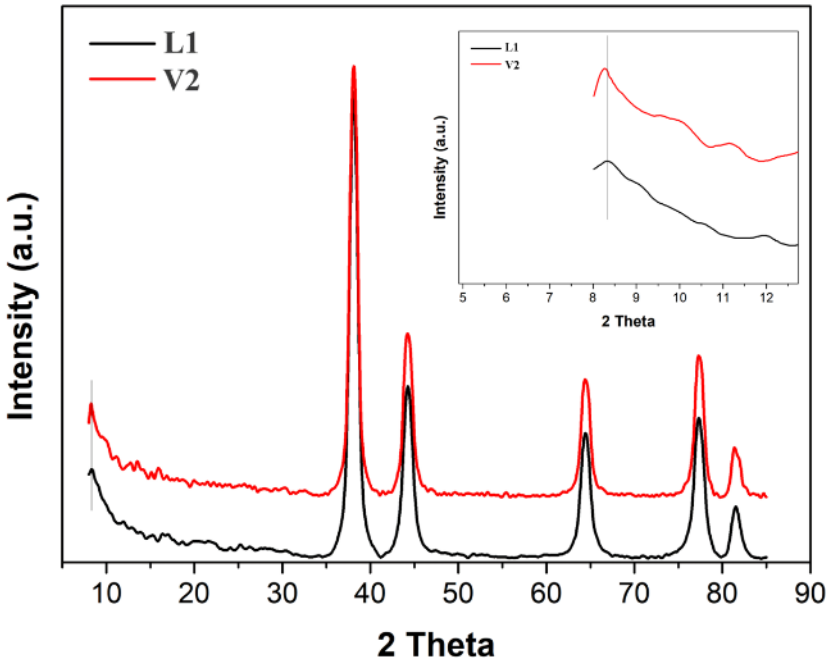

Figure 5 - 17 *The XRD patterns of L1 and V2. The inset of the enlarged image of L1, V2 for the peak of RGO.*

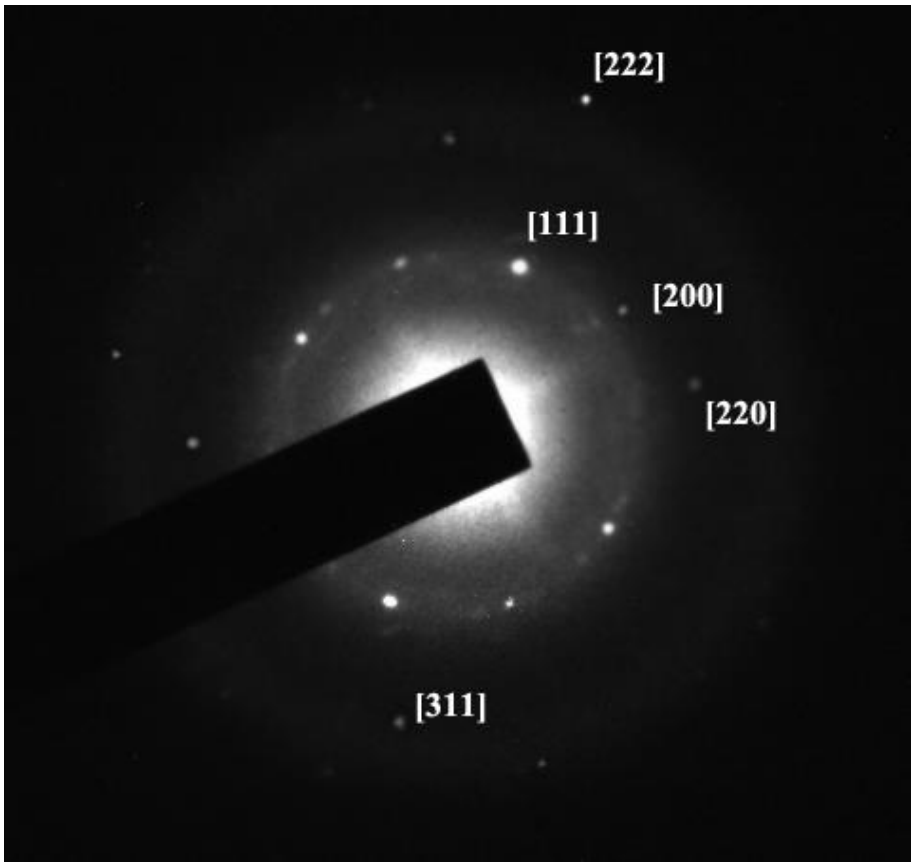

Figure 5 - 18 *The selected area electron diffraction pattern recorded from one of the AgNPs of V2 specimen. The diffraction spots have been indexed with the (111), (200), (220), (311), and (222) to the fcc silver lattice.*

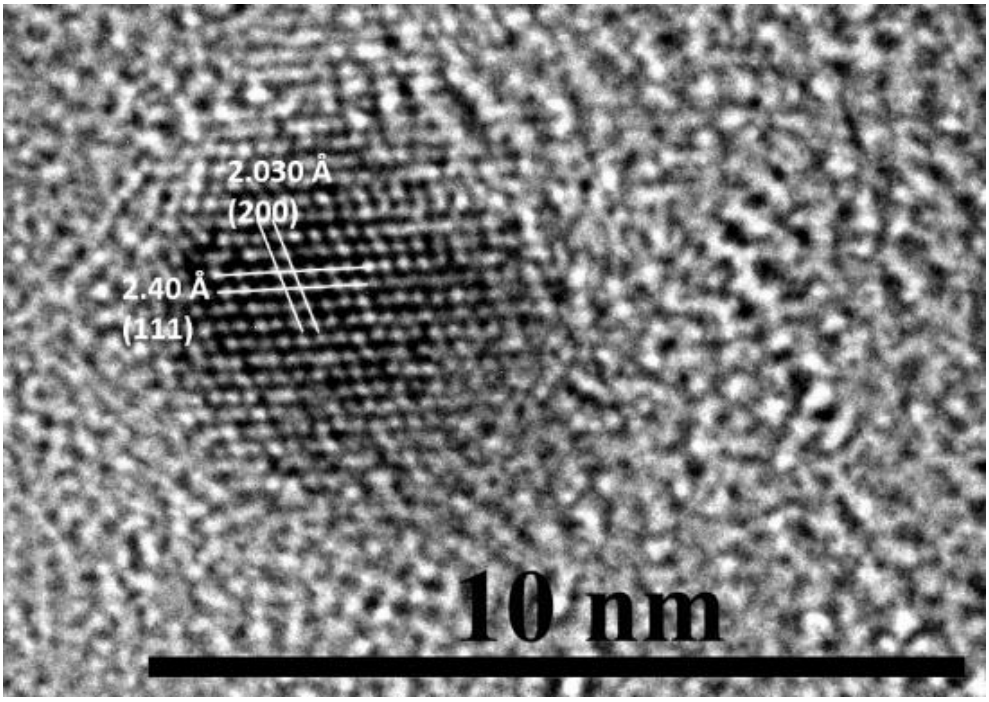

Figure 5 - 19 *The high-resolution TEM image of AgNPs in V2 specimen. Lattice spacing: 2.40 Å corresponding to (111) of the fcc Ag lattice. Lattice spacing: 2.030 Å corresponding to (200) of the fcc Ag lattice.*

5.3.2 AgNPs/RGO filled NR nanocomposites

To prepare NR nanocomposites to possess high electrical conductivity with low percolation threshold value, V2 was employed as an additive, and the composite was prepared through latex mixing, the freeze-drying, and hot press. NR particles in the NR latex acted as a template to generate a segregated conducting pathway by electrostatic self-assembly, which also prevented the graphitization of RGO sheets.

5.3.2.1 Electrostatic self-assembly between AgNPs/RGO

AgNPs/RGO was modified by PDDA, as described in Chapter 3. PDDA/V2 specimen shows a broad peak at 250-290 nm, which can be attributed to the sp^2 carbon network of graphene, and the π-π* electron transition of the PDDA at 280 nm as Feng reported (Wang et al. 2013). The TEM image has shown an increase in the size of AgNPs to within approximately 3.72 nm of the mean size, and the absorbance peak of AgNPs shifted from 418 nm to 441 nm as shown in **Figure 5-20**. It is commonly accepted that the size increase and the aggregation of AgNPs could result in a redshift of the plasmon resonance (Wiley et al. 2007). Therefore, the redshift of the AgNPs peak may be attributed to PDDA attached to the surface of AgNPs in this study. After PDDA covered the AgNPs, the surface charge potential converted to positive charge as planned, which was confirmed and detected by zeta potential. The surface charge of the PDDA modified AgNPs/RGO was present as a zeta potential as shown in **Figure 5-21**. The zeta potential of AgNPs/RGO shifted from -46.1 mV to 36.8 mV, which indicated that the PDDA/AgNPs/RGO have a positive charge. The NR particles possess negative charges as discussed in Chapter 3, which can interact with PDDA/AgNPs/RGO through electrostatic self-assembling to construct the segregated current transfer route in the NR matrix with low percolation threshold.

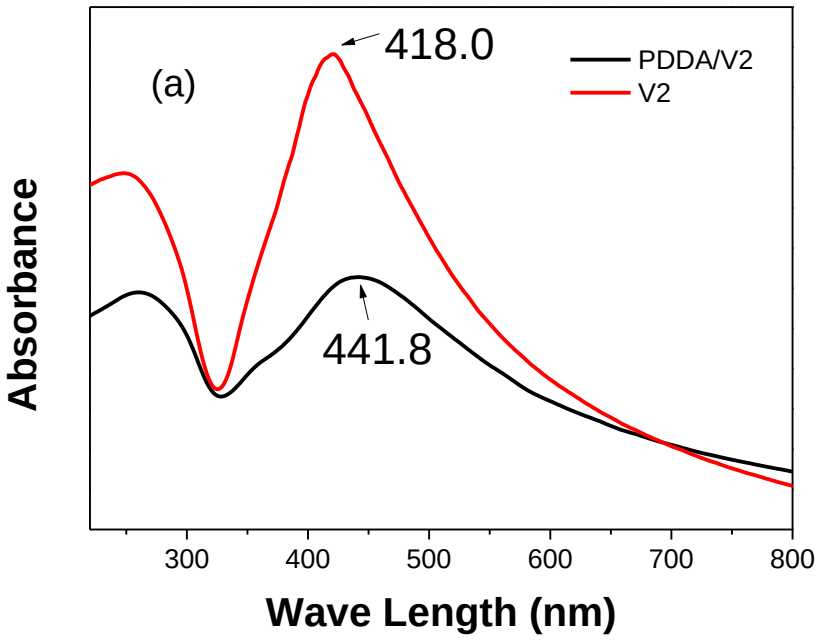

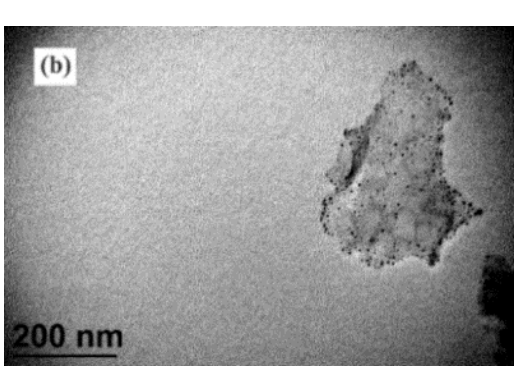

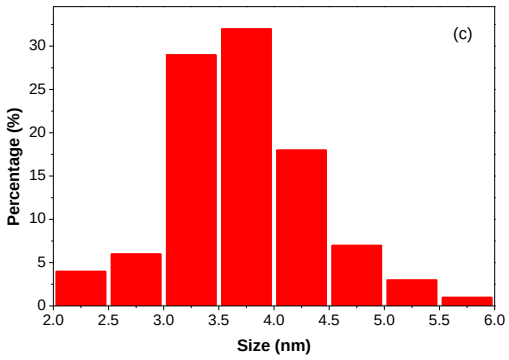

Figure 5 - 20 *The UV-vis spectra and SEM of V2, and PDDA modified V2, (a) UV-vis spectra of V2 and PDDA/V2. (b) SEM image of V2. (c) The size distribution of AgNPs on the GO sheets.*

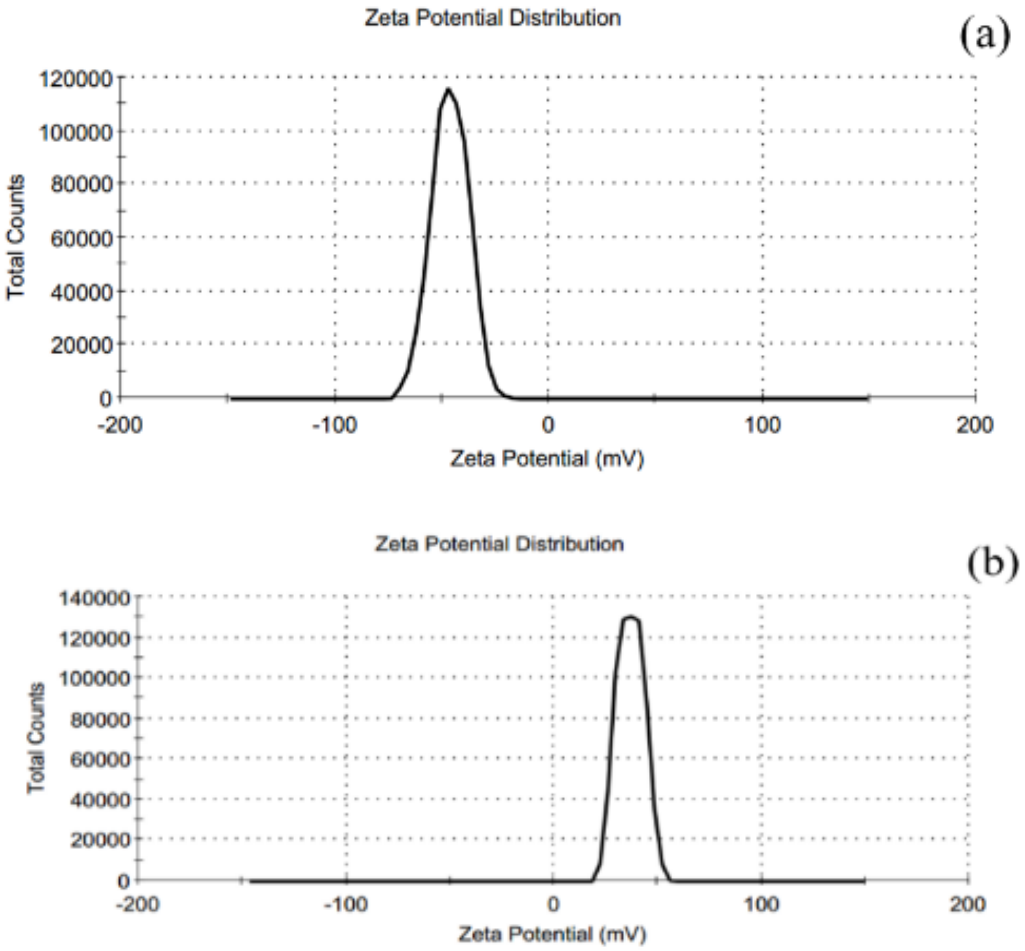

Figure 5 - 21 *The Zeta potential testing results of (a) AgNPs/RGO, and (b) PDDA modified AgNPs/RGO.*

After mixing the PDDA modified AgNPs/RGO with diluted NR latex, the morphology of the nanocomposites was shown in **Figure 5-22**. The stick-like particle could be the vulcanization particles, which have mixed with NR latex first and then added AgNPs/RGO added. The AgNPs/RGO was attached to the surface of NR particles under electrostatic attraction interactions, and no dissociative AgNPs/RGO was found; this is as shown in **Figure 5-22**. In our previous study, PDDA modified RGO encapsulated NR particles showed a similar result (Luo et al. 2014). The AgNPs/RGO covered NR particles can suppress the reaggregation of AgNPs/RGO and provide a precondition for the formation of an electrical conductivity additive 3D network in NR matrix.

However, the aggregation of AgNPs was observed in the TEM and the size of the AgNPs particles partly increased, which lead to a non-rubber component consisting of

NR latex or the curing agents as shown in **Figure 5-22 (b)**. It is reported that the surface of NR particles and serum of NR latex all have reductant properties including proteins and some compounds with the hydroxyl group appear in the NR latex, which possesses reducibility to grow the noble metal nanoparticles (Tao et al. 2015). The thickness of the AgNPs/RGO increased with increasing size of AgNPs, which increased the percolation threshold value as previously reported (Zhao et al. 2014).

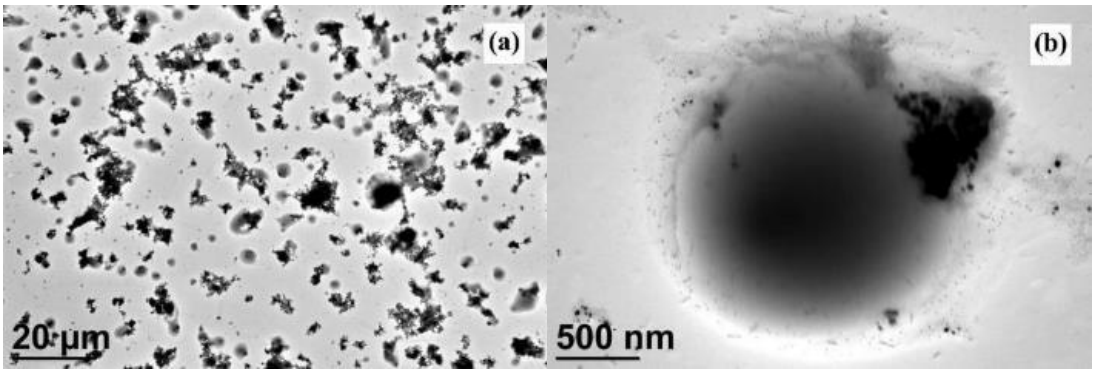

Figure 5 - 22 *The TEM images of AgNPs/RGO mixed with NR latex. The modified RGO sheets cover the NR particle surface (a) low magnification image of AgNPs/RGO mixed with NR latex, and (b) high magnification image of AgNPs/RGO mixed with NR latex.*

The photographs of AgNPs/RGO/NR latex mixture with different AgNPs/RGO content is shown in **Figure 5-23**. The assembly between the AgNPs/RGO and NR particles were observed. Adding a small amount of AgNPs/RGO resulted in the coagulation on the upper layer. The coagulation dropped to the bottom with increasing content of AgNPs/RGO because the density of NR is approximately 0.95 g/cm^3. Finally, the coagulation is separated by subsequent filtering, freeze-drying, and compression moulding.

Figure 5 - 23 *The different amount of PDDA/AgNPs/RGO added into NR latex. From left to right the content of AgNPs/RGO was added 0.1 vol.%, 0.29 vol.%, 0.52 vol.%, 1.01 vol.%, 1.65 vol.%, 2.06 vol.%, 2.87 vol.%, and 4.03 vol.%, respectively.*

The AgNPs/RGO interconnected electrical conductivity network is fabricated in the NR matrix, which is attributed to two points. First is the AgNPs/RGO encapsulated NR particles. Second is the freeze-drying and compression moulding processes, which create maximum retention of the encapsulated additives network. The relative position of additive and NR particles can be maximum retention, which is broadly employed to reduce the percolation threshold value (Zhan et al. 2012; Luo et al. 2014; Li et al. 2017).

SEM was used to characterise the microstructure of the NR nanocomposites shown the cross-section of the neat NR in **Figure 5-24**. Comparing **Figure 5-24** with **Figure 5-1(b)**, the freeze-drying and hot press procedure obtained cross-section not as smooth as the mechanical mixing specimen. As seen the morphology of NR particles are reserved for deformation, which indicated that the temple function of the NR parties for preparation of a material with a low percolation threshold could be realized under this preparation process.

As shown in **Figure 5-24**, the neat NR part is a smooth surface with a deformed spherical shape, and AgNPs/RGO are orientated upright, which makes them easy to identify as an upright honeycomb-like network structure. Another orientation of AgNPs/RGO is lying flat on the SEM image, which is observed as a rough surface with random light particles. On the low AgNPs/RGO content specimen (0.52 vol.%) shown in **Figure 5-24 (b)**, the additives honeycomb-like network was only partly connected. Meanwhile, in the neat NR region, the NR particles joined together in a densely packed twisted shape located in the middle of the network. The partly

coalesced of NR resulted in the AgNPs/RGO failed to form electrical conductor paths located in the NR matrix. Owing to the concentration of AgNPs/RGO was not high enough to cover all the surface of the NR particles.

As shown in **Figure 5-24 (c)**, almost all the area appeared to be a honeycomb-like network of AgNPs/RGO that encapsulated NR particles with a diameter of approximately 1 μm. In the high magnification image shown in **Figure 5-24 (e)**, the AgNPs/RGO interconnected honeycomb-like networks were constructed which guarantees electrical conductivity enhancement in the NR matrix loaded with 2.03 vol.% AgNPs/RGO. However, there was more than one NR particle encapsulated by AgNPs/RGO in one cell, circled with a white dashed lien in **Figure 5-24 (e)**, which should theoretically increase the size of the template and reduce the percolation threshold (Zhao et al. 2014).

Figure 5-24 (g) is calculated from **(f)** through two steps using Gatan's Digital Micrograph software. Firstly, the figure was treated by the Bandpass Filter to prominent the different between the additives and NR. Subsequently, employing the Sobel filter calculated the last result to further enhance the differences. This Figure treatment is finished by Digital micrograph as the default setting. The black area is the NR matrix, and the white sandwich line is the AgNPs/RGO interconnected network, which confirmed the formation of a current transfer path.

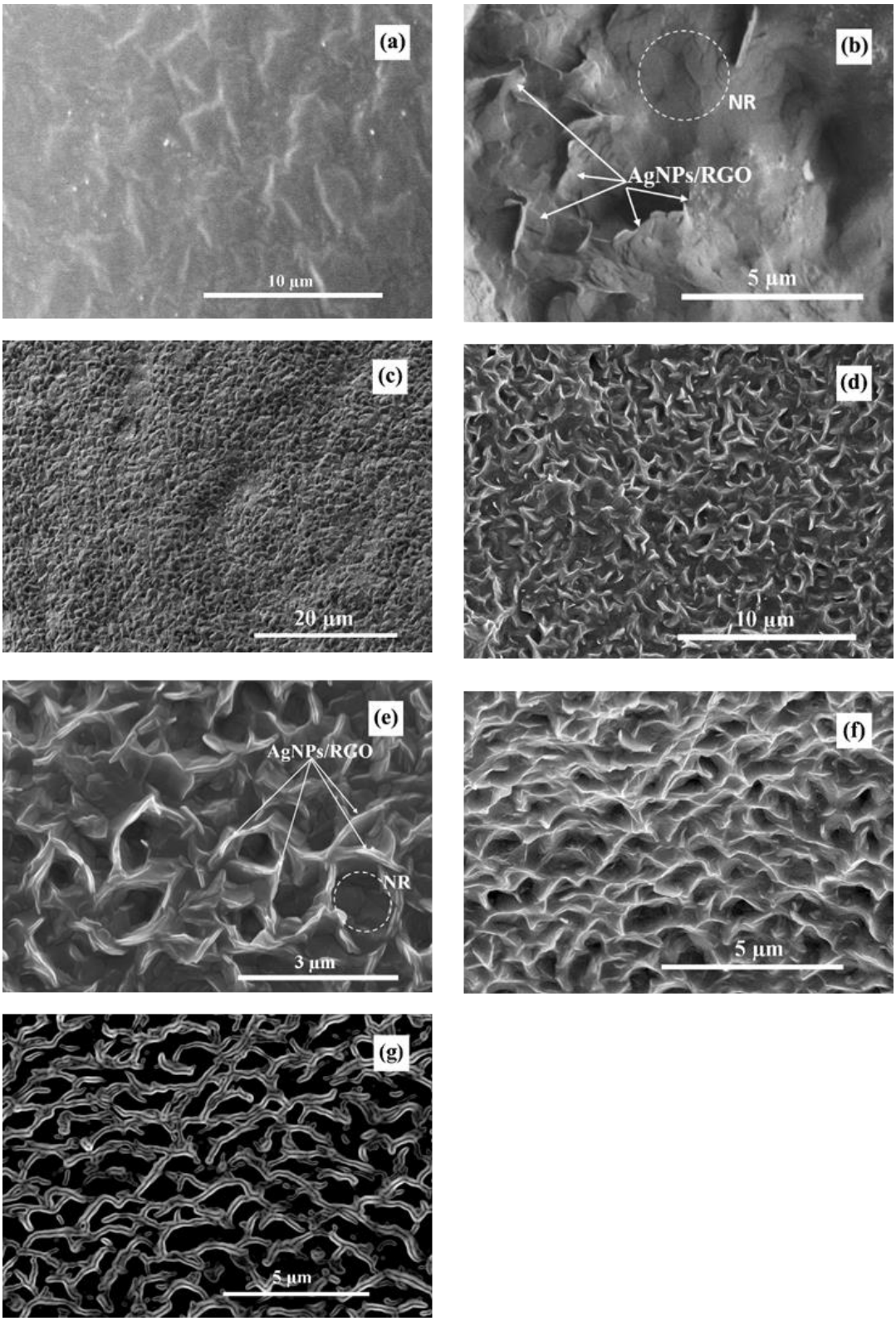

Figure 5 - 24 *The SEM images of cross section of neat NR and NR nanocomposites fabricated by freeze drying and hot press procedure. (a) is neat NR specimen, (b) is PDDA/AgNPs/RGO loaded 0.52 vol.%, (c)-(g) are 2.06 vol.% PDDA/AgNPs/RGO filled NR with different magnification.*

Thus, the target of creating high electrical conductivity was achieved. A TEM image of the cross-section of the NR nanocomposite is shown in **Figure 5-25**. The clean, bright parts are the NR matrix, and the grey plate and black are AgNPs/RGO. Although the aggregation of AgNPs is present, the modified RGO appeared to be in a well-dispersed state. Furthermore, the modified RGO segregated conductive honeycomb-like network is well fabricated as depicted.

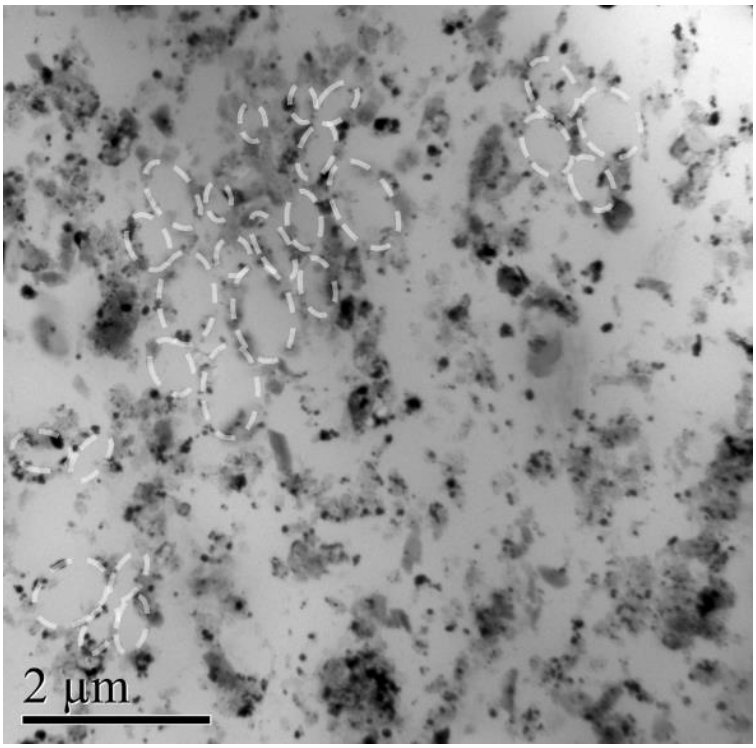

Figure 5 - 25 *The TEM image of AgNPs/RGO filled NR matrix at 2.03 vol.%. The encapsulated NR marked using white dashed line circled.*

To further identify the AgNPs/RGO dispersion in the NR matrix, EDX mapping technology is employed. **Figure 5-26 (d)** is C mapping image. The honeycomb-like network structure of RGO sheets showed promise to depict the frame of RGO connected network. Because the AgNPs/RGO fully encapsulated the NR particles, NR can be peeled off in some of the areas surrounding AgNPs/RGO during the preparation of a liquid nitrogen brittle fracture, resulting in the AgNPs/RGO appearing at the bottom, or AgNPs/RGO was removed to the other half randomly. Therefore, the signal of Ag present in the middle of the RGO surrounding area is shown in **Figure 5-26 (b)**, which confirmed the encapsulation hypothesis.

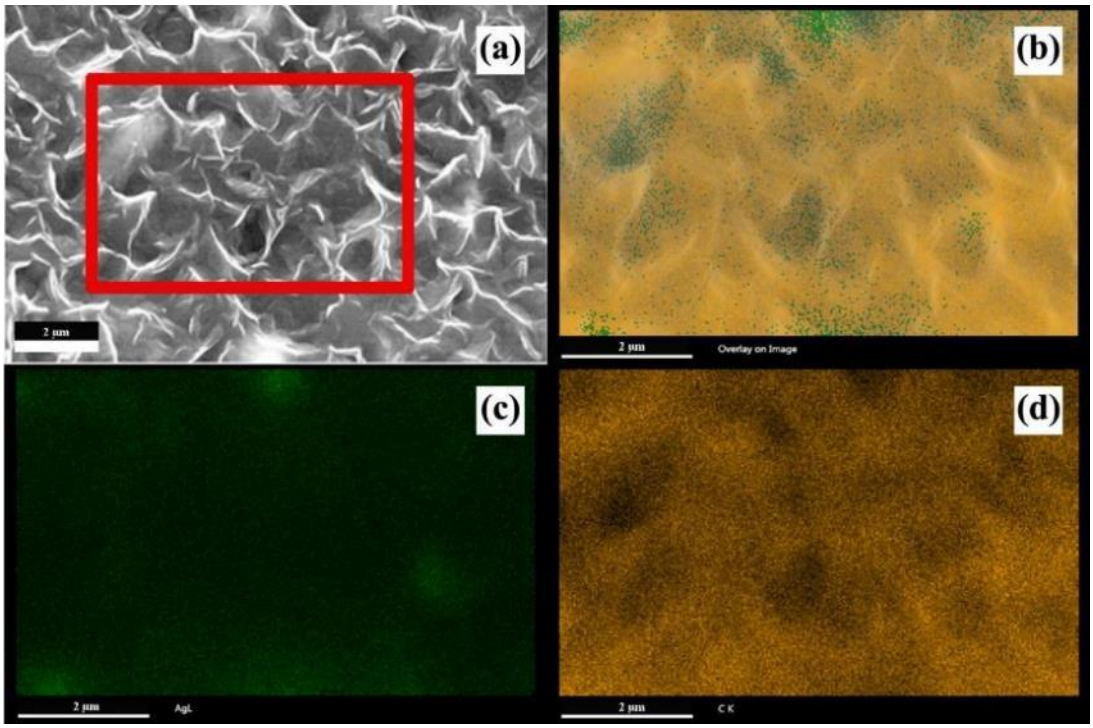

Figure 5 - 26 *The SEM-EDX mapping image of AgNPs/RGO/NR. (a) SEM image of NR nanocomposite the place in the red frame is mapping area. (b) are Ag and C mapping image overlay on the SEM image, (c) is the Ag mapping image, and (d) is C mapping image.*

5.3.2.2 Electrical behaviour of NR nanocomposites

It is commonly accepted that the potentials of novel fillers to impact valuable properties to the host polymer in the polymer nanocomposites field. In this investigation, the electrical conductivity of AgNPs/RGO is approximately 31000 S/m, and a well-organized AgNPs/RGO network was formed in the NR matrix. Therefore, this investigation obtained an electrical conductivity of AgNPs/RGO/NR nanocomposites one order of magnitude higher than pure graphene filled NR nanocomposites (Luo et al. 2014). The electrical conductivity of NR nanocomposites increases exponentially with the amount of AgNPs/RGO loaded, as shown in **Figure 5-27**, where a typical insulating-conductive percolation behaviour is observed with three-stage behaviour. The electrical conductivity of the NR nanocomposites increases significantly from 0.29 vol.% to 1.01 vol.%, which indicates the formation of an AgNPs/RGO percolating network. With the increasing content of AgNPs/RGO, the overlapped RGO sheets increase forming an electrically conductive network to carry

through the current. In this investigation, the maximum electrical conductivity is 196 S/m presented with 4.03 vol. % of AgNPs content.

The electrical conductivity of NR nanocomposites was analysed with classical percolation theory revealing the critical concentration of additives. The equation is given as below:

$$\sigma = \sigma_0(\varphi - \varphi_c)^s \ (\varphi > \varphi_c) \quad (5\text{-}1)$$

Where σ is the electrical conductivity of NR nanocomposites, σ_0 is the proportionality constant, which relates to the intrinsic conductivity of the additives. φ is the volume fraction of the fillers, φ_c is the volume of the percolation, and s is critical exponent which reflects the dimensionality of additives network system.

The critical number of additives doped to cause this insulator-to-conductor transition is named as the percolation threshold. The percolation threshold of NR nanocomposites was calculated to be approximately 0.63%, and the critical exponent to be 1.92. The critical exponent value depends only on the dimensionality of the nanocomposites in a single percolation system. In the classic percolation threshold, the critical exponent value between 1.00 to 1.35 for a two-dimensional system, and between 1.6 to 2.0 for a three-dimensional system (Garboczi & Douglas 1996). In this investigation, the critical exponent is 1.92 indicating that a 3D electrical conductivity network was formed in the NR matrix, which confirmed by the SEM and TEM results.

Theoretically, the volume fraction of percolation can be defined as the amount of AgNPs/RGO covering every NR particles. The theoretical electrical percolation threshold could be calculated with the equations shown below (Li & Shi 2012; Zhao et al. 2014):

Volume of NR particles: $\mathrm{V} = 4\pi R^3/3$ (5-2)

Volume of AgNPs/RGO: $\mathrm{V_0} = 4\pi R^2 h$ (5-3)

Theoretical volume percolation: $\varphi_{co} = (V_0/2V)100\% = (3h/2R)100\%$ (5-4)

where R is the average radius of NR particles, and h is average thickness of AgNPs/RGO sheets.

As shown as in **Figure 5-24 (e)**, and **5-25**, more than normally 2 to 5 NR particles are surrounded by AgNPs/RGO, and the distance of the surrounding area is approximately

1 µm. The mean diameter of encapsulated particles was calculated from **Figure 5-24 (c)** by Image-J, at 1.017 µm as shown **Figure 5-28**, which is larger than the mean diameter of NR particles used in this research. AgNPs/RGO encapsulating larger particles can achieve lower percolation threshold values based on Equation (5-4), which contributed to the low percolation threshold value.

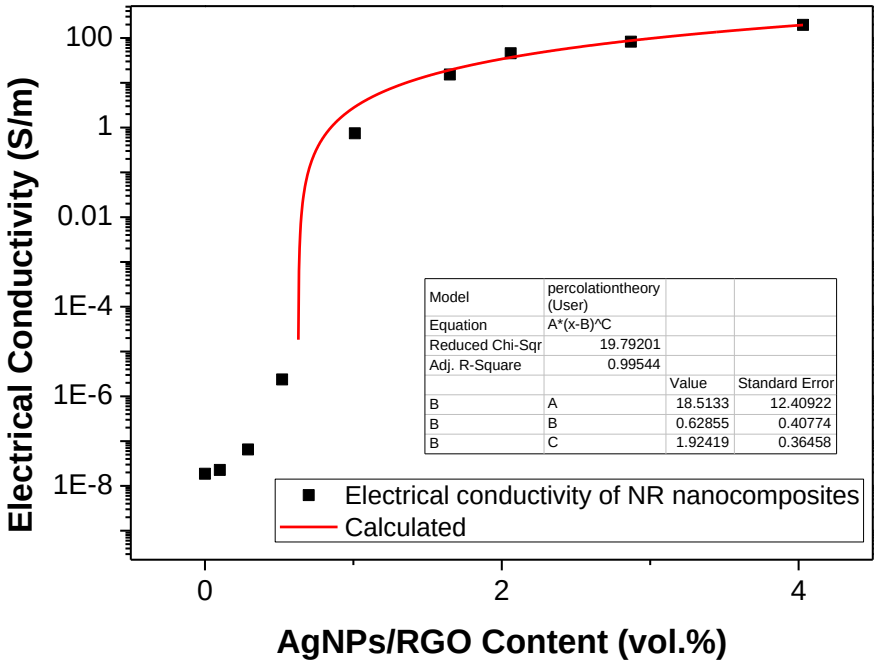

Figure 5 - 27 *The Electrical conductivity of AgNPs/RGO/NR as a function of AgNPs/RGO content. Insert table present the calculated parameters of classical percolation theory.*

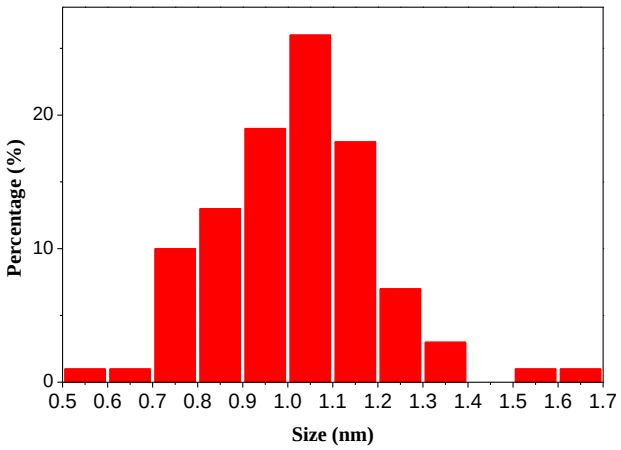

Figure 5 - 28 *The diameter distribution of encapsulated NR particles.*

It is well known that affinity of AgNPs towards sulphur atoms will reduce the electrical conductivity of composites. To achieve the enhancement of electrical conductivity of NR nanocomposites the sequence of the preparation procedures should be taken care of. The vulcanisation agents were added into the NR latex first. After stirring for 0.5 to 2 h, the AgNPs/RGO was added to the mixture to obtain the microstructure as shown in **Figure 5-29 (a)**. The vulcanisation agents attached to the surface of NR particles first, and then were covered by AgNPs/RGO sheets. One side of the AgNPs/RGO contacted with vulcanisation, and another side is explored in the water to guarantee the high electrical conductivity of the final product. When the sequences of adding additives changed, the loaded AgNPs/RGO and vulcanisation agent together can appear the condition as shown in **Figure 5-29 (b)**. In this research, the 3 vol.% AgNPs/RGO was loaded into NR matrix as the procedure of adding AgNPs/RGO and vulcanisation agent together, which produced a final product with an electrical conductivity of only approximately 10^{-10} S/m. It possessed a conductivity 12 orders of magnitude lower than the one prepared under the correct sequence (2.87 vol.% of AgNPs/RGO loaded with 82.8 S/m). The high electrical conductivity results can also be attributed to the freeze-drying and hot press, which retain relative positions of the AgNPs/RGO and NR particles by low solvent evaporation temperature and low shear in hot compression (Lou et al. 2014).

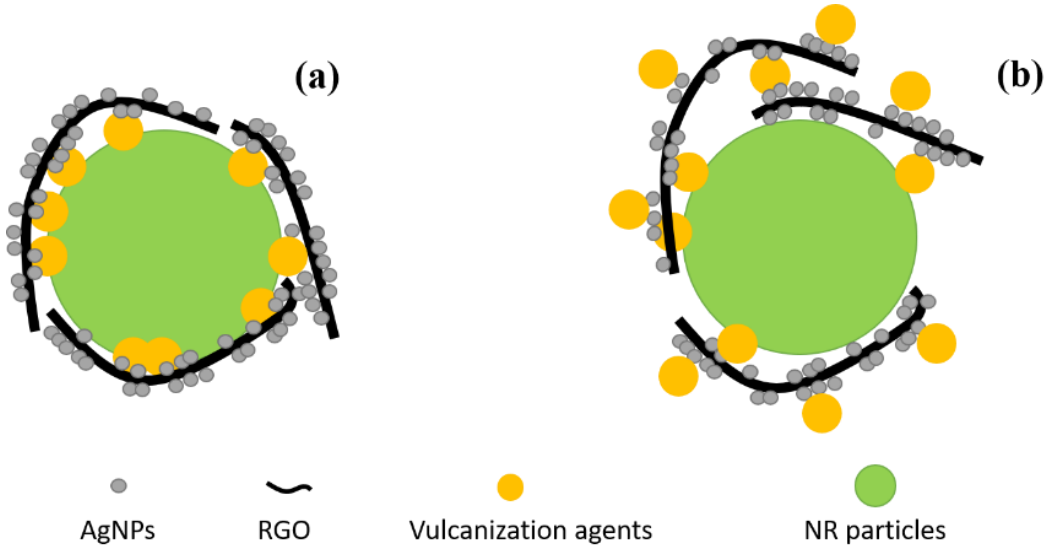

Figure 5 - 29 *The schematic representation of the relative position of V2, vulcanization agents, and NR particles.*

5.4 Concluding remarks

In this chapter, electrically conductive NR nanocomposites have been investigated though two approaches. First, GO was reduced *in-situ* in NR latex to prepare antistatic NR nanocomposites. This a one-pot method to prepare an antistatic NR latex composite, which could be used in any shape with antistatic properties by casting. An *in-situ* and latex mixing approach was employed to reduce the GO into RGO in NR latex by heating at 90 ^{o}C, avoiding high energy consumption, and dust pollution typical of mechanical mixing processes. The RGO sheets covered the surfaces of the NR particles, weakening the effects of graphitisation, and making it easy to form an electrically conductive path. As a result, the conductivity of the nanocomposites went up to 1.0×10^{-1} S/m even with a small amount of RGO doping. The incorporation of RGO also improved the tensile strength and elongation at break of NR nanocomposites. Furthermore, the highly concentrated antistatic RGO/NR latex nanocomposite can be cast into any shape of films offering potential applications in the automotive industry.

Secondly, AgNPs/RGO/NR nanocomposites with interconnected additives networks have been developed by electrostatic self-assembly, and latex compounding approaches. The nanocomposites show a high electrical conductivity of 196 S/m, with a low electrical percolation threshold of approximately 0.63 vol. %. The high electrical conductivity and low percolation threshold are attributed to the structure of the raw materials and preparation method. AgNPs with a mean diameter of approximately 3.15 nm with an *fcc* structure were decorated on the defect sites of RGO sheets. In addition to this, a charge transfer route between the AgNPs and RGO was developed with 31000 S/m of electrical conductivity of bulk specimen. Another reason is the formation of a well-organized, interconnected AgNPs/RGO honeycomb-like microstructure in the NR matrix by designed NR composites preparation approach. The electrostatic self-assembly made possible by PDDA converted the surface charge of AgNPs/RGO from negative to positive. The positive AgNPs/RGO was attached to the surface of NR particles with negative charge. The NR particles deplete the volume and keep the particles shape with the help of the freeze-drying and hot press mould.

Chapter 6: Modified graphene filled NR for mechanical reinforcement

6.1 Introduction

The mechanical properties of NR are improved by the addition of graphene as a filler because defect-free graphene possesses unique physical properties (Rao et al. 2009) better than most other additives. Two methods were reported in this thesis that focused on how to utilize oxygen groups and pores, to increase the dispersion of graphene, and graphene's interaction with NR.

First, the GO is employed as a surfactant, which is made possible by a large number of oxygen groups present on graphene sheets. The GO attached on silica particles to construct a new hybridisation filler used to enhance the mechanical properties of NR composites.

Second, the graphene sheets were decorated with pores of tuneable dimensions, which can form an interpenetrating network between the NR matrix and porous graphene for mechanical reinforcement of the composite.

6.2 Silica decorated GO filled NR

In this research, the experiment focused on the oxygen groups on the GO sheets, which not only dispersed GO in water but also assisted in the dispersal of silica to achieve mechanical reinforcement of NR. Due to polar groups on the surface, silica presents acidic, naturally hydrophilic, moisture adsorbing and strong cohesion characteristics (Prakash et al. 2015). The aggregation of silica in NR composites reduces the bound rubber content and the cross-linking density, as well as disturbs vulcanization (Wolff 1996). GO was employed to solve such issues in this section. The experiments used 0.05 phr of GO and PSS as surfactant respectively, to disperse 5 phr silica particles in NR matrix using latex mixing and casting methods.

6.2.1 Characterisation of structure of filler and NR nanocomposites by FTIR spectra

FTIR spectra of the composites were acquired to determine the transformation of the polar groups in the composites with two different dispersants used, as shown in **Figure 6-1**. The bands at 2915 cm^{-1}, and 1460 cm^{-1} are assigned to the C-H stretching and the flexural vibration in the NR matrix, respectively. Most of the bands at between 1648 cm^{-1} and 1536 cm^{-1} and are related to the amide *I* and *II* bands of proteins, respectively (Dubois & Boué 2001). In the NR/PSS/SiO_2 nanocomposites, the intensity of the silicon-oxygen groups bands at 1062 cm^{-1} was lower than the other spectra because the number of the silicon-oxygen groups decreased by hydrogen bonding with PSS molecules (Crispin et al. 2003). This phenomenon reveals that hydrogen bonds form between the sulfonic subgroups on the PSS molecules, and silicon hydride bonds to various silica particles, including silica hydroxyl and siloxane. The framework of the carbon skeleton of the PSS is formed by C-C bonds, which can fold, resulting in the encapsulation of PSS molecules in silica particles as PSS/SiO_2 clusters (Dubois & Boué 2001). The FTIR spectra of the NR/GO/SiO_2 nanocomposites are similar to the NR/SiO_2 spectra. GO possesses a number of the oxygen groups connected with the silica particles. However, the 2D carbon framework of the GO is a rigid plane, which cannot fold as PSS can; therefore, the silica particles are better encapsulated by GO than PSS.

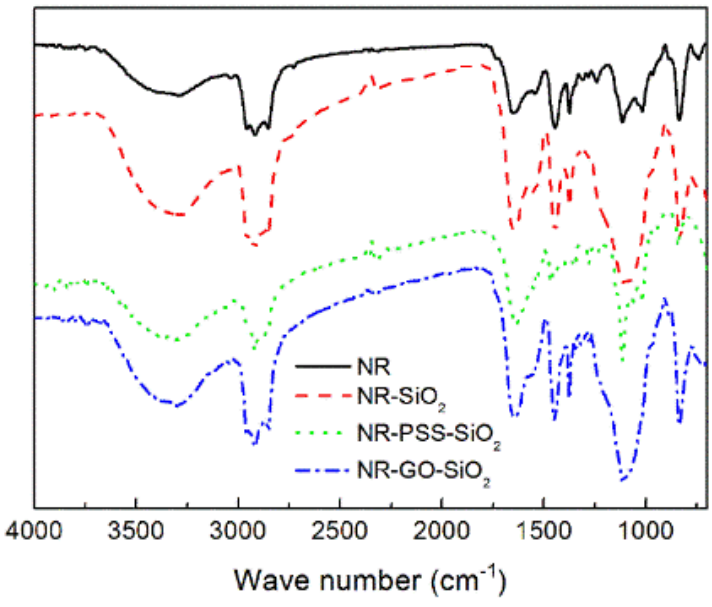

Figure 6 - 1 *The FTIR spectra of neat NR, and NR nanocomposites.*

6.2.2 XLD measurement of NR composites

XLD is used to identify the physical cross-linking densities as shown in **Table 6-1**. The XLD measurements of NR/GO/SiO_2 and NR/GO 5.62×10^{-5} and 5.78×10^{-5} mol/cm^3, respectively. Silica particles loaded into the NR matrix lead to a decrease in XLD, from 5.89×10^{-5} to 5.41×10^{-5} mol/cm^3. The XLD in NR/SiO_2 was lower than that of neat NR because of the re-aggregation of the silica particles (Sinha Ray & Okamoto 2003). The XLD of NR/PSS and NR/PSS/SiO_2 are 6.45×10^{-5} and 6.36×10^{-5} mol/cm^3, respectively, which are higher than the control. This performance occurs because of the higher flexibility of the molecular framework of PSS, compared to GO (Wang et al. 2002; Schniepp et al. 2008). PSS has a hydrocarbon frame, which provides for better deformability and compatibility with the NR matrix than GO. Compared to NR/PSS composites, the XLD of the NR/PSS/SiO_2 is lower because of loaded silica that causes weak compatibility with the NR molecule.

Compared to neat NR, NR/GO shows a lower XLD because GO is a 2D material with a rigid structure, which cannot fold or cross-link with NR molecules. The GO sheets limited the ability of NR molecules to intertwine each other on the other side of the graphene plane. Furthermore, the oxygen groups on GO also showed weak compatibility with the NR matrix. However, the XLD of NR/GO/SiO_2 was higher than NR/SiO_2 attributed to two factors. Firstly, the polar groups on the GO and silica formed hydrogen bonds reducing the polarisation of the compound fillers, thus increasing compatibility with the NR molecules. Secondly, the polymer chains tended to attach to the surface of the 2D materials (Liu et al. 2011). As the polar groups bonded with the silica particles, the NR molecules had better compatibility with the non-polar parts of GO sheets than the original GO increasing the XLD of the NR matrix (Leblanc 2002).

Table 6 - 1 *The XLD results of NR, and NR nanocomposites*

Specimen	XLD ($\times10^{-5}$ mol/cm^3)
NR	5.89
NR/SiO2	5.41
NR/PSS	6.45
NR/PSS/SiO_2	6.36
NR/GO	5.78
NR/GO/SiO_2	5.62

6.2.3 Characterisation of morphology of the NR composites

The TEM observed the microstructures of the silica mixed with dispersants. As shown in **Figure 6-2 (a)**, the silica particles combined with the PSS, which appear to be re-aggregated. However, they can also form a stick-like cluster and further assemble into a net-like filler matrix as shown in **Figure 6-3 (b)**, and **6-4 (b)**. The 1D molecule chains of PSS entangle with silica particles containing polar groups (Gamero-Quijano et al. 2015). As shown in **Figure 6-2 (b)**, the silica particles combined with the GO sheets, because the silica particles are attached to the GO sheets by hydrogen bonds. Because GO can not fold itself like PSS (Lee et al. 2008), the dispersant is not able to encapsulate silica particles. Therefore, the microstructure of the mixture presented as the GO sheets covered by a layer of silica particles as shown in **Figure 6-2 (b)**. The new hybrid filler is developed as a 2D material. Compared the **Figure 6-2 (b)** with **Figure 6-2 (c)**, the GO decrease the re-aggregation tendency of silica particles. The PSS presents much stronger re-aggregation ability than the pure silica particles as shown in **Figure 6-2 (a)**, which form a stick-like structure steadily dispersed in the water.

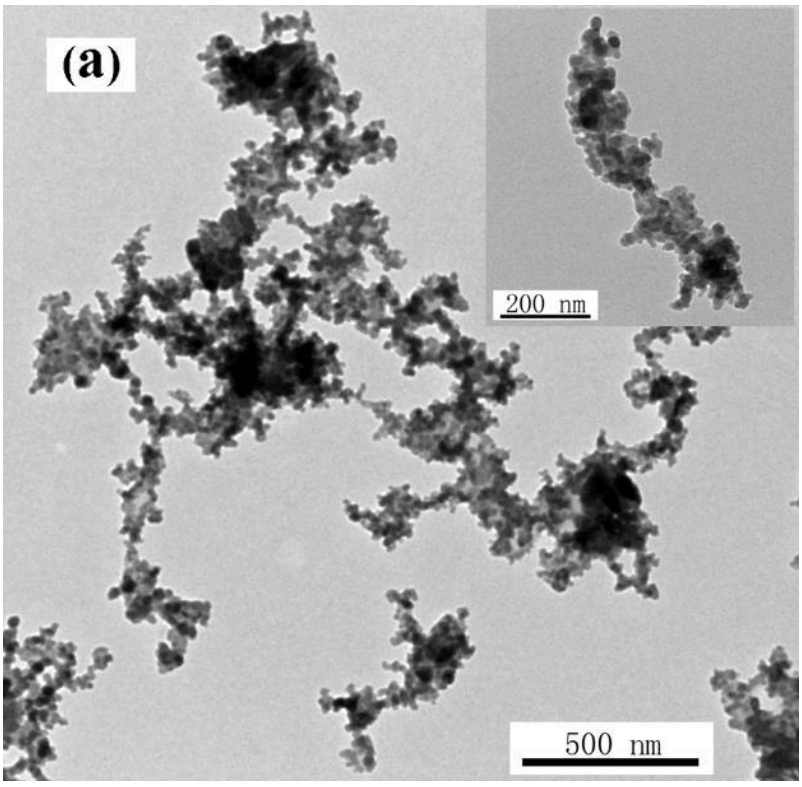

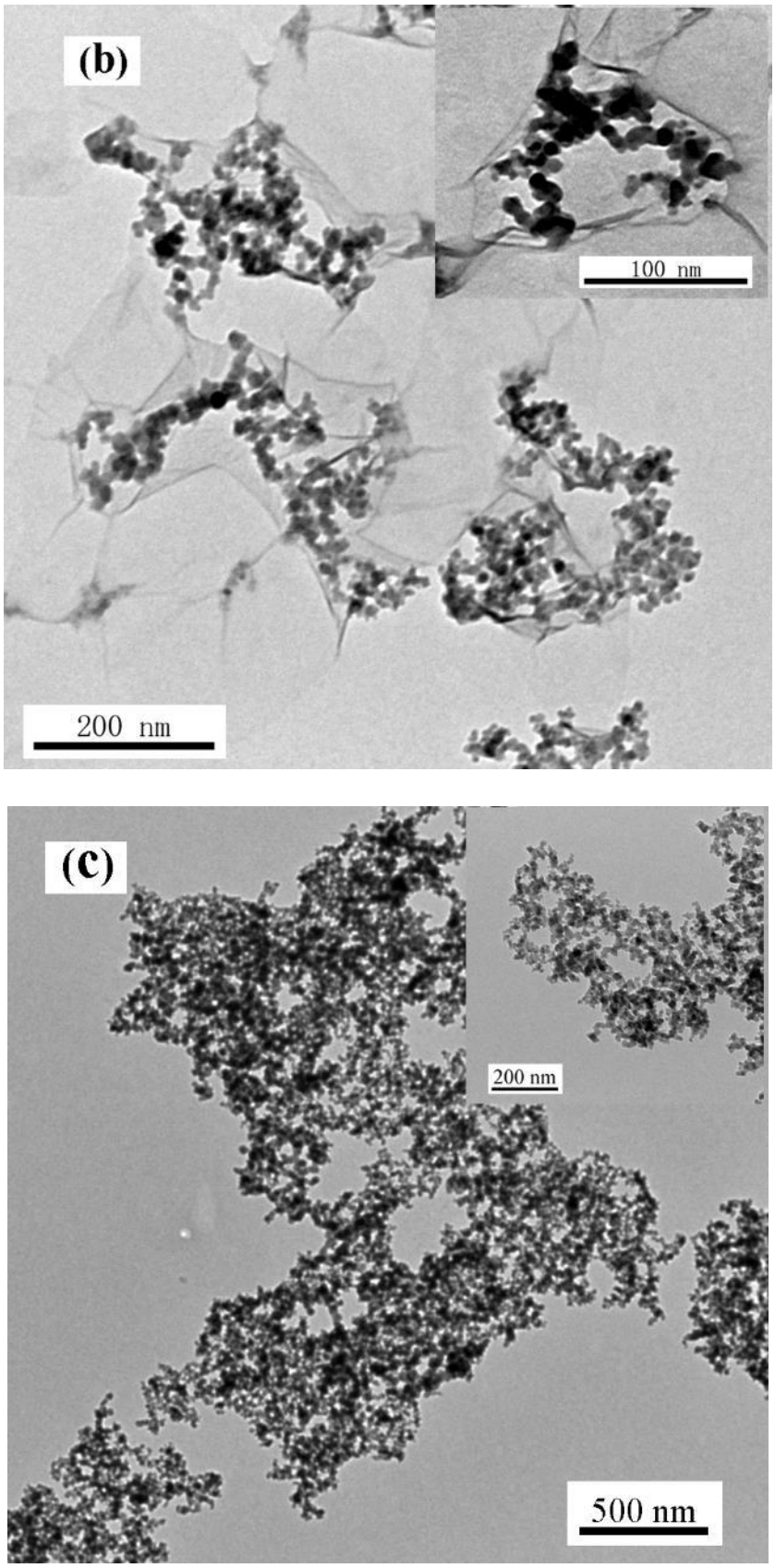

Figure 6 - 2 *The TEM images of the silica dispersed by different kinds of dispersants. (a) A specimen of PSS dispersed silica; and (b) Specimen of GO dispersed silica.*

The TEM images of a cross-section of specimens are shown in **Figure 6-3** to investigate the filler dispersion in the NR matrix further. The TEM images of pure silica particles distributed into NR latex with the casting process are shown in **Figure 6-3 (a)**, which showed SiO_2 severely agglomerated in the NR matrix with NR phase smooth and coherent. NR/PSS/SiO_2 nanocomposites shown in **Figure 6-3 (b)** present partly re-aggregated silica particles, seen as stick-like clusters surround the NR particles. The dispersion of silica particles with the help of GO was more even than observed from pure silica. As shown in **Figure 6-3 (c)**, GO/SiO_2 attaches to the surface of the NR particles in a similar way to AgNPs/RGO. The GO sheets partly cover the surface of the NR particles, preventing the spreading of the NR particles throughout drying procedures. Because the silica is dispersed as a monolayer on the GO sheet, SiO_2 shows better dispersion compared to the other two specimens.

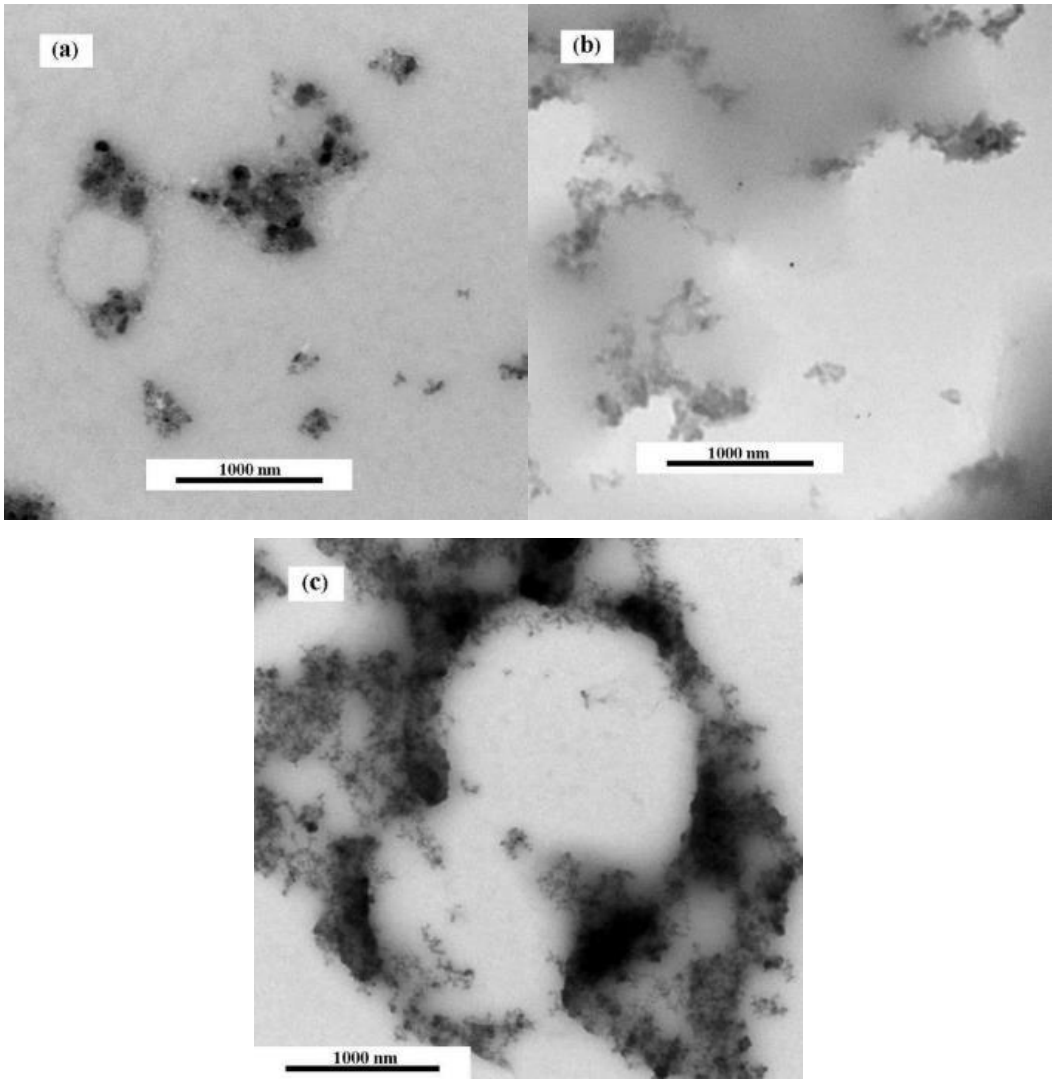

***Figure 6 - 3** The TEM images of (a) NR/SiO_2 nanocomposites, (b) NR/PSS/SiO_2 nanocomposites, and (c) NR/GO/SiO_2 nanocomposites.*

As shown in **Figure 6-4 (a)** the pure silica dispersed into NR matrix, which appears as re-aggregated. This re-aggregated part is essentially a defect in the NR nanocomposite (Leblanc 2002). As shown in **Figure 6-4 (b)**, the partially re-aggregated silica particles are observed in the NR matrix as a stick-like structure similar to the SiO_2/PSS as shown in **Figure 6-2 (b)**. More specifically, the PSS/SiO_2 filler system is stable in the NR matrix. Because the polarity of the fillers is reduced by mutual interaction through hydrogen, the new filler is more likely to have better compatibility with the NR matrix (Xu et al. 2015). The cross-section of the NR/GO/SiO_2 sample is shown in **Figure 6-4 (c)**, which is seen as NR particles covered by the GO/SiO_2 additive. The morphology of the GO/SiO_2 is steady in the NR matrix, and the re-aggregation of silica particles does not appear to be significant because of interactions between the GO and silica particles. The silica re-aggregation tendency is weaker in the GO/SiO_2 specimen as shown in **Figure 6-4**. A single layer of the silica particles attaches to the GO sheets dispersed into NR/GO/SiO_2 specimen, unlike the stick-like silica particles dispersed into NR matrix in the NR/PSS/SiO_2 specimen shown.

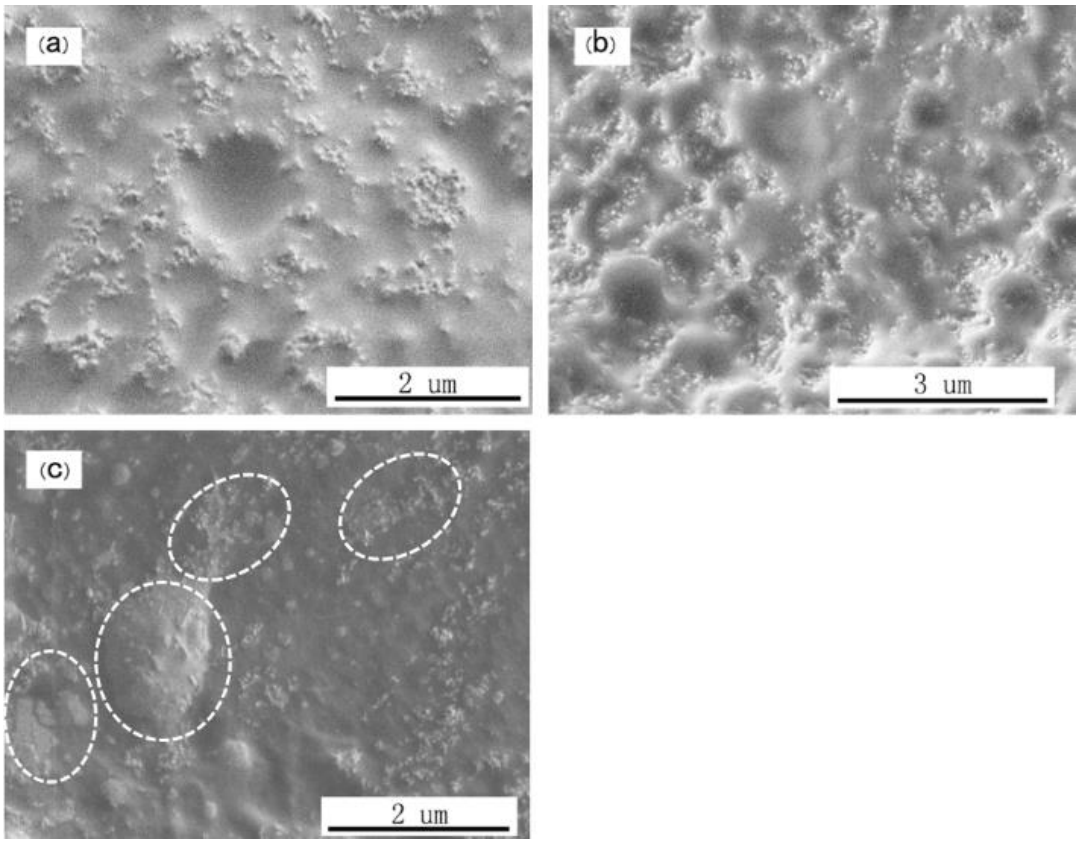

Figure 6 - 4 *The SEM images of cross-sections of NR nanocomposites materials. (a) Silica mixed into NR directly (NR/SiO_2), (b) PSS dispersed silica mixed into NR (NR/PSS/SiO_2), and (c) GO dispersed silica mixed into NR (NR/GO/SiO_2) in the side of the white circles are SiO_2/GO.*

6.2.4 Mechanical properties of NR composites

The mechanical properties of the specimens are listed in **Table 6-2**. The tensile strengths are all enhanced after loading with fillers, except the tearing strength of the control sample including NR/SiO_2 and NR/GO. The tearing strength of the NR/GO, at 7.16 KN/m was lower than that of the neat NR (7.18 KN/m), because of an XLD decrease after GO was loaded into the NR matrix. The tensile strength is controlled by the compatibility and interfacial adhesion between fillers and host materials (Hayeemasae & Ismail 2016). The compatibility between the silica and the NR molecular has been improved as SEM and TEM images show in **Figure** 6-2 and 6-3. Therefore, the tensile strength is significantly changed. The tensile strengths of the NR/GO/SiO_2 and NR/PSS/SiO_2 were 4.53 and 3.63 MPa, respectively. The GO and PSS modified specimens were much higher than the NR/SiO_2 nanocomposites. This situation occurred because the compatibility of the filler was enhanced, and the NR molecules could attach to the surfaces of layered sheets (Gao et al. 2013; Liu et al. 2011). The tearing strength of NR/PSS/SiO_2 is larger than that of NR/GO/SiO_2. This performance can be explained by the XLD of NR/PSS/SiO_2, which is higher than that of NR/GO/SiO_2. The tearing strength is controlled by the cross-linked density (Sinha Ray & Okamoto 2003). It shows the physical cross-linked densities are quite similar as **Table** 6-1 shows, which induced the tearing strength is quite similar. The tearing strength of the NR/SiO_2 was decreased because of the agglomerated defects in the NR nanocomposites (Sinha Ray & Okamoto 2003). The M_{100}, M_{200}, and M_{300} of NR nanocomposites without added GO were enhanced compared to neat NR. 1 phr of GO loading GO caused the changes to M_{100}, M_{200}, and M_{300} (Luo et al. 2014). Because the GO sheets prevent the NR particles from sprawling as TEM confirmed the less physical crosslink are established. However, the M_{500} of NR/GO/SiO_2 specimen appeared to increase rapidly to 0.79 MPa, because of the GO sheets leading the strain-induced crystallisation of NR nanocomposites during the large elongation. (Ali et al. 2013; Salaeh et al. 2014) The data of elongation at break is also confirmed by XLD. The specimen with a larger elongation at break showed a higher XLD value.

Table 6 - 2 *The mechanical performances of NR, and NR nanocomposites*

Specimen	Tensile strength (MPa)	Tear strength (KN/m)	Modulus(MPa)			Elongation at break %
			100%	300%	500%	
NR	1.85	7.18	0.54	0.62	0.70	855
NR/GO	1.89	7.16	0.49	0.56	0.71	850
NR/PSS	1.86	7.19	0.55	0.63	0.73	849
NR/SiO_2	3.17	6.92	0.62	0.68	1.09	714
NR/PSS/SiO_2	3.63	7.35	0.79	0.87	1.34	696
NR/GO/SiO_2	4.53	7.33	0.43	0.49	0.79	758

6.3 Interpenetrating network for mechanical reinforcement of modified graphene filled NR nanocomposites

Porous RGO was prepared using the etching of GO sheet with $KMnO_4$ assisted by a microwave oven. Fan reported that $KMnO_4$ could etch carbon on the graphene as the following scheme (Fan et al. 2012):

$$4MnO_4^- + 3C + H_2O \leftrightarrow 4MnO_2 + CO_3^{2-} + 2HCO_3^- \quad (6\text{-}1)$$

In this reaction, carbon acts as a reducing agent converting $KMnO_4$ to MnO_2 (Yan et al. 2010). Theoretically, an atom in perfect graphene has no chemoselective. However, the defective sites of graphene presented higher chemical reactivity, including oxygen groups will react first (Li et al. 2009; Cao et al. 2010; Li et al. 2010). Therefore, the GO is used as a raw material to prepare porous graphene, with oxygen groups and dangling bonds joining the reaction first to protect the graphene C=C network. Pores with a radius of approximately 2.5 nm are etched on the RGO sheets. These etched sheets are then loaded into the NR matrix to build an interpenetrating polymer network for mechanical reinforcement.

6.3.1 Characterisation of porous graphene

Different output power levels on the microwave were used to vary the radii of pores, irradiation at 700 W, 384 W, and 119 W for 5 min. The specimens were labeled as Lp-RGO, Mp-RGO, and Sp-RGO, respectively. The TEM image of each specimen is shown in **Figure 6-5**. The analysis reveals that Lp-RGO is not suitable for filling into NR matrix, because the 2D structure of graphene has already been altered, as shown in **Figure 6-5 (a)**, and **(b)**. After removal of one or several carbon atoms from the edge, the reconstruction of the edges of the graphene sheets occurred, resulting in a stable

zigzag re-configuration (Girit et al. 2009). When large numbers of carbon atoms were reconstructed, the whole RGO plane was twisted as shown in **Figure 6-5 (a)**, and **(b)**. The morphology of Lp-RGO is converted from a 2D material to an activated-carbon-like material, which cannot be used as a graphene filler in NR matrix.

As shown in **Figure 6-5 (c)**, **(d)**, the Mp-RGO sheet structure had pores throughout the sheet with an average diameter of 5.25 nm (radius is 2.63 nm). As shown in **Table 6-3**, the average diameter of the pores on Sp-RGO is 2.71 nm (radius is 1.36 nm). Hence, increasing the output power of the microwave oven lead to an increase in the diameter of pores in porous RGO. Based on the electrical conductivity of the C=C network on the GO sheets, GO is rapidly heated by microwave radiation through vortex currents (Voiry et al. 2016; Chaban & Prezhdo 2017). This increase can be attributed to the output power, which dictates the temperature of the reaction system. In addition, the distribution of diameter of porous GO became broader as the output power of the microwave oven was increased, because the high energy level reduced the selectivity of the oxidation reactions.

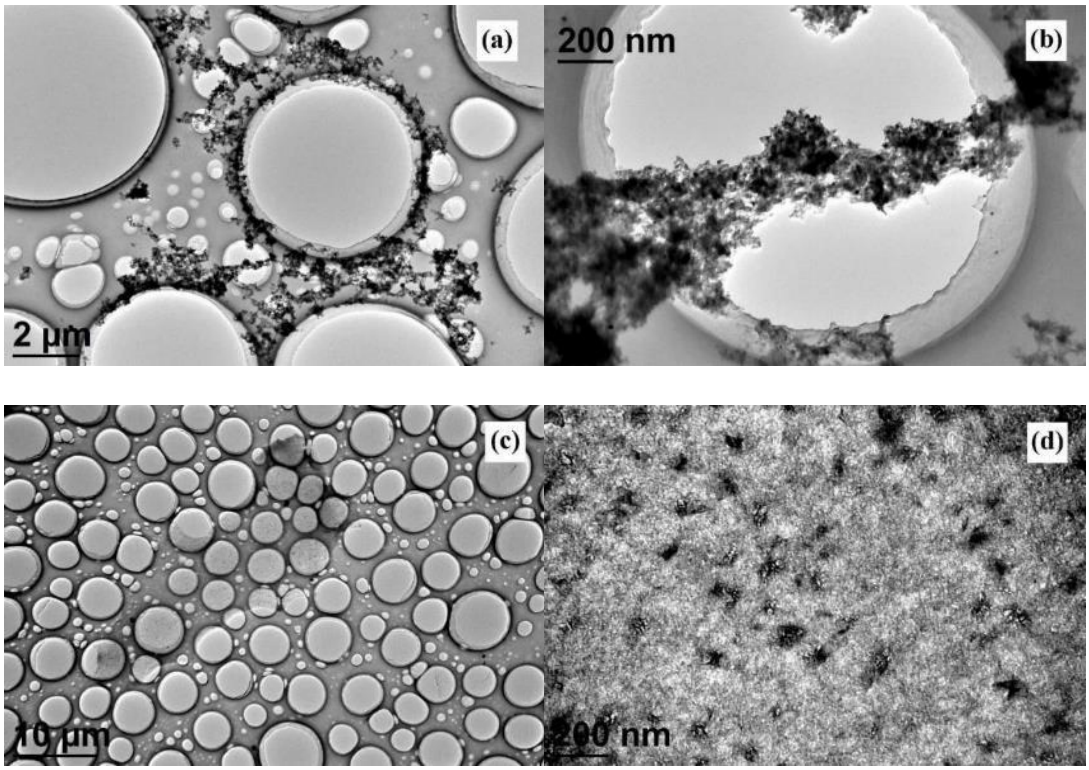

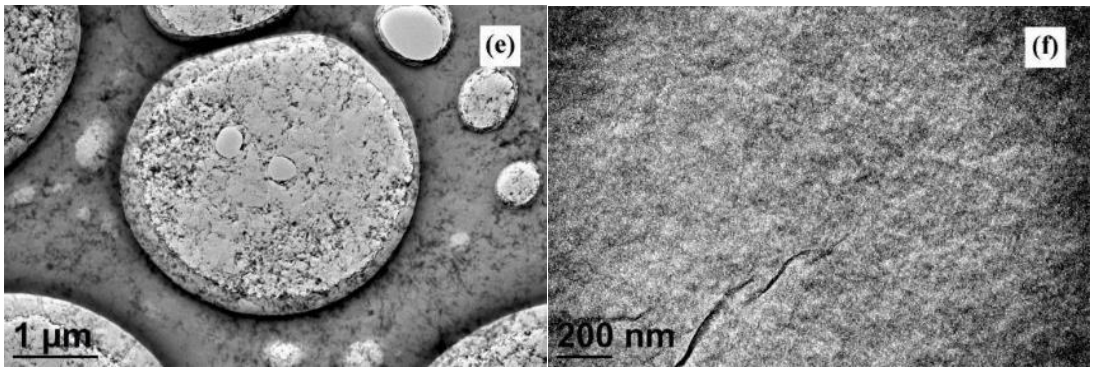

Figure 6 - 5 *The TEM image of porous graphene (a), and (b) are the TEM images of Lp-RGO; (c), and (d) are the TEM images of Mp-RGO; (e), and (f) are the TEM images of Sp-RGO.*

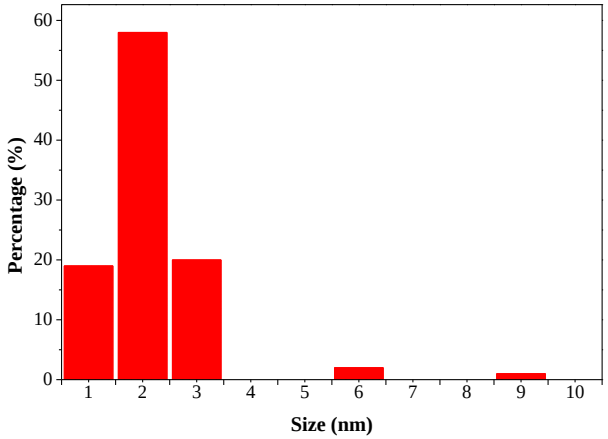

Figure 6 - 6 *The pore diameter distribution of Sp-RGO.*

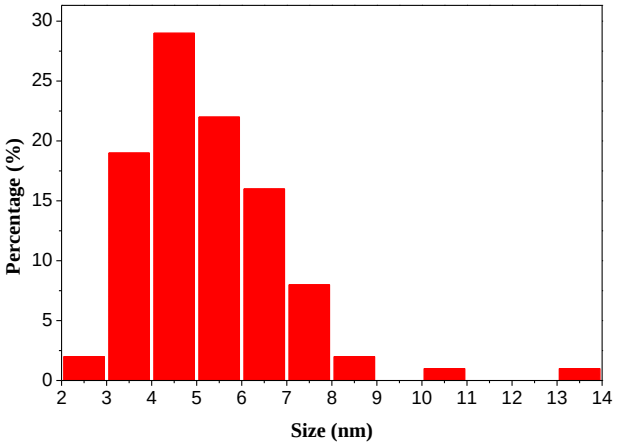

Figure 6 - 7 *The pore diameter distribution of Mp-RGO.*

Table 6 - 3 *The diameter parameters of Mp-RGO, and Sp-RGO obtained from TEM image by Image-J*

Specimens	Mean size (nm)	Standard deviation	Min size (nm)	Max size (nm)
Mp-RGO	5.25	1.63	2.78	13.05
Sp-RGO	2.71	1.02	1.55	9.42

The BET method was employed to reveal the pore radii of porous RGO as shown in **Figure 6-8** using the BJH pore size distribution method. The mean radius of the pores on Mp-RGO was 2.73 nm. The radius of pores on Sp-RGO was 1.66 nm. The BET results agree with the values calculated from TEM images. To form an interpenetrating polymer network between the porous RGO and NR matrix, a terminal of an NR molecule has to penetrate through the pores of the porous RGO. Therefore, the average size of the pores should be larger than at least one terminal on the NR molecule. There are two terminals in the NR molecule. One end is the initiating terminal (ω-terminal), and the other end is an α-terminal as explored in Chapter 2. Because the structure of ω-terminal still has not been identified, the α-terminal will be the focus of this section (Gent & Cho 1999; Wu et al. 2017). The α-terminal is assumed to be a phospholipid with two added isoprenes to facilitate the experiment. The structure was drawn by Materials Studio 2017, and space structure obtained by optimum structure function in the Forcite Modules as shown in **Figure 6-9**. Considering the Connolly surface, the length of the α-terminal design in this investigation is approximately 2.34 nm. Consequently, Sp-RGO is not suitable for building an interpenetrating NR network because of a large number of pores smaller than 2 nm in diameter. Mp-RGO is the final chosen additives to enhance tensile strength.

The Raman spectrum of Mp-RGO is shown in **Figure 6-10**, revealing that the ratio of I_D/I_G is 1.52 larger than that of GO (8.25 Å given in Chapter 5). The porous structure inducing a large number of holes increase the ratio of I_D/I_G.

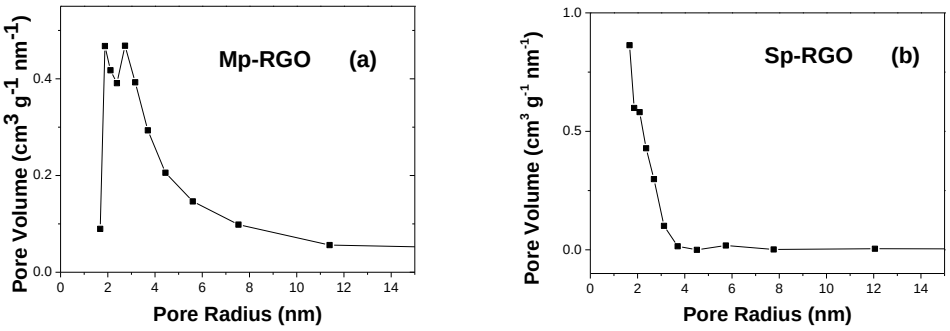

Figure 6 - 8 *Pore radius measured by BET (a) is pore radius of Mp-RGO, (b) is pore radius of Sp-RGO.*

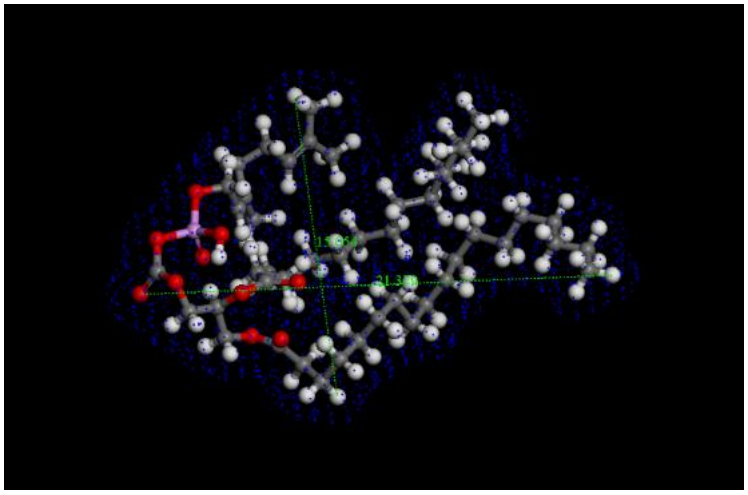

Figure 6 - 9 *The structure of α-terminal fabricated in Materials Studio. The grey atom is carbon, the white atom is hydrogen, the red one is oxygen, the purple one is phosphorus, and the blue dote is the edge of Connolly surface.*

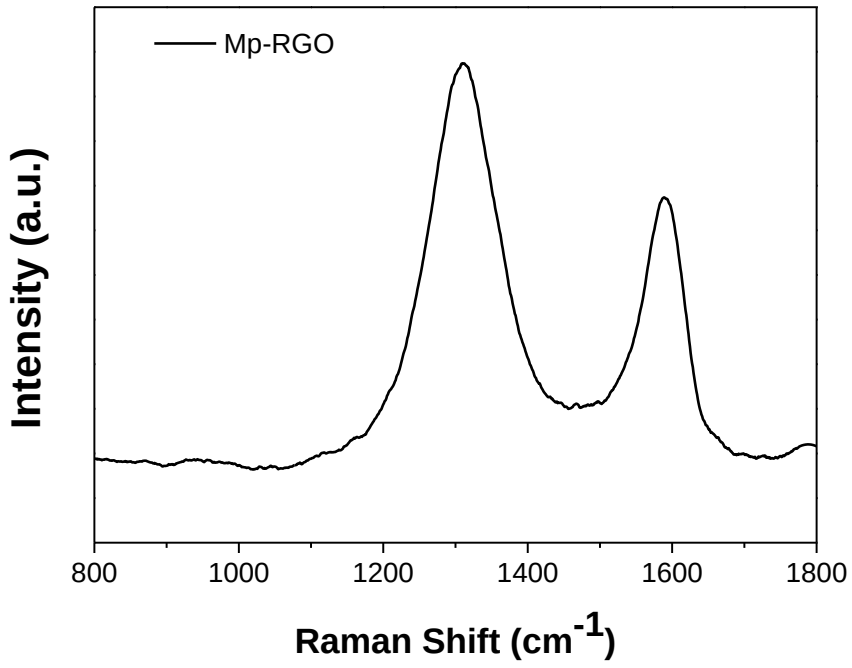

Figure 6 - 10 *The Raman spectrum of Mp-RGO.*

6.3.2 Mp-RGO filled NR nanocomposites

6.3.2.1 Morphology of Mp-RGO filled NR nanocomposites

The graphitisation and dispersion of RGO directly limited the enhancement of mechanical properties (Zhan et al. 2011). The TEM image of a cross-section of the NR nanocomposites is shown in **Figure 6-11**, which indicated that the Mp-RGO and control group all appeared well dispersed and had no obvious graphitisation. It is obvious that the high-density and low-density regions are shown in **Figure 6-11 (a)**. The region with a high density of Mp-RGO (dark) surrounds the Mp-RGO sheets, and the low-density region (bright) is neat rubber only. However, in **Figure 6-11 (c)**, it can be seen that the density of NR evenly dispersed, shows the RGO sheets. Mp-RGO loaded in the NR matrix has been magnified**,** shown in **Figure 6-11 (b)**. The colour of NR surrounding Mp-RGO is obviously deepened, which indicated that the stronger combined interactions are present at the interfacial of Mp-RGO and NR than the one in RGO/NR specimen (He et al. 2015). Therefore, the high-density region of NR surrounded Mp-RGO sheet. He reported that when RGO was filled into the epoxidized NR matrix because of the strong interconnection between RGO and epoxidized NR,

the motion of the epoxidized NR molecular chain is retarded forming a high-density interfacial region in the vicinity of the RGO sheets (He et al. 2015).

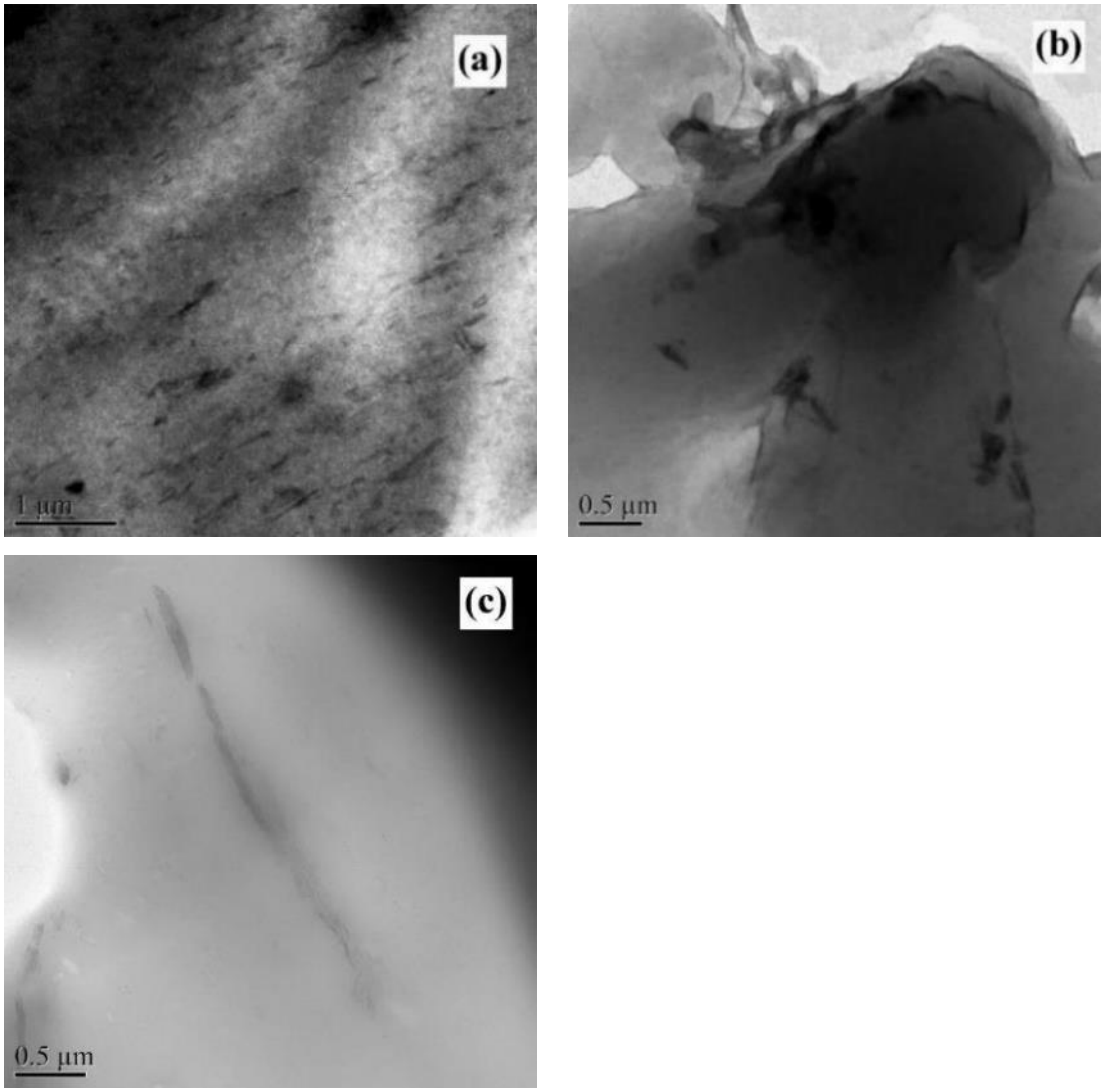

Figure 6 - 11 *The TEM images of NR nanocomposites. (a), (b) are the cross section of 1 phr Mp-RGO filled NR nanocomposites, (c) is the 1 phr RGO filled NR nanocomposites.*

The cross-section of the RGO/NR nanocomposites is smoother than Mp-RGO loaded specimen as SEM image shown in **Figure 6-12**. Under a high magnification of a cross-section of RGO/NR as shown in **Figure 6-12 (b)**, the surface of RGO appears to be wrinkle and smooth. Meanwhile, the surface of the Mp-RGO was covered by a fish scale rough layer of NR as shown in **Figure 6-12 (d)**, indicating a strong interconnection interaction between Mp-RGO and NR was constructed. The strong

interaction between the filler and host polymer indicated a potential of mechanical reinforcement (Tsagaropoulos & Eisenberg 1995; Wang 1998).

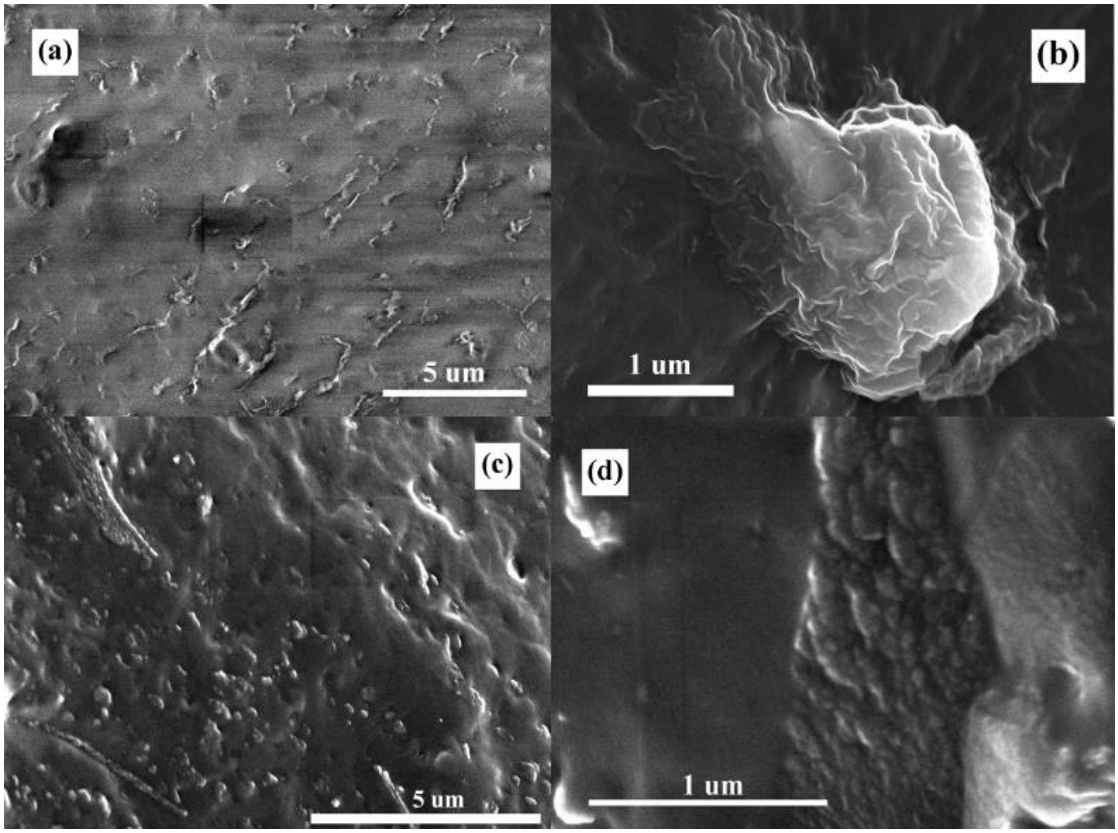

Figure 6 - 12 *The SEM image of the of NR nanocomposites. (a), (b) are the cross section of 2 phr RGO filled NR nanocomposites, (c), (d) are the 2 phr Mp-RGO filled NR nanocomposites.*

The XRD patterns show Mp-RGO/NR with different loading fractions to the evaluated dispersion of Mp-RGO as shown in **Figure 6-13**. The evidence peaks of Mp-RGO was observed that the peaks shift to a low angle, and peak position increased with increased loading of Mp-RGO. The details are given in **Table 6-4**. The distance between the neighbouring Mp-GO (Mp-GO is Mp-RGO before being reduced by hydrogen hydrate in the NR latex during latex mixing) is 8.92 Å, which is larger than the GO sheets. The Mp-GO is the product prepared from oxidized GO, which can be doped with more oxygen groups than GO and can be further oxidized deduce the integrity of graphene structure as shown in Raman, the reconstructive of graphene which disturbs the XRD value as well (Yu et al. 2017). The XRD pattern of Mp-RGO shows a broad peak located between 15^{o} and 35^{o}, which divided into two peaks one at 22.85^{o} (d value is

3.89 Å), and another at 26.43º (d value is 3.37 Å). The porous structure of Mp-RGO extended the distance between the neighbouring Mp-RGO layers from 3.35 Å (of defect graphite) to 3.89 Å because the pores reduce the integrity of the graphene layers as Raman measurements showed, which causes them to take up more space (Girit et al. 2009). Therefore, the distance of the neighbouring graphene sheets is a further extension.

Table 6 - 4 *The XRD peaks and corresponding parameters of the specimens*

Specimens	Peak position (º)	d value (Å)
GO	11.07	7.98
Mp-GO	9.90	8.92
0.5Mp-RGO/NR	5.37	16.40
1Mp-RGO/NR	6.17	14.30
2Mp-RGO/NR	6.37	13.80

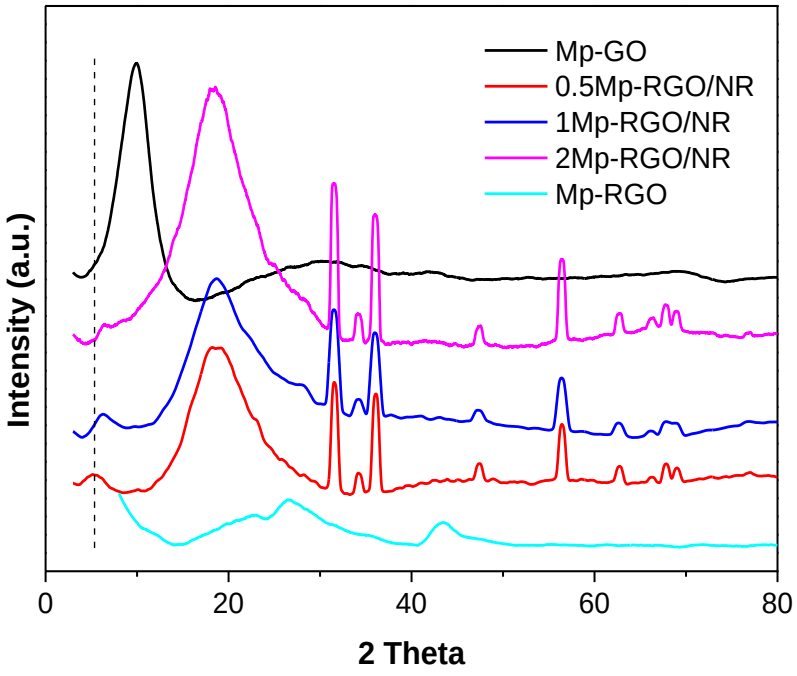

Figure 6 - 13 *The XRD patterns of Mp-RGO filled NR matrix under different content.*

The crosslink densities of Mp-RGO/NR nanocomposites are shown in **Table 6-5**. In the previous section, the barrier properties of RGO to reduce the physical crosslink

between the neighbouring NR particles has been discussed in the last section. The physical crosslink density and chemical crosslink density were all reduced with increasing amount of RGO loaded. The physical crosslink density of the Mp-RGO/NR nanocomposites decreased and were all lower than the neat NR. However, they were all higher than the corresponding RGO/NR nanocomposites specimens. The reason may be due to the NR molecule is partly penetrating through the pores on the Mp-RGO sheets under the high heating and the shearing force of the mechanical mixing procedure; it is well known that high temperature and shearing force can increase the mobilization of NR molecules. The chemical crosslink density showed a downward trend with increasing Mp-RGO content, but the gap between the RGO/NR and Mp-RGO/NR was enlarged with loading increased loading. In the 0.5 phr loading specimen, the chemical crosslink density of Mp-RGO/NR was 7.1% larger than RGO/NR. In the 1 wt.% loading specimen, the chemical crosslink density of Mp-RGO/NR was 19.5% larger than RGO/NR. Finally, in the 2 phr loading specimens, the chemical crosslink density of Mp-RGO/NR was 20.5% larger than RGO/NR. Theoretically, RGO and Mp-RGO have a similar chemical structure, namely a C=C frame reduced using $N_2H_4{\cdot}H_2O$. For a pure carbon skeleton to react with sulphur high pressure and high temperatures above 300 ^oC are required (Mattern 1984). Therefore, the differences in chemical crosslink density indicated that NR molecules penetrate the pores on the Mp-RGO sheets, increasing the connection between the neighbouring NR particles.

Theoretically, the volume of percolation can be regarded as the right concentration of Mp-RGO that ensures every NR particle is covered with a monolayer of Mp-RGO. This can be calculated with Equations 5-2 to 5-4 (Li & Shi 2012), which is approximately 0.51%. Because the experimental conditions are not perfect, the NR particles will re-aggregate, as shown in Chapter 5, so the theoretical percolation threshold values will decrease. 1 phr of Mp-RGO equal to approximately 0.4 vol. % near real threshold value of the NR particles surface all been covered by one layer of Mp-RGO. Double or triple layers of Mp-RGO will overlay when the loading amount of the MP-RGO larger than the threshold value (Zhao et al. 2014). When the two or more layers segregate appeared the connect between the neighbouring NR particles, the NR molecules cannot penetrate through multiple layers of porous graphene as easily as one layer. This phenomenon can explain the crosslink value decrease of 2Mp-RGO/NR. The 1Mp-RGO/NR is given the higher chemical crosslink than lower Mp-

RGO content could explain as NR molecule high efficiency partly penetrating through the pores on the RGO sheets because one layer of Mp-RGO is encapsulated the NR particles. The encapsulated NR particles can only penetrate through the pores to connect to neighbouring molecules after mechanical mixing and hot press. The pressure and sheared force in the mechanical mixing, and high temperature in the hot press as driving force.

To identify the impact of the hot press procedure to the formation of an interpenetrating network of porous graphene and NR molecules, the experiment was done through solution mixing instead of latex mixing integrating *into situ* reductions for masterbath, which is detailed in Chapter 3. The specimen was made by mixing NR with RGO, and a curing agent, and was labeled as 1RGO/NR-T, and the specimen made by mixing NR with Mp-RGO and a curing agent was labeled 1Mp-RGO/NR-T. The experiments are explored in detail in Chapter 3. Compared to the 1RGO/NR-T, and 1Mp-RGO/NR-T specimens, the physical crosslink density is similar, but the chemical crosslink density increases significantly in the 1Mp-RGO/NR-T specimen. The phenomenon indicated that the 150 ^{o}C increase the mobility of NR molecule to form an interpenetrating network between the NR and Mp-RGO.

Table 6 - 5 *The XLD of NR nanocomposites*

	Physical crosslink density (mol/cm^3)	Chemical crosslink density (mol/cm^3)
Neat NR	5.70×10^{-5}	11.37×10^{-5}
0.5RGO/NR	4.38×10^{-5}	10.05×10^{-5}
1RGO/NR	4.15×10^{-5}	9.33×10^{-5}
2RGO/NR	4.02×10^{-5}	7.89×10^{-5}
0.5Mp-RGO/NR	5.13×10^{-5}	10.76×10^{-5}
1Mp-RGO/NR	5.01×10^{-5}	11.15×10^{-5}
2Mp-RGO/NR	4.89×10^{-5}	9.51×10^{-5}
1RGO/NR-T	5.23×10^{-5}	3.92×10^{-5}
1Mp-RGO/NR-T	5.27×10^{-5}	5.21×10^{-5}

6.3.2.2 Mechanical reinforcement of Mp-RGO/NR nanocomposites

The vulcanisation parameters of the Mp-RGO/NR and RGO/NR nanocomposites with different amounts of filler loaded are shown in **Table 6-6**. It is reported that contents of graphene higher than 0.5 phr can observe vulcanisation-retarding effects because the vulcanisation reaction is controlled by two parts, a chemical reaction controlling stage, and a diffusion controlling stage. When the loading content of graphene is higher than 0.5 phr, the 2D structure of graphene blocks the diffusion of vulcanisation agents extending the scorch time and optimum curing time (Wu et al. 2013). The scorch time and optimum curing time extended with increasing amounts of add fillers, and the Mp-RGO groups were all shorter than the corresponding specimens of RGO group. The pores on graphene sheets can explain this phenomenon on the Mp-RGO sheets acted as mass transfer channel decreasing the time waste from the 2D structure of graphene frame.

Table 6 - 6 *The vulcanization parameters of Mp-RGO/NR, and RGO/NR nanocomposites with different fillers content*

	Neat NR	0.5RGO/NR	1RGO/NR	2RGO/NR	0.5Mp-RGO/NR	1Mp-RGO/NR	2Mp-RGO/NR
T_{10} (min)	3.2	4.1	4.6	4.4	3.9	4.5	4.9
T_{90} (min)	5.7	7.5	8.5	10.3	6.1	7.9	9.5

The mechanical properties of the NR nanocomposites prepared using different kinds of fillers and loading amounts are listed in **Table 6-7**. The tensile strength of RGO groups increased from 21.99 MPa to 24.00 MPa after 0.5 phr RGO was loaded as shown in **Figure 6-14**. The tensile strength and elongation at break of the RGO group decrease with increasing RGO content. Because the overlayed RGO sheets will appear after the loading amount of RGO higher than the encapsulated percolation threshold value. The interaction between the neighbour by graphene are weaker than the chemical bonds. Furthermore, the self-lubricating properties of graphene cause broken sites to appear (Dorri et al. 2015). The SEM image confirmed that a penetrating

network was constructed as shown in **Figure 6-12 (a)**, **(b)**. The tensile strength of the Mp-RGO is higher than that of RGO. The M_{100}, M_{300}, and M_{500} of 2Mp-RGO show a sharp increase, compared to neat NR by 81.4%, 400.0%, and 212.9%, respectively. The 2RGO/NR specimen showed increases of 67.1%, 217.1%, and 87.8%. The elongation at break of each specimen group decreased with increasing filler content as shown in **Figure 6-14**, because of the interaction between the filler and host polymer (Wang et al. 2017). Joseph reported that the ratio of M_{300} to M_{100} is indicated by reinforcement by filler in a vulcanizate the higher value indicated, the stronger reinforcement performed (Joseph et al. 2004). The values of M_{300}/M_{100} are listed in **Table 6-7**, which increased with an increase in filler content. The M_{300}/M_{100} value of 2Mp-RGO appears the highest in 6 specimens, which indicated a strong interaction between the Mp-RGO and NR molecules was constructed. This interaction between the Mp-RGO and NR molecules is attributed to the pores on the RGO sheets forming an interpenetrating network.

Table 6 - 7 *The mechanical properties of NR nanocomposites*

	M_{100} (MPa)	M_{300} (MPa)	M_{500} (MPa)	Elongation at break %	Max strength (MPa)	M_{300}/M_{100}
Neat NR	1.29	2.48	6.83	972	21.99	1.92
0.5RGO/NR	0.96	1.82	4.11	988	24.00	1.89
1RGO/NR	1.11	3.00	9.19	664	23.51	2.70
2RGO/NR	1.40	3.91	11.38	603	19.34	2.79
0.5Mp-RGO	1.96	3.54	6.79	1041	25.42	1.81
1Mp-RGO	2.03	6.46	18.04	681	29.84	3.18
2Mp-RGO	2.34	12.40	21.37	605	27.82	5.30

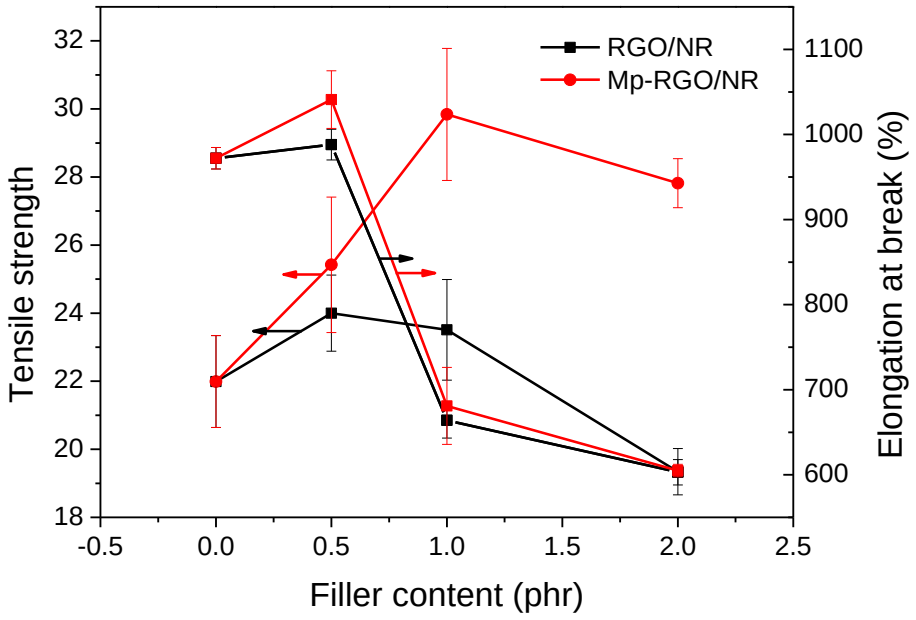

Figure 6 - 14 *The Tensile strength and elongation at break of the NR composites with different filler content.*

As shown in **Figure 6-15**, the storage modulus and damping factor (tan δ) as a function of temperature. The storage moduli of RGO/NR nanocomposites all approximately 2.2 GPa. However, the storage moduli are almost all lower than that of the neat NR because the bonds between the RGO sheets and the NR matrix are weak. The storage modulus of RGO is increased with RGO content increase because the modulus of RGO sheets is higher than that of neat NR and RGO/NR specimens. It is obvious that the storage modulus of Mp-RGO nanocomposites increased with increasing Mp-RGO content. The storage moduli of the Mp-RGO nanocomposites are all higher than the RGO/NR nanocomposites, and NR is indicating a stronger interaction between the Mp-RGO and NR molecules, which is confirmed by strength, TEM, and SEM images.

The tan δ value decreased as fillers were added, caused by the reduced mobilization of NR molecule chains during dynamic mechanical deformation. The tan δ values of the Mp-RGO group are all lower than the RGO group, which indicated that a stronger interaction between Mp-RGO and NR molecules was present compared to the RGO specimens. However, there are no further chemical reaction sites added into Mp-RGO than RGO. Therefore, the reduced NR chain mobility may be attributed to the NR molecules partly penetrating through the pores on the Mp-RGO sheets, confirming the

construction of an interpenetrating network. The *Tg* as shown in **Figure 6-15 (b)** changed with increasing content of the additives, as shown in **Table 6-8**. The *Tg* increased with an increasing fillers content, indicating a strong interaction between the filler and NR was formed, supporting mechanical reinforcement.

Table 6 - 8 *The Tg temperature of NR nanocomposites based on DSC test*

	Neat NR	0.5RGO/NR	1RGO/NR	2RGO/NR	0.5Mp-RGO/NR	1Mp-RGO/NR	2Mp-RGO/NR
Tg (^{o}C)	-62.60	-61.84	-61.47	-61.48	-61.62	-61.27	-60.75

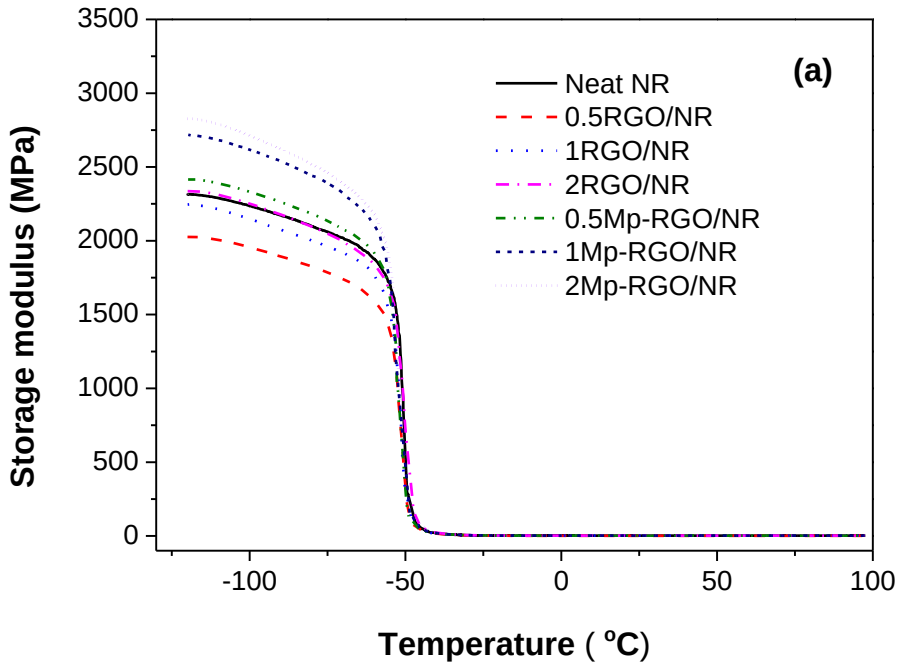

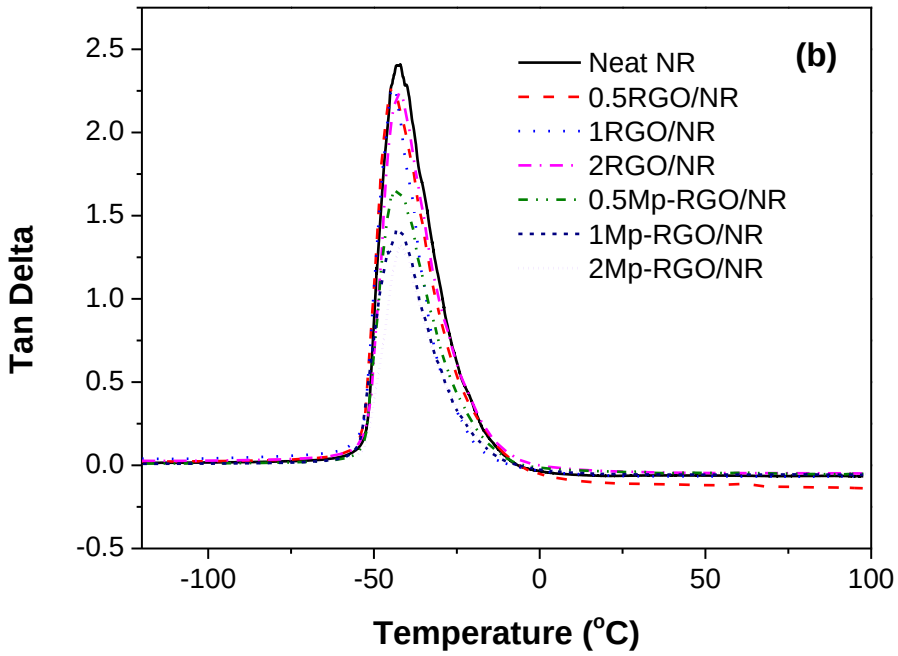

Figure 6 - 15 *The DMA temperature scans on the nanocomposites. (a) The storage modulus, and (b) loss factor as the function of temperature for neat NR and NR nanocomposites with different contents of RGO or Mp-RGO.*

6.3.2.3 MD simulation of α-terminals of NR molecules penetrating through the pores on the porous graphene

MD simulation is employed to further identify the construction of an interpenetrating network. The simulation result is given, as shown in **Figure 6-15**. Graphene possesses pores sized 2 nm, and 5 nm, and graphene modified with oxygen groups possess a pore size of 5 nm. The snapshots of 0 ps, 30 ps, 75 ps, and 85 ps, 480 ps, 915 ps, and 1000 ps of the α-terminals of NR molecules penetrating through the porous graphene with different structure in the simulation are shown in **Figure 6-15**. The α-terminals of NR molecules cannot penetrate through graphene sheet possessing only 2 nm pores during 0 to 1000 ps as shown in **Figure 6-15 (a)** to **(g)**. If the graphene possesses a pore size of 5 nm, the α-terminal of NR molecules can move closer to the porous graphene, and then some molecules penetrate through the pore at approximately 85 ps as shown in **Figure 6-15 (a')** to **(g')**. In the oxygen group modified graphene specimens with a pore size of 5 nm, the α-terminal of NR molecules favourite to move near the graphene surface and first time penetrate through the graphene on approximately 560 ps. After

1000 ps several NR α-terminals crawled along the pore and attached to the graphene surface as shown in **Figure 5-15 (a'')** to **(g'')**.

This computer simulation shows that the α-terminal of NR molecules cannot penetrate through the graphene with a pore of 2 nm within 1000 ps. However, the α-terminal of NR molecules can penetrate through the graphene with a pore of 5 nm within 1000 ps, surface oxygen groups can slow down the α-terminal of NR molecules penetrating through the 5 nm pores. However, the α-terminals of NR molecules are more likely to attach to the surface of the graphene sheets.

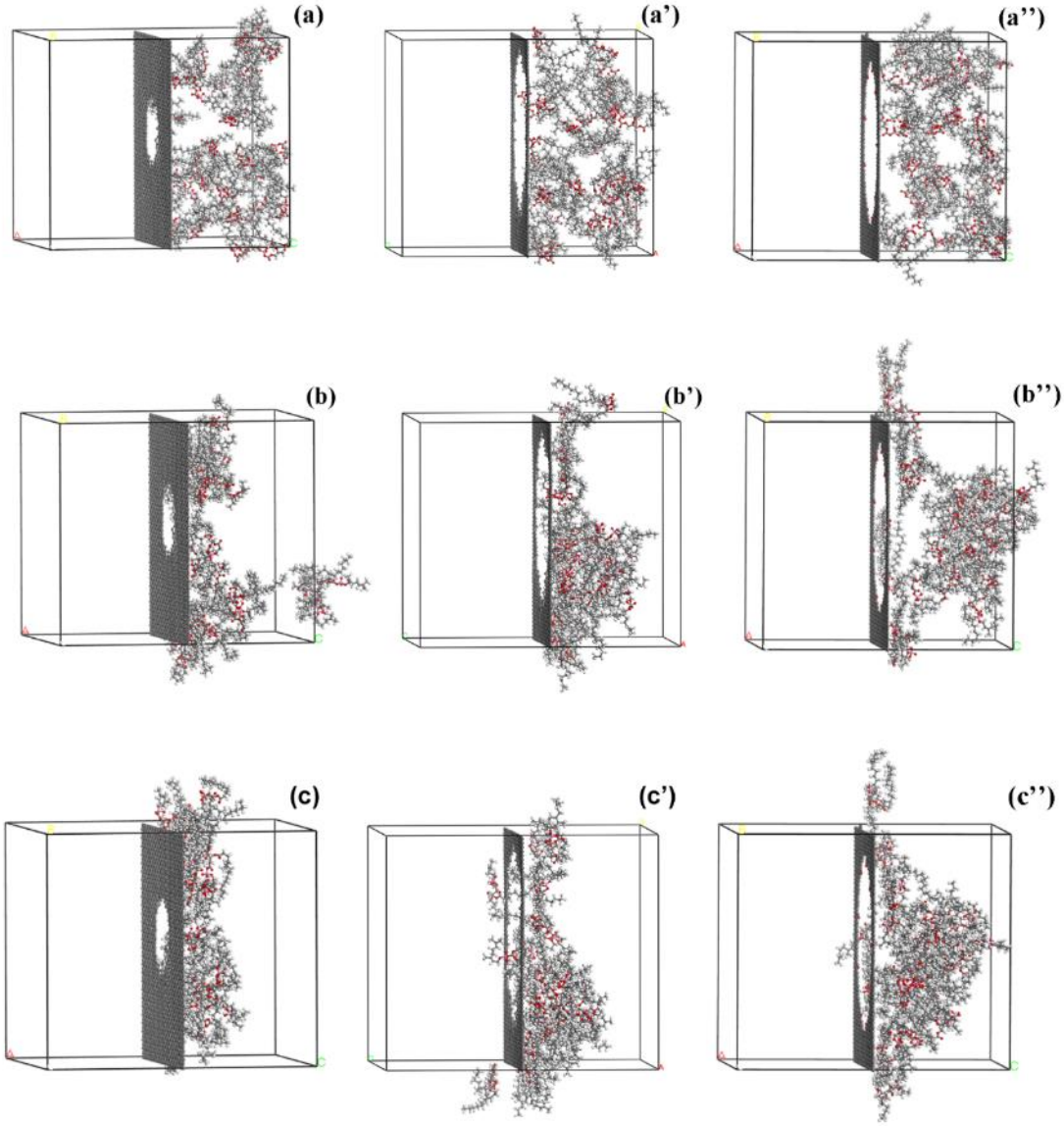

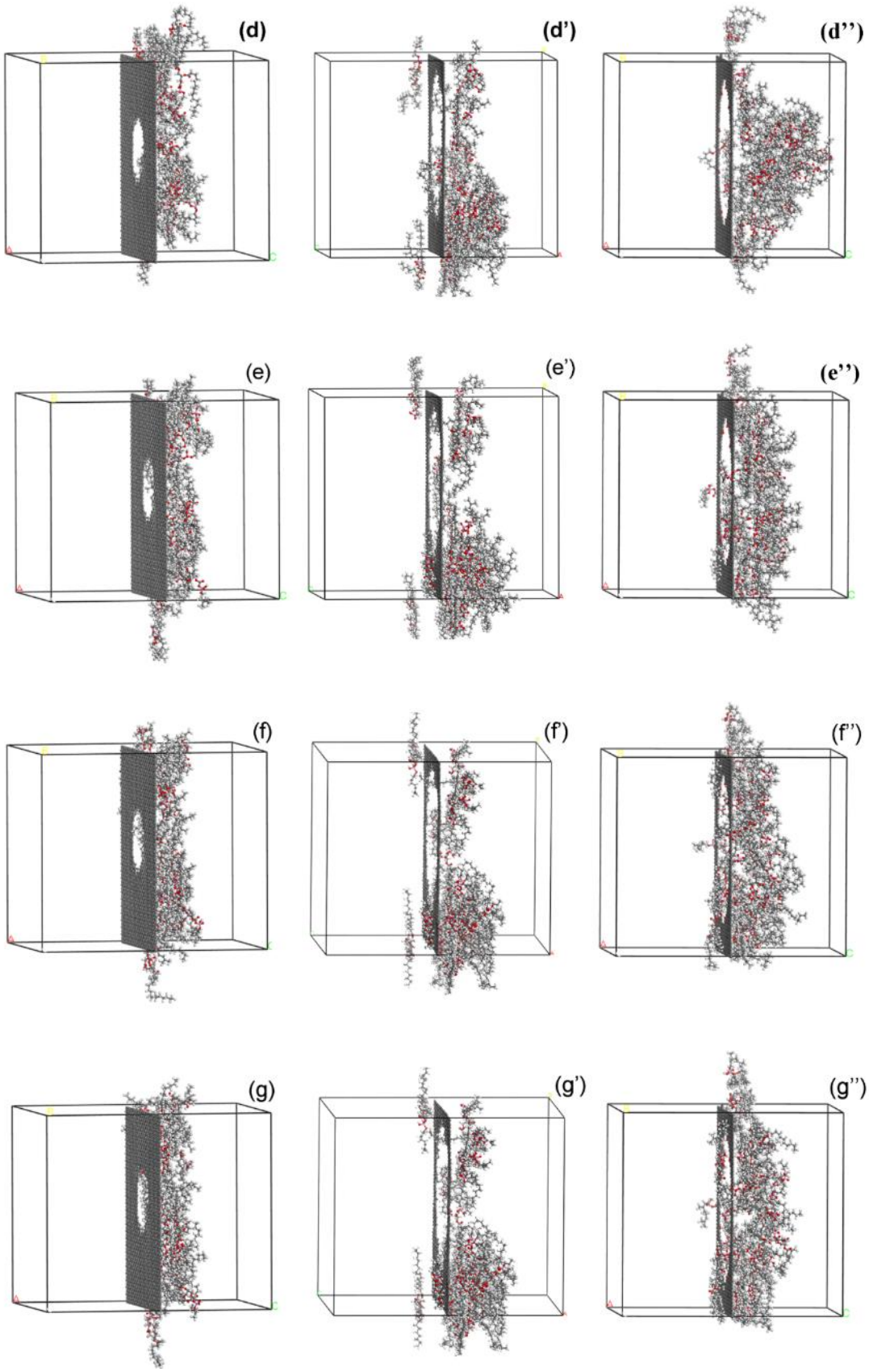

Figure 6 - 16 *Snapshots of α-terminals of NR molecules penetrating through the porous graphene with different structure in the simulation from 0 ps, 30 ps, 75 ps, 85 ps, 480 ps, 915 ps, 1000 ps. (a) to (g) are porous graphene with 2 nm diameter pore; (a') to (g') are porous graphene with 5 nm diameter pore; (a'') to (g'') are porous graphene with 5 nm diameter pore modified with oxygen groups.*

6.4 Concluding remarks

The mechanical reinforcement of NR nanocomposites was the focus of this chapter. The strategies used can be divided into two methods. First, GO is employed as a surfactant, dispersing silica into a monolayer in the NR matrix. Second, porous graphene is employed in the NR matrix to construct an interpenetrating network between the porous graphene and NR molecules.

In the first approach, the silica particles adsorbed on GO sheets and PSS molecules through hydrogen bonds. The PSS/SiO_2 acted as a stick-like filler loaded in the NR matrix. The GO sheets can readily absorb silica on their surfaces to prevent re-aggregation of silica and GO in the NR matrix. However, GO sheets block the physical crosslinking of the NR molecule.

In the second approach, Mp-RGO with an average diameter of approximately 5 nm is prepared using as a filler in the NR matrix for mechanical reinforcement. The tensile strengths of Mp-RGO/NR are higher than neat NR by 81.4%, 400.0%, and 212.9%, respectively on M_{100}, M_{200}, and M_{500} respectively, when 2 phr Mp-RGO was loaded. In addition, the tensile strength of 2Mp-RGO/NR is 67.1%, 217.1%, and 87.8% higher than the RGO/NR specimen with the same loading amount. The SEM, TEM, XLD, DMA, and computer simulation results confirmed strong interfacial interconnections between the Mp-RGO and NR molecules. The hypothesis of forming an interpenetrating network between the Mp-RGO and NR molecules is confirmed.

Chapter 7: Conclusion and recommendations

7.1 Conclusion

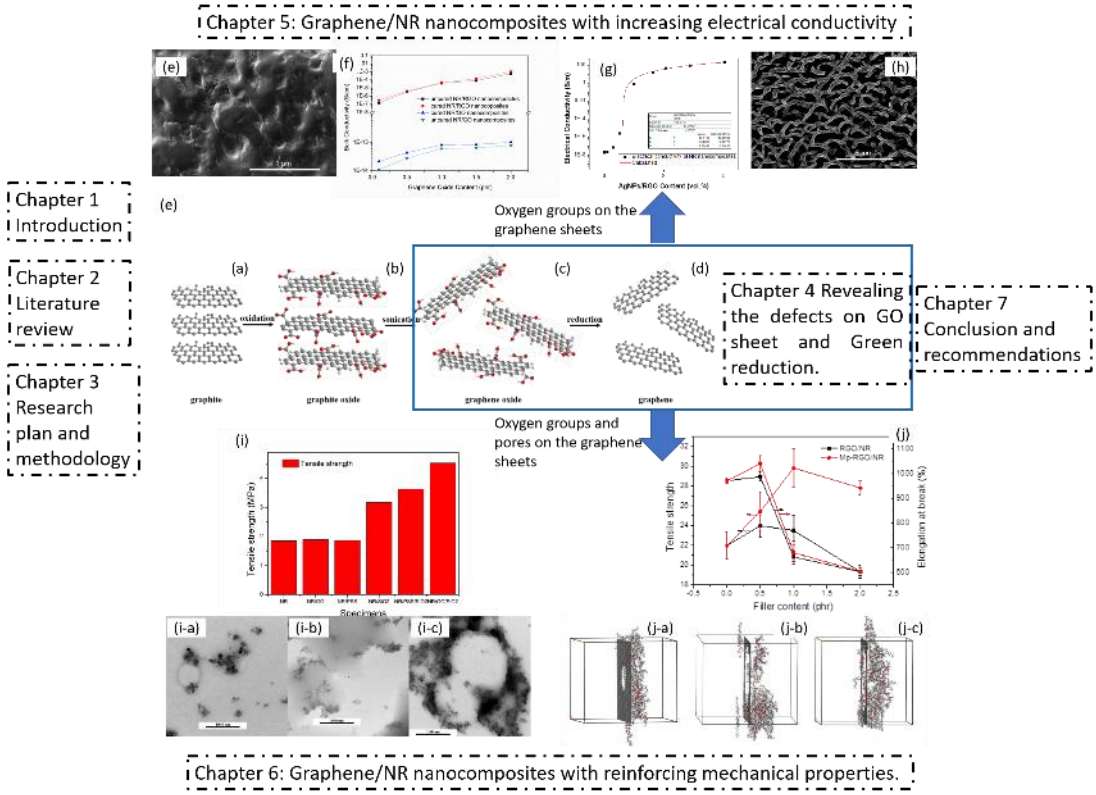

Figure 7 - 1 *The graphical abstract of this thesis.*

There are 7 chapters in this thesis. Chapter 1 is an introduction. Chapter 2 is a literature review. Chapter 3 is Research plan and methodology. Chapter 4 reveals the defects on GO sheets and green reduction. (a) graphite; (b) graphite oxide; (c) graphene oxide; (d) graphene. Chapter 5 is graphene/NR nanocomposites with increasing electrical conductivity. (e) SEM image of the cross-section of antistatic NR nanocomposites with 2 phr of GO. (f) The electrical conductivity of NR with unreduced GO, and RGO as a function of GO addition. (g) The electrical conductivity of AgNPs/RGO/NR as a function of AgNPs/RGO content. Insert table present the calculated parameters of classical percolation theory. (h) Calculated image from SEM image of NR matrix loaded with 2.03 vol.% AgNPs/RGO. Chapter 6 is graphene/NR nanocomposites with reinforcing mechanical properties. (i) The mechanical performances of NR, and NR nanocomposites. The TEM images of (i-a) NR/SiO2 nanocomposites, (i-b) NR/PSS/SiO2 nanocomposites, and (i-c) NR/GO/SiO2 nanocomposites. (j) The mechanical properties of RGO/NR and PG/NR nanocomposites. Snapshots of α-terminals of NR molecules penetrating through the porous graphene with different structure in the simulation 1000 ps. (j-a) is porous graphene with 2 nm diameter pore; (j-b) is porous graphene with 5 nm diameter pore; (j-c) is porous graphene with 5 nm diameter pore modified with oxygen groups. Chapter 7 is the conclusion and recommendations.

This thesis aimed to reveal the utility of defect sites on graphene sheets to increase the electrical conductivity and mechanical properties of NR composites as shown in **Figure 7-1**. The information of defect sites on GO has been studied first. Based on this information, GO was reduced by K_2CO_3 as a reusable reductant. The enhancement of electrical conductivity and strength are achieved through the study of the defect sites of the graphene.

The basic principle of the thesis is "in the polymer nanocomposites field, the inherent properties of nano-fillers to impart a specific function to the host polymer." After modifying the defect sites on graphene sheets using different methods, graphene with different properties have been developed which are used for the modifying the novel properties of NR composites. The key outcome of this investigation is to load modified graphene into an NR matrix for enhancement of electrical conductivity and strength. The electrical conductivity of AgNPs/RGO was 31000 S/m when loaded into NR matrix by electrostatic self-assembly and latex mixing approaches. The electrical conductivity of NR nanocomposites was increased to 196 S/m, with only approximately 4.03 vol.% AgNPs/RGO loaded. The mechanical reinforcement was realized by the formation of an interpenetrating network between the porous graphene and NR molecules. The moduli M_{100}, M_{200}, and M_{500} of porous graphene/NR nanocomposites increased by 81.4%, 400.0%, and 212.9% compared to neat NR with only 2 phr loading.

In Chapter 4, the structure of GO was revealed by XRD and positron studies, especially at defect sites. The defect on the GO and the graphite oxide are different types, which can be detected for integral graphite oxide and exfoliated graphene oxide, namely, the vacancy cluster and vacancy-oxygen complexes.

After revealing the defects on the GO sheets, a reduction method has been developed, and the mechanism was revealed. K_2CO_3 was employed as a green and reusable reductant. The mechanism of the reduction has two steps. Firstly, the ionic oxygen, generated from the electrochemical reaction, attached to the GO sheets reaction with an epoxy group and carbonyl groups open the epoxy groups to hydroxyl and removed carbonyl to carbon dioxide at 50 ^{o}C. Secondly, the hydroxyl and remaining epoxide groups were converted to carbonyl groups and finally oxygen groups removed as

carbon dioxide 90 ^{o}C. It is also observed that oxygen groups on the GO layers are not only aligned but randomly dispersed in some areas of graphene sheets.

In Chapter 5, the electrical conductivity of NR nanocomposites was investigated by two methods for different application. Although oxygen groups are defects on the graphene sheets, in this study, RGO is dispersed into the NR latex to attach to the surfaces of NR particles to form a current transfer route and, anchor the AgNPs on the RGO sheets all thanks to the existence of these oxygen groups.

The antistatic NR nanocomposites were prepared by a one-pot reaction in the NR latex under using an NR latex concentration of approximately 30 wt. %. The antistatic NR nanocomposites latex could be cast through dip coating methods. GO suspension mixed with a suitable concentration of the NR latex under vigorous stirring. GO attached to the surface of NR particles through hydrogen bonds, which were constructed using the oxygen groups on the GO and the polar groups on the NR surfaces. With the help of Vc, GO is reduced to RGO constructed current transfer routes to enhance the electrical conductivity of the NR matrix. The conductivity of the nanocomposites increased to 1.0×10^{-1} S/m, even with 2 phr of GO doping.

AgNPs was employed to modify the defect site on the graphene sheets improving the electrical conductivity of RGO sheets. Oxygen groups on the graphene sheets acted as an anchor for AgNPs growth. The hole or vacancy site had a higher energy level than the C=C frame and surrounding oxygen groups, leading to the AgNPs growth on the edge of these defects. When the size of the AgNPs is large enough, the defect will be covered AgNPs and formation of the charge transfer between AgNPs and RGO resulting the electrical conductivity of AgNPs/RGO increased to 31000 S/m. After preparation of the high electrical conductivity filler, AgNPs/RGO/NR nanocomposites with interconnected additive networks have been developed by electrostatic self-assembly and latex mixing approaches. The nanocomposites show a high electrical conductivity of 196 S/m, with a low electrical percolation threshold of approximately 0.63 vol. %.

In Chapter 6, the target of mechanically reinforcing NR nanocomposites was achieved. The defects on the graphene sheets were used in two ways. First, oxygen groups suspended from GO in the water, and converted graphene to a 2D surfactant. Second, etching pores with suitable size on the graphene sheets. These pores constructed mass

transfer route for a terminal of NR molecule penetrating through, which can form an interpenetrating network between the porous graphene and NR molecules.

SiO_2 loading into the NR/SiO_2 composites with GO and PSS as two different dispersants was investigated. The silica particles can be adsorbed on GO and PSS through hydrogen bonds with the polar groups. The GO sheet absorbed silica on the surface to prevent the aggregation of both GO and silica in NR matrix, to achieve the mechanical reinforcement.

$KMnO_4$ etching prepared the porous graphene under microwave irradiation. The porous graphene presented an average pore diameter of approximately 5 nm, loaded in the NR matrix by latex premixing, and mechanical mixing adding vulcanisation agent. The strength of Mp-RGO/NR is higher than the neat NR specimen by 81.4%, 400.0%, and 212.9% on M_{100}, M_{200}, and M_{500}, respectively, during only 2 phr of porous graphene loaded. 2Mp-RGO/NR is 67.1%, 217.1%, and 87.8% higher than the RGO/NR specimen with same loading amount. The hypothesis of the construction of an interpenetrating network between the porous graphene and NR molecules is confirmed using different characterizations.

7.2 Challenges

This research successfully prepared a series of RGO/NR nanocomposites that possess high electrical conductivity or mechanical reinforcement. However, in the research, two important challenges were encountered, i.e., (1) materials in the NR latex, and (2) carbon framework of the RGO made by the oxidation-reduction method.

7.2.1 The materials in the NR latex

In this research, the particles size of the NR particles presents different dimensions as discussed in Chapter 3, which could interrupt the formation of the fillers network. Theoretically, the volume fraction of percolation defined as the number of fillers covering sphere particles. The equations are shown below (Li & Shi 2012; Zhao et al. 2014):

Volume of sphere particles: $V = 4\pi R^3/3$ (7-1)

Theoretical volume percolation: $\varphi_{co} = (V_0/2V)100\% = (3h/2R)100\%$ (7-2)

Where R is the radius of sphere particles, V_o is the volume of filler and h is average thickness of filler.

The size of the NR particles has broad distribution from 40 nm to 2 μm as shown in **Figure 3-2**. The particles with small size contribute to the large theoretical volume percolation value, and the particles with big size give opposite contribution. However, the well-organized filler network can increase the electrical conductivity of the NR composites. Therefore, controlling the NR particles size should be focused to control the volume percolation value stable.

Moreover, the undefined materials in the NR latex apparent chemical reduction. In Chapter 5, size of AgNPs increased and re-aggregation when the AgNPs/RGO added into NR latex. These phenomena reduce the efficiency of the formation of current transfer route leading the percolation threshold value increase. Based on the equation 7-2, the volume of the filler particles increase can induce a negative effect on the volume percolation value.

7.2.2 The carbon frame of RGO made by oxidation-reduction method

In this research, defects including oxygen groups and vacancies are studied. However, the carbon frame of graphene who undertaken all the defect is ignored most of the time. When altering the type and amount of the defects, the atomic structure, electronic cloud structure, and the energy structure are all changed. The non-planar structure of graphene can affect all the properties of the composites. As shown in **Figure 4-7 a**, the large amount of C-C single bonds are present on the GO sheets. The C-C bond present in the graphene sheet could induce in a stable zigzag re-configuration (Girit et al. 2009). The graphene sheets unravel under this condition, which will expend more graphene sheets to cover the NR particles leading to increasing the volume percolation value. Furthermore, the researchers investigate the different structure of graphene affect the mechanical properties of the composites as well (Li et al. 2017).

7.3 Recommendation for future research

Based on the outcome and the challenges of this investigation undertaker in this thesis and issues that noticed related to the graphene and NR, there are at least two areas that require further investigation, as recommended in the following section, before graphene/NR can be fully used in the application.

7.3.1 Investigation detail of NR

The preparation of the NR latex with narrow NR particles size distribution, which influences the matrix of fillers and NR. This will limit the properties of the final products. Neat NR product in different batch shows different physical properties, as discussed in Chapter 3. The particles size has the same situation, as the **Figure 7-2** shows. The average particle size D50 is 0.619 μm of diameter with one broad peak distribution of this fresh NR latex sample. Therefore, the physical parameters should be given whenever you use NR or its derivative product. When research do experiments in the future, they should think about how to control these parameters. Take particles size for example. The specific strain of Hevea brasiliensis with the same age, same climate, same soil structure, and same cultivation habit could get similar particles distributions. The centrifugation is an effective technic in the size control. However, when you use centrifugation to the NR latex, the surfactant has to be added to prevent the coagulated. Whether this surfactant will disturb your future experiments and how to remove them are tough questions to be answered.

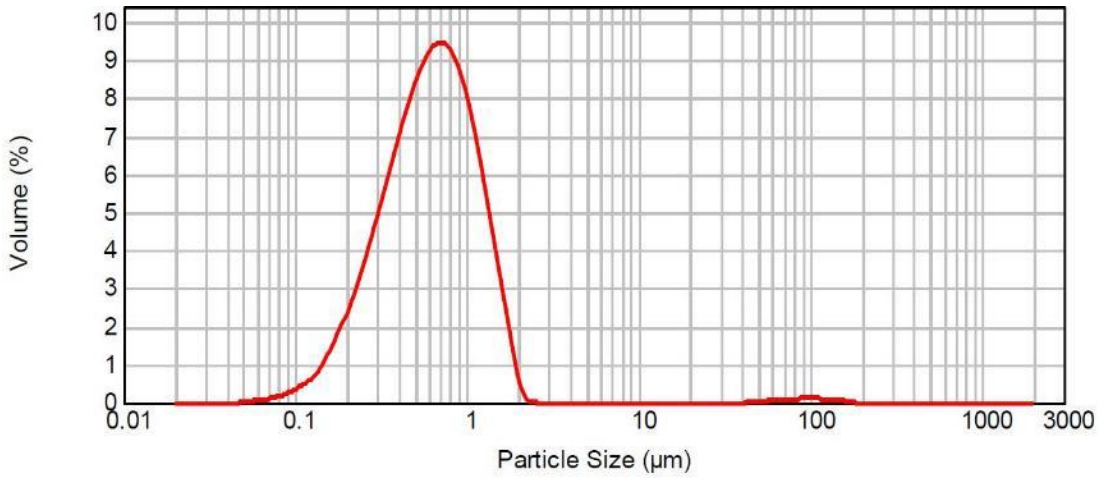

Figure 7 - 2 *The particle size distribution of NR latex based on the fresh NR latex including the one collected from* ***Figure 2-1****.*

In addition, the accurate structure of NR and non-rubber materials should be developed including molecular weight, molecular structure, the condensed state structure under different manufacturing process, chemical activity, which will all influence the interaction between NR and fillers to perform different properties.

7.3.2 Investigation structure of RGO

The unique physical properties of graphene are strongly dependent on its structural integrity. However, the RGO with different deformation structures of each preparation method should be the focus of researchers who want to use it. The RGO prepared by different methods has different types, and numbers of defects resulting from the RGO have a variation of structures. The physicochemical properties of RGO should be different based on the variation of the deformation structure. The deformation of the graphene frame can change the interfacial behaviour of the molecule nearing its surface leading to the final products process different properties as well. Size of graphene can be controlled relatively easily, and the enhancement of modulus is strongly dependent on the size of incorporated graphene. The small sheet size provides the maximum reinforcement effect compared to a large one (Wu et al. 2015). Whether other defects will induce the same result can be considered for future studies.

References

Abdelkader, AM, Vallés, C, Cooper, AJ, Kinloch, IA & Dryfe, RAW 2014, 'Alkali Reduction of Graphene Oxide in Molten Halide Salts: Production of Corrugated Graphene Derivatives for High-Performance Supercapacitors', *ACS Nano*, vol. 8, pp. 11225-33.

Aghigh, A, Alizadeh, V, Wong, HY, Islam, MS, Amin, N & Zaman, M 2015, 'Recent advances in utilization of graphene for filtration and desalination of water: A review', *Desalination*, vol. 365, pp. 389-97.

Aguilar-Bolados, H, Yazdani-Pedram, M, Brasero, J & Lopez-Manchado, MA 2015, 'Influence of the surfactant nature on the occurrence of self-assembly between rubber particles and thermally reduced graphite oxide during the preparation of natural rubber nanocomposites', *Journal of Nanomaterials*, vol. 16, no. 1, pp. 1-7.

Aguilar-Bolados, H, Yazdani-Pedram, M, Contreras-Cid, A, Lopez-Manchado, MA, May-Pat, A & Aviles, F 2017, 'Influence of the morphology of carbon nanostructures on the piezoresistivity of hybrid natural rubber nanocomposites', *Composites Part B-Engineering*, vol. 109, pp. 147-54.

Ates, M, Bayrak, Y, Yoruk, O & Caliskan, S 2017, 'Reduced graphene oxide/Titanium oxide nanocomposite synthesis via microwave-assisted method and supercapacitor behaviors', *Journal of Alloys and Compounds*, vol. 728, no. Supplement C, pp. 541-51.

Balandin, AA, Ghosh, S, Bao, W, Calizo, I, Teweldebrhan, D, Miao, F & Lau, CN 2008, 'Superior Thermal Conductivity of Single-Layer Graphene', *Nano Letters*, vol. 8, no. 3, pp. 902-7.

Banhart, F, Kotakoski, J & Krasheninnikov, AV 2011, 'Structural Defects in Graphene', *ACS Nano*, vol. 5, no. 1, pp. 26-41.

Becerril, HA, Mao, J, Liu, Z, Stoltenberg, RM, Bao, Z & Chen, Y 2008, 'Evaluation of Solution-Processed Reduced Graphene Oxide Films as Transparent Conductors', *ACS Nano*, vol. 2, no. 3, pp. 463-70.

Berger, C, Song, Z, Li, T, Li, X, Ogbazghi, AY, Feng, R, Dai, Z, Marchenkov, AN, Conrad, EH, First, PN & de Heer, WA 2004, 'Ultrathin Epitaxial Graphite: 2D Electron Gas Properties and a Route toward Graphene-based Nanoelectronics', *The Journal of Physical Chemistry B*, vol. 108, no. 52, pp. 19912-6.

Bo, X, Li, M, Han, C & Guo, L 2013, 'The influence of boron dopant on the electrochemical properties of graphene as an electrode material and a support for Pt catalysts', *Electrochimica Acta*, vol. 114, no. Supplement C, pp. 582-9.

Bolotin, KI, Sikes, KJ, Jiang, Z, Klima, M, Fudenberg, G, Hone, J, Kim, P & Stormer, HL 2008, 'Ultrahigh electron mobility in suspended graphene', *Solid State Communications*, vol. 146, no. 9-10, pp. 351-5.

Boukhvalov, DW & Katsnelson, MI 2008, 'Chemical Functionalization of Graphene with Defects', *Nano Letters*, vol. 8, no. 12, pp. 4373-9.

Brodie, BC 1860, 'Sur le poids atomique du graphite', *Ann. Chim. Phys.*, vol. 59. pp. 466-72.

Bunch, JS, Verbridge, SS, Alden, JS, van der Zande, AM, Parpia, JM, Craighead, HG & McEuen, PL 2008, 'Impermeable Atomic Membranes from Graphene Sheets', *Nano Letters*, vol. 8, no. 8, pp. 2458-62.

Cai, W, Zhong, H & Zhang, L 1998, 'Optical measurements of oxidation behavior of silver nanometer particle within pores of silica host', *Journal of Applied Physics*, vol. 83, no. 3, pp. 1705-10.

Candau, N, Laghmach, R, Chazeau, L, Chenal, J-M, Gauthier, C, Biben, T & Munch, E 2015, 'Temperature dependence of strain-induced crystallization in natural rubber: On the presence of different crystallite populations', *Polymer*, vol. 60, no. Supplement C, pp. 115-24.

Carbonell-Sanromà, E, Brandimarte, P, Balog, R, Corso, M, Kawai, S, Garcia-Lekue, A, Saito, S, Yamaguchi, S, Meyer, E, Sánchez-Portal, D & Pascual, JI 2017, 'Quantum Dots Embedded in Graphene Nanoribbons by Chemical Substitution', *Nano Letters*, vol. 17, no. 1, pp. 50-6.

Castro Neto, AH, Guinea, F, Peres, NMR, Novoselov, KS & Geim, AK 2009, 'The electronic properties

of graphene', *Reviews of Modern Physics*, vol. 81, no. 1, pp. 109-62.

Chaban, VV & Prezhdo, OV 2017, 'Microwave reduction of graphene oxide rationalized by reactive molecular dynamics', *Nanoscale*, vol. 9, no. 11, pp. 4024-33.

Chen, CM, Zhang, Q, Huang, CH, Zhao, XC, Zhang, BS, Kong, QQ, Wang, MZ, Yang, YG, Cai, R & Sheng Su, D 2012, 'Macroporous 'bubble' graphene film via template-directed ordered-assembly for high rate supercapacitors', *Chem Commun (Camb)*, vol. 48, no. 57, pp. 7149-51.

Chen, JH, Jang, C, Adam, S, Fuhrer, MS, Williams, ED & Ishigami, M 2008, 'Charged-impurity scattering in graphene', *Nature Physics*, vol. 4, p. 377-81.

Chen, L, Zhou, W, Lu, J, Li, J, Zhang, W, Huang, N, Wu, L & Li, L 2015, 'Unveiling Reinforcement and Toughening Mechanism of Filler Network in Natural Rubber with Synchrotron Radiation X-ray Nano-Computed Tomography', *Macromolecules*, vol. 48, no. 21, pp. 7923-8.

Chen, ZQ, Uedono, A, Ogura, A, Ono, H, Suzuki, R, Ohdaira, T & Mikado, T 2002, 'Oxygen-related defects and their annealing behavior in low-dose Separation-by-IMplanted OXygen (SIMOX) wafers studied by slow positron beams', *Applied Surface Science*, vol. 194, no. 1, pp. 112-5.

Cheng, M, Yang, R, Zhang, L, Shi, Z, Yang, W, Wang, D, Xie, G, Shi, D & Zhang, G 2012, 'Restoration of graphene from graphene oxide by defect repair', *Carbon*, vol. 50, no. 7, pp. 2581-7.

Choi, E, Kim, J, Cui, Y, Choi, K, Gao, Y, Han, S, Pyo, SG & Yoon, S 2017, 'Effect of the graphene oxide reduction temperature on supercapacitor performance', *Electronic Materials Letters*, vol. 13, no. 4, pp. 324-9.

Ci, L, Song, L, Jin, C, Jariwala, D, Wu, D, Li, Y, Srivastava, A, Wang, ZF, Storr, K, Balicas, L, Liu, F & Ajayan, PM 2010, 'Atomic layers of hybridized boron nitride and graphene domains', *Nat Mater*, vol. 9, no. 5, pp. 430-5.

Coraux, J, N'Diaye, AT, Busse, C & Michely, T 2008, 'Structural Coherency of Graphene on Ir(111)', *Nano Letters*, vol. 8, no. 2, pp. 565-70.

Cortijo, A & Vozmediano, MAH 2007, 'Effects of topological defects and local curvature on the electronic properties of planar graphene', *Nuclear Physics B*, vol. 763, no. 3, pp. 293-308.

Cretu, O, Krasheninnikov, AV, Rodríguez-Manzo, JA, Sun, L, Nieminen, RM & Banhart, F 2010, 'Migration and Localization of Metal Atoms on Strained Graphene', *Physical Review Letters*, vol. 105, no. 19, pp. 196102-4.

Crispin, X, Marciniak, S, Osikowicz, W, Zotti, G, van der Gon, AWD, Louwet, F, Fahlman, M, Groenendaal, L, De Schryver, F & Salaneck, WR 2003, 'Conductivity, morphology, interfacial chemistry, and stability of poly(3,4-ethylene dioxythiophene)–poly(styrene sulfonate): A photoelectron spectroscopy study', *Journal of Polymer Science Part B: Polymer Physics*, vol. 41, no. 21, pp. 2561-83.

Dahlan, HM, Khairul Zaman, MD & Ibrahim, A 2000, 'Liquid natural rubber (LNR) as a compatibilizer in NR/LLDPE blends', *Journal of Applied Polymer Science*, vol. 78, no. 10, pp. 1776-82.

Dai, B, Fu, L, Liao, L, Liu, N, Yan, K, Chen, Y & Liu, Z 2011, 'High-quality single-layer graphene via reparative reduction of graphene oxide', *Nano Research*, vol. 4, no. 5, pp. 434-9.

Dalziel, CF 1972, 'Electric shock hazard', *IEEE Spectrum*, vol. 9, no. 2, pp. 41-50.

Das, A, Pisana, S, Chakraborty, B, Piscanec, S, Saha, SK, Waghmare, UV, Novoselov, KS, Krishnamurthy, HR, Geim, AK, Ferrari, AC & Sood, AK 2008, 'Monitoring dopants by Raman scattering in an electrochemically top-gated graphene transistor', *nature nanotechnology*, vol. 3, pp. 210-15.

Didosyan, YS, Hauser, H, Reider, GA & Toriser, W 2004, 'Fast latching type optical switch', *Journal of Applied Physics*, vol. 95, no. 11, pp. 7339-41.

Dong, B, Zhang, L & Wu, Y 2017, 'Influences of different dimensional carbon-based nanofillers on fracture and fatigue resistance of natural rubber composites', *Polymer Testing*, vol. 63, pp. 281-8.

Dong, B, Wu, SZ, Zhang, LQ & Wu, YP 2016, 'High Performance Natural Rubber Composites with Well-Organized Interconnected Graphene Networks for Strain-Sensing Application', *Industrial & Engineering Chemistry Research*, vol. 55, no. 17, pp. 4919-29.

Dorri Moghadam, A, Omrani, E, Menezes, PL & Rohatgi, PK 2015, 'Mechanical and tribological

properties of self-lubricating metal matrix nanocomposites reinforced by carbon nanotubes (CNTs) and graphene – A review', *Composites Part B: Engineering*, vol. 77, pp. 402-20.

Dreyer, DR, Park, S, Bielawski, CW & Ruoff, RS 2010, 'The chemistry of graphene oxide', *Chem Soc Rev*, vol. 39, no. 1, pp. 228-40.

Dubois, E & Boué, F 2001, 'Conformation of Poly(styrenesulfonate) Polyions in the Presence of Multivalent Ions: Small-Angle Neutron Scattering Experiments', *Macromolecules*, vol. 34, no. 11, pp. 3684-97.

Edelstein, AS, Das, BN, Holtz, RL, Koon, NC, Rubinstein, M, Wolf, SA & Kihlstrom, KE 1987, 'Phase-separated Fe and Co particles in a BN matrix', *Journal of Applied Physics*, vol. 61, no. 8, pp. 3320-2.

Fan, H, Wang, L, Zhao, K, Li, N, Shi, Z, Ge, Z & Jin, Z 2010, 'Fabrication, Mechanical Properties, and Biocompatibility of Graphene-Reinforced Chitosan Composites', *Biomacromolecules*, vol. 11, no. 9, pp. 2345-51.

Fan, X, Peng, W, Li, Y, Li, X, Wang, S, Zhang, G & Zhang, F 2008, 'Deoxygenation of Exfoliated Graphite Oxide under Alkaline Conditions: A Green Route to Graphene Preparation', *Advanced Materials*, vol. 20, no. 23, pp. 4490-3.

Fan, Z, Wang, K, Wei, T, Yan, J, Song, L & Shao, B 2010, 'An environmentally friendly and efficient route for the reduction of graphene oxide by aluminum powder', *Carbon*, vol. 48, no. 5, pp. 1686-9.

Fan, Z, Zhao, Q, Li, T, Yan, J, Ren, Y, Feng, J & Wei, T 2012, 'Easy synthesis of porous graphene nanosheets and their use in supercapacitors', *Carbon*, vol. 50, no. 4, pp. 1699-703.

Fernández-Merino, MJ, Guardia, L, Paredes, JI, Villar-Rodil, S, Solís-Fernández, P, Martínez-Alonso, A & Tascón, JMD 2010, 'Vitamin C Is an Ideal Substitute for Hydrazine in the Reduction of Graphene Oxide Suspensions', *The Journal of Physical Chemistry C*, vol. 114, no. 14, pp. 6426-32.

Fu, DH, Zhan, YH, Yan, N & Xia, HS 2015, 'A comparative investigation on strain induced crystallization for graphene and carbon nanotubes filled natural rubber composites', *Express Polymer Letters*, vol. 9, no. 7, pp. 597-607.

Fu, X, Bei, F, Wang, X, O'Brien, S & Lombardi, JR 2010, 'Excitation profile of surface-enhanced Raman scattering in graphene-metal nanoparticle based derivatives', *Nanoscale*, vol. 2, no. 8, pp. 1461-6.

Fukuhara, L, Kosugi, K, Yamamoto, Y, Jinnai, H, Nishioka, H, Ishii, H & Kawahara, S 2015, 'FIB processing for natural rubber with nanomatrix structure', *Polymer*, vol. 57, pp. 143-9.

Gamero-Quijano, A, Huerta, F, Salinas-Torres, D, Morallón, E & Montilla, F 2015, 'Electrochemical Behaviour of PSS-Functionalized Silica Films Prepared by Electroassisted Deposition of Sol–Gel Precursors', *Electrocatalysis*, vol. 6, no. 1, pp. 33-41.

Gao, Y, Liu, J, Zhang, L & Cao, D 2014, 'Existence of a Glassy Layer in the Polymer-Nanosheet Interface: Evidence from Molecular Dynamics', *Macromolecular Theory and Simulations*, vol. 23, no. 1, pp. 36-48.

Garboczi, EJ & Douglas, JF 1996, 'Intrinsic conductivity of objects having arbitrary shape and conductivity', *Physical Review E*, vol. 53, no. 6, pp. 6169-80.

Garishin, OK, Shadrin, VVe, Svistkov, ALv, Sokolov, AK & Stöckelhuber, WK 2017, 'Visco-elastic-plastic properties of natural rubber filled with carbon black and layered clay nanoparticles. Experiment and simulation', *Polymer Testing*, vol. 63, pp. 133-40.

Gent, AN & Cho, IS 1999, 'Surface Instabilities in Compressed or Bent Rubber Blocks', *Rubber Chemistry and Technology*, vol. 72, no. 2, pp. 253-62.

George, N, Bipinbal, PK, Bhadran, B, Mathiazhagan, A & Joseph, R 2017, 'Segregated network formation of multiwalled carbon nanotubes in natural rubber through surfactant assisted latex compounding: A novel technique for multifunctional properties', *Polymer*, vol. 112, no. Supplement C, pp. 264-77.

Girit, ÇÖ, Meyer, JC, Erni, R, Rossell, MD, Kisielowski, C, Yang, L, Park, C-H, Crommie, MF, Cohen, ML, Louie, SG & Zettl, A 2009, 'Graphene at the Edge: Stability and Dynamics', *Science*, vol. 323, no. 5922, pp. 1705-8.

Gong, W, He, D, Tao, J, Zhao, P, Kong, L, Luo, Y, Peng, Z & Wang, H 2015, 'Formation of defects in

the graphite oxidization process: a positron study', *Rsc Advances*, vol. 5, no. 108, pp. 88908-14.

Han, Q, Yang, L, Liang, Q & Ding, M 2017, 'Three-dimensional hierarchical porous graphene aerogel for efficient adsorption and preconcentration of chemical warfare agents', *Carbon*, vol. 122, no. Supplement C, pp. 556-63.

Han, Y, Luo, Z, Yuwen, L, Tian, J, Zhu, X & Wang, L 2013, 'Synthesis of silver nanoparticles on reduced graphene oxide under microwave irradiation with starch as an ideal reductant and stabilizer', Applied Surface Science, vol. 266, pp. 188-93.

Hao, F, Fang, D & Xu, Z 2011, 'Mechanical and thermal transport properties of graphene with defects', *Applied Physics Letters*, vol. 99, no. 4, p. 041901-3.

Hayeemasae, N & Ismail, H 2016, 'Improving the Tensile Properties of Natural Rubber Compounds Containing Ground Ethylene Propylene Diene Rubber Waste by Two-stage Processing', *Procedia Chemistry*, vol. 19, pp. 810-5.

He, C, She, X, Peng, Z, Zhong, J, Liao, S, Gong, W, Liao, J & Kong, L 2015, 'Graphene networks and their influence on free-volume properties of graphene-epoxidized natural rubber composites with a segregated structure: rheological and positron annihilation studies', *Physical Chemistry Chemical Physics*, vol. 17, no. 18, pp. 12175-84.

He, H, Klinowski, J, Forster, M & Lerf, A 1998, 'A new structural model for graphite oxide', *Chemical Physics Letters*, vol. 287, no. 1, pp. 53-6.

Hernandez, Y, Nicolosi, V, Lotya, M, Blighe, FM, Sun, Z, De, S, McGovern, IT, Holland, B, Byrne, M, Gun'Ko, YK, Boland, JJ, Niraj, P, Duesberg, G, Krishnamurthy, S, Goodhue, R, Hutchison, J, Scardaci, V, Ferrari, AC & Coleman, JN 2008, 'High-yield production of graphene by liquid-phase exfoliation of graphite', *nature nanotechnology*, vol. 3, pp. 563-8.

Hirsch, A 2009, 'Unzipping Carbon Nanotubes: A Peeling Method for the Formation of Graphene Nanoribbons', *Angewandte Chemie International Edition*, vol. 48, no. 36, pp. 6594-6.

Ho, CC & Khew, MC 1999, 'Surface Morphology of Prevulcanized Natural Rubber Latex Films by Atomic Force Microscopy: New Insight into the Prevulcanization Mechanism', *Langmuir*, vol. 15, no. 19, pp. 6208-19.

Hu, S, Chen, J, Yang, N & Li, B 2017, 'Thermal transport in graphene with defect and doping: Phonon modes analysis', *Carbon*, vol. 116, no. Supplement C, pp. 139-44.

Huang, G, Hou, C, Shao, Y, Zhu, B, Jia, B, Wang, H, Zhang, Q & Li, Y 2015, 'High-performance all-solid-state yarn supercapacitors based on porous graphene ribbons', *Nano Energy*, vol. 12, pp. 26-32.

Hui, KS, Hui, KN, Dinh, DA, Tsang, CH, Cho, YR, Zhou, W, Hong, X & Chun, H-H 2014, 'Green synthesis of dimension-controlled silver nanoparticle–graphene oxide with in situ ultrasonication', *Acta Materialia*, vol. 64, no. Supplement C, pp. 326-32.

Hummers, WS & Offeman, RE 1958, 'Preparation of Graphitic Oxide', *Journal of the American Chemical Society*, vol. 80, no. 6, pp. 1339.

Jean, YC, Venkateswaran, K, Parsai, E & Cheng, KL 1984, 'Temperature dependence of positron annihilation characteristics on the surfaces of graphite powders', *Applied Physics A*, vol. 35, no. 3, pp. 169-76.

Jeon, HS, Rameshwaram, JK, Kim, G & Weinkauf, DH 2003, 'Characterization of polyisoprene–clay nanocomposites prepared by solution blending', *Polymer*, vol. 44, no. 19, pp. 5749-58.

Joseph, R, Alex, R, Madhusoodanan, KN, Premalatha, CK & Kuriakose, B 2004, 'Use of epoxidized rubber seed oil as a coupling agent and a plasticizer in silica-filled natural rubber compounds', *Journal of Applied Polymer Science*, vol. 92, no. 6, pp. 3531-6.

Kaciulis, S, Mezzi, A, Balijepalli, SK, Lavorgna, M, & Xia, HS 2015, 'Electron spectroscopy of rubber and resin-based composites containing 2D carbon', *Thin Solid Films*, vol. 581, pp. 80-85.

Kalhor, N, Boden, SA & Mizuta, H 2014, 'Sub-10nm patterning by focused He-ion beam milling for fabrication of downscaled graphene nano devices', *Microelectronic Engineering*, vol. 114, no. Supplement C, pp. 70-7.

Kargarzadeh, H, Sheltami, RM, Ahmad, I, Abdullah, I & Dufresne, A 2015, 'Cellulose nanocrystal

reinforced liquid natural rubber toughened unsaturated polyester: Effects of filler content and surface treatment on its morphological, thermal, mechanical, and viscoelastic properties', *Polymer*, vol. 71, no. Supplement C, pp. 51-9.

Kausar, A, Ilyas, H & Siddiq, M 2018, 'Aptitude of Graphene Oxide–Silver in Advance Polymer Nanocomposite: A Review', *Polymer-Plastics Technology and Engineering*, vol. 57, no. 4, pp. 283-301.

Kawahara, S, Chaikumpollert, O, Akabori, K & Yamamoto, Y 2011, 'Morphology and properties of natural rubber with nanomatrix of non-rubber components', *Polymers for Advanced Technologies*, vol. 22, no. 12, pp. 2665-7.

Keilen, JJ & Pollak, A 1947, 'Lignin for Reinforcing Rubber', *Industrial & Engineering Chemistry*, vol. 39, no. 4, pp. 480-3.

Khalid, M, Ratnam, CT, Walvekar, R, Ketabchi, MR & Hoque, ME 2017, 'Reinforced Natural Rubber Nanocomposites: Next Generation Advanced Material', in M Jawaid, et al. (eds), *Green Biocomposites: Design and Applications*, Springer International Publishing, Cham, pp. 309-45.

Kim, S, Song, Y, Ibsen, S, Ko, S-Y & Heller, MJ 2016, 'Controlled degrees of oxidation of nanoporous graphene filters for water purification using an aqueous arc discharge', *Carbon*, vol. 109, no. Supplement C, pp. 624-31.

Koch, KR 1982, 'Oxidation by Mn207: An impressive demonstration of the powerful oxidizing property of dimanganeseheptoxide', *Journal of Chemical Education*, vol. 59, no. 11, p. 973-4.

Kohjiya, S & Ikeda, Y 2014, *Chemistry, manufacture and applications of natural rubber*, Elsevier.

Korattanawittaya, S & Sirivat, A 2014, 'Fabrication of compliant electrode based on natural rubber filled with graphene nanofiller', *Journal of Biotechnology*, vol. 185, pp. S102.

Kosugi, K, Sutthangkul, R, Chaikumpollert, O, Yamamoto, Y, Sakdapipanich, J, Isono, Y & Kawahara, S 2012, 'Preparation and characterization of natural rubber with soft nanomatrix structure', *Colloid and Polymer Science*, vol. 290, no. 14, pp. 1457-62.

Kou, L, Liu, Z, Huang, T, Zheng, B, Tian, Z, Deng, Z & Gao, C 2015, 'Wet-spun, porous, orientational graphene hydrogel films for high-performance supercapacitor electrodes', *Nanoscale*, vol. 7, no. 9, pp. 4080-7.

Krasheninnikov, AV & Banhart, F 2007, 'Engineering of nanostructured carbon materials with electron or ion beams', *Nat Mater*, vol. 6, no. 10, pp. 723-33.

Krasheninnikov, AV & Nordlund, K 2010, 'Ion and electron irradiation-induced effects in nanostructured materials', *Journal of Applied Physics*, vol. 107, no. 7, p. 071301.

Kumar, R, Oh, J-H, Kim, H-J, Jung, J-H, Jung, C-H, Hong, WG, Kim, H-J, Park, J-Y & Oh, I-K 2015, 'Nanohole-Structured and Palladium-Embedded 3D Porous Graphene for Ultrahigh Hydrogen Storage and CO Oxidation Multifunctionalities', *ACS Nano*, vol. 9, no. 7, pp. 7343-51.

Lahiri, J, Lin, Y, Bozkurt, P, Oleynik, II & Batzill, M 2010, 'An extended defect in graphene as a metallic wire', *nature nanotechnology*, vol. 5, p. 326.

Leblanc, JL 2002, 'Rubber–filler interactions and rheological properties in filled compounds', *Progress in Polymer Science*, vol. 27, no. 4, pp. 627-87.

Lee, C, Wei, X, Kysar, JW & Hone, J 2008, 'Measurement of the Elastic Properties and Intrinsic Strength of Monolayer Graphene', *Science*, vol. 321, no. 5887, pp. 385-8.

Lee, JY, Kumar, V, Tang, XW & Lee, DJ 2017, 'Mechanical and electrical behavior of rubber nanocomposites under static and cyclic strain', *Composites Science and Technology*, vol. 142, pp. 1-9.

Lee, RR, von Stetten, EC, Hasegawa, M & Berko, S 1987, 'Evidence for Quasi Two-Dimensional Positronium Formation in Potassium-Intercalated Graphite', *Physical Review Letters*, vol. 58, no. 22, pp. 2363-6.

Lemme, MC, Bell, DC, Williams, JR, Stern, LA, Baugher, BWH, Jarillo-Herrero, P & Marcus, CM 2009, 'Etching of Graphene Devices with a Helium Ion Beam', *ACS Nano*, vol. 3, no. 9, pp. 2674-6.

Lerf, A, He, H, Forster, M & Klinowski, J 1998, 'Structure of Graphite Oxide Revisited', *The Journal of Physical Chemistry B*, vol. 102, no. 23, pp. 4477-82.

Li, C & Shi, G 2012, 'Three-dimensional graphene architectures', *Nanoscale*, vol. 4, no. 18, pp. 5549-63.

Li, C, Feng, C, Peng, Z, Gong, W & Kong, L 2013, 'Ammonium-assisted green fabrication of graphene/natural rubber latex composite', *Polymer Composites*, vol. 34, no. 1, pp. 88-95.

Li, S, Li, Z, Burnett, TL, Slater, TJA, Hashimoto, T & Young, RJ 2017, 'Nanocomposites of graphene nanoplatelets in natural rubber: microstructure and mechanisms of reinforcement', Journal of Materials Science, vol. 52, no. 16, pp. 9558-72.

Li, CQ, Wang, J, Chen, X, Song, YZ, Jiang, KJ, Fan, HB, Tang, M, Zhan, WT & Liao, SQ 2017, 'Structure and Properties of Reduced Graphene Oxide/Natural Rubber Latex Nanocomposites', *Journal of Nanoscience and Nanotechnology*, vol. 17, no. 2, pp. 1133-9.

Li, F, Yan, N, Zhan, Y, Fei, G & Xia, H 2013, 'Probing the reinforcing mechanism of graphene and graphene oxide in natural rubber', *Journal of Applied Polymer Science*, vol. 129, no. 4, pp. 2342-51.

Li, LF, Zhao, PF, Luo, YY, Yu, HP, Tao, JL, He, DM, Gong, W, Li, DJ, Wang, ZF & Peng, Z 2017, 'Compatibility-tuned distribution of nanoparticles in co-continuous rubber structures toward microwave absorption enhancements', *Rsc Advances*, vol. 7, no. 2, pp. 1093-100.

Li, X, Wang, X, Zhang, L, Lee, S & Dai, H 2008, 'Chemically Derived, Ultrasmooth Graphene Nanoribbon Semiconductors', *Science*, vol. 319, no. 5867, pp. 1229-32.

Li, XS, Cai, WW, An, JH, Kim, S, Nah, J, Yang, DX, Piner, R, Velamakanni, A, Jung, I, Tutuc, E, Banerjee, SK, Colombo, L & Ruoff, RS 2009, 'Large-Area Synthesis of High-Quality and Uniform Graphene Films on Copper Foils', *Science*, vol. 324, no. 5932, pp. 1312-4.

Li, Y, Xu, F, Lin, Z, Sun, X, Peng, Q, Yuan, Y, Wang, S, Yang, Z, He, X & Li, Y 2017, 'Electrically and Thermally Conductive Underwater Acoustically Absorptive Graphene/Rubber Nanocomposites for Multifunctional Applications', *Nanoscale*. Vol. 9, no. 38, pp. 14476-85.

Li, Z, Zhang, P, Wang, K, Xu, Z, Wei, J, Fan, L, Wu, D & Zhu, H 2011, 'Graphene buffered galvanic synthesis of graphene-metal hybrids', *Journal of Materials Chemistry*, vol. 21, no. 35, pp. 13241-6.

Lin, Y, Watson, KA, Kim, JW, Baggett, DW, Working, DC & Connell, JW 2013, 'Bulk preparation of holey graphene via controlled catalytic oxidation', *Nanoscale*, vol. 5, no. 17, pp. 7814-24.

Lin, Z, Yang, J, Tang, Z, Li, G & Hu, Y 2018, 'Nitrogen dots as reductant and stabilizer for the synthesis of AgNPs/N-dots nanocomposites for efficient surface-enhanced Raman scattering detection', *Talanta*, vol. 178, no. 1 , pp. 515-21.

Liu, H, Zhong, L, Yun, K & Samal, M 2016, 'Synthesis, characterization, and antibacterial properties of silver nanoparticles-graphene and graphene oxide composites', *Biotechnology and Bioprocess Engineering*, vol. 21, no. 1, pp. 1-18.

Liu, J, Wu, Y, Shen, J, Gao, Y, Zhang, L & Cao, D 2011, 'Polymer-nanoparticle interfacial behavior revisited: A molecular dynamics study', *Physical Chemistry Chemical Physics*, vol. 13, no. 28, pp. 13058-69.

Liu, S, Tian, J, Wang, L & Sun, X 2011a, 'Microwave-assisted rapid synthesis of Ag nanoparticles/graphene nanosheet composites and their application for hydrogen peroxide detection', *Journal of Nanoparticle Research*, vol. 13, no. 10, pp. 4539-48.

Liu, S, Tian, J, Wang, L & Sun, X 2011b, 'A method for the production of reduced graphene oxide using benzylamine as a reducing and stabilizing agent and its subsequent decoration with Ag nanoparticles for enzymeless hydrogen peroxide detection', *Carbon*, vol. 49, no. 10, pp. 3158-64.

LIU Yaohua, LY, ZHANG Dongge, CHEN Chunlei, WU Guozhang, ZHANG Yan, LUAN Weiling 2016, 'Fabrication of Natural Rubber/Chemically Reduced Graphene Oxide Nanocomposites and Nuclear Radiation Resistant Behavior', *Chemical Journal of Chinese Universities*, vol. 37, no. 7, pp. 1402-7.

Lombardi, JR & Birke, RL 2008, 'A Unified Approach to Surface-Enhanced Raman Spectroscopy', *The Journal of Physical Chemistry C*, vol. 112, no. 14, pp. 5605-17.

Lozano-Castelló, D, Cazorla-Amorós, D, Linares-Solano, A & Quinn, DF 2002, 'Influence of pore size distribution on methane storage at relatively low pressure: preparation of activated carbon with optimum pore size', *Carbon*, vol. 40, no. 7, pp. 989-1002.

Lucchese, MM, Stavale, F, Ferreira, EHM, Vilani, C, Moutinho, MVO, Capaz, RB, Achete, CA & Jorio, A 2010, 'Quantifying ion-induced defects and Raman relaxation length in graphene', *Carbon*, vol. 48, no. 5, pp. 1592-7.

Lui, CH, Liu, L, Mak, KF, Flynn, GW & Heinz, TF 2009, 'Ultraflat graphene', *Nature*, vol. 462, no. 7271, pp. 339-41.

Luo, J-J & Daniel, IM 2003, 'Characterization and modeling of mechanical behavior of polymer/clay nanocomposites', *Composites Science and Technology*, vol. 63, no. 11, pp. 1607-16.

Luo, Y, Zhao, P, Yang, Q, He, D, Kong, L & Peng, Z 2014, 'Fabrication of conductive elastic nanocomposites via framing intact interconnected graphene networks', *Composites Science and Technology*, vol. 100, pp. 143-51.

Lusk, MT, Wu, DT & Carr, LD 2010, 'Graphene nanoengineering and the inverse Stone-Thrower-Wales defect', *Physical Review B*, vol. 81, no. 15, pp. 155444-10.

Ma, J, Alfè, D, Michaelides, A & Wang, E 2009, 'Stone-Wales defects in graphene and other planar -bonded materials', *Physical Review B*, vol. 80, no. 3, pp. 033407-4.

Marckmann, G & Verron, E 2006, 'Comparison of Hyperelastic Models for Rubber-Like Materials', *Rubber Chemistry and Technology*, vol. 79, no. 5, pp. 835-58.

Mark, JE, Erman, B & Roland, M 2013, *The science and technology of rubber*, Academic press.

Marsh, H & Rodríguez-Reinoso, F 2006, 'CHAPTER 5 - Activation Processes (Thermal or Physical)', in *Activated Carbon*, Elsevier Science Ltd, Oxford, pp. 243-321.

Marsh, H, Yan, DS, O'Grady, TM & Wennerberg, A 1984, 'Formation of active carbons from cokes using potassium hydroxide', *Carbon*, vol. 22, no. 6, pp. 603-11.

Matsuda, H, Seo, DS, Yoshida, N, Fujibayashi, K, Kobayashi, S & Yabe, Y 1995, 'Estimation of the Static Electricity and Optical Retardation Produced by Rubbing Polyimide and Polyamide Films with Different Fabrics', *Molecular Crystals and Liquid Crystals Science and Technology. Section A. Molecular Crystals and Liquid Crystals*, vol. 264, no. 1, pp. 23-8.

Mattern, DL 1984, 'Direct aromatic periodination', *The Journal of Organic Chemistry*, vol. 49, no. 17, pp. 3051-3.

Meyer, JC, Kisielowski, C, Erni, R, Rossell, MD, Crommie, MF & Zettl, A 2008, 'Direct Imaging of Lattice Atoms and Topological Defects in Graphene Membranes', *Nano Letters*, vol. 8, no. 11, pp. 3582-6.

Mohanty, N, Nagaraja, A, Armesto, J & Berry, V 2010, 'High-Throughput, Ultrafast Synthesis of Solution- Dispersed Graphene via a Facile Hydride Chemistry', *Small*, vol. 6, no. 2, pp. 226-31.

Mondal, T, Bhowmick, AK, Ghosal, R & Mukhopadhyay, R 2017, 'Graphene-Based Elastomer Nanocomposites: Functionalization Techniques, Morphology, and Physical Properties', in KW Stockelhuber, et al. (eds), *Designing of Elastomer Nanocomposites: From Theory to Applications*, vol. 275, pp. 267-318.

Muszynski, R, Seger, B & Kamat, PV 2008, 'Decorating Graphene Sheets with Gold Nanoparticles', *The Journal of Physical Chemistry C*, vol. 112, no. 14, pp. 5263-6.

Nemec, N, Tománek, D & Cuniberti, G 2006, 'Contact Dependence of Carrier Injection in Carbon Nanotubes: An Ab Initio Study', *Physical Review Letters*, vol. 96, no. 7, pp. 076802-4.

Nguyen, GD, Toma, FM, Cao, T, Pedramrazi, Z, Chen, C, Rizzo, DJ, Joshi, T, Bronner, C, Chen, Y-C, Favaro, M, Louie, SG, Fischer, FR & Crommie, MF 2016, 'Bottom-Up Synthesis of N = 13 Sulfur-Doped Graphene Nanoribbons', *The Journal of Physical Chemistry C*, vol. 120, no. 5, pp. 2684-7.

Nie, Y, Huang, G, Qu, L, Zhang, P, Weng, G & Wu, J 2010, 'Cure kinetics and morphology of natural rubber reinforced by the in situ polymerization of zinc dimethacrylate', *Journal of Applied Polymer Science*, vol. 115, no. 1, pp. 99-106.

Niu, T, Zhang, J & Chen, W 2017, 'Atomic mechanism for the growth of wafer-scale single-crystal graphene: theoretical perspective and scanning tunneling microscopy investigations', *2D Materials*, vol. 4, no. 4, pp. 042002.

Novoselov, KS, Jiang, D, Schedin, F, Booth, TJ, Khotkevich, VV, Morozov, SV & Geim, AK 2005,

'Two-dimensional atomic crystals', *Proceedings of the National Academy of Sciences of the United States of America*, vol. 102, no. 30, pp. 10451-3.

Novoselov, KS, Geim, AK, Morozov, SV, Jiang, D, Zhang, Y, Dubonos, SV, Grigorieva, IV & Firsov, AA 2004, 'Electric Field Effect in Atomically Thin Carbon Films', *Science*, vol. 306, no. 5696, pp. 666-9.

Novoselov, KS, Geim, AK, Morozov, SV, Jiang, D, Katsnelson, MI, Grigorieva, IV, Dubonos, SV & Firsov, AA 2005, 'Two-dimensional gas of massless Dirac fermions in graphene', *Nature*, vol. 438, no. 7065, pp. 197-200.

O'Hern, SC, Boutilier, MS, Idrobo, JC, Song, Y, Kong, J, Laoui, T, Atieh, M & Karnik, R 2014, 'Selective ionic transport through tunable subnanometer pores in single-layer graphene membranes', *Nano Lett*, vol. 14, no. 3, pp. 1234-41.

Ozbas, B, O'Neill, CD, Register, RA, Aksay, IA, Prud'homme, RK & Adamson, DH 2012, 'Multifunctional elastomer nanocomposites with functionalized graphene single sheets', *Journal of Polymer Science Part B-Polymer Physics*, vol. 50, no. 13, pp. 910-6.

Ozbas, B, Toki, S, Hsiao, BS, Chu, B, Register, RA, Aksay, IA, Prud'homme, RK & Adamson, DH 2012, 'Strain-induced crystallization and mechanical properties of functionalized graphene sheet-filled natural rubber', *Journal of Polymer Science Part B-Polymer Physics*, vol. 50, no. 10, pp. 718-23.

Park, S, An, J, Piner, RD, Jung, I, Yang, D, Velamakanni, A, Nguyen, ST & Ruoff, RS 2008, 'Aqueous Suspension and Characterization of Chemically Modified Graphene Sheets', *Chemistry of Materials*, vol. 20, no. 21, pp. 6592-4.

Paul, DR & Robeson, LM 2008, 'Polymer nanotechnology: Nanocomposites', *Polymer*, vol. 49, no. 15, pp. 3187-204.

Peng, Z, Kong, LX, Li, S-D, Chen, Y & Huang, MF 2007, 'Self-assembled natural rubber/silica nanocomposites: Its preparation and characterization', *Composites Science and Technology*, vol. 67, no. 15, pp. 3130-9.

Pol, VG, Srivastava, DN, Palchik, O, Palchik, V, Slifkin, MA, Weiss, AM & Gedanken, A 2002, 'Sonochemical Deposition of Silver Nanoparticles on Silica Spheres', *Langmuir*, vol. 18, no. 8, pp. 3352-7.

Potts, JR, Shankar, O, Du, L & Ruoff, RS 2012a, 'Processing–Morphology–Property Relationships and Composite Theory Analysis of Reduced Graphene Oxide/Natural Rubber Nanocomposites', *Macromolecules*, vol. 45, no. 15, pp. 6045-55.

Potts, JR, Shankar, O, Du, L & Ruoff, RS 2012b, 'Processing-Morphology-Property Relationships and Composite Theory Analysis of Reduced Graphene Oxide/Natural Rubber Nanocomposites', *Macromolecules*, vol. 45, no. 15, pp. 6045-55.

Prakash, C, Dhananjay, SD, Shubhangi, BU, Kumar, V, & Ankush VB 2015 'Silica microspheres containing high density surface hydroxyl groups as efficient epoxidation catalysts' *Rsc Advances*, vol. 5, pp. 21125-21131.

Qiu, Y, Wang, Z, Owens, ACE, Kulaots, I, Chen, Y, Kane, AB & Hurt, RH 2014, 'Antioxidant chemistry of graphene-based materials and its role in oxidation protection technology', *Nanoscale*, vol. 6, no. 20, pp. 11744-55.

Qu, L, Liu, Y, Baek, J-B & Dai, L 2010, 'Nitrogen-Doped Graphene as Efficient Metal-Free Electrocatalyst for Oxygen Reduction in Fuel Cells', *ACS Nano*, vol. 4, no. 3, pp. 1321-6.

Ramarad, S, Khalid, M, Ratnam, CT, Chuah, AL & Rashmi, W 2015, 'Waste tire rubber in polymer blends: A review on the evolution, properties and future', *Progress in Materials Science*, vol. 72, no. Supplement C, pp. 100-40.

Rao, CNR, Sood, AK, Subrahmanyam, KS & Govindaraj, A 2009, 'Graphene: The New Two-Dimensional Nanomaterial', *Angewandte Chemie International Edition*, vol. 48, no. 42, pp. 7752-77.

Ravindran, T, Nayar, MRG & Francis, DJ 1988, 'Production of hydroxyl-terminated liquid natural rubber—mechanism of photochemical depolymerization and hydroxylation', *Journal of Applied Polymer Science*, vol. 35, no. 5, pp. 1227-39.

Reich, S, Maultzsch, J, Thomsen, C & Ordejón, P 2002, 'Tight-binding description of graphene',

Physical Review B, vol. 66, no. 3, pp. 035412-5.

Reina, A, Jia, XT, Ho, J, Nezich, D, Son, HB, Bulovic, V, Dresselhaus, MS & Kong, J 2009, 'Large Area, Few-Layer Graphene Films on Arbitrary Substrates by Chemical Vapor Deposition', *Nano Letters*, vol. 9, no. 1, pp. 30-5.

Ruiz-Hitzky, E 1993, 'Conducting polymers intercalated in layered solids', *Advanced Materials*, vol. 5, no. 5, pp. 334-40.

Rutter, GM, Crain, JN, Guisinger, NP, Li, T, First, PN & Stroscio, JA 2007, 'Scattering and Interference in Epitaxial Graphene', *Science*, vol. 317, no. 5835, pp. 219-22.

Rychagov, AY, Gubin, SP, Chuprov, PN, Kornilov, DY, Karaseva, AS, Krasnova, ES, Voronov, VA & Tkachev, SV 2017, 'Electrochemical reduction and electric conductivity of graphene oxide films', *Russian Journal of Electrochemistry*, vol. 53, no. 7, pp. 721-7.

Sanhawong, W, Banhalee, P, Boonsang, S & Kaewpirom, S 2017, 'Effect of concentrated natural rubber latex on the properties and degradation behavior of cotton-fiber-reinforced cassava starch biofoam', *Industrial Crops and Products*, vol. 108, pp. 756-66.

Sarkawi, ss, aziz, aa, aziz, akc, rahim, ra & ismail, nin 2017, 'properties of graphene nano-filler reinforced epoxidized natural rubber composites', *Journal of Polymer Science and Technology*, vol. 2, no. 1, pp. 36-44.

Scherillo, G, Lavorgna, M, Buonocore, GG, Zhan, YH, Xia, HS, Mensitieri, G & Ambrosio, L 2014, 'Tailoring Assembly of Reduced Graphene Oxide Nanosheets to Control Gas Barrier Properties of Natural Rubber Nanocomposites', *Acs Applied Materials & Interfaces*, vol. 6, no. 4, pp. 2230-4.

Schniepp, HC, Kudin, KN, Li, J-L, Prud'homme, RK, Car, R, Saville, DA & Aksay, IA 2008, 'Bending Properties of Single Functionalized Graphene Sheets Probed by Atomic Force Microscopy', ACS Nano, vol. 2, no. 12, pp. 2577-84.

Sekitani, T, Noguchi, Y, Hata, K, Fukushima, T, Aida, T & Someya, T 2008, 'A Rubberlike Stretchable Active Matrix Using Elastic Conductors', *Science*, vol. 321, no. 5895, pp. 1468-72.

Sengloyluan, K, Sahakaro, K, Dierkes, W & Noordermeer, J 2017, 'Silane grafted natural rubber and its compatibilization effect on silica-reinforced rubber tire compounds', *Express Polymer Letters*, vol. 11, no. 12, pp. 1003-1022.

Senyildiz, D, Ogurtani, OT & Buke, GC 2017, 'The effects of acid pretreatment and surface stresses on the evolution of impurity clusters and graphene formation on Cu foil', *Applied Surface Science*, vol. 425, pp. 873-8.

Sharma, SC 1988, *International Symposium on Positron Annihilation Studies of Fluids*, World Scientific Pub Co Inc.

Sheng, K-x, Xu, Y-x, Li, C & Shi, G-q 2011, 'High-performance self-assembled graphene hydrogels prepared by chemical reduction of graphene oxide', *New Carbon Materials*, vol. 26, no. 1, pp. 9-15.

Singha, D, Barman, N & Sahu, K 2014, 'A facile synthesis of high optical quality silver nanoparticles by ascorbic acid reduction in reverse micelles at room temperature', Journal of Colloid and Interface Science, vol. 413, no. Supplement C, pp. 37-42.

Sinha Ray, S & Okamoto, M 2003, 'Polymer/layered silicate nanocomposites: a review from preparation to processing', *Progress in Polymer Science*, vol. 28, no. 11, pp. 1539-641.

Sirirttikrai, N, Thanawan, S, Suchiva, K & Amornsakchai, T 2017, 'Comparative study of natural rubber/clay nanocomposites prepared from fresh or concentrated latex', *Polymer Testing*, vol. 63, pp. 244-50.

Srinivasarao, Y, Ri Hanum, YS, Chin, CH, Nandakumar, K & Thomas, S 2013, 'Electrical Properties of Graphene Filled Natural Rubber Composites', in D Kamarun, et al. (eds), Progress in Polymer and Rubber Technology, vol. 812, pp. 263-6.

Stankovich, S, Dikin, DA, Dommett, GH, Kohlhaas, KM, Zimney, EJ, Stach, EA, Piner, RD, Nguyen, ST & Ruoff, RS 2006, 'Graphene-based composite materials', *Nature*, vol. 442, no. 7100, pp. 282-6.

Stankovich, S, Dikin, DA, Piner, RD, Kohlhaas, KA, Kleinhammes, A, Jia, Y, Wu, Y, Nguyen, ST & Ruoff, RS 2007, 'Synthesis of graphene-based nanosheets via chemical reduction of exfoliated graphite

oxide', *Carbon*, vol. 45, no. 7, pp. 1558-65.

Staudenmaier, L 1898, 'Verfahren zur Darstellung der Graphitsäure', *Berichte der deutschen chemischen Gesellschaft*, vol. 31, no. 2, pp. 1481-7.

Stone, AJ & Wales, DJ 1986, 'Theoretical studies of icosahedral C60 and some related species', *Chemical Physics Letters*, vol. 128, no. 5, pp. 501-3.

Subramanian, S, Deng, DD, Xu, K, Simonson, N, Wang, K, Zhang, KH, Li, J, Feenstra, R, Fullerton-Shirey, SK & Robinson, JA 2017, 'Properties of synthetic epitaxial graphene/molybdenum disulfide lateral heterostructures', *Carbon*, vol. 125, pp. 551-6.

Suriani, AB, Nurhafizah, MD, Mohamed, A, Masrom, AK, Sahajwalla, V & Joshi, RK 2016, 'Highly conductive electrodes of graphene oxide/natural rubber latex-based electrodes by using a hyper-branched surfactant', *Materials & Design*, vol. 99, pp. 174-81.

Suriani, AB, Nurhafizah, MD, Mohamed, A, Masrom, AK, Mamat, MH, Malek, MF, Ahmad, MK, Rosmi, MS & Tanemura, M 2017, 'Electrical enhancement of radiation-vulcanized natural rubber latex added with reduced graphene oxide additives for supercapacitor electrodes', *Journal of Materials Science*, vol. 52, no. 11, pp. 6611-22.

Taluja, Y, SanthiBhushan, B, Yadav, S & Srivastava, A 2016, 'Defect and functionalized graphene for supercapacitor electrodes', *Superlattices and Microstructures*, vol. 98, no. Supplement C, pp. 306-15.

Tan, h 2006, *Naturral rubber latex product technology*, China Agriculture Press.

Tanahashi, H, Osanai, S, Shigekuni, M, Murakami, K, Ikeda, Y & Kohjiya, S 1998, 'Reinforcement of Acrylonitrile—Butadiene Rubber by Silica Generated in situ', *Rubber Chemistry and Technology*, vol. 71, no. 1, pp. 38-52.

Tanaka, Y & Tarachiwin, L 2009, 'Recent Advances in Structural Characterization of Natural Rubber', *Rubber Chemistry and Technology*, vol. 82, no. 3, pp. 283-314.

Tang, Z, Shen, S, Zhuang, J & Wang, X 2010, 'Noble-metal-promoted three-dimensional macroassembly of single-layered graphene oxide', *Angew Chem Int Ed Engl*, vol. 49, no. 27, pp. 4603-7.

Tangpakdee, J & Tanaka, Y 1997, 'Characterization of Sol and Gel in Hevea Natural Rubber', *Rubber Chemistry and Technology*, vol. 70, no. 5, pp. 707-13.

Tao, J, He, D, Tang, B, Kong, L, Luo, Y, Zhao, P, Gong, W & Peng, Z 2015, 'In situ synthesis of natural rubber latex-supported gold nanoparticles for flexible SERS substrates', *Rsc Advances*, vol. 5, no. 61, pp. 49168-74.

Tarachiwin, L, Sakdapipanich, J, Ute, K, Kitayama, T & Tanaka, Y 2005, 'Structural Characterization of α-Terminal Group of Natural Rubber. 2. Decomposition of Branch-Points by Phospholipase and Chemical Treatments', *Biomacromolecules*, vol. 6, no. 4, pp. 1858-63.

Terrones, M, Botello-Méndez, AR, Campos-Delgado, J, López-Urías, F, Vega-Cantú, YI, Rodríguez-Macías, FJ, Elías, AL, Muñoz-Sandoval, E, Cano-Márquez, AG, Charlier, J-C & Terrones, H 2010, 'Graphene and graphite nanoribbons: Morphology, properties, synthesis, defects and applications', *Nano Today*, vol. 5, no. 4, pp. 351-72.

Thomas, S & Stephen, R 2010, *Rubber nanocomposites: preparation, properties and applications*, John Wiley & Sons.

Tian, J, Liu, S, Zhang, Y, Li, H, Wang, L, Luo, Y, Asiri, AM, Al-Youbi, AO & Sun, X 2012, 'Environmentally Friendly, One-Pot Synthesis of Ag Nanoparticle-Decorated Reduced Graphene Oxide Composites and Their Application to Photocurrent Generation', *Inorganic Chemistry*, vol. 51, no. 8, pp. 4742-6.

Tsagaropoulos, G & Eisenberg, A 1995, 'Dynamic mechanical study of the factors affecting the two glass transition behavior of filled polymers. Similarities and differences with random ionomers', *Macromolecules*, vol. 28, no. 18, pp. 6067-77.

Ugeda, MM, Brihuega, I, Guinea, F & Gómez-Rodríguez, JM 2010, 'Missing Atom as a Source of Carbon Magnetism', *Physical Review Letters*, vol. 104, no. 9, pp. 096804-4.

Van Beilen, JB & Poirier, Y 2007, 'Establishment of new crops for the production of natural rubber',

Trends in Biotechnology, vol. 25, no. 11, pp. 522-9.

Velikov, KP, Zegers, GE & van Blaaderen, A 2003, 'Synthesis and Characterization of Large Colloidal Silver Particles', *Langmuir*, vol. 19, no. 4, pp. 1384-9.

Vineis, CJ, Shakouri, A, Majumdar, A & Kanatzidis, MG 2010, 'Nanostructured Thermoelectrics: Big Efficiency Gains from Small Features', *Advanced Materials*, vol. 22, no. 36, pp. 3970-80.

Voiry, D, Yang, J, Kupferberg, J, Fullon, R, Lee, C, Jeong, HY, Shin, HS & Chhowalla, M 2016, 'High-quality graphene via microwave reduction of solution-exfoliated graphene oxide', *Science*. pp. 1-6

Wang, F, Han, R, Liu, G, Chen, H, Ren, T, Yang, H & Wen, Y 2013, 'Construction of polydopamine/silver nanoparticles multilayer film for hydrogen peroxide detection', *Journal of Electroanalytical Chemistry*, vol. 706, pp. 102-7.

Wang, G, Yang, J, Park, J, Gou, X, Wang, B, Liu, H & Yao, J 2008, 'Facile Synthesis and Characterization of Graphene Nanosheets', *The Journal of Physical Chemistry C*, vol. 112, no. 22, pp. 8192-5.

Wang, H, Maiyalagan, T, & Wang, X 2012, 'Review on Recent Progress in Nitrogen-Doped Graphene: Synthesis, Characterization, and Its Potential Applications', *ACS Catalysis*, vol. 2, no. 5, pp. 781-794.

Wang, H, Xu, G & Dong, S 2002, 'Electrochemiluminescence of Tris(2,2′-bipyridyl)ruthenium(II) Ion-Exchanged in Polyelectrolyte-Silica Composite Thin-Films', Electroanalysis, vol. 14, no. 12, pp. 853-7.

Wang, J, Zhang, K, Bu, Q, Lavorgna, M & Xia, H 2017, 'Graphene-Rubber Nanocomposites: Preparation, Structure, and Properties', in S Kaneko, et al. (eds), *Carbon-related Materials in Recognition of Nobel Lectures by Prof Akira Suzuki in ICCE*, Springer International Publishing, Cham, pp. 175-209.

Wang, M-J 1998, 'Effect of Polymer-Filler and Filler-Filler Interactions on Dynamic Properties of Filled Vulcanizates', *Rubber Chemistry and Technology*, vol. 71, no. 3, pp. 520-89.

Wang, S, Tang, LAl, Bao, Q, Lin, M, Deng, S, Goh, BM & Loh, KP 2009, 'Room-Temperature Synthesis of Soluble Carbon Nanotubes by the Sonication of Graphene Oxide Nanosheets', *Journal of the American Chemical Society*, vol. 131, no. 46, pp. 16832-7.

Wang, SJ & Jean, YC 1988, 'Positron annihilation spectroscopy of methane monolayers adsorbed on graphite', *Physical Review B*, vol. 37, no. 10, pp. 4869-74.

Wang, X, Jiao, L, Sheng, K, Li, C, Dai, L & Shi, G 2013, 'Solution-processable graphene nanomeshes with controlled pore structures', *Sci Rep*, vol. 3, pp. 1996-5.

Wang, Y, Shi, Z & Yin, J 2011, 'Facile Synthesis of Soluble Graphene via a Green Reduction of Graphene Oxide in Tea Solution and Its Biocomposites', *Acs Applied Materials & Interfaces*, vol. 3, no. 4, pp. 1127-33.

Wang, Z-L, Xu, D, Wang, H-G, Wu, Z & Zhang, X-B 2013, 'In Situ Fabrication of Porous Graphene Electrodes for High-Performance Energy Storage', *ACS Nano*, vol. 7, no. 3, pp. 2422-30.

Warman, JM, de Haas, MP, Dicker, G, Grozema, FC, Piris, J & Debije, MG 2004, 'Charge Mobilities in Organic Semiconducting Materials Determined by Pulse-Radiolysis Time-Resolved Microwave Conductivity: π-Bond-Conjugated Polymers versus π−π-Stacked Discotics', *Chemistry of Materials*, vol. 16, no. 23, pp. 4600-9.

Weeraratne, W, Liyanage, N, Nadarajah, M, Amarasinghe, U & Eliatamby, D 1972, 'The use of natural rubber latex resin blends as an adhesive for plywood'. vol. 49, pp. 37-48.

Wiley, B, Sun, Y & Xia, Y 2007, 'Synthesis of Silver Nanostructures with Controlled Shapes and Properties', *Accounts of Chemical Research*, vol. 40, no. 10, pp. 1067-76.

Wolff, S 1996, 'Chemical aspects of rubber reinforcement by fillers', *Rubber Chemistry and Technology*, vol. 69, no. 3, pp. 325-346.

Wu, J, Qu, W, Huang, G, Wang, S, Huang, C & Liu, H 2017, 'Super-Resolution Fluorescence Imaging of Spatial Organization of Proteins and Lipids in Natural Rubber', *Biomacromolecules*, vol. 18, no. 6, pp. 1705-12.

Wu, J, Xing, W, Huang, G, Li, H, Tang, M, Wu, S & Liu, Y 2013, 'Vulcanization kinetics of graphene/natural rubber nanocomposites', *Polymer*, vol. 54, no. 13, pp. 3314-23.

Wu, M-C, Deokar, AR, Liao, J-H, Shih, P-Y & Ling, Y-C 2013, 'Graphene-Based Photothermal Agent for Rapid and Effective Killing of Bacteria', ACS Nano, vol. 7, no. 2, pp. 1281-90.

Wu, X, Lin, TF, Tang, ZH, Gou, BC, & Huang, GS 2015, 'Natural rubber/graphene oxide composites: Effect of sheet size on mechanical properties and straininduced crystallization behavior', *Express Polymer Letters*, vol. 9, no. 8, pp. 672-685.

Wu, Z-S, Ren, W, Xu, L, Li, F & Cheng, H-M 2011, 'Doped Graphene Sheets As Anode Materials with Superhigh Rate and Large Capacity for Lithium Ion Batteries', *ACS Nano*, vol. 5, no. 7, pp. 5463-71.

Xianjian, D, Liquan, z, Shemao, W & Yizhong, W 2000, '*In- situ* silica reinforcing rubber by sol- gel method', *China Synthetic Rubber Industry*, no. 03, pp. 148-52.

Xu, T, Jia, Z, Luo, Y, Jia, D & Peng, Z 2015, 'Interfacial interaction between the epoxidized natural rubber and silica in natural rubber/silica composites', *Applied Surface Science*, vol. 328, no. Supplement C, pp. 306-13.

Xu, T, Jia, Z, Wu, L, Chen, Y, Luo, Y, Jia, D & Peng, Z 2017, 'Influence of acetone extract from natural rubber on the structure and interface interaction in NR/silica composites', *Applied Surface Science*, vol. 423, no. Supplement C, pp. 43-52.

Yan, J, Fan, Z, Wei, T, Qian, W, Zhang, M & Wei, F 2010, 'Fast and reversible surface redox reaction of graphene–MnO2 composites as supercapacitor electrodes', *Carbon*, vol. 48, no. 13, pp. 3825-33.

Yan, N, Xia, H, Zhan, Y & Fei, G 2013, 'New Insights into Fatigue Crack Growth in Graphene-Filled Natural Rubber Composites by Microfocus Hard-X-Ray Beamline Radiation', *Macromolecular Materials and Engineering*, vol. 298, no. 1, pp. 38-44.

Yan, N, Xia, H, Wu, J, Zhan, Y, Fei, G & Chen, C 2013, 'Compatibilization of natural rubber/high density polyethylene thermoplastic vulcanizate with graphene oxide through ultrasonically assisted latex mixing', *Journal of Applied Polymer Science*, vol. 127, no. 2, pp. 933-41.

Yan, N, Buonocore, G, Lavorgna, M, Kaciulis, S, Balijepalli, SK, Zhan, Y, Xia, H & Ambrosio, L 2014, 'The role of reduced graphene oxide on chemical, mechanical and barrier properties of natural rubber composites', *Composites Science and Technology*, vol. 102, pp. 74-81.

Yang, D, Velamakanni, A, Bozoklu, G, Park, S, Stoller, M, Piner, RD, Stankovich, S, Jung, I, Field, DA, Ventrice, CA & Ruoff, RS 2009, 'Chemical analysis of graphene oxide films after heat and chemical treatments by X-ray photoelectron and Micro-Raman spectroscopy', *Carbon*, vol. 47, no. 1, pp. 145-52.

Yang, X, Dou, X, Rouhanipour, A, Zhi, L, Räder, HJ & Müllen, K 2008, 'Two-Dimensional Graphene Nanoribbons', *Journal of the American Chemical Society*, vol. 130, no. 13, pp. 4216-7.

Yang, Z, Guo, B & Zhang, L 2017, 'CHALLENGE OF RUBBER/GRAPHENE COMPOSITES AIMING AT REAL APPLICATIONS', *Rubber Chemistry and Technology*, vol. 90, no. 2, pp. 225-37.

Yanhua, L 2012, 'Structure and performance study on silica in situ modified NR', master thesis, Hunan University of Technology.

Yazyev, OV & Louie, SG 2010, 'Topological defects in graphene: Dislocations and grain boundaries', *Physical Review B*, vol. 81, no. 19, pp. 195420-7.

Yi, J, Lee, DH, Lee, WW & Park, WI 2013, 'Direct Synthesis of Graphene Meshes and Semipermanent Electrical Doping', *The Journal of Physical Chemistry Letters*, vol. 4, no. 13, pp. 2099-104.

Yu, ZR, Shi, ZX, Xu, HJ, Ma, XD, Tian, M & Yin, J 2017, 'Green chemistry: Co-assembly of tannin-assisted exfoliated low-defect graphene and epoxy natural rubber latex to form soft and elastic nacre-like film with good electrical conductivity', *Carbon*, vol. 114, pp. 649-60.

Yuan, QW & Mark, JE 1999, 'Reinforcement of poly(dimethylsiloxane) networks by blended and in-situgenerated silica fillers having various sizes, size distributions, and modified surfaces', *Macromolecular Chemistry and Physics*, vol. 200, no. 1, pp. 206-20.

Yuan, W, Gu, Y & Li, L 2012, 'Green synthesis of graphene/Ag nanocomposites', *Applied Surface Science*, vol. 261, pp. 753-8.

Zandiatashbar, A, Lee, G-H, An, SJ, Lee, S, Mathew, N, Terrones, M, Hayashi, T, Picu, CR, Hone, J & Koratkar, N 2014, 'Effect of defects on the intrinsic strength and stiffness of graphene', *nature communications*, vol. 5, pp. 3186-94.

Zhan, Y, Lavorgna, M, Buonocore, G & Xia, H 2012, 'Enhancing electrical conductivity of rubber composites by constructing interconnected network of self-assembled graphene with latex mixing', *Journal of Materials Chemistry*, vol. 22, no. 21, pp. 10464-8.

Zhan, Y, Wu, J, Xia, H, Yan, N, Fei, G & Yuan, G 2011, 'Dispersion and Exfoliation of Graphene in Rubber by an Ultrasonically-Assisted Latex Mixing and In situ Reduction Process', *Macromolecular Materials and Engineering*, vol. 296, no. 7, pp. 590-602.

Zhan, YH, Meng, YY & Li, YC 2017, 'Electric heating behavior of flexible grapheneinatural rubber conductor with self-healing conductive network', *Materials Letters*, vol. 192, pp. 115-8.

Zhang, L, Li, H, Lai, X, Wu, W & Zeng, X 2018, 'Hindered phenol functionalized graphene oxide for natural rubber', *Materials Letters*, vol. 210, pp. 239-42.

Zhang, L, Zhang, F, Yang, X, Long, G, Wu, Y, Zhang, T, Leng, K, Huang, Y, Ma, Y, Yu, A & Chen, Y 2013, 'Porous 3D graphene-based bulk materials with exceptional high surface area and excellent conductivity for supercapacitors', *Sci Rep*, vol. 3, pp. 1408-16.

Zhang, S, Shao, Y, Liao, H, Engelhard, MH, Yin, G & Lin, Y 2011, 'Polyelectrolyte-Induced Reduction of Exfoliated Graphite Oxide: A Facile Route to Synthesis of Soluble Graphene Nanosheets', *ACS Nano*, vol. 5, no. 3, pp. 1785-91.

Zhang, W, Cui, J, Tao, CA, Wu, Y, Li, Z, Ma, L, Wen, Y & Li, G 2009, 'A strategy for producing pure single-layer graphene sheets based on a confined self-assembly approach', *Angew Chem Int Ed Engl*, vol. 48, no. 32, pp. 5864-8.

Zhang, XM, Xue, XD, Yin, Q, Jia, HB, Wang, JY, Ji, QM & Xu, ZD 2017, 'Enhanced compatibility and mechanical properties of carboxylated acrylonitrile butadiene rubber/styrene butadiene rubber by using graphene oxide as reinforcing filler', *Composites Part B-Engineering*, vol. 111, pp. 243-50.

Zhang, Y, Tan, Y-W, Stormer, HL & Kim, P 2005, 'Experimental observation of the quantum Hall effect and Berry's phase in graphene', *Nature*, vol. 438, no. 7065, pp. 201-4.

Zhang, Y, Chen, L, Xu, Z, Li, Y, Zhou, B, Shan, M, Wang, Z, Guo, Q & Qian, X 2012, 'Preparing graphene with notched edges and nanopore defects by γ-ray etching of graphite oxide', *Materials Letters*, vol. 89, pp. 226-8.

Zhao, J, Pei, S, Ren, W, Gao, L & Cheng, H-M 2010, 'Efficient Preparation of Large-Area Graphene Oxide Sheets for Transparent Conductive Films', *ACS Nano*, vol. 4, no. 9, pp. 5245-52.

Zhao, P, Luo, Y, Yang, J, He, D, Kong, L, Zheng, P & Yang, Q 2014, 'Electrically conductive graphene-filled polymer composites with well organized three-dimensional microstructure', *Materials Letters*, vol. 121, pp. 74-7.

Zhao, X, Hayner, CM, Kung, MC & Kung, HH 2011, 'Flexible Holey Graphene Paper Electrodes with Enhanced Rate Capability for Energy Storage Applications', *ACS Nano*, vol. 5, no. 11, pp. 8739-49.

Zhiping, X & Kun, X 2010, 'Engineering graphene by oxidation: a first-principles study', *Nanotechnology*, vol. 21, no. 4, p. 045704-9.

Zhou, Y, Ge, L, Fan, N, Dai, L & Xia, M 2018, 'Cure characteristics, mechanical, thermal, and coloring properties of natural rubber/dye-loaded shell powder composites', *Journal of Applied Polymer Science*, vol. 135, no. 4. pp. 45750-61.

Zhu, C, Liu, T, Qian, F, Chen, W, Chandrasekaran, S, Yao, B, Song, Y, Duoss, EB, Kuntz, JD, Spadaccini, CM, Worsley, MA & Li, Y 2017, '3D printed functional nanomaterials for electrochemical energy storage', *Nano Today*, vol. 15, no. Supplement C, pp. 107-20.

Zhu, Y, Murali, S, Cai, W, Li, X, Suk, JW, Potts, JR & Ruoff, RS 2010, 'Graphene and graphene oxide: synthesis, properties, and applications', *Adv Mater*, vol. 22, no. 35, pp. 3906-24.

Zhu, Y, Stoller, MD, Cai, W, Velamakanni, A, Piner, RD, Chen, D & Ruoff, RS 2010, 'Exfoliation of Graphite Oxide in Propylene Carbonate and Thermal Reduction of the Resulting Graphene Oxide Platelets', *ACS Nano*, vol. 4, no. 2, pp. 1227-33.

Zhu, Y, Murali, S, Stoller, MD, Ganesh, KJ, Cai, W, Ferreira, PJ, Pirkle, A, Wallace, RM, Cychosz, KA, Thommes, M, Su, D, Stach, EA & Ruoff, RS 2011, 'Carbon-Based Supercapacitors Produced by Activation of Graphene', *Science*, vol. 332, no. 6037, pp. 1537-4.